Energy and Buoyancy Transport by Inertia-Gravity Waves in Non-Linear Stratifications. Application to the Ocean

Samuel Boury

Numéro National de Thèse : 2020LYSEN014

THÈSE de DOCTORAT DE L'UNIVERSITÉ DE LYON
opérée par
l'École Normale Supérieure de Lyon

École Doctorale N°52
Physique et Astrophysique de Lyon (PHAST)

Discipline : Physique

Soutenue publiquement le 14/05/2020, par :
Samuel BOURY

Energy and Buoyancy Transport by Inertia-Gravity Waves in Non-Linear Stratifications. Application to the Ocean.

Transport d'énergie et de flottabilité par ondes gravito-inertielles dans des stratifications non-linéaires. Application à l'océan.

Devant le jury composé de :

Chillà, Francesca	Professor	ENS de Lyon, LabPHYS	Présidente
Caulfield, Colm-Cille	Professor	Univ. of Cambridge, DAMTP	Rapporteur
Maas, Leo	Professor	Univ. of Twente, NIOZ	Rapporteur
Meunier, Patrice	DR CNRS	Univ. Aix-Marseille, IRPHÉ	Examinateur
Muller, Caroline	CR CNRS	ENS Ulm, LMD	Examinatrice
Odier, Philippe	MCF	ENS de Lyon, LabPHYS	Directeur de thèse
Peacock, Thomas	Professor	MIT, MechE ENDLab	Co-directeur de thèse

Contents

Acknowledgements

First of all, I would like to express my deepest gratitude to my two thesis advisors, Philippe and Tom, whose sincere trust and profound belief in my abilities never faltered. Their availability, support, and friendship meant a lot to me and allowed me to undertake this life-changing scientific and personal journey. Under their unwavering guidance, and through our always fruitful and constructive exchanges, I was able to discover and explore the marvelous and fascinating physics of internal waves and stratified flows. Particularly meaningful to me are all the memories of the moments spent together and of our little adventures: the bike rides from Jamaica Plains to MIT; the working sessions at the gym near Boston and in Concord; the good restaurants we discovered together; the expedition to Alaska and the five-week Arctic cruise on the Sikuliaq. Thank you Philippe for your constant investment by my side in this thesis. Thanks again, Tom, for having introduced me to physical oceanography and for having entrusted me with the Chukchi project from scratch. I consider myself very fortunate to have been your advisee and, with the both of you, I can really say that I benefitted from the best possible supervision. It has been a great pleasure to work with you. Today, I am glad to say that, new ideas and new side projects popping up here and there, the end of this thesis is not the end of our collaboration.

I also wish to address my sincere thanks to the members of my jury: first of all to my reviewers, Colm-Cille Caulfield and Leo Maas, for taking the time to read my manuscript carefully and for allowing me to defend; to Francesca Chillà, for agreeing to be the chair of my committee; and to Caroline Muller and Patrice Meunier, who also gave me very useful feedback. I very much appreciated them making sure that my defense went very smoothly despite the total lockdown and confinement that were enforced at the time, compelling me to defend online. To quote Philippe's words: it is somewhat ironic to have spent nearly three years trying to confine waves, to end up being confined myself just after writing the thesis. I would like to take this opportunity to thank all those who attended my defense from home.

I would like to acknowledge the Laboratoire de Physique de l'École Normale Supérieure de Lyon, and especially its directors Thierry and more recently Jean-Christophe, for offering me a very pleasant working environment. Likewise, it has been a great pleasure to come so often to the Environmental Dynamic Laboratory at the Massachusetts Institute of Technology, where Tom did so much to welcome me in the best possible way. I also wish to acknowledge the École Doctorale de Lyon for their assistance, as well as the different programs that granted me fundings throughout this thesis.

During this time period, I have had the great pleasure of working and starting projects with various collaborators: Matthew Alford, Thierry Dauxois, Evgeny Ermanyuk, Elizabeth Fine, Chanhyung Jeon, Sylvain Joubaud, Michael Le Bars, Min Li, Peigen Lin, Jennifer MacKinnon, Jae-Hun Park, Paco Maurer, Robert Pickart, Ilias Sibgatullin, Harper Simmons, and Bruce Sutherland. I am grateful to Thierry and Evgeny for reaching out to me with new attractor ideas to explore, and I would also like to extend my gratitude to Sylvain, whose experimental expertise has repeatedly been an invaluable support to me. I am deeply indebted to Jennifer and Tom who took me with them to the Arctic and, without naming them, I would like to sincerely thank all the people with

whom I shared these 5 weeks on the Sikuliaq. Many thanks to the fluid dynamicists of the Geophysical Fluid Dynamics program in Woods Hole, the fellows with whom I had such good times and intense softball games, all the researchers who keep this program alive, and of course Colin Meyer, Geoff Vasil, and Andrew Wells, who brought me back to my early astronomical interests by taking me near the geysers of the tiny mushy moon of Enceladus.

It would be a long list to mention them all, but I also wish to thank the PhD students, post-docs, and researchers of the Laboratoire de Physique de l'ENS de Lyon and of the MIT, with whom I have had the pleasure of sharing numerous coffee breaks, often around quite lively discussions. Especially important to me during this time were my colleagues from the junior laboratory *Géophysique et Fluides Planétaires*, the several *Fêtes de la Science*, and all the experiments we did together. More broadly, of course, I would like to acknowledge the assistance of the mechanic and electronic teams of the laboratory, as well as the PSMN, without whom this thesis could not have been completed. I cannot leave the laboratory without mentioning the secretaries, especially Fatiha, whose help with administrative tasks and mission orders should not be underestimated.

I also want to say a more specific word about my experiment, more intimately known as "Cuve" – we often forget to say how important an experiment, and even more so of this size, is in a thesis and in a life. I would like to thank, among others, Paco Maurer for setting it up and for passing on his knowledge to me at the end of his own thesis, in the unconventional context of a bonus internship. This manuscript is an opportunity to say goodbye with a heavy heart to this marvelous experiment, now that it is going to be dismantled to make space for a new project.

Here, I would also like to extend my gratitude to my former professors and teachers back in Brittany who played a decisive role in encouraging me to follow a scientific path. You supported what seemed to be at the time, perhaps, a wild dream, and for that I thank you. Even if some of you are now gone, having been your student will continue to inspire me.

Many thanks to my family and friends, of course, who have supported me for a very long time without necessarily understanding what I was doing. Thanks in particular to my parents, who had no idea, even a few years ago, what journey I was going to undertake and what I was going to experience through my PhD.

A very special thanks to Jeanne who knows the full story. I really cannot say how grateful I am: you have always encouraged me since the very beginning, and this thesis straddling two continents would simply not have happened, let alone started, if you had not been here by my side.

Notations

Commonly used notations in the manuscript:

Symbol	Meaning	Symbol	Meaning
a	Wave generator amplitude	Y_n	2nd Bessel function of order n
b	Buoyancy	$\mathcal{F}$	Fourier transform
$\mathbf{e_r}$	Radial unit vector	$\mathcal{F}_n$	Any one of J_n, Y_n, $H_n^{(1)}$, and $H_n^{(2)}$
$\mathbf{e_x}$	x horizontal unit vector	$\mathcal{H}$	Hankel transform
$\mathbf{e_y}$	y horizontal unit vector	$\mathcal{J}$	Cartesian Jacobian
$\mathbf{e_z}$	Angular unit vector	$\mathcal{J}^{\odot}$	Cylindrical Jacobian
$\mathbf{e}_\theta$	Vertical unit vector	$\mathcal{L}$	Linear equations
f	Coriolis frequency	$\mathcal{N}$	Non-linear equations
g	Gravity	C	Cosine Fresnel integral
k	Magnitude of the wave vector	F	Fresnel integral
k_x, k_y, k_z	Cartesian wave numbers	S	Sine Fresnel integral
l	Radial wavenumber	α	Buoyancy frequency ratio
m	Vertical wavenumber	β	Propagation angle
n	Index	γ	Coriolis frequency ratio
p	Pressure field	δ	Interface width
(p, q)	Cavity mode	ε	Viscosity-based parameter
r	Radial coordinate	λ	Vertical wave length
t	Temporal coordinate	ψ	Streamfunction
v_g	Group velocity	ϕ	Vertical dependence
v_r	Radial velocity	μ	Dynamic viscosity
v_z	Vertical velocity	ν	Viscosity
v_θ	Azimuthal (orthoradial) velocity	ω	Frequency of the wave field
v_ϕ	Phase velocity	ρ	Density
x, y, z	Cartesian coordinates	$\bar{\rho}$	Background density
E	Ekman number	ρ'	Density fluctuation
G	Green function	σ	Growth rate
$H_n^{(1)}$	1st Hankel function of order n	θ	Angular coordinate
$H_n^{(2)}$	2nd Hankel function of order n	ξ	Vorticity
J_n	1st Bessel function of order n	ξ_z	Enstrophy
$\tilde{J}_n$	Asymptotic Bessel function	Δ	Laplacian
L	Vertical characteristic length	Δ_h	Horizontal Laplacian
N	Brunt-Väisälä (buoyancy) frequency	$\Delta^{\odot}$	Cylindrical Laplacian
R	Radius of the wave generator	Γ	Dispersion relation parameter
R_X	Reflexion coefficient of X	$\Gamma(...)$	Asymptotic Bessel integrals
Ro	Rossby number	Ω	Rotation frequency
T	Temporal period of the wave field	Ξ	Triple Bessel integral
T_X	Transmission coefficient of X	∇	Nabla operator

Introduction

Geophysical fluids such as the oceans and the atmosphere are density stratified fluids in rotation, creating anisotropies that support the propagation of waves over large scales, called inertia-gravity waves. Ubiquitious in the oceans, these waves are believed to play a key role in the transport of energy and buoyancy across the global ocean, by maintaining the thermohaline circulation and connecting scales from tidal macroscale energy inputs to turbulent microscale dissipation.

In his *abyssal recipes* [156], Munk introduced an eddy diffusivity to characterise a uniform unidimensional upwelling over the entire abyssal ocean as a possible mechanism to contribute to drive oceanic mixing. Since then, oceanographers have tried to provide an even more accurate description of stratified mixing in the oceans [157, 186, 242]. A recent study from MacKinnon *et al.* [133] details internal wave driven mixing in the oceans. They present various generation mechanisms of such waves in the oceans as well as possible contributions to oceanic mixing: excitation by tidal motion and interaction with topographies [59], inertial oscillations created in the near-surface mixed layer, mesoscale interactions with eddies and currents [190], wave-wave interaction, instabilities and wave breaking [12, 132].

Of primary importance are energy and buoyancy transport phenomenon by inertia-gravity waves in the oceans as, according to estimates from satellite observations [70, 71], a third of the 3 TW input from tidal forcing is being dissipated on deep ocean topographies, and a significant part of it is transferred to internal waves [249]. Since about 1 to 2 TW energy is needed to close the energetic balance in the oceans and help cold and salty water rise to the surface [157], comparable to inertia-gravity waves total energy, making them a very likely candidate to sustain stratified mixing and link energy input in the ocean to turbulent mixing. In that sense, internal wave activity is a major phenomenon connecting large scale events (e.g. tidal forcing) to small scale dissipation processes (turbulent mixing).

Through linear and non-linear processes, energy can be transported from place to place over the world and propagate within the oceanic stratification, from the surface to the deep ocean and vice versa, but also from scale to scale until energy input is being dissipated at the smallest scales. Thanks to laboratory experiments supported by theoretical and numerical derivations, this thesis proposes to closely study the effect of geometry on internal waves and energy transport by using an axisymmetric wave generator [92, 141] to excite cylindrical wave fields, and by investigating how the transition from two-dimensional Cartesian plane waves to three-dimensional axisymmetric wave fields impacts classical results on linear propagation and non-linear interactions in internal wave studies, with a clear link to oceanic applications.

This manuscript is divided in five parts:

- **Internal Waves: From Theory and Experiments to Real-World**

  The first part gives a broad introduction to internal waves. Chapter 1 presents the physics of density stratified and rotating fluids, and the theory of inertia-gravity waves in Cartesian, axisymmetric, and cylindrical geometry. In the following chapter 2, the experimental setup and methods are detailed. This chapter, notably, describes the wave generator used to produce axisymmetric wave fields in the laboratory. Then, in chapter 3, we discuss the relevance of internal waves in geophysical fluids, more particularly the atmosphere and the oceans, and we explain the importance of studying such phenomena in oceanography and for climate dynamics. This part led to the publication of a pedagogical article:

  [30] S. Boury, S. Joubaud, and M. Le Bars. Pourquoi les meddies existent-ils ? *Bulletin de l'Union des Physiciens*, 2020.

- **Axisymmetric Waves in the Linear Regime**

  The second part deals with axisymmetric waves in the linear regime, meaning that the wave equations we consider are all linearised. The simplest case of uniform density stratification without rotation is presented in chapter 4, in which modes (radial standing wave fields) propagating downwards are analytically described and experimentally observed, as well as the effect of confinement. Chapter 5 then presents the case of two-layer stratifications with a buoyancy frequency interface, at which the wave can be transmitted and reflected. This study was extended to the case of real-world stratifications in the Arctic to investigate the amount of energy transmitted from the surface of the ocean to the deep abyss. Finally, chapter 6 presents preliminary results on internal wave tunneling in the case of three-layer stratifications with an intermediate layer at constant density. These works led to two articles, plus two in preparation:

  [33] S. Boury, T. Peacock, and P. Odier. Excitation and resonant enhancement of axisymmetric internal wave modes. *Physical Review Fluids*, 4 : 034802, 2019.

  [32] S. Boury, P. Odier, and T. Peacock. Axisymmetric internal wave transmission and resonance in non-linear stratifications. *Journal of Fluid Mechanics*, 886 : A8, 2020.

  [105] C. Jeon, S. Boury, T. Peacock, J.-H. Park, and K.-H. Cho. Observation of spatial and temporal variability of deep near-inertial waves in the western Arctic Ocean. *Geophysical Research Letters*, in preparation.

  [37] S. Boury, B.R. Sutherland, P. Odier, and T. Peacock. Axisymmetric internal wave tunneling. *Physical Review Fluids*, in preparation.

- **Non-Linear Effects and Axisymmetry Breaking**

  The third part delves further into the non-linear contributions of the internal wave equations that were left aside in the previous part. The generation of super-harmonics and of sub-harmonics is explored in chapter 7, with the possibility of self-interaction in linear stratification and the impact of the geometry on the non-linear equations. Chapter 8 presents an experimental realisation of an axisymmetric inertial wave attractor, in unstratified rotating fluid, that goes unstable and whose non-linearities result in the creation of vertical vortices and in axisymmetry breaking. These works will lead to three articles:

  [34] S. Boury, T. Peacock, and P. Odier. Experimental self-generation of axisymmetric internal wave super-harmonics. *Physical Review Fluids*, in preparation.

  [31] S. Boury, P. Maurer, S. Joubaud, T. Peacock, and P. Odier. Triadic resonant instability in confined and unconfined axisymmetric geometries. *Journal of Fluid Mechanics*, in preparation.

  [36] S. Boury, I. Sibgatullin, E. Ermanyuk, N. Shmakova, P. Odier, S. Joubaud, and T. Dauxois. Vortex cluster arising from an axisymmetric wave attractor. *Journal of Fluid Mechanics*, in preparation.

- **Energy and Buoyancy Transport in the Arctic: A Case Study**

  Although indirectly related to internal wave studies, the fourth part describes work undertaken within the Stratified Ocean Dynamics of the Arctic (SODA) research campaign, in which I took part in September 2018. Motivated by the increasingly rapid warming of the Arctic Ocean, the project consisted of deploying five SOLO floats as quasi-Lagrangian particles in the core of a newly discovered current, the Chukchi Slope Current, to track its trajectory and provide insights on the transport of heat and nutrients in the cold Arctic waters. Chapter 9 corresponds to the following article:

  [35] S. Boury, R.S. Pickart, P. Odier, P. Lin, M. Li, E.C. Fine, H.L. Simmons, J.A. MacKinnon, and T. Peacock. Whither the Chukchi Slope Current? *Journal of Physical Oceanography*, 50 : 1717–1732, 2020.

- **Conclusion**

  The fifth part presents our conclusions and discussion on this thesis work and its implications on the transport of energy and buoyancy in the oceans by inertia-gravity waves. Perspectives for further studies are also presented.

Part I

Internal Waves: From Theory and Experiments to Real-World

CHAPTER 1

Theory of Internal Inertia-Gravity Waves

Et comme un éclatant abrégé des saisons,
Mon cœur découvre en soi tropiques et banquises
Voyageant d'île en cap et de port en surprise
Il démêle un écheveau d'horizons.
Jules Supervielle, DÉBARCADÈRES.

As any geophysical fluid, the oceans are suitable media for the propagation of particular waves called *internal waves*, which have both the properties of *gravity waves* and *inertial waves*.

The first ones result from the existence of a vertical anisotropy within the fluid: its density ρ varies either with altitude, as in the atmosphere, or with depth, as in oceans and lakes [171, 220]. Several origins of such stratifications can be found, the most important being the varying temperature T and salinity S, the density being a function of T and S. As an example, water is usually far more salty and colder in the deep regions of the oceans than it is close to the surface, so that deep oceanic water has the highest density. This property of the fluid allows the propagation of *gravity waves* thanks to an oscillatory mechanism involving variations of density and restoring forces due to gravity, namely the weight and the Archimedes forces.

The second type of waves is a direct consequence of the intrinsic rotation of geophysical fluids, which is the Earth rotation in the case of the atmosphere and the oceans. In order to take this phenomenon into account, a pseudo-force is introduced in the Navier-Stokes equations, known as the Coriolis force, that leads to a horizontal stratification of angular momentum allowing the propagation of oscillatory movements within the fluid. These motions are called *inertial waves*.

This chapter derives the fundamentals of internal inertia-gravity waves theory, starting from the description of the physics of a rotating stratified fluid in section 1.1 to explain the two oscillatory phenomena due to gravity and inertia. In section 1.2 we derive the mathematical framework for 2D internal waves in Cartesian geometry, with a translation invariance along the transverse direction. This analytical derivation is extended in section 1.3 to axisymmetric geometry, which means in cylindrical coordinates with an invariance by rotation around a symmetry axis. To take into account the inherent 3D effects, the rotation invariance is relaxed in section 1.4 to consider fully 3D cylindrical wave fields.

1.1 Physics of a Rotating Stratified Fluid

This section explains how density stratification and rotation help support wave propagation in geophysical fluids thanks to theoretical considerations. For further reading, experimental illustrations of rotating stratified fluid physics can be found in Boury *et al.* [30].

1.1.1 Physics of a Stratified Fluid

To begin with, we consider a density stratified fluid. This homogeneous medium presents an anisotropy along the vertical direction, associated to the vertical ascendant z-axis, meaning that its density ρ is a function of z, noted $\rho(z)$.

In a static mechanical equilibrium, the balance between gravity and pressure forces leads to the hydrostatic equation

$$\frac{\partial p}{\partial z} = -\bar{\rho}(z)g, \tag{1.1}$$

where p is the pressure within the fluid, g the gravity acceleration, and $\bar{\rho}$ the local density at equilibrium, called *background density*.

We now consider an elementary volume of fluid located at $z = z_\upsilon$ that is assumed to be small enough to be considered of uniform density. At rest, the parcel of fluid has the same density ρ_υ as the background density, $\rho_\upsilon = \bar{\rho}(z_\upsilon)$. To provide some details on the dynamics of such a particle when moved at an altitude z, a classical mechanics approach can be used. This particle undergoes a downward gravity force which is, per unit of volume, proportional to its density

$$\mathbf{P} = -\rho_\upsilon g \mathbf{e_z}, \tag{1.2}$$

and an upward Archimedes force, representing the fluid displaced, proportional to the background density taken at the particle's position

$$\mathbf{\Pi} = \bar{\rho}(z) g \mathbf{e_z}, \tag{1.3}$$

two vertically-oriented forces whose sum $\mathbf{R}$ can be written as

$$\mathbf{R} = (\bar{\rho}(z) - \rho_\upsilon) g \mathbf{e_z}. \tag{1.4}$$

Equation (1.4) shows that the overall force points upwards if the system is surrounded by lighter fluid, and downwards if it is surrounded by heavier fluid, when neglecting all diffusive effects so that the fluid particle remains at constant density ρ_υ. At rest, $z = z_\nu$ and, by definition, $\mathbf{R} = 0$ so that the particle's weight and the Archimedes force exaclty balance each other. As a result, moving the particle along the vertical axis will change the reaction force $\mathbf{R}$, that draws the particle back to its equilibrium position $z = z_\upsilon$, starting an oscillatory movement.

In a more quantitative way, according to Newton's law, the vertical dynamics is given by

$$\rho_\upsilon \frac{\mathrm{d}^2 z}{\mathrm{d}t^2} = (\bar{\rho}(z) - \rho_\upsilon) g. \tag{1.5}$$

Considering a small displacement δz of the fluid particle along the vertical axis, equation (1.5) leads to the following development at the lowest non-trivial order

$$\begin{aligned} \frac{\mathrm{d}^2 \delta z}{\mathrm{d}t^2} &= \frac{g}{\rho_\upsilon}(\bar{\rho}(z_\upsilon + \delta z) - \rho_\upsilon), & (1.6)\\ &= \frac{g}{\rho_\upsilon} \left.\frac{\partial \bar{\rho}}{\partial z}\right|_{z=z_\upsilon} \delta z + \mathcal{O}(\delta z^2), & (1.7)\\ &= -N^2(z_\upsilon)\delta z + \mathcal{O}(\delta z^2). & (1.8) \end{aligned}$$

Hence, at order $\mathcal{O}(\delta z)$, equation (1.8) describes a harmonic oscillator of pulsation N, called *buoyancy* or *Brünt-Väisälä* frequency, and defined by

$$N(z_\upsilon) = \sqrt{-\frac{g}{\bar{\rho}(z_\upsilon)} \left.\frac{\partial \bar{\rho}}{\partial z}\right|_{z_\upsilon}}. \tag{1.9}$$

Note that N is only defined for stratifications with a negative vertical density gradient, which means fluids in which ρ decreases with altitude, so that $N^2 \geq 0$. Such a gradient is often given as a stability condition for the fluid, though opposite gradients can exist locally and trigger mixing events (see, e.g., the case of Kelvin-Helmholtz billows [230]). In the limit case of an unstratified

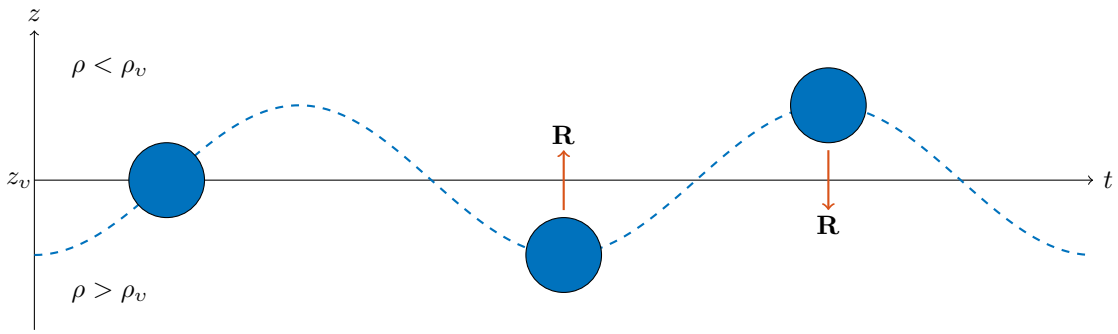

Figure 1.1: Oscillating movement due to the balance of weight and Archimedes response, acting as a restoring force. The resultant $\mathbf{R}$ is pointing upwards or downwards if the surrounding fluid is heavier ($\rho > \rho_\upsilon$) or lighter ($\rho < \rho_\upsilon$), leading to an harmonic vertical displacement.

homogeneous fluid, there is no gradient of density and $N = 0$, preventing this oscillatory motion from existing.

This restoring force leads to an oscillatory system depicted in figure 1.1 and is a key mechanism of wave propagation in stratified fluids. When lifted above its rest position, the fluid particle undergoes a downward force and, conversely, when pushed below its rest position, the fluid particle undergoes an upward force. In both cases, the restoring force $\mathbf{R}$, also called *buoyancy*, draws the particle back to its equilibrium position. As this phenomenon is induced by gravity, through weight and Archimedes forces, these waves are named *gravity waves*.

1.1.2 Physics of a Rotating Fluid

To investigate the effect of a rotation on the fluid dynamics, we consider an ideal situation by assuming that the whole fluid is in constant and uniform solid rotation characterized by the rotating vector $\mathbf{\Omega} = \Omega\mathbf{e_z}$. In this subsection, to avoid misleading notations, the distinction between the different frames will be enhanced by using L and R indices to refer to the quantities respectively expressed in the laboratory frame (L) and in the rotating frame (R).

For purpose of simplifying the discussion, we focus on a small horizontal ring-shaped fluid particle centred on the rotation axis. In the rotating frame, this fluid particle undergoes the inertial Coriolis force

$$\mathbf{C} = -2\Omega\mathbf{e_z} \times \mathbf{v_R}, \tag{1.10}$$

which is null when $\mathbf{v_R} = \mathbf{0}$ (meaning that the particle is at rest in the rotating frame), though the solid rotation imposes $\mathbf{v_L} = r_\upsilon\Omega\mathbf{e}_\theta$ in the laboratory frame.

The general expression of $\mathbf{v_R}$ for a particle located in $\mathbf{r} = r\mathbf{e_r}$ is given by the following expression

$$\mathbf{v_R} = \frac{\mathrm{d}\mathbf{r}}{\mathrm{d}t} = \frac{\partial r}{\partial t}\mathbf{e_r} + r\frac{\partial \theta}{\partial t}\mathbf{e}_\theta = \frac{\partial r}{\partial t}\mathbf{e_r} + r\Omega_R(r)\mathbf{e}_\theta, \tag{1.11}$$

where $\Omega_R(r) = (\Omega_L(r) - \Omega)$ is the particle rotation as a function of r. Considering a small radial displacement δr around the equilibrium position $r = r_\upsilon$, the velocity $\mathbf{v_R}$ is modified as

$$\mathbf{v_R} = \frac{\partial(r_\upsilon + \delta r)}{\partial t}\mathbf{e_r} + (r_\upsilon + \delta r)\Omega_R(r_\upsilon + \delta r)\mathbf{e}_\theta, \tag{1.12}$$

and is no longer equal to zero. To give an approximation of the $\mathbf{e}_\theta$ term we recall that, in the laboratory frame, the angular momentum is conserved

$$r_\upsilon^2\Omega_L(r_\upsilon) = (r_\upsilon + \delta r)^2\Omega_L(r_\upsilon + \delta r), \tag{1.13}$$

which means that at order $\mathcal{O}(\delta r^2)$ the angular velocity can be approximated by

$$\Omega_L(r_\upsilon + \delta r) = \Omega_L(r_\upsilon)\left(1 - 2\frac{\delta r}{r_\upsilon}\right) + \mathcal{O}(\delta r^2). \tag{1.14}$$

As the particle is initially in rotation with the fluid, the angular velocity satisfies $\Omega_L(r_v) = \Omega$, leading to the following development

$$\Omega_R(r_v + \delta r) = \Omega_L(r_v + \delta r) - \Omega = -2\Omega\frac{\delta r}{r_v} + \mathcal{O}(\delta r^2). \tag{1.15}$$

Using Newton's law, the radial dynamics of the particle writes at the lowest order in δr

$$\begin{aligned}
\frac{\mathrm{d}^2\delta r}{\mathrm{d}t^2} &= (-2\Omega\mathbf{e_z} \times \mathbf{v_R}) \cdot \mathbf{e_r}, &(1.16)\\
&= -2\Omega\mathbf{e_z} \times \left(\frac{\partial \delta r}{\partial t}\mathbf{e_r} - 2\delta r\Omega\mathbf{e}_\theta\right) \cdot \mathbf{e_r} + \mathcal{O}(\delta r^2), &(1.17)\\
&= -4\Omega^2\delta r + \mathcal{O}(\delta r^2), &(1.18)\\
&= -f^2\delta r + \mathcal{O}(\delta r^2). &(1.19)
\end{aligned}$$

At order $\mathcal{O}(\delta r^2)$, equation (1.19) describes a harmonic oscillator, meaning that the fluid particle oscillates along the radial direction at the Coriolis frequency $f = 2\Omega$. The elementary ring of fluid, after being expanded, contracts towards its original radius and, conversely, after being contracted, expanses in the opposite way.

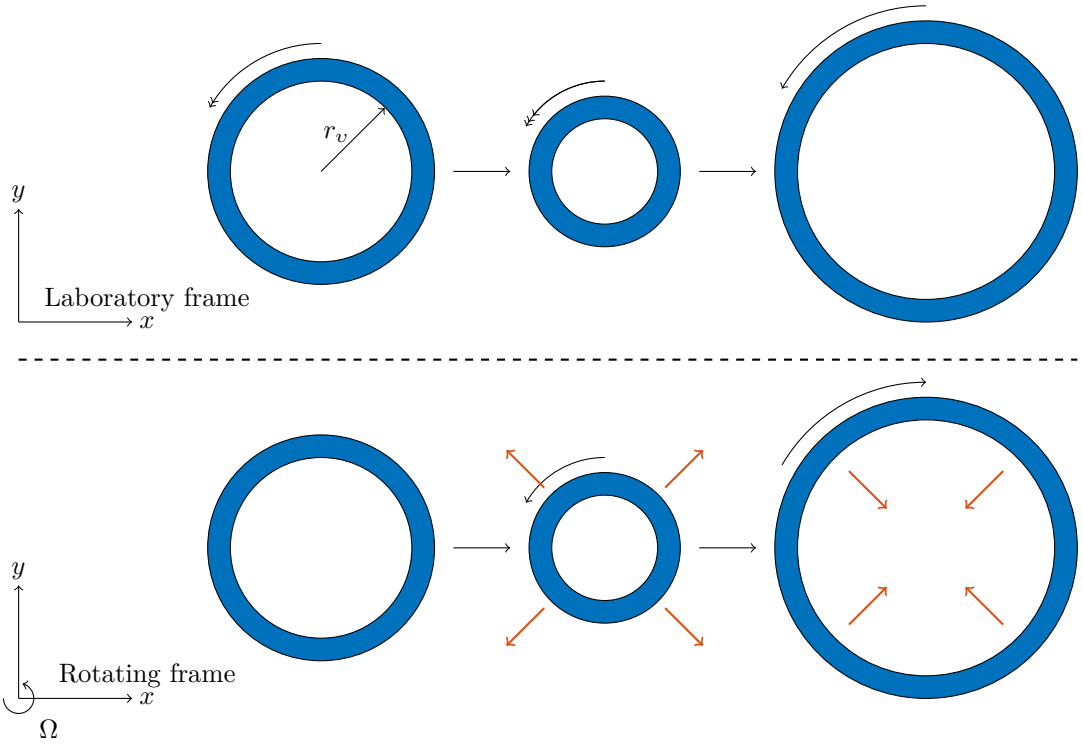

Figure 1.2: Oscillating movement induced by the Coriolis force. In the rotating frame (bottom), the action of this force is either centrifugal while the ring-shaped particle is contracting, or centripetal while it is dilating, leading to a harmonic horizontal displacement. Adapted from Maurer [140].

The inertial Coriolis force acts as a restoring force, driving an oscillatory system as shown in figure 1.2. Within geophysical fluids, submitted to rotation, this mechanism leads to the propagation of *inertial waves*.

As a result, a combination of the two restoring forces discussed in this section leads to waves that propagates thanks to gravity and inertia. They are called *inertia-gravity waves* or *internal waves*[1], the adjective *internal* being used to distinguish these waves propagating within the fluid from surface (or interfacial) waves that can also be driven by gravity forces.

[1]From now, except when explicitly stated in the text, *inertia-gravity waves* and *internal waves* are to be understood with a synonymous meaning.

1.2 Cartesian Internal Waves

In the previous section we focused on two properties of geophysical fluids, showing that they both induce harmonic oscillatory movements in response to small spatial perturbations. In this section, we derive the general theory to describe internal wave propagation in a Cartesian framework.

1.2.1 General Equations

We consider, in a Cartesian domain ($\mathbf{e_x}$, $\mathbf{e_y}$, $\mathbf{e_z}$), a stably stratified fluid in solid rotation at an angular velocity $\Omega = f/2$, with a density ρ that is a function of the depth z. The dynamics of such a flow is governed by the Navier-Stokes equation

$$\rho_0 \left(\frac{\partial \mathbf{v}}{\partial t} + (\mathbf{v} \cdot \nabla)\mathbf{v} \right) = -\rho_0 f \mathbf{e_z} \times \mathbf{v} - \nabla p - (\rho - \bar{\rho}) g \mathbf{e_z} + \rho_0 \nu \Delta \mathbf{v}, \tag{1.20}$$

the volume conservation for an incompressible fluid[2]

$$\nabla \cdot \mathbf{v} = 0, \tag{1.21}$$

and the mass conservation, which takes into account the density perturbations

$$\frac{\partial \rho}{\partial t} + \mathbf{v} \cdot \nabla \rho = \kappa \Delta \rho, \tag{1.22}$$

where $\mathbf{v} = (v_x, v_y, v_z)$ and p are the velocity and the pressure fields, ν stands for the kinematic viscosity of the fluid, κ for the diffusive coefficient of the stratifying agent. The total density field $\rho(x, y, z, t) = \bar{\rho}(z) + \rho'(x, y, z, t)$ is expressed as a sum of the background density $\bar{\rho}(z)$ and of a small perturbation $\rho'(x, y, z, t)$. As the density variations are small in comparison with the mean density ρ_0 in the fluid column, the Boussinesq approximation allows us to consider $\rho \approx \rho_0$, which is a constant, in all equations except for the buoyancy term, as written above [211, 254]. As a result, the system forms a set of five equations for five unknown quantities: the velocity $\mathbf{v}$, the pressure p, and the density fluctuation ρ'.

To simplify the study, we assume that the flow is y-independent. Note that such an invariance does not mean that the velocity has no component along the y direction, which intervenes in the expression of the Coriolis force. Using the volume conservation equation (1.21), we introduce the stream function ψ and the stream function vector $\mathbf{\Psi} = (0, 0, \psi)$ such that[3]

$$\mathbf{v} = \nabla \times \mathbf{\Psi} + v_y \mathbf{e_y}, \tag{1.23}$$

with

$$v_x = -\frac{\partial \psi}{\partial z} \qquad \text{and} \qquad v_z = \frac{\partial \psi}{\partial x}, \tag{1.24}$$

allowing us to rewrite equations (1.20) and (1.22) as the following system

$$\partial^2_{tz}\psi + \mathcal{J}(\psi, \partial_z \psi) = -f v_y + \frac{1}{\rho_0} \partial_x p + \nu \Delta \partial_z \psi, \tag{1.25}$$

$$\partial_t v_y + \mathcal{J}(\psi, v_y) = f \partial_z \psi + \nu \Delta v_y, \tag{1.26}$$

$$\partial^2_{tx}\psi + \mathcal{J}(\psi, \partial_x \psi) = -\frac{1}{\rho_0} \partial_z p - g \frac{\rho'}{\rho_0} + \nu \Delta \partial_x \psi, \tag{1.27}$$

$$\partial_t \rho' + \mathcal{J}(\psi, \rho') = -\partial_z \bar{\rho} \partial_x \psi + \kappa \Delta \rho', \tag{1.28}$$

where $\mathcal{J}$ is the Jacobian defined as

$$\mathcal{J}(f, g) = \frac{\partial f}{\partial x}\frac{\partial g}{\partial z} - \frac{\partial f}{\partial z}\frac{\partial g}{\partial x}. \tag{1.29}$$

[2] Compressibility introduces slight changes in the equations and is necessary in order to describe atmospheric internal waves, as well as for acoustic waves [220].

[3] The stream function can be defined though the flow is not 2D, as it relies on the translation invariance.

Note that the derivatives are written using the convention $\partial_j f = \partial f/\partial j$, where j is a mute variable.

As the fluid is stratified, based on results from the previous section, we introduce the buoyancy b and the Brunt-Väisälä frequency $N(z)$ to describe its dynamics

$$b = -g\frac{\rho'}{\rho_0} \qquad \text{and} \qquad N(z) = \sqrt{-\frac{g}{\rho_0}\left.\frac{\partial\bar{\rho}}{\partial z}\right|_z}. \tag{1.30}$$

The buoyancy b can be interpreted as the norm of the vertical restoring force per unit mass of the stratified fluid, driving the vertical wave dynamics.

Through the use of cross-derivatives $\partial_z(1.25)+\partial_x(1.27)$, the pressure term can be eliminated from equations (1.25) to (1.28) so that the system reduces to

$$\begin{aligned}
\partial_t\Delta\psi + \mathcal{J}(\psi,\Delta\psi) &= -f\partial_z v_y + \partial_x b + \nu\Delta(\Delta\psi), &(1.31)\\
\partial_t v_y + \mathcal{J}(\psi, v_y) &= f\partial_z\psi + \nu\Delta v_y, &(1.32)\\
\partial_t b + \mathcal{J}(\psi, b) &= -N^2(z)\partial_x\psi + \kappa\Delta b. &(1.33)
\end{aligned}$$

1.2.2 Linear Theory and Dispersion Relation

We consider small amplitude waves for which non-linear interactions can be neglected, which means that the Jacobians $\mathcal{J}$ are equal to zero. Under this assumption, the linearised equations obtained from (1.31), (1.32), and (1.33), write

$$\begin{aligned}
\partial_t\Delta\psi &= -f\partial_z v_y + \partial_x b + \nu\Delta(\Delta\psi), &(1.34)\\
\partial_t v_y &= f\partial_z\psi + \nu\Delta v_y, &(1.35)\\
\partial_t b &= -N^2(z)\partial_x\psi + \kappa\Delta b. &(1.36)
\end{aligned}$$

Looking for a solution as a monochromatic plane wave like $\psi = \psi_0 e^{i(\omega t - \mathbf{k}\cdot\mathbf{r})}$ (and the same for b and v_y) with a wave number $\mathbf{k} = (l, 0, m) = k(\sin\beta, 0, \cos\beta)$, we derive from equations (1.34) to (1.36) the matrix equation

$$\begin{bmatrix} -k^2(i\omega+\nu k^2) & -ifm & il \\ ifm & (i\omega+\nu k^2) & 0 \\ -iN^2 l & 0 & (i\omega+\kappa k^2) \end{bmatrix} \begin{bmatrix} \psi \\ v_y \\ b \end{bmatrix} = \begin{bmatrix} 0 \\ 0 \\ 0 \end{bmatrix}, \tag{1.37}$$

that admits a non-trivial solution if and only if its determinant is equal to zero. This condition gives the dispersion relation

$$-k^2(i\omega+\nu k^2)^2(i\omega+\kappa k^2) - N^2 l^2(i\omega+\nu k^2) - f^2 m^2(i\omega+\kappa k^2) = 0. \tag{1.38}$$

The frequency ω and the wave number k are therefore linked through a relation involving four parameters: the Coriolis frequency f, the buoyancy frequency N, the kinematic viscosity ν, and the diffusive coefficient κ. The role and importance of each contribution in the propagation of the waves will now be discussed.

Inviscid Dispersion Relation in a Stratified Rotating Fluid

For an inviscid ($\nu = 0$) and non-diffusive ($\kappa = 0$) fluid, the dispersion relation (1.38) becomes

$$k^2\omega^2 = N^2 l^2 + f^2 m^2. \tag{1.39}$$

Due to the y-invariance, the wave vector $\mathbf{k}$ is in the vertical plane ($\mathbf{e_x}$, $\mathbf{e_z}$), and can be expressed in terms of its amplitude k and an angle β with the vertical axis, giving its direction such as $\mathbf{k} = (l, 0, m) = k(\sin\beta, 0, \cos\beta)$. Using this notation, equation (1.39) can be written as a constraint on the propagation angle β

$$\omega^2 = N^2\sin^2\beta + f^2\cos^2\beta. \tag{1.40}$$

This relation (1.40) is illustrated in the series of plots presented in figure 1.3 using polar plots of ω as a function of the wave vector angle β. Each angle is associated to a unique frequency ω on

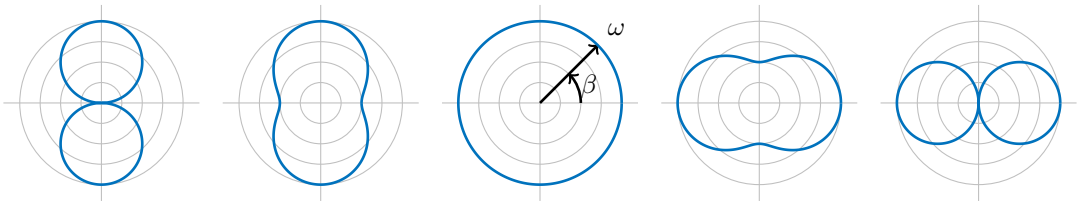

Figure 1.3: Dispersion relation (1.40) plotted in the (ω, β) polar plane, for dimensionless parameters N and f: to each angle β corresponds a unique frequency ω given by the blue curve.

the blue curve, but we note that a given value of ω is associated to different angles β. In the case $N = f$, a unique degenerated value of ω is allowed, equal to f and N, and valid for all angles. This schematic illustrates the symmetry between N and f, as the plots are rotated by 90° between gravity ($f = 0$) and inertial ($N = 0$) waves, transiting through the particular case $N = f$.

Using trigonometric identities, the angle β can be expressed from (1.40) as a function of the frequencies involved in the problem, ω, N, and f, as

$$\sin\beta = \pm\sqrt{\frac{\omega^2 - f^2}{N^2 - f^2}}. \tag{1.41}$$

Equation (1.39) shows that for a same excitation ω correspond four different directions: $(l, 0, m)$, $(-l, 0, m)$, $(l, 0, -m)$, and $(-l, 0, -m)$. Moreover, equation (1.40) limits the allowed values of ω to either $f < \omega < N$ or $N < \omega < f$. The propagating angle can be determined thanks to equation (1.41), leading to two different cases as depicted in figure 1.4. When considering the well-known experimental apparatus of a vertically oscillating cylinder in a 2D salt-stratified fluid, the excited wave beams align according to the angle β and form a *St. Andrew's cross* as shown, for example, in Mowbray and Rarity [155] and Ermanyuk and Gavrilov [75], and as drawn in the schematic figure 1.4.

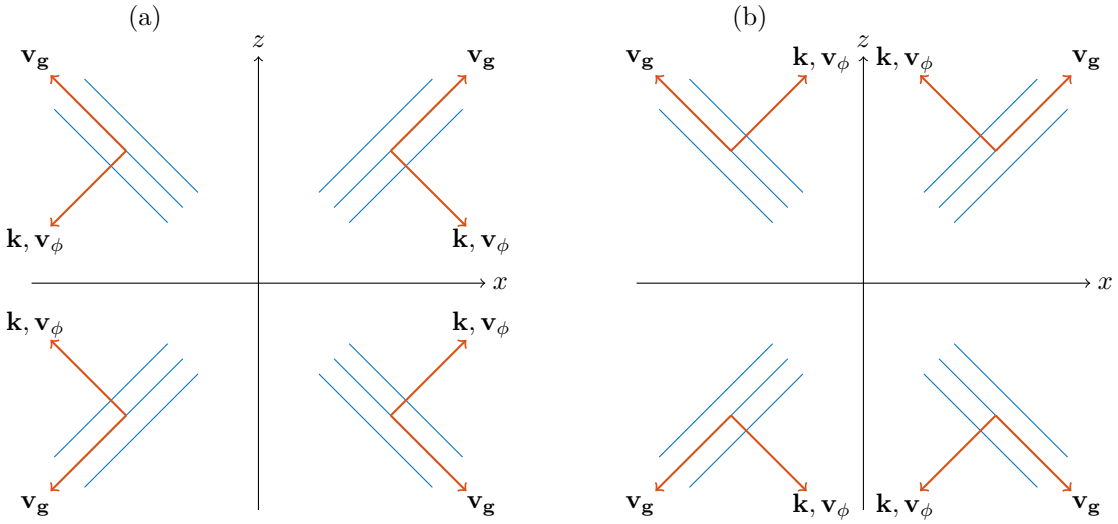

Figure 1.4: Schematic view of the four directions of propagations created at the same excitation frequency ω, in the case (a) $f < \omega < N$, and (b) $N < \omega < f$. Parallel blue lines are sections of the wave isophases planes. Adapted from Maurer [140].

The phase and group velocities can be computed from the dispersion relation (1.39). The phase

velocity is obtained by determining the propagating velocity of the phase in the exponential term

$$\mathbf{v}_\phi = \frac{\omega}{k^2}\mathbf{k} \tag{1.42}$$

$$= \sqrt{N^2l^2 + f^2m^2}\frac{\mathbf{k}}{k^2}, \tag{1.43}$$

and the group velocity by differentiating ω in respect with k

$$\mathbf{v_g} = \frac{ml}{\omega k^4}(N^2 - f^2)(m\mathbf{e_x} - l\mathbf{e_z}). \tag{1.44}$$

Note that the phase and group velocities are orthogonal ($\mathbf{v}_\phi \cdot \mathbf{v_g} = 0$ as $\mathbf{k} \cdot \mathbf{v_g} = 0$). While true in the case of wave beams, this observation is not valid anymore when considering standing waves[4] obtained in confined domains. For example, Mercier *et al.* [148] have shown in an experimental 2D study that, for horizontally propagating vertical modes, the group and the phase velocities are aligned with the horizontal axis and are of same direction. Conversely, we have shown that for radial modes in a 3D axisymmetric setup and, by extension, vertically propagating horizontal modes in Cartesian geometry, these two velocities are aligned with the vertical axis and are of opposite direction [33].

Inviscid Fluid and Viscous Correction

In a viscous fluid, the relation (1.38) is slightly modified and, still considering that the fluid is non-diffusive ($\kappa = 0$), the dispersion relation now writes

$$k^2(i\omega + \nu k^2)^2 i\omega + N^2l^2(i\omega + \nu k^2) + f^2m^2 i\omega = 0, \tag{1.45}$$

or, in another form

$$k^2\omega^2 = N^2l^2 + f^2m^2 + i\nu\left(2\omega k^4 - \frac{N^2l^2k^2}{\omega}\right) + \nu^2k^6. \tag{1.46}$$

This equation shows that the viscosity adds to equation (1.38) several terms proportional to ν or ν^2. To investigate their role in the propagation of internal waves, we use a development of ω to the first order of a small viscous parameter $\varepsilon = \nu k^2/N$ [42, 140]

$$\omega = \omega^{(0)} + \varepsilon\omega^{(1)} + \mathcal{O}(\varepsilon^2). \tag{1.47}$$

From (1.46), the following correction can be deduced

$$\varepsilon\omega^{(1)} = i\varepsilon k^2\left(1 - \frac{N^2}{2\omega^2}\left(\frac{\omega^2 - f^2}{N^2 - f^2}\right)\right) + \mathcal{O}(\varepsilon^2). \tag{1.48}$$

As $\omega^{(1)}$ is purely imaginary, the first order effect of viscosity is to add an attenuating term in the plane wave formulation proposed before. Note that the higher the wave number k, the more important the attenuation is. Another method to take into account the viscous correction, in the particular case of modes discussed in chapter 4, is to expand the vertical wave number m instead of the frequency ω [32, 35, 110].

Diffusive Effects

The diffusive effects are taken into account through the diffusive coefficient of the stratifying agent, κ. The complete dispersion relation writes

$$k^2(i\omega + \nu k^2)^2(i\omega + \kappa k^2) + N^2l^2(i\omega + \nu k^2) + f^2m^2(i\omega + \kappa k^2) = 0, \tag{1.49}$$

which leads to

$$k^2\omega^2 = N^2l^2 + f^2m^2 + \nu\left(2ik^4\omega + N^2l^2\frac{(1 - \kappa/\nu)k^2}{(i\omega + \kappa k^2)}\right) + \nu^2k^6. \tag{1.50}$$

[4] In this manuscript, we make indifferent use of the terms *standing wave* and *mode*.

Assuming that the diffusive correction would be small, a low order development gives

$$k^2\omega^2 = N^2l^2 + f^2m^2 + i\nu\left(2k^4\omega - N^2l^2\frac{(1-\kappa/\nu)k^2}{\omega}\right) + \nu^2k^6. \tag{1.51}$$

The dispersion relation (1.51) enhances a characteristic number in fluid mechanics, Sc, the Schmidt number $\mathrm{Sc} = \nu/\kappa$, comparing the viscous effects with the diffusive ones. For salt water, the value $\mathrm{Sc} \approx 700$ allows to neglect the diffusive contribution so that the wave propagation is once again governed by (1.46), relation for a non-diffusive fluid. Though diffusive effects have relevance in the oceans to describe double diffusive systems, we will only focus on non-diffusive internal waves in the course of this thesis.

1.3 Axisymmetric Internal Waves

Adding rotation imposes a natural geometry for the system which is cylindrical. Thus, we are interested in the derivation of similar equations in an axisymmetric framework of unit vectors $(\mathbf{e_r}, \mathbf{e}_\theta, \mathbf{e_z})$. To simplify the study, the fluid is considered to be inviscid ($\nu = 0$) and non-diffusive ($\kappa = 0$), as these corrections can be added in a similar way as in Cartesian geometry. The whole system is assumed to be in solid rotation at an angular velocity $\Omega = f/2$.

In this section, we derive the equations for axisymmetric internal waves. For us, and during this entire manuscript, axisymmetric is synonym of θ-independence. As we will see this is a strong assumption that may not be entirely satisfied by the wave fields. Equations for cylindrical internal waves, for which we allow an angular dependence, will be discussed in the next section 1.4.

1.3.1 Stream Function Equation

As in Cartesian coordinates, in a cylindrical geometry the fluid dynamics is still given by the Navier-Stokes equation (1.20), the volume conservation (1.21), and the mass conservation (1.22), linking the density ρ to the velocity and pressure fields $\mathbf{v}$ and p, except that all vectorial quantities are now defined in cylindrical coordinates such as $\mathbf{v} = (v_r, v_\theta, v_z)$.

We assume that the problem is axisymmetric, which means that the functions are θ-independent and only depend on r and z. Such an assumption is equivalent to the y-independence hypothesis set in the Cartesian framework in section 1.2, and does not mean that the orthoradial velocity v_θ is null. Very similarly to the Cartesian case, the volume conservation equation allows us to define the stream function ψ associated to a vector $\mathbf{\Psi} = \psi\mathbf{e}_\theta$ such as[5]

$$\mathbf{v} = \nabla \times \mathbf{\Psi} + v_\theta\mathbf{e}_\theta. \tag{1.52}$$

Thus, in the rotating frame, the radial and vertical velocities are given by[6]

$$v_r = -\frac{1}{r}\frac{\partial(r\psi)}{\partial z} \qquad \text{and} \qquad v_z = \frac{1}{r}\frac{\partial(r\psi)}{\partial r}. \tag{1.53}$$

Equations (1.20) and (1.22) then rewrite

$$\partial_t\left(\frac{1}{r}\partial_z(r\psi)\right) + \frac{1}{r}\mathcal{J}^\odot\left(r\psi, \frac{1}{r}\partial_z(r\psi)\right) + \frac{v_\theta^2}{r} = -fv_\theta + \frac{1}{\bar\rho}\partial_r p, \tag{1.54}$$

$$\partial_t v_\theta + \frac{1}{r^2}\mathcal{J}^\odot(r\psi, rv_\theta) = f\partial_z\psi, \tag{1.55}$$

$$\partial_t\left(\frac{1}{r}\partial_r(r\psi)\right) + \frac{1}{r}\mathcal{J}^\odot\left(r\psi, \frac{1}{r}\partial_r(r\psi)\right) = -\frac{1}{\bar\rho}\partial_z p + b, \tag{1.56}$$

$$\partial_t b + \frac{1}{r}\mathcal{J}^\odot(r\psi, b) = -N^2(z)\frac{1}{r}\partial_r(r\psi), \tag{1.57}$$

[5]The stream function is defined as a vectorial quantity. Though in the Cartesian framework it does not matter whether we are considering the vectorial or the scalar quantity, this is different in the axisymmetric case.

[6]Though the radial velocity v_r can be written as $v_r = -\partial_z\psi$, we will prefer this equivalent form as it is symmetric with the expression of the vertical velocity v_z.

where the cylindrical Jacobian[7] is defined by

$$\mathcal{J}^{\odot}(f,g) = \frac{\partial f}{\partial r}\frac{\partial g}{\partial z} - \frac{\partial g}{\partial r}\frac{\partial f}{\partial z}. \tag{1.58}$$

Once again, the pressure term is eliminated by adding ∂_r(1.54) and ∂_z(1.56). A non-trivial calculus leads to the following system

$$\partial_t \Delta_h \psi + \mathcal{J}^{\odot}\left(r\psi, \frac{\Delta_h \psi}{r}\right) = -\left(\frac{2v_\theta}{r} + f\right)\partial_z v_\theta + \partial_r b, \tag{1.59}$$

$$\partial_t v_\theta + \frac{1}{r^2}\mathcal{J}^{\odot}(r\psi, rv_\theta) = f\partial_z \psi, \tag{1.60}$$

$$\partial_t b + \frac{1}{r}\mathcal{J}^{\odot}(r\psi, b) = -N^2\frac{1}{r}\partial_r(r\psi), \tag{1.61}$$

with Δ_h the azimuthal Laplacian

$$\Delta_h \psi = \frac{\partial^2 \psi}{\partial z^2} + \frac{\partial}{\partial r}\left(\frac{1}{r}\frac{\partial (r\psi)}{\partial r}\right), \tag{1.62}$$

$$= \frac{\partial^2 \psi}{\partial z^2} + \frac{\partial^2 \psi}{\partial r^2} + \frac{1}{r}\frac{\partial \psi}{\partial r} - \frac{\psi}{r^2}. \tag{1.63}$$

Contrary to the Cartesian system of equations (1.31), (1.31), and (1.31), non-linearities not only come from the cylindrical Jacobians $\mathcal{J}^{\odot}$ (equivalent to the Cartesian Jacobians $\mathcal{J}$), but also from a self-interacting azimuthal term $v_\theta \partial_z v_\theta$ in equation (1.59).

1.3.2 Linear Theory and Dispersion Relation

Considering waves at low amplitudes, the problem can be first studied without taking into account the non-linear terms, reducing the system to

$$\partial_t \Delta_h \psi = -f\partial_z v_\theta + \partial_r b, \tag{1.64}$$

$$\partial_t v_\theta = f\partial_z \psi, \tag{1.65}$$

$$\partial_t b = -N^2\frac{1}{r}\partial_r(r\psi). \tag{1.66}$$

This system is now very similar to equations (1.34), (1.35), and (1.36), in the inviscid and non-diffusive limit. Solutions were previously found by considering plane waves, motivated by the use of Fourier transform on the different equations. Whereas the natural basis in the Cartesian framework is the exponential series, the use of the cylindrical framework leads to consider the basis drawn from the Bessel functions J_n[8] that appear through a Hankel transform and which are

[7] The operator $\mathcal{J}^{\odot}$ is the equivalent in axisymmetric coordinates of the Cartesian Jacobian $\mathcal{J}$. Calculations with the cylindrical Jacobian quickly become tricky. By chance, some properties can be used like the antisymmetry of the operator

$$\mathcal{J}^{\odot}(f,g) = -\mathcal{J}^{\odot}(g,f),$$

its bi-linearity

$$\mathcal{J}^{\odot}(f+g,h) = \mathcal{J}^{\odot}(f,h) + \mathcal{J}^{\odot}(g,h),$$

and its distributivity

$$\mathcal{J}^{\odot}(fg,h) = g\mathcal{J}^{\odot}(f,h) + f\mathcal{J}^{\odot}(g,h).$$

[8] We recall the general properties of the Bessel functions. The J_n functions are defined as the orthogonal basis in axisymmetric coordinates for the solutions of the Bessel differential equation

$$r^2\frac{\mathrm{d}^2 f}{\mathrm{d}r^2} + r\frac{\mathrm{d}f}{\mathrm{d}r} + (r^2 - n^2)f = 0.$$

Among the mathematical properties of theses functions, we note the recurrence relation

$$J_{n+1}(r) = \frac{nJ_n(r)}{r} - \frac{\mathrm{d}J_n(r)}{\mathrm{d}r},$$

giving us

$$J_1(r) = -\frac{\mathrm{d}J_0(r)}{\mathrm{d}r} \qquad \text{and} \qquad \frac{\mathrm{d}r^n J_n(r)}{\mathrm{d}r} = r^n J_{n-1}(r).$$

natural solutions of the cylindrical Laplacian for the radial dependence (see Appendix C). Thus, assuming that ψ is a harmonic solution given by a product of a first order Bessel function J_1 that describes the standing wave field structure along the radial direction, and of a monochromatic plane wave propagating along z, the following expression

$$\psi(r,z,t) = \psi^0 J_1(lr) e^{i(\omega t - mz)} + \text{c.c.}, \tag{1.67}$$

is a good ansatz. Note that it respects the condition $\psi(r=0)=0$ imposed by the mass conservation, avoiding radial velocity at the center of the domain. With the use of a Bessel function of first order *via* its definition through a differential equation, the azimuthal Laplacian operator simply reduces to

$$\Delta_h \psi = -(l^2+m^2)\psi = -k^2\psi. \tag{1.68}$$

As a consequence, we derive from the linear equations the following expressions for the stream function ψ, the orthoradial velocity v_θ, and the buoyancy b

$$\psi(r,z,t) = \psi^0 J_1(lr) e^{i(\omega t - mz)} + \text{c.c.}, \tag{1.69}$$

$$v_\theta(r,z,t) = -\frac{fm}{\omega}\psi^0 J_1(lr) e^{i(\omega t - mz)} + \text{c.c.}, \tag{1.70}$$

$$b(r,z,t) = i\frac{lN^2}{\omega}\psi^0 J_0(lr) e^{i(\omega t - mz)} + \text{c.c.}, \tag{1.71}$$

where J_0 and J_1 are respectively the first order Bessel functions of degree 0 and 1, as pictured in figure 1.5(a). Other solutions, the second order Bessel functions Y_0 and Y_1 (figure 1.5(b)), also called Neumann functions, are not considered due to their divergence when r goes to zero. Both the J_n and the Y_n functions are real and can be used to describe standing wave fields, as will be discussed in chapter 4. Other complex solutions called Hankel functions, $H_n^{(1)}$ and $H_n^{(2)}$, can be used to describe wave fields propagating inwards or outwards. They are defined by a linear combination of J_n and Y_n as

$$H_n^{(1)} = J_n + iY_n, \tag{1.72}$$

$$H_n^{(2)} = J_n - iY_n, \tag{1.73}$$

with the same divergence at $r=0$.

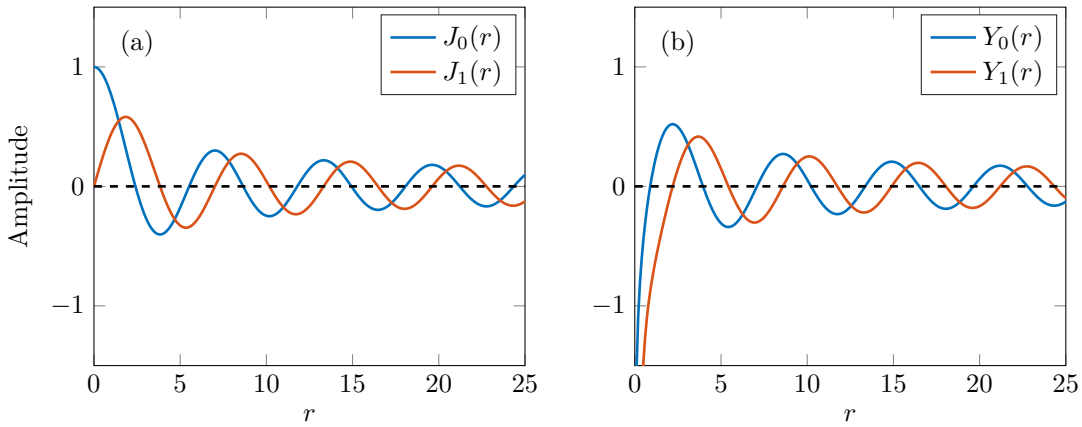

Figure 1.5: Natural solutions of the Bessel differential equation of orders 0 and 1.

The dispersion relation can be derived by introducing a 2D wave vector $\mathbf{k}$ contained in the vertical plane, $\mathbf{k} = (l,0,m) = k(\sin\beta, 0, \cos\beta)$ of squared magnitude $k^2 = l^2 + m^2$. From equations

The orthogonality of the Bessel functions is characterized by the relation

$$\int_0^1 r J_n(\lambda r) J_n(\mu r) \mathrm{d}r = \frac{\delta(\lambda-\mu)}{2}\left(J_n'(\lambda)\right)^2,$$

where λ and μ are two zeros of the function J_n.

(1.59), (1.60), and (1.61), it follows that

$$k^2\omega^2 = N^2l^2 + f^2m^2. \tag{1.74}$$

Using the angle β, this relation can be written as

$$\omega^2 = N^2 \sin^2\beta + f^2 \cos^2\beta, \tag{1.75}$$

from which the angle β can be extracted

$$\sin\beta = \pm\sqrt{\frac{\omega^2 - f^2}{N^2 - f^2}}, \tag{1.76}$$

exactly as in Cartesian geometry.

The derivation of the stream function and velocities for axisymmetric modes, as well as their study, will be done in some more details in chapter 4. For additional mathematical information on the Bessel functions, see Appendix C and the NIST Handbook of Mathematical Functions [163].

1.4 Cylindrical Internal Waves

The derivation of the axisymmetric theory in section 1.3 relies on the strong assumption of a θ-independent flow. Such an invariance prevents waves of higher complexity from existing, and is not always true. In this section, we relax this assumption and we derive a more general framework of fully 3D cylindrical internal waves.

1.4.1 Vorticity Equation

In sections 1.2 and 1.3, the wave equation has been derived using the stream function ψ. As we already mentioned, the existence of a stream function relies on an invariance with respect to one of the spatial coordinates, which allows for the definition of a potential, the stream function, to solve the continuity equation $\nabla\cdot\mathbf{v} = 0$. As there is no invariance in the problem we are now discussing, no stream function can be used. Instead, we introduce the vorticity ξ as

$$\xi = \nabla\times\mathbf{v}. \tag{1.77}$$

This vectorial quantity characterises the propensity of the fluid to follow a rotational movement.

For clarity, we recall the system of equation (1.20), (1.21), and (1.22), in terms of the velocity and buoyancy fields $\mathbf{v}$ and $\mathbf{b} = b\mathbf{e_z}$ as follow

$$\partial_t\mathbf{v} + (\mathbf{v}\cdot\nabla)\mathbf{v} = -f\mathbf{e_z}\times\mathbf{v} - \frac{1}{\rho_0}\nabla p + \mathbf{b}, \tag{1.78}$$

$$\partial_t\mathbf{b} + (\mathbf{v}\cdot\nabla)\mathbf{b} = -N^2 v_z\mathbf{e_z}, \tag{1.79}$$

$$\nabla\cdot\mathbf{v} = 0. \tag{1.80}$$

The pressure term ∇p can be eliminated by taking the curl of equation (1.78) and, after some algebra, we obtain

$$\partial_t\xi + \nabla\times[(\mathbf{v}\cdot\nabla)\mathbf{v}] = f\partial_z\mathbf{v} + \nabla\times(b\mathbf{e_z}). \tag{1.81}$$

Equations (1.79) and (1.81) collapse together using the time derivative of (1.81) and the curl of (1.79), leading to

$$\partial_t^2\xi + \mathcal{N}(\mathbf{v},\mathbf{b}) = f\partial_t\partial_z\mathbf{v} - N^2\nabla\times(v_z\mathbf{e_z}), \tag{1.82}$$

with the non-linear terms

$$\mathcal{N}(\mathbf{v},\mathbf{b}) = \nabla\times\left[\partial_t\left((\mathbf{v}\cdot\nabla)\mathbf{v}\right) + (\mathbf{v}\cdot\nabla)\mathbf{b}\right]. \tag{1.83}$$

Then, the curl of (1.83) allows us to write the non-linear equation for vorticity

$$\partial_t^2\nabla\times\xi + \nabla\times\mathcal{N}(\mathbf{v},\mathbf{b}) = f\partial_t\partial_z\xi - N^2\nabla\times[\nabla\times(v_z\mathbf{e_z})]. \tag{1.84}$$

1.4.2 Linear Theory

We first consider low amplitude waves, for which non-linear effects can be neglected. Hence, the linearised equations are obtained by setting the non-linear term $\mathcal{N}$ to zero, leading to the time evolution equation

$$\partial_t^2 \nabla \times \xi = f \partial_t \partial_z \xi - N^2 \nabla \times [\nabla \times (v_z \mathbf{e_z})] \,. \tag{1.85}$$

Using the volume conservation equation $\nabla \cdot \mathbf{v} = 0$, the curl of the vorticity simply writes in terms of the Laplacian of the velocity. Equation (1.85) writes

$$\partial_t^2 \Delta^{\odot} \mathbf{v} = -f \partial_t \partial_z \xi + N^2 \nabla \times [\nabla \times (v_z \mathbf{e_z})] \,, \tag{1.86}$$

in terms of the velocities v_r, v_θ, and v_z. We recall that the vectorial cylindrical Laplacian $\Delta^{\odot}$ is defined involving a coupling between the radial and orthoradial velocities v_r and v_θ as

$$\Delta^{\odot} \mathbf{v} = \begin{bmatrix} \Delta v_r - \frac{1}{r^2} \left(v_r + 2 \partial_\theta v_\theta \right) \\ \Delta v_\theta - \frac{1}{r^2} \left(v_\theta - 2 \partial_\theta v_r \right) \\ \Delta v_z \end{bmatrix} , \tag{1.87}$$

with the cylindrical Laplacian

$$\Delta v = \frac{1}{r} \partial_r \left(r \partial_r v \right) + \frac{1}{r^2} \partial_\theta^2 v + \partial_z^2 v. \tag{1.88}$$

From equation (1.86) we obtain an uncoupled equation on the vertical velocity

$$\partial_t^2 \Delta v_z + f^2 \partial_z^2 v_z + N^2 \left(\frac{1}{r} \partial_r (r \partial_r v_z) + \frac{1}{r^2} \partial_\theta^2 v_z \right) = 0, \tag{1.89}$$

and two coupled equations on the radial and orthoradial velocities

$$\partial_t^2 \Delta v_r - \frac{1}{r^2} \partial_t^2 \left(v_r + 2 \partial_\theta v_\theta \right) + f \partial_t \partial_z \left(\frac{1}{r} \partial_\theta v_z - \partial_z v_\theta \right) - N^2 \partial_r \partial_z v_z = 0, \tag{1.90}$$

and

$$\partial_t^2 \Delta v_\theta - \frac{1}{r^2} \partial_t^2 \left(v_\theta - 2 \partial_\theta v_r \right) + f \partial_t \partial_z \left(\partial_z v_r - \partial_r v_z \right) - N^2 \frac{1}{r} \partial_\theta \partial_z v_z = 0. \tag{1.91}$$

As a result, it appears that the problem can be solved by first studying the behaviour of the vertical velocity field and then, considering the horizontal velocity field.

1.4.3 Canonical Cylindrical Modes

Vertical Velocity

Solutions of equation (1.89) can be found by extension of the axisymmetric solution derived for the vertical velocity in section 1.3 using a separation of variables method. Introducing an azimuthal wave number $p \in \mathbb{N}$, we verify that

$$v_z(r, \theta, z, t) = v_z^0 J_p(lr) e^{i(\omega t - mz - p\theta)} + \text{c.c.}, \tag{1.92}$$

satisfies equation (1.89), where the wave numbers l and m are linked through the following dispersion relation

$$\omega^2 (l^2 + m^2) = f^2 m^2 + N^2 l^2. \tag{1.93}$$

This equation suggests that the influence of the rotation, characterised by the Coriolis frequency f, is contained in the vertical structure with the vertical wave number m, whereas the influence of the salt stratification, *via* the Brunt-Väisälä frequency N, is displayed in the horizontal structure with the radial wave number l. This is similar to 2D Cartesian and 3D axisymmetric studies, and we note that there is no direct influence of the azimuthal number p on the dispersion relation. Nevertheless, at a given l, the nodes and antinodes of the vertical velocity are shifted in the horizontal plane as p varies, which means that to satisfy relevant boundary conditions, l and p

have to be set accordingly. Note that for $p = 0$ the structure of the velocity field is axisymmetric, and the expression of v_z is the same as derived in section 1.3.

Figure 1.6 presents horizontal cross-sections of the unconstraint vertical velocity v_z, to illustrate the radial and azimuthal structure of the first cylindrical modes. We set $l = 51$ m^{-1} (corresponding to a mode 3 in our experiments, as will be shown in chapter 4) and p varying from 0 to 3. The value $p = 0$ corresponds to the axisymmetric mode which is θ-independent.

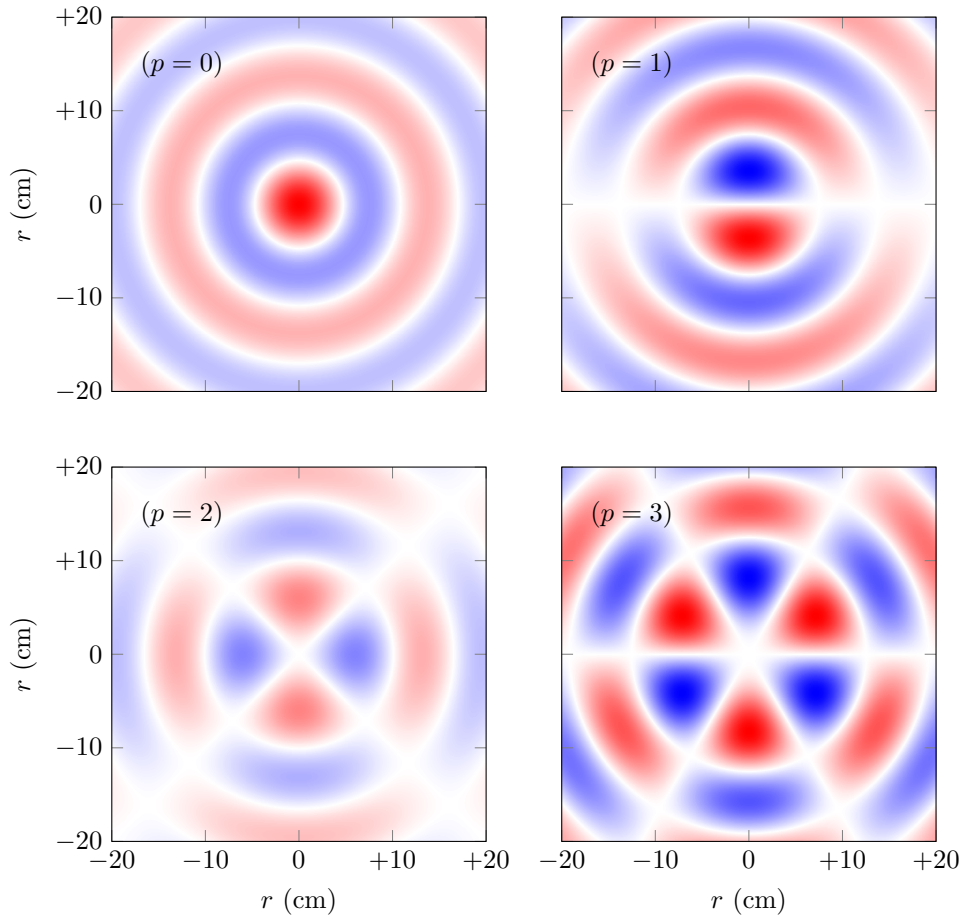

Figure 1.6: Horizontal cross-sections of the unconstraint vertical velocity v_z for cylindrical modes, with a radial wave number $l = 51$ m^{-1} and an azimuthal wave number p varying from 0 to 3.

At large radius, the cylindrical Bessel-shaped wave field can be approximated by a Cartesian plane wave field. Although equation (1.93) does not involve the azimuthal wave number p, this dependence is explicit in the plane wave approximation. Close to a given (r_0, θ_0), the corresponding Cartesian wave numbers (k_x, k_y, k_z) can be expressed thanks to (l, m, p) through

$$k_x = \sqrt{l^2 \cos^2\theta_0 - \left(\frac{p}{2\pi r_0}\right)^2 (\cos^2\theta_0 - \sin^2\theta_0)}, \tag{1.94}$$

$$k_y = \sqrt{l^2 \sin^2\theta_0 + \left(\frac{p}{2\pi r_0}\right)^2 (\cos^2\theta_0 - \sin^2\theta_0)}, \tag{1.95}$$

$$k_z = m. \tag{1.96}$$

Hence, locally, the horizontal structure of the wave field is set by both l and p, and a change in either l or p leads to a change in k_x and k_y. This is shown in figure 1.7, in which the cylindrical wave field is plotted for $l = 51$ m^{-1} with $p = 10$ (top) and $p = 20$ (bottom). The left pannel presents the cylindrical wave fields centered on $r = 0$, and the right pannel presents a closer

view of the regions indentified by the blue squares on the overall wave field. On these zoomed-in pictures, we can clearly see that both the along-x and along-y wave lengths are impacted by the increase of azimuthal wave number p, although the radial wave number l is kept constant. Under this Cartesian plane wave approximation, one would write the dispersion relation (1.93) as

$$\omega^2 k^2 = f^2 m^2 + N^2 l^2 = f^2 k_z^2 + N^2 (k_x^2 + k_y^2), \tag{1.97}$$

with k_x, k_y, and k_z previously defined, in order to explicitly state the dependence in p and l.

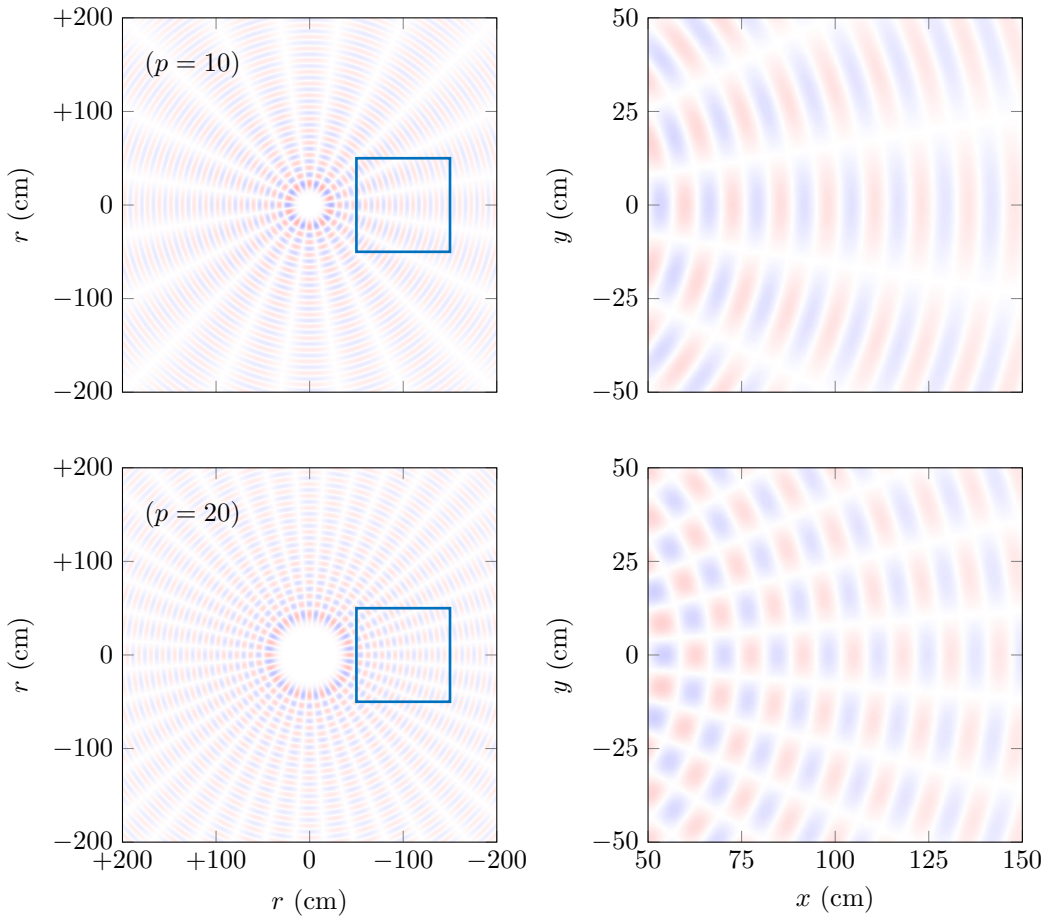

Figure 1.7: Horizontal cross-sections of the vertical velocity v_z for cylindrical modes, with a radial wave number $l = 51$ m^{-1} and an azimuthal wave number $p = 10$ (top row) and $p = 20$ (bottom row). The cylindrical Bessel-shaped wave field is shown on the left, and the zoomed-in regions corresponding to the blue squares are shown on the right.

Horizontal Velocities

As seen before, the radial and orthoradial velocities are coupled. Hence, a modal decomposition is not straightforward. Equations (1.90) and (1.91), however, can be solved. To do so, we define the matrix equation

$$\partial_t^2 \begin{bmatrix} \Delta - \frac{1}{r^2} & -\frac{2}{r^2}\partial_\theta \\ \frac{2}{r^2}\partial_\theta & \Delta - \frac{1}{r^2} \end{bmatrix} \begin{bmatrix} v_r \\ v_\theta \end{bmatrix} = -f\partial_t\partial_z \begin{bmatrix} \frac{1}{r}\partial_\theta v_z - \partial_z v_\theta \\ \partial_z v_r - \partial_r v_z \end{bmatrix} + N^2 \begin{bmatrix} \partial_r \partial_z v_z \\ \frac{1}{r}\partial_\theta \partial_z v_z \end{bmatrix}, \tag{1.98}$$

that can be written as

$$\mathcal{D} \begin{bmatrix} v_r \\ v_\theta \end{bmatrix} = \mathcal{S}, \tag{1.99}$$

where $\mathcal{D}$ is a differential operator and $\mathcal{S}$ a source term, representing the coupling to the vertical velocity, expressed as

$$\mathcal{D} = \begin{bmatrix} \partial_t^2\Delta - \frac{1}{r^2}\partial_t^2 & -\frac{2}{r^2}\partial_t^2\partial_\theta - f\partial_t\partial_z^2 \\ \frac{2}{r^2}\partial_t^2\partial_\theta + f\partial_t\partial_z^2 & \partial_t^2\Delta - \frac{1}{r^2}\partial_t^2 \end{bmatrix}, \qquad \text{and} \qquad \mathcal{S} = \begin{bmatrix} -\frac{f}{r}\partial_t\partial_z\partial_\theta v_z + N^2\partial_r\partial_z v_z \\ -f\partial_t\partial_z\partial_r v_z + \frac{N^2}{r}\partial_\theta\partial_z v_z \end{bmatrix}. \tag{1.100}$$

We define the rotation matrix $\mathcal{R}(\theta)$ as

$$\mathcal{R}(\theta) = \begin{bmatrix} \cos\theta & -\sin\theta \\ \sin\theta & \cos\theta \end{bmatrix}, \tag{1.101}$$

which satisfies $\mathcal{R}(-\theta) = \mathcal{R}^T(\theta) = \mathcal{R}^{-1}(\theta)$. This rotation matrix corresponds to the transfer matrix from polar coordinates $(O, \mathbf{e_r}, \mathbf{e}_\theta)$ to Cartesian coordinates $(O, \mathbf{e_x}, \mathbf{e_y})$, as depicted in figure 1.6. Then, we can transform the matrix equation (1.98) into

$$(\mathcal{R}\mathcal{D}\mathcal{R}^{-1})\mathcal{R}\begin{bmatrix} v_r \\ v_\theta \end{bmatrix} = \mathcal{R}\mathcal{S}. \tag{1.102}$$

Such a transformation leads us to consider a new matrix differential equation, with the operator $\tilde{\mathcal{D}} = \mathcal{R}\mathcal{D}\mathcal{R}^{-1}$ and a transformed velocity variable and source term. This new differential operator writes

$$\tilde{\mathcal{D}} = \mathcal{R}\mathcal{D}\mathcal{R}^{-1} = \begin{bmatrix} \partial_t^2\Delta & -f\partial_t\partial_z^2 \\ f\partial_t\partial_z^2 & \partial_t^2\Delta \end{bmatrix}, \tag{1.103}$$

and, defining u_x and u_y – which are functions of r and θ – as the two components of the transformed velocity

$$\begin{bmatrix} u_x \\ u_y \end{bmatrix} = \mathcal{R}\begin{bmatrix} v_r \\ v_\theta \end{bmatrix}, \tag{1.104}$$

the new matricial equation writes

$$\tilde{\mathcal{D}}\begin{bmatrix} u_x \\ u_y \end{bmatrix} = \mathcal{R}\mathcal{S}, \tag{1.105}$$

and, explicitly

$$\begin{bmatrix} \partial_t^2\Delta & -f\partial_t\partial_z^2 \\ f\partial_t\partial_z^2 & \partial_t^2\Delta \end{bmatrix}\begin{bmatrix} u_x \\ u_y \end{bmatrix} = \begin{bmatrix} \cos\theta\left(-\frac{f}{r}\partial_t\partial_\theta + N^2\partial_r\right) - \sin\theta\left(-f\partial_t\partial_r + \frac{N^2}{r}\partial_\theta\right) \\ \sin\theta\left(-\frac{f}{r}\partial_t\partial_\theta + N^2\partial_r\right) + \cos\theta\left(-f\partial_t\partial_r + \frac{N^2}{r}\partial_\theta\right) \end{bmatrix}\partial_z v_z. \tag{1.106}$$

The horizontal velocities in polar coordinates (v_r, v_θ) can be obtained with the inverse transform of (u_x, u_y) into (see figure 1.8), and simply write

$$v_r = \cos\theta u_x + \sin\theta u_y, \tag{1.107}$$
$$v_\theta = -\sin\theta u_x + \cos\theta u_y. \tag{1.108}$$

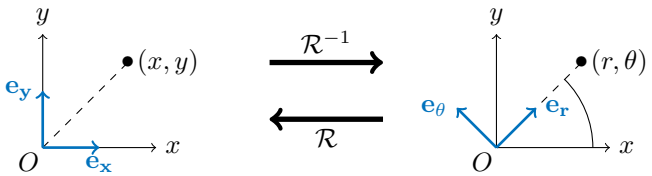

Figure 1.8: Transformation between polar and Cartesian coordinates with the transfer matrix $\mathcal{R}$.

Note that, in the non-rotating case ($f = 0$), the operator $\tilde{\mathcal{D}}$ becomes diagonal and we obtain uncoupled equations on u_x and u_y. The system is thus very similar to Cartesian equations, except that the Laplacian operator Δ is still in cylindrical coordinates. In this particular case, the system writes

$$\begin{bmatrix} \partial_t^2\Delta & 0 \\ 0 & \partial_t^2\Delta \end{bmatrix}\begin{bmatrix} u_x \\ u_y \end{bmatrix} = \begin{bmatrix} \cos\theta N^2\partial_r - \sin\theta\frac{N^2}{r}\partial_\theta \\ \sin\theta N^2\partial_r + \cos\theta\frac{N^2}{r}\partial_\theta \end{bmatrix}\partial_z v_z. \tag{1.109}$$

Though we do not solve the problem, this equation can be discussed in some more details. The velocities u_x and u_y are a combination of homogeneous and particular solutions of the matrix equation (1.109). The homogeneous equations write $\partial_t^2 \Delta u_x = 0$ and $\partial_t^2 \Delta u_y = 0$, therefore it can be showed that if the amplitude of the velocity field is bounded and is initially zero, then the homogeneous solution is a time-independent mean flow. Hence, the horizontal velocity is a combination of mean currents at $\omega = 0$ and the only time varying part is enslaved by the vertical velocity field, which is the particular solution of the partial differential equation. This solution is oscillating at a frequency ω and has a vertical wave number m, both set by v_z. In the case of $p = 0$ (axisymmetric), the system can be solved straightforwardly and the solution is the same as the one derived in section 1.3.

Kelvin Modes

The solutions of the system of equations (1.89), (1.90), and (1.91) can be derived analytically. They are known as *Kelvin modes*[9] and form the canonical basis of functions in cylindrical geometry that satisfy the internal wave equations [95, 96, 150, 226]. The complete non-trivial calculus, presented in appendix E, yields

$$v_r(r,\theta,z,t) = i\frac{mv_z^0}{4l\omega}\left[(f-2\omega)J_{p-1}(lr)+(f+2\omega)J_{p+1}(lr)\right]e^{i(\omega t-mz-p\theta)} + \text{c.c.}, \quad (1.110)$$

$$v_\theta(r,\theta,z,t) = \frac{mv_z^0}{4l\omega}\left[(2f-\omega)J_{p-1}(lr)-(2f+\omega)J_{p+1}(lr)\right]e^{i(\omega t-mz-p\theta)} + \text{c.c.}, \quad (1.111)$$

$$v_z(r,\theta,z,t) = v_z^0 J_p(lr)e^{i(\omega t-mz-p\theta)} + \text{c.c.}. \quad (1.112)$$

In their most general shape, i.e. in unconfined domains, these modes are helical with zeros at fixed radii in the horizontal plane. Their helicity, however, is lost if the modes are vertically confined as m and p become uncoupled. Note that, by setting $p = 0$, the velocities (1.110), (1.111), and (1.112) correspond to the axisymmetric case (see equations (1.69) and (1.70)).

Coercion by Boundary Conditions

In this subsection, we explore the influence of boundary conditions on the allowed values of wave numbers l, m, and p. A more thorough study adapted to our experimental apparatus is presented in chapter 4 in the case of purely axisymmetric modes ($p = 0$).

Let us consider a cylindrical domain of height H and radius R with the revolution axis aligned with the vertical. Boundary conditions apply at three different boundaries: on the top and bottom horizontal walls, and on the vertical cylindrical wall.

A the top and at the bottom, static walls impose that

$$v_z(z=0) = 0 \qquad \text{and} \qquad v_z(z=H) = 0, \quad (1.113)$$

where the first condition is automatically fulfilled when writing the vertical dependence of the mode as a sine function; the second condition can be solved analytically, leading to

$$mH = z^\star = \frac{n\pi}{2} \qquad \text{with} \qquad n \in \mathbb{N}. \quad (1.114)$$

As discussed in chapter 4, in our experiments, the constraint will be slightly different as the top boundary corresponds to the wave generator that is still rigid but oscillating.

The cylindrical boundary is constraining the allowed values of horizontal wave numbers through the non-penetration condition

$$v_r(r=R) = 0, \quad (1.115)$$

that can be written

$$(f-2\omega)J_{p-1}(lR)+(f+2\omega)J_{p+1}(lR) = 0. \quad (1.116)$$

[9] These modes have been first studied by Lord Kelvin for inertial flows in cylindrical coordinates [226].

Contrary to the vertical condition (1.114), this equation shows that the horizontal description of the wave field, contained in the wave numbers l and p, depends on the frequency for inertia-gravity waves. In the peculiar case of stratified non-rotating fluids, this relation simply writes

$$J_{p-1}(lR) - J_{p+1}(lR) = 0. \tag{1.117}$$

Note that, for axisymmetric modes ($p = 0$), the condition reduces to

$$J_1(lR) = 0, \tag{1.118}$$

for both gravity and inertial waves.

In a more general case, the zeros $lR = r^\star$ of equation (1.116) can be determined numerically. We present, in figure 1.9, plots of the left-hand side of equation (1.116) for $p = 0$ (top left) and $p = 2$ (bottom left), both for $f = 0$, and the three first non-zeros solutions $r^\star$ as a function of f/ω (right). The colours stand for the value of p from 0 through 4, and the solid, dashed, and dotted styles correspond to the first, second, and third solutions, respectively. A vertical dashed line at $f/\omega = 1$ indicates the cut-off between the gravity-dominated region ($f < \omega < N$) and the inertia-dominated region ($N < \omega < f$). As expected from the calculus done with the axisymmetric assumption, for $p = 0$ the solutions of equation (1.116) do not depend on the frequency, but this is no longer the case as soon as $p \neq 0$.

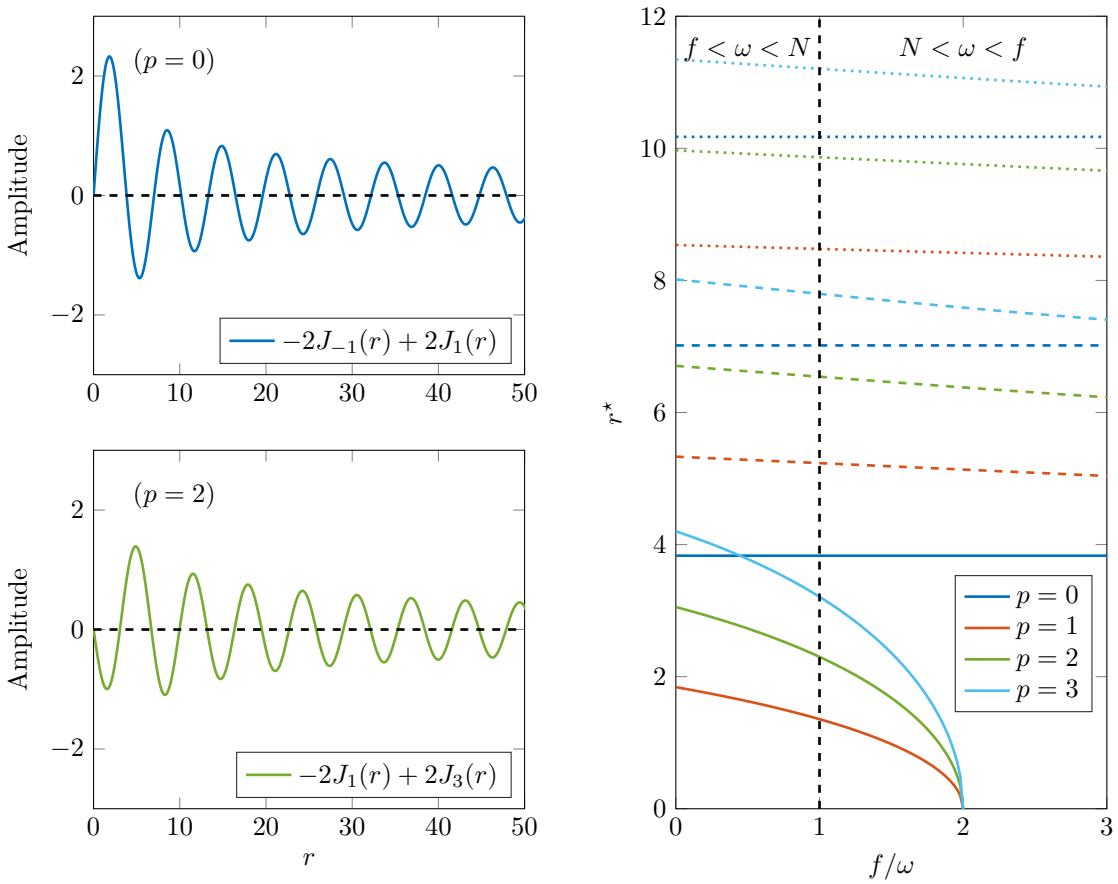

Figure 1.9: Illustration of condition (1.116) imposed by the cylindrical boundary condition. Left: plots of (1.116) for $f = 0$ with $p = 0$ (top) and $p = 2$ (bottom). Right: locations $r^\star$ of the first (solid line), second (dashed line), and third (dotted line) non-zero nodes of (1.116), for p from 1 through 4. The vertical dashed line helps distinguish the domains $f < \omega < N$ and $N < \omega < f$.

1.5 Conclusion

In this chapter, we presented the general theory of internal inertia-gravity waves in stratified and rotating fluids. In such media, vertical stratification in density and rotation introduce a vertical and a horizontal anisotropy that support gravity waves and inertial waves, respectively. Their dynamics depends on two characteristic frequencies: the Coriolis (or inertial) frequency f, set by rotation, and the Brunt-Väisälä (or buoyancy) frequency N, set by the density stratification. These two parameters limit propagating waves to a given range of frequency, so that a wave at frequency ω can propagate only if $f < \omega < N$ or $N < \omega < f$. In the oceans, due to low Coriolis frequency values, more attention is devoted to the case $f < \omega < N$. In the deep ocean, however, it is possible to find regions of very weak stratification with $N < f$.

Different configurations have been explored: 2D Cartesian waves, as a case study, and waves in cylindrical geometry, among which purely axisymmetric (θ-independent) and cylindrical waves (θ-dependent). In 3D, such waves, which are the subject of our study, involve different wave numbers: a radial and an azimuthal wave number, l and p, that set the shape of the Bessel function used to describe the horizontal structure of the wave field, and a vertical wave number, m, which parametrises the vertical structure. Wave numbers m and l are linked to the frequencies ω, f, and N, by the dispersion relation

$$\omega^2(l^2 + m^2) = f^2 m^2 + N^2 l^2, \tag{1.119}$$

similar to previous 2D Cartesian studies. Interestingly, this relation does not directly involve the azimuthal quantification p, though the radial wave number l is, actually, a function of p. In this manuscript, we mainly focus on the case $p = 0$, corresponding to axisymmetric wave fields as derived in detail in chapter 4, but we discuss the existence of cylindrical internal waves through non-linear interactions in chapters 7 and 8.

CHAPTER 2

Axisymmetric Waves at the Laboratory

Every day is a new day. It is better to be lucky. But I would rather be exact. Then when luck comes you are ready.
Ernest Hemingway, The Old Man and the Sea

Laboratory internal wave experiments are usually performed using a very simple recipe: water, salt, rotation, and a generation mechanism. Homogenous anisotropic media are hence created, with a stable stratification in density (salt) and inertial properties (rotation), and excited through localised displacements of fluid (e.g. a rising sphere [154]) or periodic oscillatory motions (for example oscillating cylinders [155], spheres [14], and pendulum [42]). Later on, planar wave generators have been developed [92] and proven efficient to generate internal waves, first step towards more complex wave generators.

The setup described here is located at the *Laboratoire de Physique de l'ENS de Lyon* (Lyon, France), where all the experiments were performed. Its main difference with other systems lies in the use of a novel wave generator design able to reliably produce axisymmetric wave fields that can be customised on wish.

In this chapter, the experimental techniques are presented. Sections 2.1 and 2.2 respectively depict the tank used to perform the experiments and the wave generator that produces the axisymmetric wave field. The visualisation technique through Particle Image Velocimetry (PIV) is presented in section 2.3, and data processing methods are explained in section 2.4.

2.1 A Small-scale Ocean in a Laboratory Tank

This section describes the facility used to create an environment suitable for axisymmetric internal wave propagation. The whole apparatus, as described further, is constituted of a cylindrical tank, filled with salt-stratified water, placed on a rotating table, and is therefore able to support both gravity and inertial waves.

2.1.1 A Cylindrical Tank

Experiments were conducted in a cylindrical acrylic tank of diameter 1 m and height 0.65 m, representing the observation domain. To prevent optical distorsion due to refraction through the air-acrylic-water curved interface, this cylinder is inserted in a square acrylic tank of base 1 m $\times$ 1 m and height 0.65 m. The sizing of the experiments has been previously designed by Maurer *et al.* [141] thanks to the proficiency of Denis Letourneau, and has been choosen to be the largest possible within the weight limit supported by the rotating table (see next subsections). Four injectors, one in each angle of the square base of the tank, are used to fill the domain with salt

water. Thanks to small apertures at the bottom of the cylindrical tank, both the inside cylinder and the corners are filled while pumping water into the experiment. The system is presented by a schematic in figure 2.1. Non-pictured in this figure is the additional inner cylinder added afterwards to study standing wave structures (see chapter 4). At the top, the fluid is surface free.

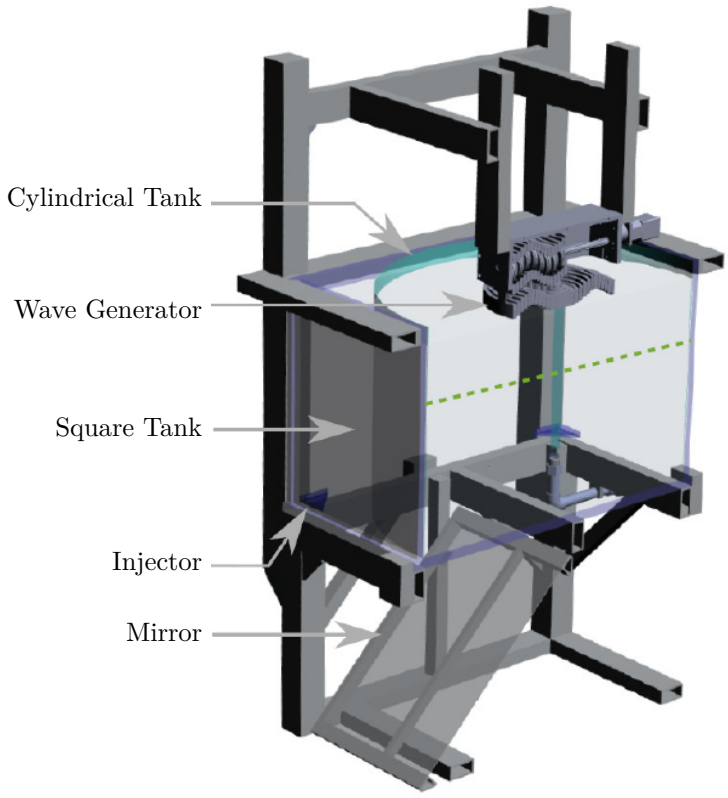

Figure 2.1: Schematic of the experimental apparatus. A cylindrical tank in inserted in a surrelevated square tank. Adapted from [141, 140], courtesy of Denis Letourneau.

2.1.2 Going Stratified: The Double-Bucket Method

As previously mentionned, four injectors placed at the bottom of the tank are used to fill the entire domain with salt-stratified water. In order to do so, we use the double-bucket method [81, 164] to produce linearly stratified fluids and, after some modifications, fluids with arbitrary stratification. The method is derived below.

We consider two filling tanks (labeled 1 and 2) and the apparatus tank as shown in the schematic in figure 2.2. The temporal variation of the volumes of water in the two filling tanks is linked to their flow rates Q_1 (time-dependent) and Q_2 (constant) as

$$\frac{\mathrm{d}V_1}{\mathrm{d}t} = -Q_1 \qquad \text{and} \qquad \frac{\mathrm{d}V_2}{\mathrm{d}t} = Q_1 - Q_2, \tag{2.1}$$

considering that the water going out of tank 1 is going in tank 2. Moreover, the water mass ρV satisfies the following equation in tank 2

$$\frac{\mathrm{d}(\rho_2 V_2)}{\mathrm{d}t} = \rho_1 Q_1 - \rho_2 Q_2. \tag{2.2}$$

These equations lead to

$$V_2(t) = V_2^0 - Q_2 t + \Phi_1(t) \qquad \text{with} \qquad \Phi_1(t) = \int_0^t Q_1(u)\mathrm{d}u. \tag{2.3}$$

Hence, the temporal evolution of the density ρ_2 in tank 2 is given by

$$\frac{\mathrm{d}\rho_2}{\mathrm{d}t} = \frac{\rho_1 - \rho_2(t)}{V_2(t)} Q_1(t) = \frac{\rho_1 - \rho_2(t)}{V_2^0 - Q_2 t + \Phi_1(t)} Q_1(t). \tag{2.4}$$

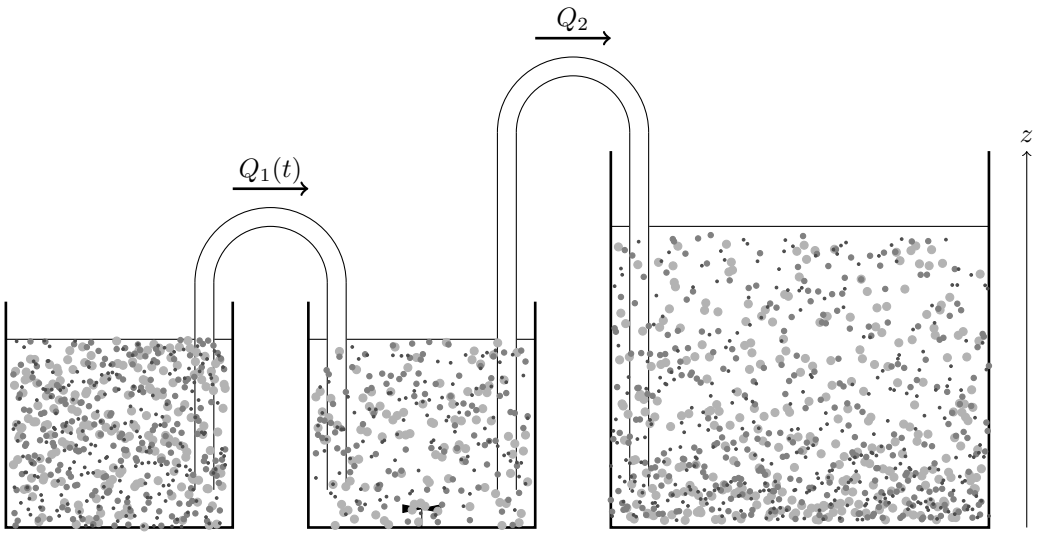

Figure 2.2: Schematic illustrating the double-bucket method, with water transiting from two filling tanks 1 and 2 to the experimental apparatus, with a filling from the bottom.

Different kind of stratifications have been used in the experiments, and we refer to them as linear, bi-linear, and non-linear stratifications. The methods are described below.

Linear Stratification

A linear stratification is defined by its density ρ that increases linearly with depth, which means a constant buoyancy N. To satisfy this condition while filling the apparatus tank, the density in tank 2 has to increase linearly with t. Hence, the previous equations gives $Q_1 = 2Q_2$. If we choose $V_1^0 = V_2^0$, we obtain that during the whole filling process the volumes of tanks 1 and 2 are the same: $V_1(t) = V_2(t)$. The use of a "siphon" to equilibrate the two filling tanks by hydrostatic balance while filling the apparatus is therefore a simple means to produce high quality linear stratifications.

Bi-linear Stratification

We define, by *bi-linear stratification*, a stratification with a buoyancy frequency interface such as the ones we used to explore the transmission properties in chapter 5. Such a stratification has two layers linearly stratified of buoyancy frequencies N_1 and N_2. We adapt the filling process for linear stratification to produce these structures. Our procedure is the following: first, we start filling the apparatus with a "siphon" to produce a linear stratification N_1; then, we stop the filling, close the siphon, and change the salinity of tank 1 by removing salty water and adding the same amount of fresh water; finally, we resume filling the apparatus. As the new salinity is lower and we fill from the bottom, we produce a bottom linear stratification of buoyancy frequency $N_2 < N_1$. As described in chapter 5, we obtain high quality stratifications with sharp interfaces (thickness can be smaller than 1 cm).

Other Non-Linear Stratifications

Other non-linear stratifications are more complex to produce. In our experiments, we used two methods: the first one is to regularly stop the tank filling and modify the salinity of the filling

tanks, the second one is to use a controlable second pump. In the second case, we have to solve numerically the differential system following this path: $N(z) \rightarrow \rho_2(t) \rightarrow \Phi_1(t) \rightarrow Q_1(t)$. Hence we need two pumps, one between each tank, and the pump that connects the two filling tanks is controled by computer. Stratifications with buoyancy discontinuities can be produced, with linear or non-linear variations, as described in chapter 6. For more details on this method, the reader is refered to [140].

Measuring the Stratification

Density and buoyancy were measured as a function of depth using a calibrated PME conductivity and temperature probe mounted on a motorized vertical axis: the probe slowly goes down in the fluid and records conductivity and temperature. Buoyancy frequency is estimated from the mean value of the N profile obtained from the density function $\rho(z)$ measured from the free surface to the bottom, actually a couple of centimeters from the bottom of the tank as limited to the construction of the probe. The stratification is slightly mixed over the top few centimeters, but the wave generator is immersed at a depth of 2 cm so there is no impact on the experiments. Errors on the buoyancy frequency are estimated using the standard deviation of this N profile and are in most cases about 4% of the estimated N value. We usually used buoyancy frequencies in the range $N \simeq 0.6$ rad $\cdot$ s^{-1} to $N \simeq 1$ rad $\cdot$ s^{-1}.

Figure 2.3 presents different experimental realisations of density stratifications measured in the tank. The classical linear stratification obtained using the double-bucket method is shown in figure 2.3(a), and a bi-linear stratification obtained by stopping the filling at a given depth is plotted in figure 2.3(b). Figures 2.3(c) and 2.3(d) present two examples of non-linear stratifications, with (c) an interrupted stratification suitable for studying tunnel effect (see chapter 6) obtained by superimposed linear fillings, and (d) an exponential stratification used for focusing of internal waves (see [140]) obtained using a computer controlled pump.

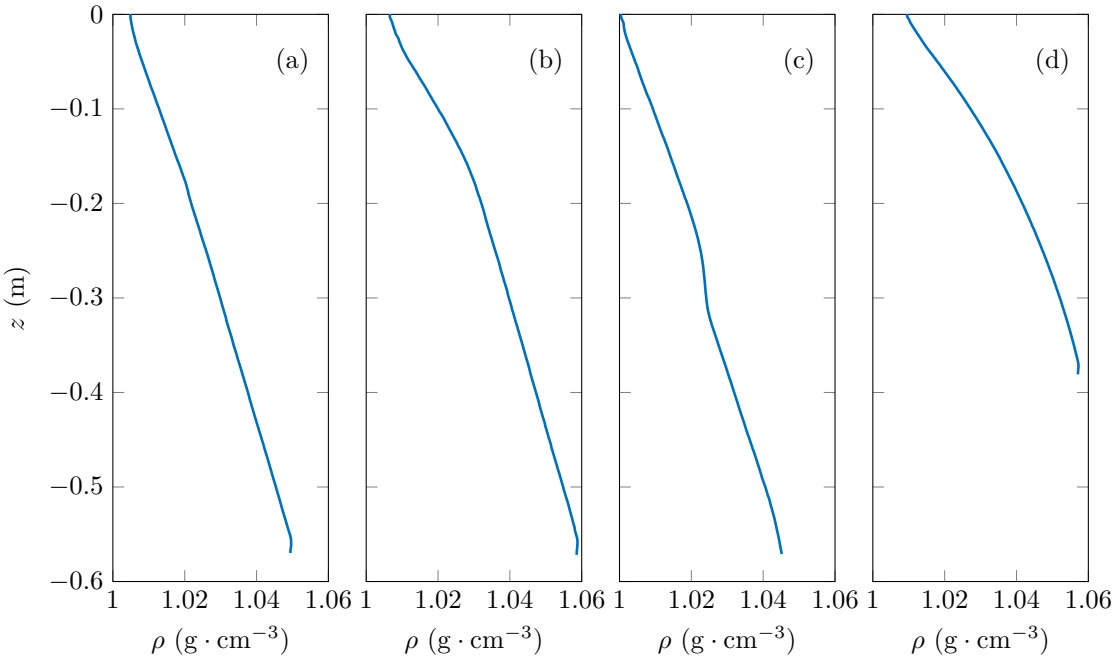

Figure 2.3: Examples of experimental stratifications, from left to right: (a) linear, (b) bi-linear, (c) non-uniform with a constant density layer, and (d) non-uniform with exponential profile.

2.1.3 Going Inertial: The *PERPET* Facility

Since Maurer's thesis [140], the experimental appartus presented in figure 2.1 is mounted on a 2 m rotating table called *PERPET* (*Plateforme d'Études en Rotation de Phénomènes et Écoulements*

de la Terre). This facility can provide a rotation from 0 to 60 rpm, which means that the range of Coriolis frequency that can be used in the experiments varies from 0 to 12.5 rad $\cdot$ s^{-1}, with an error of 0.1%. The axis of rotation of the table is aligned with the center of the cylindrical tank, and with the vertical axis (the angle between the rotation axis and gravity is less than 10^{-3} degrees).

Electronic systems are all embeded and remotely controlled through a computer located inside the table.

The whole experiment is shown in the photography in figure 2.4, with the tank mounted on the rotating table . The particular configuration that can be seen in the tank will be discussed in chapter 8.

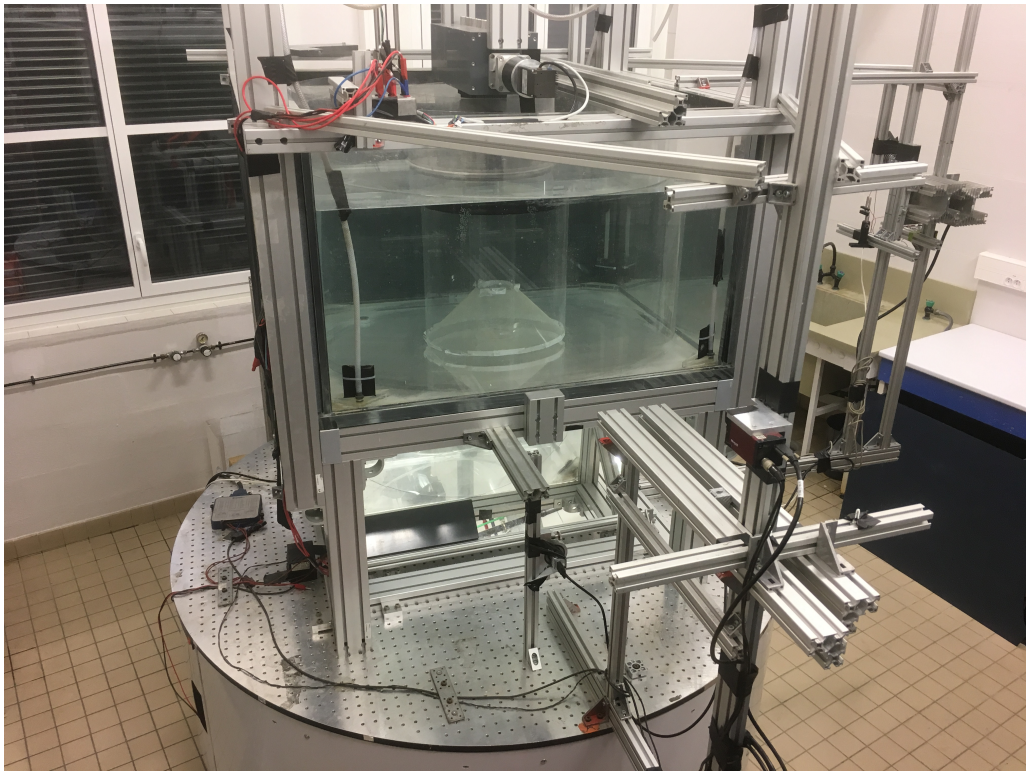

Figure 2.4: Photography of the experimental setup on the rotating table *PERPET*.

2.2 An Axisymmetric Wave Generator

The double-bucket method and the *PERPET* facility allow us to produce a stratified rotating fluid in a cylindrical tank, suitable for internal wave experiments. We now discuss the wave generation mechanism used to excite axisymmetric wave fields in the experimental domain.

Historically, the long-going tradition of internal wave experiments was initiated by Görtler [91] and Mowbray & Rarity [155] through the use of oscillating cylinders in density stratified fluids. Such a device has led to the first experimental verification of the dispersion relation and of the existence of the *Saint Andrew Cross*. Later on, paddle generators have been developped to excite vertical [51] or horizontal [228, 229] two-dimensional standing wave fields, a system improved to produce amplitude and frequency controlled excitations by a lateral excitation [42]. In most cases, much of the focus was on two-dimensional internal wave beams generated by excitation methods such as an oscillating cylinder [155, 223] or moving topography [3, 68]. For modeling purposes, such a wave field can be treated as nominally invariant in the transverse direction and thus described in terms of plane waves *via* Fourier transforms [122, 220].

Axisymmetric wave fields have traditionally been experimentally excited using a vertically oscillating sphere and exploring the shape of the wave beams [74, 80, 87, 154, 169, 215]. The radially decreasing amplitude and the viscous decay of the conical wave beam emitted by an

oscillating sphere has been explored in laboratory experiments by Flynn *et al* [80] showing good agreement with theoretical predictions. More sophisticated axisymmetric experimental geometries have been investigated using a vertically and a horizontally oscillating torus, respectively [66, 76], in which case a highly non-linear process occurs due to the three-dimensional geometric focusing, able to transport momentum and break into turbulence. None of these experimental configurations, however, readily permitted a change in the form nor the wave number of the wave field being excited.

Based upon previous wave generator technologies and, in particular, the planar wave generator designed by Gostiaux *et al.* [92] that has been proven efficient in generating internal wave fields [92, 25, 148, 140], an axisymmetric wave generator has been developed and tested by Maurer *et al.* [141, 140] with the help of Marc Moulin at the *Laboratoire de Physique de l'ENS de Lyon.* A photography of the device is presented in figure 2.5.

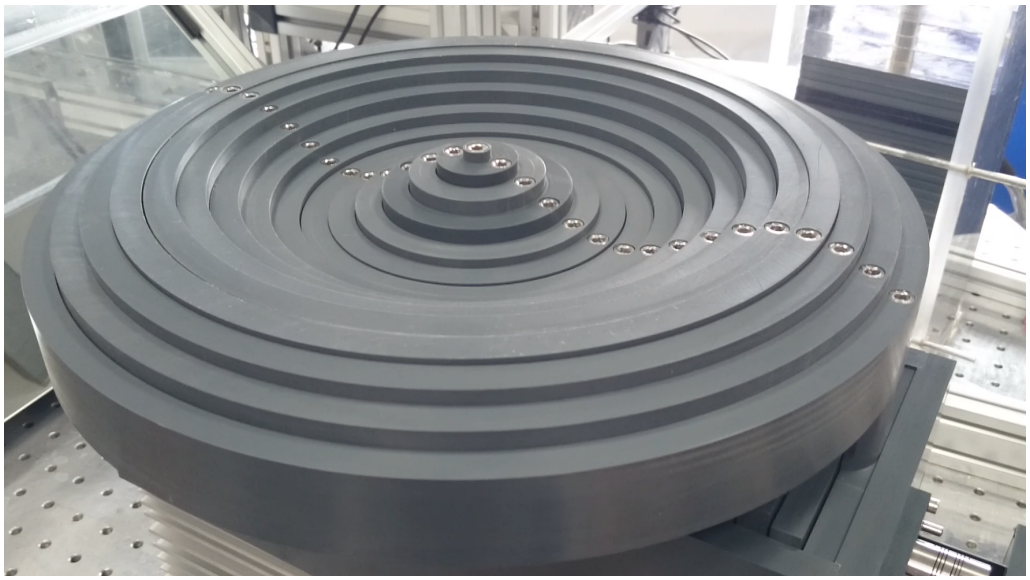

Figure 2.5: Photography of the axisymmetric wave generator (reversed).

The generator comprises sixteen, 12 mm thick, concentric PVC cylinders periodically oscillating, each of them being forced by two eccentric cams. These cams are presented with a schematic in figure 2.6(left) and shown mounted on the camshaft in the photography in figure 2.6(right). The disk, with a non-zero eccentricity e, allows for a circular motion to be converted into a unidirectional translational motion. As can be seen in figure 2.6, the six-branches cam axis is not aligned with the direction of translation, but is shifted by 15°. As described in [27], this allows for a wide variety of configurations as the the eccentricities can be set to introduce a phase shift between the cylinders, in addition to the oscillating amplitude that can be set for each individual cylinder. As a result, the vertical displacement of the n^{th} cylinder can be described by

$$a_n(t) = A_n \cos(\omega t + \alpha_n), \tag{2.5}$$

with A_n its amplitude, ω the forcing frequency, and α_n a phase shift. For a smooth motion of the PVC cylinders, a 1 mm gap is kept between each cylinder and the total diameter of the wave generator is then 402 mm. In the experimental setup, the generator is mounted at the surface of the water to force downwards internal waves by imposing the vertical velocity at the top boundary.

Once the amplitudes of the cams are set, the wave generator can excite a wide range of wave fields, all axisymmetric as the forcing cylinders are θ-invariant. As described in chapter 4, the device is enclosed in a cylindrical tank of the same radius $R = 20.4$ cm and a volume preservation over the whole cylindrical domain therefore applies, as

$$\int_0^{2\pi} \int_0^R A(r,\theta) r \mathrm{d}r \mathrm{d}\theta = 0. \tag{2.6}$$

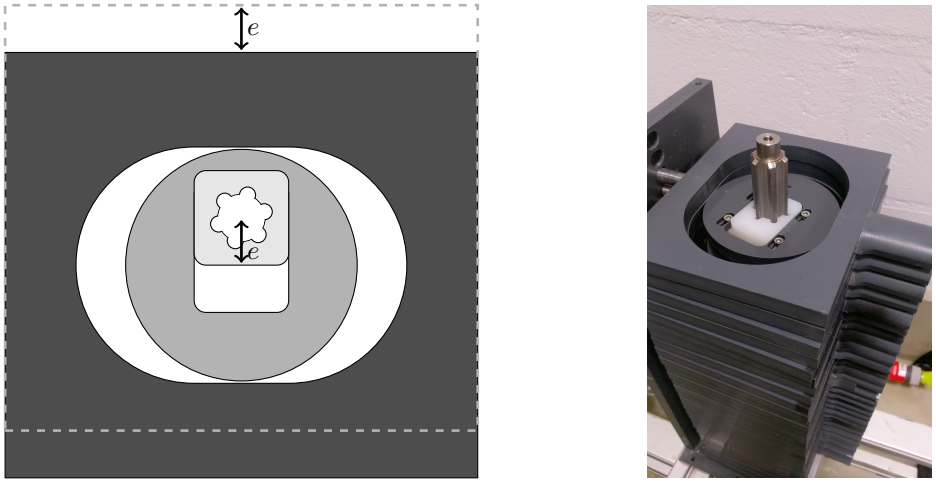

Figure 2.6: Left: schematic of the cam system. The eccentricity e can be changed by moving the light grey part. The rotational motion of the star shaped axis is changed to a translational motion of the plate (dark grey part). Right: photography of the cams mounted on the camshaft.

In addition, a relevant boundary condition of zero radial velocity has to be satisfied at the cylinder wall to prevent pumping behaviours and unwanted fluid motions, i.e.

$$v_r(r = R, z, t) = 0. \tag{2.7}$$

In the particular case of modal forcing, which means forcing by a zeroth order Bessel function (see chapters 1 and 4), the volume preservation equation is always satisfied if the radial boundary condition is satisfied too due to integration properties of Bessel functions of the first kind. This leads to discretised values of the radial wave number l that can be chosen for the generator profile, the first ones corresponding to mode 1 ($l = 19$ m^{-1}), mode 2 ($l = 35$ m^{-1}), and mode 3 ($l = 51$ m^{-1}). The generator has been proven efficient in generating these modes, as detailed in chapter 5 and in Boury *et al.* [33]. Higher order modes have not been tested due to the discretisation of the Bessel profile that poorly reproduces short wave lengths when the steepness, product of the wave number l by the amplitude at the center a, increases. With the smallest steepness for a given amplitude, the mode 1 is the most reliable to use and experiments were conducted using this mode with two amplitudes, the first one called *low amplitude* that prevents nonlinear effects from arising too quickly in the experiment, and the second one called *high amplitude*. Results with this confguration are described in chapters 4, 5, 6, and 7.

A last configuration, with zero amplitude for the five inner cylinders, has been used to produce inertial wave attractors (chapter 8). The five inner cylinders being removed and the experimental domain being confined between two PVC cylinders, two boundary conditions must be taken into account for the radial velocity and, as a consequence, the volume conservation condition cannot be obtained straightforwardly. To fit our needs, the motion amplitudes of the remaining eleven outer cylinders have been especially adjusted to cancel the volume of fluid displaced during its motion, such that the profile $A(r)$ of the generator satisfies

$$\int_{R_0}^{R_1} A(r) r \mathrm{d}r = 0, \tag{2.8}$$

with R_0 and R_1 the radii of the inner and outer cylinders. In order to preserve the boundary condition of non pumping fluid at the cylinder edges, the radial velocity v_r has to be zero at R_0 and R_1. This condition writes, in terms of the profile $A(r)$, as[1]

$$\frac{\mathrm{d}A}{\mathrm{d}r}(r = R_0) = \frac{\mathrm{d}A}{\mathrm{d}r}(r = R_1) = 0. \tag{2.9}$$

[1]This relation is only true for axisymmetric modes. In general, for non-axisymmetric modes, the relation between the vertical amplitude and the radial and vertical velocities is more complicated.

In order to fulfill these conditions, a Bessel function truncated from R_0 to R_1 could be used, but with too many nodes for the discretisation of our wave generator. Instead, the simplest profile that could be used, a cubic function, was then designed according to these two equations. Note that the steepness cannot be defined in the same way as the modes for such a profile, so we use the derivative of the cubic function where its sign changes.

The radial structures of the generator profiles used to force wave fields are presented by schematics in figure 2.7, and the corresponding steepness and cam amplitudes are listed in table 2.1. The first three profiles in figure 2.7 correspond to modes 1 through 3, with different radial wave numbers, and the fourth profile is the truncated cubic function used for wave forcing in the annular axisymmetric domain.

Profile	mode 1 (high amplitude)	mode 1 (low amplitude)	mode 2	mode 3	cubic profile (attractor)
Steepness	0.095	0.048	0.175	0.255	0.030
Cam number	Cam amplitude (mm)				
1	5	2.5	5	5	0
2	4.9	2.4	4.7	4.5	0
3	4.7	2.3	4	3	0
4	4.3	2.1	2.9	1.2	0
5	3.9	1.9	1.6	−0.6	0
6	3.3	1.6	0.3	−1.7	2.45
7	2.6	1.3	−0.8	−2	2.23
8	1.9	0.9	−1.6	−1.4	1.88
9	1.2	0.6	−2	−0.4	1.43
10	0.5	0.2	−1.9	0.7	0.9
11	−0.2	−0.1	−1.5	1.4	0.35
12	−0.6	−0.3	−0.9	1.5	−0.18
13	−1.2	−0.6	−0.1	0.9	−0.68
14	−1.6	−0.8	0.6	0	−1.1
15	−1.9	−0.9	1.2	−0.8	−1.4
16	−2	−1	1.5	−1.2	−1.55

Table 2.1: Steepness la of the profile, and amplitudes (in mm) of the cams of the generator in the different mode profiles we used. The first cam is located at $r = 0$.

2.3 Visualisation: Particle Image Velocimetry

Velocity fields were obtained in all our experiments via Particle Image Velocimetry (PIV), which principle is illustrated in figure 2.8. The fluid is seeded with tracing particles and successive snapshots taken at regular time intervals $\mathrm{d}t$ are recorded in the observation plane. In this time interval, the particles undergo a coherent displacement noted $\mathrm{d}\mathbf{r}$ so that the local velocity is given by $\mathrm{d}\mathbf{r}/\mathrm{d}t$. A correlation algorithm is performed over boxes of particles to determine the local displacement.

In practice, a laser sheet is created by a laser beam (Ti:Sapphire, 2 watts, wave length 532 nm) going through a cylindrical lens. It can be oriented either horizontally (to measure the radial and orthoradial velocity) or vertically (to measure the vertical and the radial velocity). Visualisation of the horizontal plane with the same co-rotating camera embedded on the rotating table is made possible by the use of a 45° mirror placed under the tank.

For the purpose of visualisation, 10 μm diameter hollow glass spheres of volumetric mass 1.1 $\mathrm{kg \cdot L^{-1}}$ are added to the fluid while filling the tank. In some experiments, to obtain good quality velocity fields near the bottom of the tank and while imaging in a horizontal plane, 10 μm silver-covered spheres of volumetric mass 1.4 $\mathrm{kg \cdot L^{-1}}$ are added when needed. Images are usually recorded at 1 Hz, 4 Hz, or 40 Hz, and data processing of the PIV raw images is done using

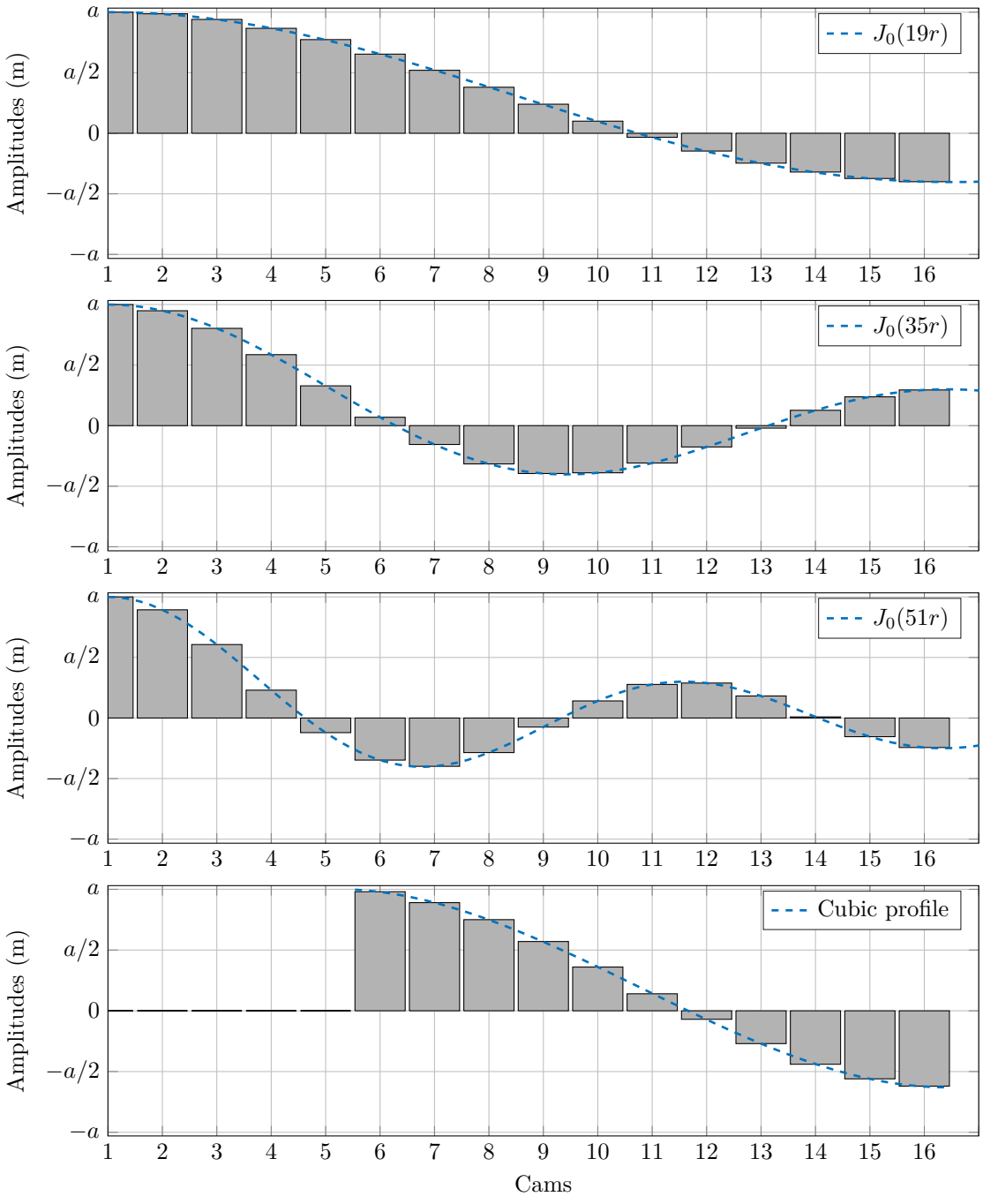

Figure 2.7: The four generator configurations of interest with, from top to bottom: mode 1, mode 2, mode 3, and truncated cubic profile.

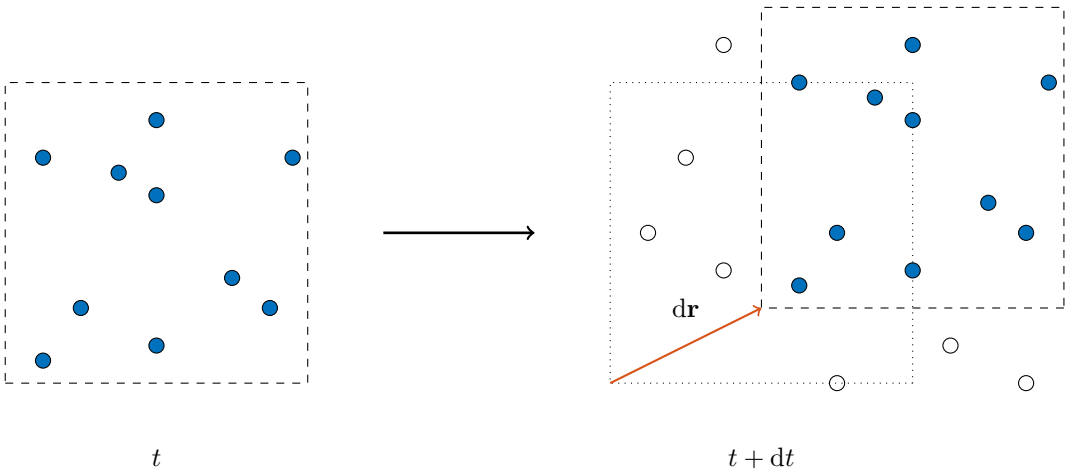

Figure 2.8: Schematic illustration of the PIV technique, with a displaced field of seeding particles d$\mathbf{r}$ (in blue) during dt in a box contained in the observation plane. Adapted from [104].

the CIVx (Correlation Imaging Velocimetry) algorithm [77] thanks to the capabilities of the Pôle Scientifique de Modélisation Numérique (PSMN) hosted at the ENS de Lyon.

2.4 Fourier, Hankel and Hilbert Filtering

Data processing usually involved a few mathematical operations. In 2D, solutions of linear systems can be described by plane wave decomposition using Fourier transforms. In the axisymmetric case, the Fourier transform can only be performed along the vertical axis and for temporal evolution. The radial description, in terms of Bessel functions, is given by a Fourier-like transform called the Hankel transform (see [163] and Appendix C). If we consider a radial function f, its direct transform g is

$$g(y) = \mathcal{H}[f](y) = \int_0^{+\infty} f(x) J_n(xy) \sqrt{xy}\, \mathrm{d}x, \tag{2.10}$$

and the inverse transform of g is

$$f(x) = \mathcal{H}^{-1}[g](x) = \int_0^{+\infty} g(y) J_n(xy) \sqrt{xy}\, \mathrm{d}y. \tag{2.11}$$

As for the Fourier transform, the combination of the direct and inverse transform gives the original function back

$$\mathcal{H}^{-1}[\mathcal{H}[f]](x) = f(x). \tag{2.12}$$

When dealing with propagating wave fields, it is interesting to separate the different components according to their direction of propagation. An analytical method, called Hilbert Filtering, has been developed by Mercier *et al.* [149] and successfully tested in laboratory experiments.

2.5 Numerical Methods

Apart from data processing, our modellings and experimental results are, in some cases, compared to numerical computations.

We performed several Direct Numerical Simulations (DNS) in 2D to get insights of the results. These DNS were run in Python using the spectral method based code Dedalus [50], developped by K. Burns, G. Vasil, J. Oishi, D. Lecoanet, and B. Brown, and available online (`http://dedalus-project.org`). In order to apply forcing and boundary conditions accordingly, we used a CosSin base in the horizontal direction (that corresponds, in 3D, to the radial axis) and a Chebyshev base in the vertical direction.

More complex 3D DNS have been run by Ilias Sibgatullin using spectral element method, based on Nek5000 open solver, to explore the properties of cylindrical inertial wave attractors. They are mentioned in more details in chapter 8.

We developped several Matlab codes using `bvp4c` to solve boundary value problems, in order to investigate properties of non-linear stratifications. For example, in chapter 5, we describe transmission of internal waves through a buoyancy interface, which means a transition between two buoyancy frequencies N_1 and N_2, that can be either sharp or smooth. The sharp case was computed analytically and checked with the numerics. The smooth case was estimated numerically and then compared to experimental results. To avoid numerical singularities due to abrupt transitions between two different values of N, and for a more physical model, our DNS and boundary value problems were run with buoyancy profiles modelled by hyperbolic tangents.

2.6 Conclusion

In this chapter, we have presented a review of the techniques used to perform laboratory experiments. The apparatus, constituted of a $\sim$ 600 L tank mounted on a rotating table, allows for both gravity and inertial wave experiments when filled with salt-stratified water and put in rotation. Additional cylindrical tanks are inserted in the experimental domain to create axisymmetric boundary conditions and confine the excited wave field. PIV technique is then used to record velocity fields in vertical and horizontal cross sections.

A novel axisymmetric wave generator, developped by Maurer *et al.* [141] at the *Laboratoire de Physique de l'ENS de Lyon*, has been described. This device is used throughout the thesis with various configurations, designed according to boundary conditions, to produce modal wave fields of given radial wave length (see chapter 4), and a cubic profile used for attractor experiments (see chapter 7), both volume preserving.

Finally, we have described numerical methods used for data processing and numerical simulations used either to do preliminary tests (in 2D) or to complete the experimental study over wider ranges of parameters (see chapter 7).

CHAPTER 3

Internal Waves in the Ocean and in the Atmosphere

Stank ha skañv war varlenn an noz
E kouez eur vrumenn hlao,
Ganti blaz c'hwero ar ranngalon.
Troet ar bed da voged briz
Ha teuzet e alan peb tra, peb tra,
Na hent dirazañ na roud a-dreñv,
Dall e valean er vro vud.
Per-Jakez Helias, Maner Kuz – Manoir Secret

As mentioned in the previous chapters, the atmosphere and the oceans are media that can support internal waves, either *gravity waves*, due to their inherent stratification in density, or *inertial waves*, due to the Earth rotation.

Of primary importance are internal waves in the oceans. Since Munk's *Abyssal Recipes* [156] and Wunsch's works [157, 249], the importance of internal waves in the global Earth energetic balance is well known, and the study of dissipation phenomena through wave breaking and turbulence is a very active field in stratified mixing and oceanography communities. In a recent review paper, MacKinnon *et al.* [133] discuss the mechanisms and implications of the dissipation of internal wave energy in the oceans, reminding the 2 ± 0.6 TW estimate of turbulent dissipation caused by tidal flow over topographies, low-frequency lee waves, and near-inertial waves produced by wind forcing [16, 114, 242].

This chapter explores some properties of the atmosphere and the oceans, from stratification and rotation in section 3.1 to internal wave generation in section 3.2. More detailed implications on the dynamics of the oceans are given in section 3.3 before concluding remarks in section 3.4.

3.1 Stratification and rotation

3.1.1 Stratified Fluids

The atmosphere was the first of the geophysical fluids to be accurately sounded. Estimated from local Earth-based measurements on plains and mountains, and from weather balloon probes, the atmospheric stratification shows an important thermal variability with altitude. Temperature and pressure variations help divide the atmosphere into different layers called, starting from the ground: *troposphere*, *stratosphere*, *mesosphere*, and *thermosphere* [220]. Figure 3.1 shows a schematic diagram of the atmosphere structure. The density profile of the atmosphere, and its physics, strongly depend on pressure (which varies over six orders of magnitude) due to air compressibility.

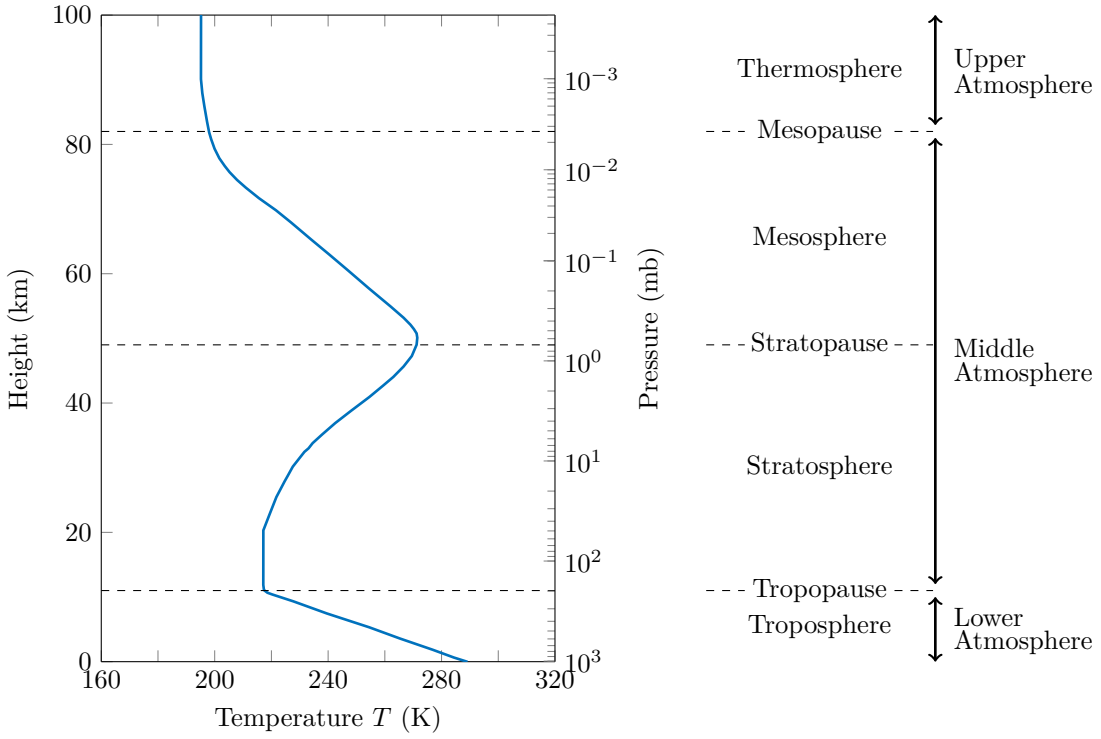

Figure 3.1: Simplified structure of the Earth's atmosphere. Adapted from [124, 234].

As to the oceans, the recent use of profiling shipboard devices (e.g. Conductivity-Temperature-Depth (CTD) casts, or yo-yo probes going up and down) and of profiling floats, such as the worldwide ARGO program, has led to an increasing knowledge of their properties. Models have been developped and successfully tested to describe oceanic stratifications. For example, a fairly accurate parametrisation for density of sea is the equation of state [151, 220]

$$\rho(T,S) = \rho_0 \left[1 - \alpha_T (T - T_0) + \alpha_S (S - S_0)\right], \tag{3.1}$$

where ρ_0, T_0, and S_0, are the reference density, temperature, and salinity, and α_T and α_S are first order thermodynamic coefficients to take into account the variations of density with temperature T and salinity S. Density variations with temperature are expressed through α_T, which can be either positive or negative depending on the range of temperatures (fresh water has a minimum in density at 4°C). The other coefficient, α_S, is always positive so that the saltier the water, the higher the density. Extracted from [220], figure 3.2 depicts generic profiles of temperature (solid line) and salinity (dashed line) in the ocean at different locations, from polar regions (a) to mid-latitudes (b) and tropics (c). In the oceans, in general, temperature variation is the most important contribution to density changes, especially in the first 500 or 1000 m, in a layer called *thermocline*. When salinity variation dominates, a similar layer exists called *halocline*.

Most of the oceanic stratifications can be divided into three different regions. The first hundred meters below the surface are called the *mixed layer*, quasi-homogeneous in temperature and salinity due to interactions with the atmosphere and subsequent mixing events. Then, until 1 km depth, the *pycnocline* (combination of thermocline and halocline) is a strongly stratified layer with buoyancy frequencies of about $10^{-1} - 10^{-2}$ rad $\cdot$ s^{-1}. The *deep ocean*, which is the remaining part of the water column, is very weakly stratified and has buoyancy frequencies in the range $10^{-3} - 10^{-4}$ rad $\cdot$ s^{-1}, often with unstratified water at the very bottom. Near the poles, due to the presence of melting ice at the surface during summer, and of river runoffs throughout the year, the top layer may differ and be colder and fresher than usual.

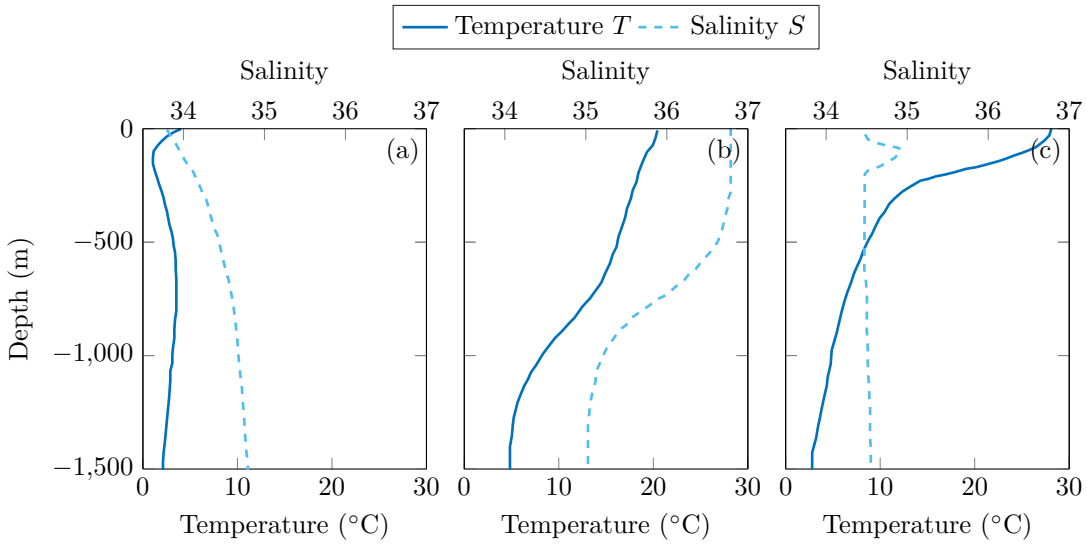

Figure 3.2: Schematic profiles of temperature (solid line) and salinity (dashed line) for oceanic stratifications at different latitudes: (a) near the poles; (b) at mid-latitudes; (c) around the tropics. Adapted from [220].

3.1.2 Rotation and f-plane Approximation

The Coriolis force $\mathbf{C}$ introduced in chapter 1 is related to the rotation vector $\mathbf{\Omega} = \Omega \mathbf{e_z}$, with $\mathbf{e_z}$ the unit vector along the vertical, and the particle velocity $\mathbf{v}$, by

$$\mathbf{C} = -2\Omega \mathbf{e_z} \times \mathbf{v}. \tag{3.2}$$

On Earth, however, at a given latitude φ the rotation vector $\mathbf{\Omega_T}$ is not aligned with the vertical axis, except at the poles. As depicted in figure 3.3, one can consider the projection of $\mathbf{\Omega_T}$ over local z and y axis for a point at latitude φ, $\Omega_z = \Omega_T \sin\varphi$ and $\Omega_y = \Omega_T \cos\varphi$, respectively. A common approximation, when the height of fluid is small, is to neglect the tangental projection Ω_y and only use the vertical projection Ω_z to compute the Coriolis frequency, so that $f \equiv f_0 = 2\Omega \sin\varphi$. This zeroth order development is called the *f-plane approximation* (see [18] for more details). At first order, the variation of f with latitude within a small region can be estimated using a constant coefficient β as $f = f_0 + \beta y$, which is called the *β-plane approximation*.

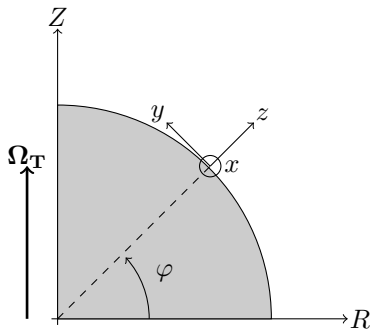

Figure 3.3: f-plane approximation.

The f-plane approximation is valid for polar to mid-latitudes, where variations of f are small with the latitude[1]. With an Earth rotation rate of $\Omega_T \simeq 7.3 \cdot 10^{-5}$ rad $\cdot$ s^{-1}, typical values of the Coriolis frequency f are about 10^{-4} rad $\cdot$ s^{-1}.

[1] As detailed in Gerkema *et al.* [85] and recalled in Beckebanze's thesis [18], non-physical effects are known to be created with this approximation, for example when considering internal waves close to the equator.

3.2 Atmospheric and Oceanic Internal Waves

Internal waves can be excited in a stratified fluid through various processes: it can be an immersed body moving within the fluid or, the dual situation, the whole fluid itself moving over a rough topography [220]; but waves can also be generated from free surface activity [187].

In the atmosphere, internal waves can be radiated from large scale storms localised in the troposphere, as measured by Sentman *et al.* [206] in a US MidWest thunderstorm, but the most common generation mechanism is flow moving over the topography. Figure 3.5(left) shows an example of atmospheric internal waves created in the wake of a flow behind Amsterdam Island, with a clear spatial lengthscale highlighted by white crests formed by clouds. In both cases, waves are mostly generated in the lowest layers of the atmosphere and radiated upwards.

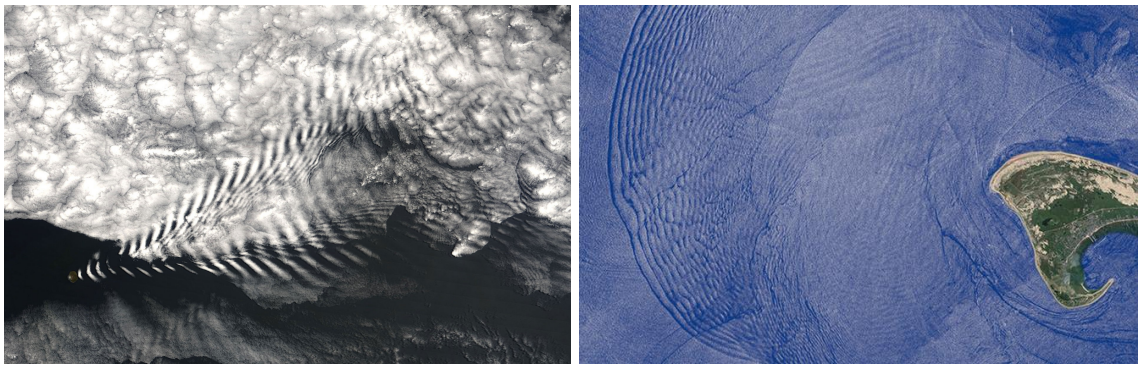

Figure 3.4: Satellite photographies of internal waves. Left: atmospheric internal waves, above Amsterdam island in the Indian Ocean. Source: Wikipedia. Right: oceanic internal waves, around Cape Cod (MA,USA). Source: Jose da Silva, University of Porto.

As shown by the schematic in figure 3.5, extracted from [133] and based upon [84], a wide diversity of processes are involved in wave generation in the oceans. Internal waves can be generated either in deep layers due to the topography of the oceanic floor, or near the surface due to the ocean-atmosphere interaction. Topographic generation, linked to currents, subduction, and tidal motions [162], is likely to create near-inertial wave fields (NIW) with a frequency close to the local Coriolis frequency. Such a generation is of particular importance as, in the global energetic balance, a large part of the tidal energy is transfered to internal waves before being dissipated in the oceans [249]. Storms and winds can also generate internal waves in the pycnlocline after having excited inertial oscillations across the mixed layer. A satellite photography of oceanic internal waves created near Cape Cod (MA) is presented in figure 3.4(right).

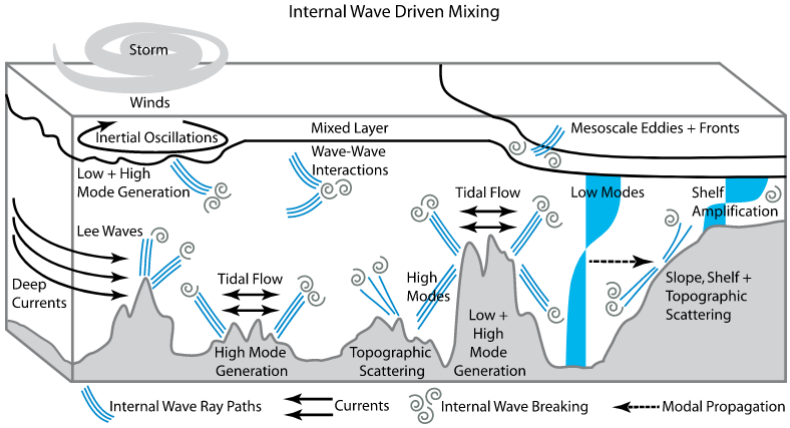

Figure 3.5: Schematic of internal wave generation in the oceans. Extracted from [133]

Qualitatively, from a remote point of view, huge atmospheric perturbations such as hurricanes [113], typhoons, and tropical cyclones [202], taking part in this wave generation, behave like disk-shaped structures moving at the surface of the ocean (figure 3.6) and are able to excite wave fields with the same cylindrical symmetry. A first order approximation, supported by in-situ measurements [113, 202], is to consider purely axisymmetric wave fields described by a linear combination of Bessel functions with various frequencies and wave lengths. Other evidences of such wave fields can be found in the wake of rising bubbles or falling solids in stratified fluids [154], or plumes penetrating in a density stratification [13]. These considerations motivate the new wave generator used in our experimental apparatus and presented in chapter 2.

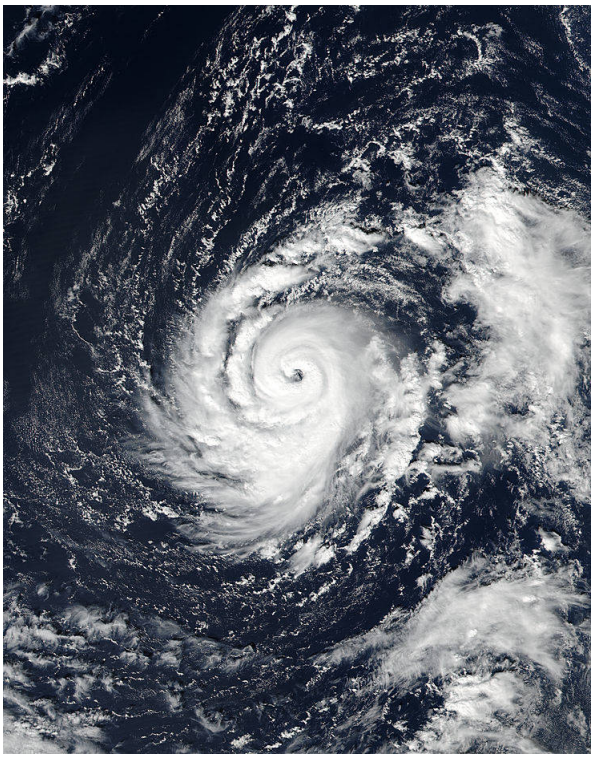

Figure 3.6: *Ophelia* hurricane (source: NASA).

3.3 Oceanic Implications

As detailed in section 3.2, internal waves are ubiquitous in the oceans. This activity leads to a complex dynamics that influences global currents and circulations, and density stratification, as will be discussed in the following subsections.

3.3.1 Thermohaline Circulation

The world's oceans are all connected together and water masses can be transfered between them by currents. The large scale circulation, taking place into this global ocean with a transit time of about 1000 years, is called the *thermohaline circulation*, or *Great Ocean Conveyor Belt* [41]. It is driven by differences in density between various types of water, due to temperature (*thermo*) and salinity (*haline*). The map in figure 3.7 depicts the common representation of this worldwide circulation, with warmer and fresher waters at the surface in red, and colder and saltier waters more in depth in blue, with downwelling and upwelling regions. Allowing for water exchanges and mixing in a closed loop between the Earth's oceans, the thermohaline circulation is primordial for energy transport at the globe scale and, as such, for climate regulation.

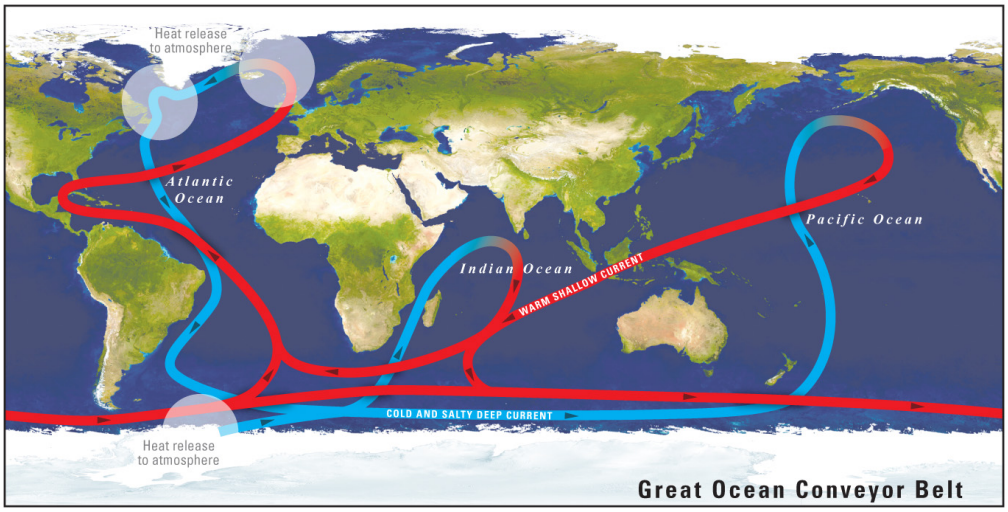

Figure 3.7: Simplified map of the Thermohaline Circulation, also called Great Ocean Conveyor Belt [41], that transports water masses worldwide. Warm shallow currents are shown in red, whereas cold and salty deep currents are shown in blue. Downwelling occurs near the poles with heat release to the atmosphere (source: USGS).

3.3.2 Stratified Mixing

Since the in-situ measurements of Polzin *et al.* [186] in the Brazil Basin, and Munk and Wunsh's collection of data [157], the maintenance of the oceanic stratification and its correlated mixing processes have drawn increasing attention. Though downwelling (i.e. sinking of heavy water) is located at high latitudes near the poles, where oceanic water gets colder in contact with the ice, and also saltier in winter due to brine rejection from sea ice formation, the opposite phenomenon of upwelling (i.e. rising of light water) is way more diffuse and widely distributed.

In his *abyssal recipes*, assuming a uniform uni-dimensional upwelling over the entire abyssal ocean, Munk [156] infered from an advection-diffusion balance the existence of an *eddy diffusivity* characterising oceanic mixing. This diffusivity has been consistently measured in the works of Polzin *et al.* [186] and Munk and Wunsch [157]. Figure 3.8 reproduces the in-situ eddy diffusivity measurements in the Brazil Basin performed by Polzin *et al.* [186], showing heterogeneous and anisotropic variations, influenced by topography: the eddy diffusivity is about an order of magnitude larger above rough topographies (on the right-handside) than flat topographies (on the left-handside).

Estimates from Egbert and Ray [71] indicates that 1/3 of the 3 TW input from tidal forcing is being dissipated on deep ocean topographies, and a significant part of it is transfered to internal waves [249]. Since about 1 to 2 TW energy is needed to close the energetic balance in the oceans and help cold and salty water rise to the surface [157], inertia-gravity waves are a very likely candidate to sustain stratified mixing and link energy input in the ocean to turbulent mixing. In that sense, internal wave activity is a major phenomenon connecting large scale events (e.g. tidal forcing) to small scale dissipation processes (turbulent mixing).

The exact mechanisms for stratified mixing, however, remain unknown. Overturnings and localised mixing events due to instabilities (Kelvin-Helmholtz, Holmboe, Taylor-Caulfield) can usually be triggered by shear at density interfaces [67], leading to exchanges in the energetic balance of the stratification [245]. Internal wave breaking has also been pointed as a mechanism for mixing and triggering turbulent events with decreased Richardson number [236], occuring for high amplitude waves. Interestingly, in the oceans, a broad diversity of phenomena can lead to high amplitude internal waves, for example: reflections on a slope [59], attractors [43, 44], focusing effects [49], constructive interference and resonant cavity-like behaviors [33, 69, 219], and Lee wave generation and breaking [11, 160]. Subsequently, non-linear behaviours may trigger instabilities (e.g. Triadic Resonant Instability (TRI) [107]) and cascades to small scales [42]. Such phenomena

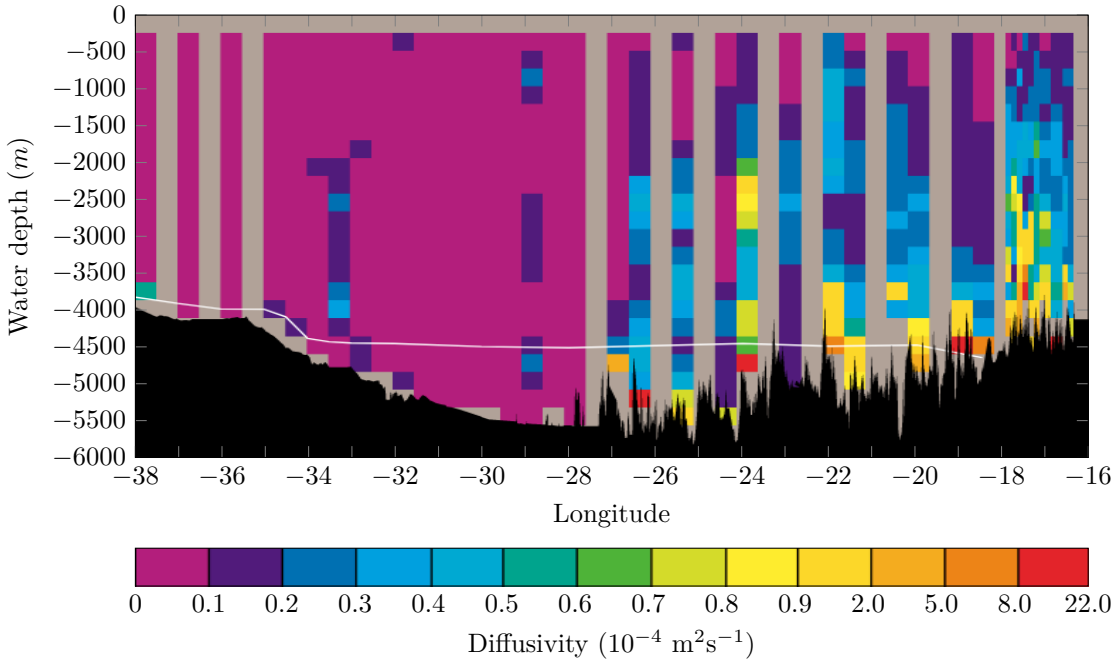

Figure 3.8: In-situ measurements of eddy diffusivity over a longitudinal transect in the Brazil Basin. Extracted from [186].

are more likely to occur close to rough topographies where inceased eddy diffusivity has been measured [186], so there is a chance that they have a significant role in oceanic mixing processes.

3.3.3 Arctic Ocean

Since the last decades, the two polar oceans of the Arctic and Antarctic are drawing more and more attention in a context of increasing global warming. Due to its particular location, confined between American and Eurasian continental mainlands, and contrary to the Antarctic Ocean, the Arctic is poorly connected to the "global ocean" and mostly preserved from the activity of worldwide currents such as the Thermohaline Circulation (figure 3.7).

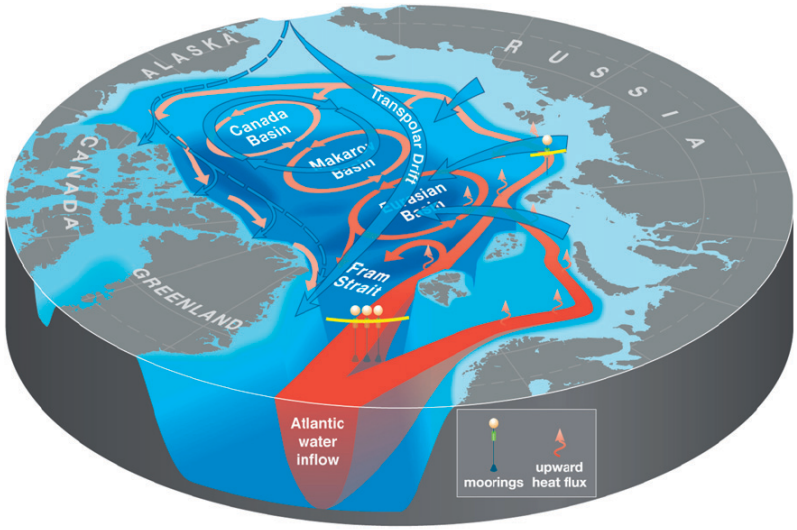

Figure 3.9: Schematic showing current circulation in the Arctic Ocean. Extracted from [185].

As illustrated in figure 3.9, the two water inflows in the Arctic Ocean come from the Bering Strait between Alaska and Siberia (Pacific water entering through the Chukchi Sea) and from the Fram Strait between Greenland and Norway (Atlantic water flowing into the Arctic basins). Moreover, the Arctic is also alimented by river runoffs from the continents and by ice melting, providing additionnal fresh and cold water masses. Fed by several types of water with different temperature and salinity properties, poorly impacted by global currents and isolated from the atmosphere with year-round ice coverage, the Arctic Ocean is therefore highly stratified with water masses of very different temperatures and salinity layered on top of each other (e.g., as detailed in chapter 9, inflows with warm water with up to 6°C can exist at ten meter depth though surface water temperature is about -2°C).

A simplified representation of oceanic stratification is presented in figure 3.10 for purpose of comparison. The left pannel shows a typical oceanic stratification that can be found in the Atlantic or in the Pacific Ocean, with a homogeneous mixed layer on top of a highly stratified pycnoclyne, and a bottom deep ocean weakly stratified. The right pannel is a schematic of the Arctic stratification, with fresh water on top (coming from melting ice and river runoffs), on top of the Pacific and Atlantic Haloclines, followed by a wider layer of Atlantic Water and an even deeper abyssal Arctic water mass. As such, mixing mechanisms are very important in such a strongly stratified ocean, where layers alternate between cold fresh waters and warm salty waters.

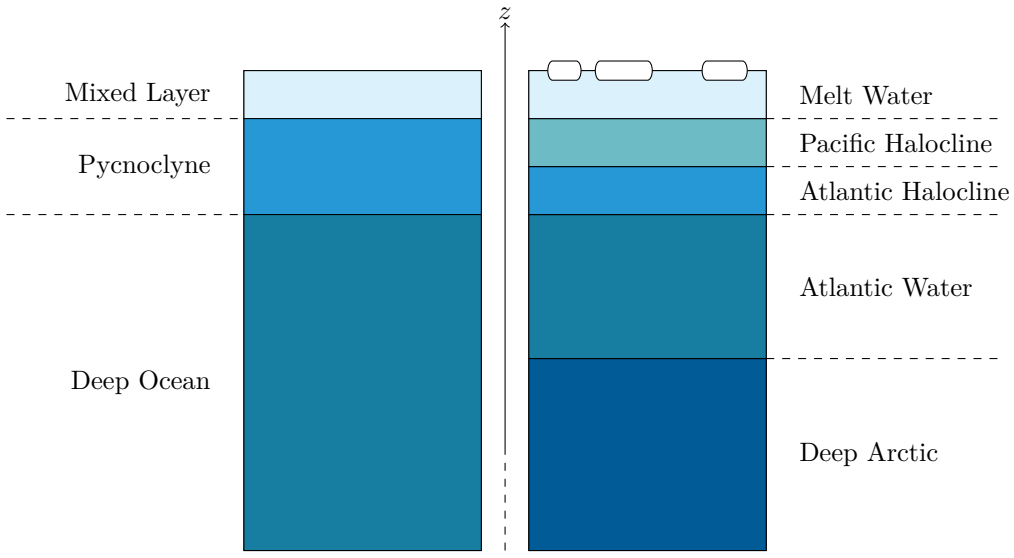

Figure 3.10: Simplified models of mid-latitude oceanic stratification (e.g. Atlantic and Pacific Oceans) and of the Arctic Ocean stratification. Adapted from [161].

The reason for the Arctic to be so stratified compared to other oceans is mainly its remote location and isolation from atmosphere interaction. Ice coverage indeed prevents atmospheric storms from interacting with the underneath ocean, protecting the stratification from internal wave generation and subsequent mixing processes. This, however, is due to change as the ice coverage is shrinking and leaves the Arctic surface open to winds and atmospheric disturbances. As shown in figure 3.11, Arctic sea ice extent has almost continuously decreased since 1979 (trend with measurements in September, with a 13.4% decline per decade), and polar oceanographers are now expecting an ice-free Arctic Ocean during Summer in the horizon 2030. Hence the Arctic, that used to be preserved from atmosphere influence, is likely to experience strong mixing processes that will durably impact its stratification over the next century, motivating research campaigns, and theoretical and experimental studies, amongst which internal wave studies.

Of primary importance are these studies today, as the exact impact on climate change is still unknown. In the Arctic Ocean, the observed melting rate of sea ice is more important than models can predict, and the proportion of thin and weak young ice (formed within the last 5 years) over old ice (present for more than 5 years) keeps increasing [218]. Newly discovered paths for transports of heat and nutrients in the cold northern regions of the Arctic, such as the Chukchi

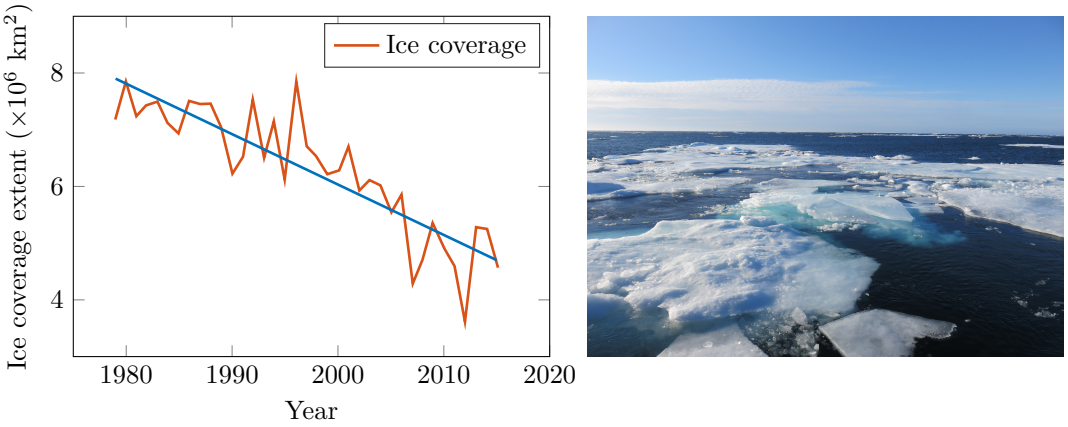

Figure 3.11: Left: average monthly Arctic ice extent from 1979 to 2015 measured in September (orange curve), and linear fit (blue curve), from: National Snow and Ice Data Center. Right: photography of melting Arctic ice (SODA research cruise, September 2018).

Slope Current (see [35, 57] and chapter 9), also tend to modify the environment. Warmer polar oceans with weaker stratifications would durably impact the world wide ecosystem and climate evolution, with possible feedback on the large scale currents.

3.4 Conclusion

We have presented, in this chapter, general properties on stratification and rotation on Earth's geophysical fluids, namely the atmosphere and the oceans, with density variations with salinity and temperature, and variations of the Coriolis frequency with latitude. In this thesis, however, we only focus on the oceans and our experimental works do not involve temperature.

Atmospheric and oceanic internal waves are ubiquitous, and have been seen (through satellite photographies) and measured (in-situ probes) in both media. They can be generated through various mechanisms, one of them being storms moving over the ocean surface, which motivates the axisymmetric study of wave fields, more relevant than usual two-dimensional plane waves studies. In the oceans, this wave activity is believed to be a key phenomenon in stratified mixing, connecting large scale forcings such as tides to small scale turbulent dissipation. In particular, and due to renewed climatic conditions, the strongly stratified Arctic Ocean might be highly impacted by internal wave related processes, making polar studies of primary relevance.

Part II

Axisymmetric Waves in the Linear Regime

CHAPTER 4

Confined Waves and Stationarity

O som das ondas à noite é um som da noite.
Fernando Pessoa, Livro do Desassossego.

Inspired by oceanographic considerations, and building on earlier experiments that used paddle generators to excite vertical [51] or horizontal [228, 229] modes, the novel internal wave generator technology of Gostiaux *et al.* [92] has been used for a variety of studies of two-dimensional internal wave modes. In all the following chapters, we refer to modes as standing waves produced *via* the interference between two waves of the same magnitude but different directions. In doubly-confined geometries (i.e. sidewalls, top and bottom), two-dimensional modes of various orders, determined by the combination of stratification, imposed frequency, and dimensions of confinement, have been studied [21, 220]. The propension of Gostiaux's generator technology to investigate wave beams and two-dimensional modes was thoroughly explored by Mercier *et al* [148]. Such capabilities have been employed to investigate, for example, the Triadic Resonant Instability (TRI) in a vertical mode propagating horizontally [107] or the formation of a multilayered stratification [64]. While theoretical studies for linear stratifications describe such wave fields in terms of the natural modal basis of sines and cosines, it should be recalled that the modal pattern can be considered as a combination of plane waves propagating and reflecting from the system boundaries [148].

In this chapter, we investigate axisymmetric modes and perform laboratory experimental realisations of such wave fields. A thorough description of Cartesian modes is drawn in section 4.1 in order to distinguish wave beams from standing wave modes. In section 4.2 we establish the general theory for axisymmetric modes of internal waves by considering both radial and vertical confinement as well as weakly viscous effects. Experimental results are presented in section 4.3, followed by conclusions and discussion in section 4.4.

Results from this chapter have been published in *Physical Review Fluids* [33].

4.1 Wave Beams vs. Standing Waves

Linear theory of Cartesian internal waves has been reviewed in chapter 1, enhancing particular solutions of the wave equation in terms of plane wave description. Other solutions exist, expressed by cosine and sine functions, and provide better description of the wave field when confined, creating standing waves, as shown in this section.

4.1.1 Wave Beams and St. Andrew's Cross

Let's consider a density stratified fluid of buoyancy frequency N, in solid rotation at Ω so that the Coriolis frequency $f = 2\Omega$. In an unconfined domain, waves forced at ω such that $f < \omega < N$ or $N < \omega < f$ propagate freely along a particular angle β with the vertical axis, set by the dispersion relation (1.40) and recalled here

$$\sin\beta = \pm\sqrt{\frac{\omega^2 - f^2}{N^2 - f^2}}. \tag{4.1}$$

As previously discussed (see chapter 1), this relation allows for the propagation of four different wave beams along symmetric directions, as experimentally observed by Mowbray and Rarity [154], whose observations are presented in figure 4.1. These beams form the well-known pattern of a *St. Andrew's Cross* and the wave field can be described, locally, by plane waves

$$\psi(x, z, t) = \psi_0 e^{i(\omega t - lx - mz)}. \tag{4.2}$$

The exact profile of the wave beams, however, is not exactly a plane wave and are better described using the Thomas and Stevenson's profile [225].

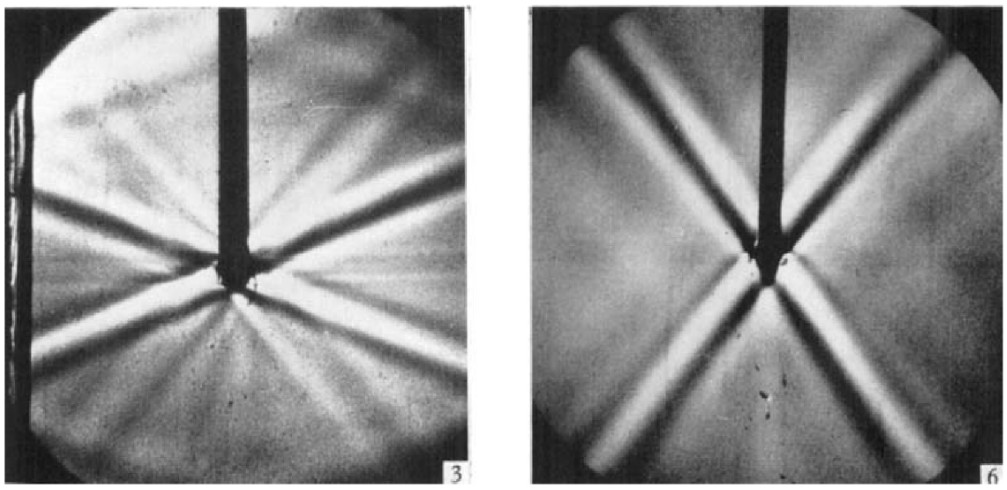

Figure 4.1: Internal wave beams and St. Andrew's Cross created by a vertically oscillating cylinder in a stratified fluid at two different excitation frequencies. Extracted from [154].

4.1.2 Cartesian Modes

The plane wave description previously mentioned is valid for unconfined wave fields or, at least, domains way larger than the wave generation mechanism. This condition is not always fulfilled as, for example, oceanic waves can be confined due to the finite depth of the oceans and particular topographies, or, in laboratory experiments, the wave generator and the tank can have the same aspect ratio. Both cases lead to consider standing wave fields, or modes, that can be either vertical modes described by

$$\psi^V(x, z, t) = \psi_0 \phi^V(z) e^{i(\omega t - lx)}, \tag{4.3}$$

or horizontal modes

$$\psi^H(x, z, t) = \psi_0 \phi^H(x) e^{i(\omega t - mz)}. \tag{4.4}$$

Using these expressions, the propagating part involves only one of the two directions $\mathbf{e_x}$ or $\mathbf{e_z}$. When inserted in the following linear Cartesian wave equation [48, 220]

$$\partial_t^2 \Delta\psi + N^2 \partial_x^2 \psi + f^2 \partial_z^2 \psi = 0, \tag{4.5}$$

the two spatial directions are uncoupled and we obtain equations on ϕ^V and ϕ^H as

$$\frac{\mathrm{d}^2\phi^V}{\mathrm{d}z^2} - l^2\left(\frac{N^2-\omega^2}{f^2-\omega^2}\right)\phi^V = 0, \tag{4.6}$$

and

$$\frac{\mathrm{d}^2\phi^H}{\mathrm{d}x^2} - m^2\left(\frac{f^2-\omega^2}{N^2-\omega^2}\right)\phi^H = 0. \tag{4.7}$$

In order to solve these equations, we need two boundary conditions on ϕ, that are zero velocity orthogonal to the solid boundaries. For vertically bounded domains of given height H, the vertical velocity is zero at $z = 0$ and $z = H$, leading to

$$\phi_p^V(z) \propto \sin(m_p^V z) \qquad \text{with} \qquad m_p^V = \frac{p\pi}{H}, \tag{4.8}$$

with $p \in \mathbb{N}$. Similarly, for horizontally bounded domains of given width L, the lateral velocity is zero at $x = 0$ and $x = L$, and

$$\phi_p^H(x) \propto \sin(l_p^H x) \qquad \text{with} \qquad l_p^H = \frac{p\pi}{L}. \tag{4.9}$$

As the wave equations are linear, the stream function writes as a sum over all possible modes, which corresponds to a spatial Fourier transform, so that

$$\psi^V(x,z,t) = \sum_{p=0}^{\infty} \psi_p^V \sin(m_p z) e^{i(\omega t - l_p x)}, \tag{4.10}$$

and

$$\psi^H(x,z,t) = \sum_{p=0}^{\infty} \psi_p^H \sin(l_p x) e^{i(\omega t - m_p x)} \tag{4.11}$$

where l_p^V and m_p^V are linked through the dispersion relation (and so are l_p^H and m_p^H).

With the definition of the stream function from equation 1.53, the 2D horizontal and vertical velocities for a single mode $p \in \mathbb{N}$ hence writes

$$v_x^V(x,z,t) = v_x^V \cos(m_p^V z)\cos(\omega t - l_p^V x), \tag{4.12}$$
$$v_z^V(x,z,t) = v_z^V \sin(m_p^V z)\sin(\omega t - l_p^V x), \tag{4.13}$$

for a vertical mode, and

$$v_x^H(x,z,t) = v_x^H \sin(l_p^H x)\sin(\omega t - m_p^H z), \tag{4.14}$$
$$v_z^H(x,z,t) = v_z^H \cos(l_p^H x)\cos(\omega t - m_p^H z), \tag{4.15}$$

for a horizontal mode. This theory has been experimentally verified by Mercier *et al.* [148] for horizontally propagating vertical modes 1 and 2. Such modes have been used in various experiments, such as 2D Triadic Resonant Instability (TRI) observation of Joubaud *et al.* [107].

As detailed in chapter 1, the group and phase velocities $\mathbf{v_g}$ and $\mathbf{v}_\phi$ are orthogonal for plane wave beams. This characteristic, however, is not true in the case of standing waves, as these velocities are summed through the recombination of wave beams and are therefore parallel for modes, aligned with the direction of propagation. In the case of horizontally propagating wave fields, $\mathbf{v_g}$ and $\mathbf{v}_\phi$ share the same orientation. Conversely, in the case of vertically propagating wave fields, they have opposed orientation as, for instance, a downwards propagating wave field has downward group velocity but upward phase velocity.

Snapshots of 2D Direct Numerical Simulations (DNS) of downward propagating modal wave fields in a linear stratification are presented in figure 4.2, showing vertical velocity fields for a mode 1 (left) and for a mode 2 (right), at $\omega/N = 0.67$. DNS were run in the linear regime (nonlinear terms set to zero) using Dedalus on a SinCos basis in x and a Chebyshev basis in z, with a 128×128 nodes resolution. A boundary forcing of sinusoidal shape is applied at the top on the stream function, to impose the vertical velocity. In both cases, the wave field is a mode (standing

wave) along the horizontal direction, and is vertically propagating. The wave field is progressively filling the domain from the top towards the bottom, as the group velocity is oriented downwards. When established, the vertical wave length of the mode looks badly defined, but converges quickly towards a given value set by the dispersion relation on top of the domain. The horizontal wave length, however, remains identical to the forcing when the mode propagates.

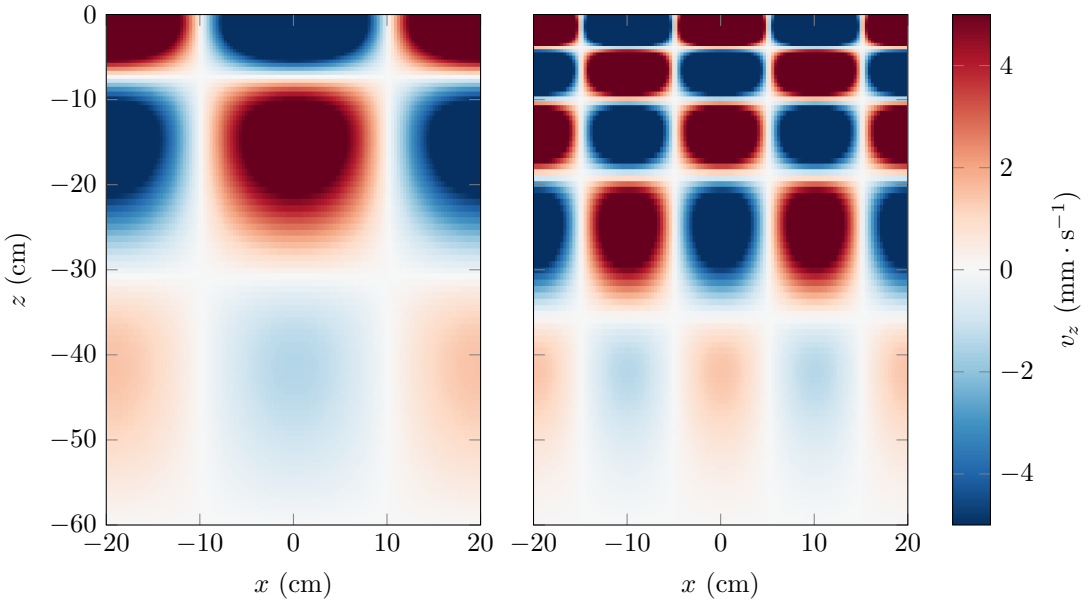

Figure 4.2: Snapshots of vertical velocity fields in a DNS of 2D Cartesian modes in a linear stratification (at $\omega/N = 0.67$) run using Dedalus. Left: mode 1. Right: mode 2. Both modes are excited from the top and are propagating downwards.

In doubly confined domains, standing wave field theory has been extended and formulated as entirely non-propagating modes [228, 220]. We discuss, in the next section 4.2, the axisymmetric transposition of the Cartesian standing waves.

4.2 Theory of Axisymmetric Modes

The wave generator described in chapter 3 is well designed to excite customisable axisymmetric wave fields, as the amplitude of each cylinder can be set individually. In particular, Bessel functions, which are sines and cosines alikes in cylindrical geometry, can be reproduced by setting the correct amplitudes from a discretised function.

In a previous study, Maurer *et al* [141] analysed the production of a conical wave field generated by an axisymmetric moving form at the surface, for which the radial profile was a truncated Bessel function. Such a wave field is analoguous to the Cartesian wave beams previously described. Although Bessel functions form a natural basis of study for axisymmetric wave fields, the analytical form of the wave field for a truncated Bessel function is not so simple because it contains various radial wave lengths. The stream function is therefore a superposition of Bessel functions, as shown by Maurer [140]. In previous studies, such conical wave beams have been described in terms of plane waves with a spherical amplitude decreasing as $r^{-1/2}$, r being the radial distance from the sphere, computed from the Green function of the moving source [237], or as infinite sums of Bessel functions with complex coefficients [60, 220].

An illustration is presented in figure 4.3(a), which displays a vertical cut of the spatial structure of the wave field studied in [141]. Immediately below the generator (region 1 in figure 4.3(a)), the wave field preserves its radial form, but further below, the wave field develops a conical beam-shaped profile (region 2), which can locally be modelled by a plane wave. Finally, due to the propagation angle set by the dispersion relation and to the finite extent of the wave generator,

sufficiently far below the oscillating body around the vertical axis the wave field is absent (region 3). Analytically, this evolution of the wave field is a natural consequence of the truncated Bessel function (i.e. non-zero only over a finite radial interval) forcing being expressed as an integral over Bessel functions of different wave lengths, with coefficients depending on the spatial forcing. Axymptotic complex models have been set up to understand the nature of such radiated wave fields [60, 80, 238].

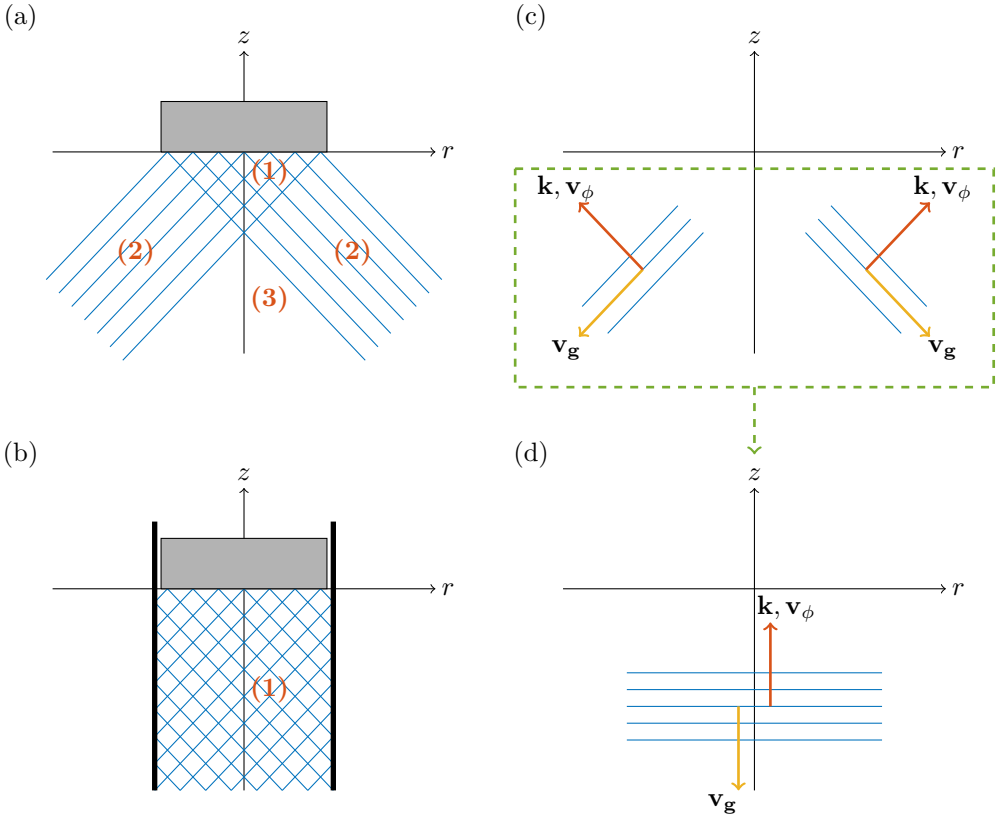

Figure 4.3: Schematic representation of the wave field in a vertical cross-section. Left: beams for downward propagating wave generation in (a) unconfined and (b) confined geometries produced by a wave generator or an oscillating body (light grey rectangle). Right: (c) phase lines of two different wave beams allowed by the dispersion relation and (d) phase lines of the wave re-recombination for vertically propagating horizontal (radial) modes. See chapter 2 for practical details on the wave generation process.

Starting from the Navier-Stokes equations, this section aims at deriving the rigorous theory for axisymmetric internal wave fields in confined domains for non-rotating density stratified fluids.

4.2.1 Stream Function Equation

In a cylindrical framework ($\mathbf{e_r}$, $\mathbf{e}_\theta$, $\mathbf{e_z}$), with $\mathbf{e_z}$ vertically upwards, small amplitude inertia gravity waves in an inviscid fluid with a constant background stratification satisfy the following equations in the Boussinesq approximation

$$\rho_0 \left(\frac{\partial \mathbf{v}}{\partial t} + (\mathbf{v} \cdot \nabla)\, \mathbf{v} \right) = -\nabla p - (\rho - \bar{\rho}) g \mathbf{e_z}, \tag{4.16}$$

$$\frac{\partial \rho}{\partial t} + (\mathbf{v} \cdot \nabla)\, \rho = 0, \tag{4.17}$$

$$\nabla \cdot \mathbf{v} = 0, \tag{4.18}$$

where $\mathbf{v} = (v_r,\ v_\theta,\ v_z)$ is the velocity field, p the pressure field, ρ the density field, and $\bar{\rho}$ the background density field. The buoyancy frequency N is defined *via* the relation $N^2 = (-g/\rho_0)\partial\bar{\rho}/\partial z$

with ρ_0 being a reference density.

Considering axisymmetric wave fields, we assume that there is no variation in the azimuthal direction and hence all functions only depend on $(r,\, z,\, t)$. The radial and vertical velocities can be written using the axisymmetric stream function ψ introduced in chapter 1 such that

$$v_r = -\frac{1}{r}\frac{\partial(r\psi)}{\partial z} \qquad \text{and} \qquad v_z = \frac{1}{r}\frac{\partial(r\psi)}{\partial r}, \tag{4.19}$$

and, a direct calculus shows that equations (4.16), (4.17), and (4.18) collapse into

$$\partial_t^2\left(\partial_z^2\psi + \partial_r\left(\frac{1}{r}\partial_r(r\psi)\right)\right) + N^2\partial_r\left(\frac{1}{r}\partial_r(r\psi)\right) = 0. \tag{4.20}$$

Natural axisymmetric solutions of this equation can be found through a Fourier-Hankel decomposition. Using a modal basis, the solutions write as linear combinations of Bessel functions of the first kind J_1 and of the second kind Y_1. The later has a singularity at $r = 0$ so only the J_1 function will be considered. As different radial wave numbers may enter in the decomposition, the stream function ψ can then be written as a modal sum

$$\psi(r, z, t) = \iint \phi(z)J_1(lr)\exp(-i\omega t)\mathrm{d}l\mathrm{d}\omega. \tag{4.21}$$

Radial and vertical velocities can be derived from equation (4.21) using classic relations for the Bessel derivatives, as follows

$$v_r = \iint \phi'(z)J_1(lr)\exp(-i\omega t)\mathrm{d}l\mathrm{d}\omega, \tag{4.22}$$

$$v_z = \iint l\phi(z)J_0(lr)\exp(-i\omega t)\mathrm{d}l\mathrm{d}\omega. \tag{4.23}$$

For a given frequency ω and radial mode l, $\phi(z)$ satisfies

$$\omega^2\phi''(z) - l^2(N^2 - \omega^2)\phi(z) = 0. \tag{4.24}$$

Solutions of equation (4.24) are exponential functions, either complex or real. They can be either propagative or evanescent waves, depending on the frequency, as long as the vertical wave number m satisfies the dispersion relation

$$m^2 = l^2\frac{N^2 - \omega^2}{\omega^2}. \tag{4.25}$$

With $\beta = \sin^{-1}(l/k)$ the angle between the vertical axis and the wave vector $\mathbf{k} = (l, 0, m)$ of magnitude $k = \sqrt{l^2 + m^2}$, the dispersion relation (4.25) simplifies in

$$\sin\beta = \pm\frac{\omega}{N}. \tag{4.26}$$

According to equation (4.26), internal gravity waves propagate along a direction fixed by the angle β. As detailed in section 4.1, in a two dimensional geometry, four wave beams on a St Andrew's Cross are formed [155, 223]. In a three dimensional axisymmetric geometry, the dispersion relation sets two cones aligned along the vertical direction and connected by the apex [169, 220].

4.2.2 Radial Confinement

Given the finite spatial extent of the forcing, to generate a modal wave field described by a single radial Bessel function, confinement can be imposed experimentally to the fluid, as illustrated in figure 4.3(b). As for planar geometries, confinement prevents the wave from propagating in the bounded direction. Given the assumption of axisymmetry, we seek a wave field that is radially confined by a cylinder of radius R equal to the radius of the generator, and vertically propagating, which is in contrast to the planar scenario that has vertical confinement and permits lateral propagation [64, 107, 148]. We impose the radial boundary condition

$$v_r(r = R, z) = -\left(\frac{\partial\psi}{\partial z}\right)_{(r=R,z)} = 0, \tag{4.27}$$

which means that $\psi(r = R, z)$ is a constant, corresponding to a maximum of vertical velocity and a vanishing radial velocity at the outer boundary, and conserving volume in the domain. Condition (4.27) limits possible values of the radial wave number l, as the product lR has to be a zero of the J_1 Bessel function, and if the fluid is excited with one of these wavenumbers at frequency ω, a single propagating mode is expected to result.

Figure 4.3(c) shows the two directions of propagation allowed for the wave beams by the dispersion relation (1.74), in a vertical planar cross-section, for a wave generation at the surface. In our experiment, the radial confinement leads to downward propagating modes which are, as depicted in figure 4.3(c,d) (still in a vertical planar cross-section) a re-combination of conically propagating beams. Due to the symmetry with respect to the vertical axis, the radial direction of propagation cancels out and, for a downwards propagating wave at a selected frequency ω and wavenumber $\mathbf{k}$, the phase and group velocities can be computed from the dispersion relation (1.74)

$$\mathbf{v}_\phi = \frac{1}{2\pi}\int_0^{2\pi} \frac{Nl}{k}(l\mathbf{e_r} + m\mathbf{e_z})\mathrm{d}\theta = \frac{Nlm}{k}\mathbf{e_z}, \tag{4.28}$$

$$\mathbf{v_g} = \frac{1}{2\pi}\int_0^{2\pi} \frac{mlN^2}{\omega k^4}(m\mathbf{e_r} - l\mathbf{e_z})\mathrm{d}\theta = -\frac{ml^2N^2}{\omega k^4}\mathbf{e_z}. \tag{4.29}$$

Equations (4.28) and (4.29) show phase and group velocity oriented in opposite directions, illustrated in figure 4.1(d), consistent with oceanic signatures identified by oceanographers looking for internal waves [8, 9]. This feature contrasts with horizontally propagating modes, only relevant in cartesian geometry, which show phase and group velocities pointing towards the same direction [148].

To investigate the shape of the wave field in the experimental domain, and more specifically its amplitude, we extend the axisymmetric analysis of Sutherland [220, chapter 5], first derived for an oscillating cylinder in a two-dimensional geometry, by applying it to our axisymmetric flat generator in a confined domain. Through a Fourier transform, the time dependency of the streamfunction can be expressed in complex coordinates as $\psi \propto e^{-i\omega t}$, the velocity field being the real part of the stream function derivatives. Neglecting rotation and introducing $\Gamma^2 = 1 - N^2/\omega^2$, the linear system of equations (1.64), (1.65), and (1.66), can be rewritten as a collapsed equation

$$\Gamma^2 \frac{\partial}{\partial r}\left(\frac{1}{r}\frac{\partial(r\psi)}{\partial r}\right) + \frac{\partial^2\psi}{\partial z^2} = 0. \tag{4.30}$$

Considering that the cylindrical plates of the generator are moving vertically (as described in chapter 2, and detailed in [141]) and are injecting a vertical velocity $a\omega$, with a being a sufficiently small displacement so that the fluid surface can be considered to reside at $z = 0$, the boundary conditions that apply to the streamfunction field are

$$v_z(r, z = 0) = \left(\frac{1}{r}\frac{\partial(r\psi)}{\partial r}\right)_{(r,z=0)} = a\omega J_0(lr), \tag{4.31}$$

$$v_r(r = R, z) = \left(\frac{\partial\psi}{\partial z}\right)_{(r=R,z)} = 0. \tag{4.32}$$

Equation (4.31) means that the generator imposes its own movement to the fluid at the top of the domain. The modal boundary condition is expressed by equation (4.32) as detailed before.

For $N < \omega$, the problem can be readily solved *via* a coordinate transformation: $(r' = \Gamma r,\ z' = z)$ so that equation (4.30) becomes

$$\Delta'_h\psi = 0, \tag{4.33}$$

where Δ'_h is the horizontal Laplacian. The solution can be obtained using separation of variables. The radial part of the equation satisfies a Bessel differential equation of first order, leading to $\psi \propto J_1(lr)$. The vertical component is found to be exponential, and $\psi \propto \exp(\Gamma lz)$ as the amplitude decreases as z goes to $-\infty$. From the boundary conditions, the different coefficients can be set. Recasting the solution in the original coordinates, we obtain

$$\psi_{N<\omega}(r, z, t) = -\frac{a\omega}{l}J_1(lr)\exp(mz)\cos(\omega t), \tag{4.34}$$

where we define $m = \Gamma l$, which contains the influence of the stratification.

In the case $N > \omega$, the term $1 - N^2/\omega^2$ is negative. We thus define $\gamma^2 = \omega^2/N^2 - 1$ and, by analytic continuation, the problem can be solved using the same method as before. Thanks to the second order derivatives, the problem remains well-defined though we are using complex analysis and the final stream function belongs to the real space of functions

$$\psi_{N>\omega}(r, z, t) = -\frac{a\omega}{l} J_1(lr) \cos(mz - \omega t), \tag{4.35}$$

with m the vertical wave number defined as $m^2 = -\gamma^2 l^2$. Hence, we obtain two different radial modes, one being evanescent (4.34) and the other one propagating in the vertical direction (4.35).

Henceforth, we are only considering the case of propagative waves with $\omega < N$. The vertical velocity being a radial derivative, it behaves as $v_z \propto a\omega$

$$v_z(r, z) = \frac{1}{r}\frac{\partial(r\psi)}{\partial r} = a\omega J_0(lr) \cos(mz - \omega t), \tag{4.36}$$

$$v_r(r, z) = \frac{\partial \psi}{\partial z} = -\frac{a\omega m}{l} J_1(lr) \sin(mz - \omega t). \tag{4.37}$$

4.2.3 Vertical Confinement

In our experiments, boundaries at the top ($z = 0$) and at the bottom ($z = -L$) are to be taken into account. This confinement creates a finite domain where a behaviour similar to an opto-electromagnetic cavity [103] or a Melde's string for accoustic or mechanical waves [147] can take place, with different modes and resonances. The total wave field in the cavity is obtained by a superposition of all the reflected waves, from the top and the bottom of the tank, causing constructive or destructive interferences. In this configuration, the generator is continuously exciting a velocity field given by a stream function ψ_1, described in complex notation by

$$\psi_1(r, z, t) = \psi_1^0 J_1(lr) e^{i(\omega t - mz)}, \tag{4.38}$$

with $\psi^0 = a\omega/l$. At $z = -L$, the downwards wave field ψ_1 is reflected into an upwards wave field ψ_2, and at $z = 0$ (when assuming small amplitude forcing at the surface), the ψ_2 stream function is reflected into another downwards wave ψ_3. Repeated reflections occur at $z = 0$ and $z = -L$, and as a result the total stream field is composed of an infinite sum of reflected wave fields.

We denote by odd numbers the downwards waves and by even numbers the upwards waves. At the boundaries, as well as changing direction, reflection also induces a π phase shift, and if we assume that there is no dissipation the amplitudes of the stream functions are equal before and after reflection. Boundary conditions at the top and at the bottom of the tank then apply as

$$\psi_{2k-1}(z = -L) = \psi_{2k}(z = -L) e^{i\pi}, \tag{4.39}$$

$$\psi_{2k+1}(z = 0) = \psi_{2k}(z = 0) e^{i\pi}, \tag{4.40}$$

leading to

$$\psi_{2k}^0 = \psi_{2k-1}^0 e^{-2imL - i\pi}, \tag{4.41}$$

$$\psi_{2k}^0 = \psi_{2k+1}^0 e^{i\pi}. \tag{4.42}$$

We deduce that the general expression of these wave amplitudes are

$$\psi_{2k}^0 = \psi_1^0 e^{-2ikmL + (2k-1)\pi}, \tag{4.43}$$

$$\psi_{2k+1}^0 = \psi_1^0 e^{-2ikmL + (2k)\pi}. \tag{4.44}$$

As the tank is filled by infinite wave reflections, we describe the total wave field by a sum over all the reflected waves

$$\psi = \sum_{k=1}^{\infty} \psi_k = \psi_1^0 J_1(lr) e^{i\pi/2} e^{i\omega t} \frac{\sin(m(z - L))}{i \sin(mL)}, \tag{4.45}$$

hence the real field becomes

$$\Re(\psi) = \psi_1^0 J_1(lr)\frac{\cos(\omega t)\sin(m(z-L))}{\sin(mL)}. \tag{4.46}$$

Waves that contribute to the total wave field interact either constructively or destructively. In the first case, we would be able to define a temporal and a spatial period, fixed by the wave parameters ω, l, and m, and by the size of the cavity L, as in any wave resonator. Exact cavity modes are obtained if the reflection at $z = -L$ produces a reflected wave in phase with the incoming wave, which means that this position is already a node of the wave field. This resonance condition can be expressed as

$$L = n\frac{\lambda}{2}, \text{ for } n \in \mathbb{N}, \tag{4.47}$$

with $\lambda = 2\pi/m$ being the vertical wave length. A direct consequence is that the reflection at $z = 0$ also produces a wave in phase with the incoming wave, so all reflected waves will be interacting constructively. Therefore, this relation can be written as a condition involving resonant frequencies ω_n

$$\frac{\omega_n}{N} = \frac{(Ll)^2}{\pi^2 n^2 + (Ll)^2}. \tag{4.48}$$

Similar to electromagnetic waves, the cavity operates as a frequency selector, as a discrete number of frequencies ω_n fulfills the resonance condition. We present in table 4.1 a list of the first ten resonant frequencies that can be selected in a radial mode 1 configuration with $L = 60$ cm and $l = 19$ m^{-1}.

n	0	1	2	3	4	5	6	7	8	9	10
ω_n/N	1	0.964	0.876	0.771	0.672	0.588	0.518	0.460	0.413	0.374	0.341

Table 4.1: First ten resonant frequencies computed for $L = 60$ cm and $l = 19$ m^{-1}.

4.2.4 Weakly Viscous Effects

In the preceding derivations, an inviscid fluid was assumed. This made possible the propagation of a single mode at all frequencies without damping effect, and the existence of exact resonant cavity modes. As we will see, however, such an approximation is only relevant for a selected range of frequencies. Inspired by the approach detailed in chapter 1 to quantify the viscous effects on the wave propagation, we write the vertical wave number as the following expansion

$$m = m^{(0)} + i\varepsilon m^{(1)} + \mathcal{O}(\varepsilon^2), \tag{4.49}$$

with $\varepsilon = \nu l^2/\omega$, $m^{(0)}$ being the inviscid wave number (equation (1.74)), and $m^{(1)}$ being the first order correction. Including viscous terms, equation (4.24) becomes

$$\phi^{(4)}(z) - \left(2l^2 - i\frac{\omega^2}{\nu}\right)\phi''(z) + l^2\left(l^2 + i\frac{N^2-\omega^2}{\nu\omega}\right)\phi(z) = 0. \tag{4.50}$$

Hence, with the vertical dependence being $\exp(imz)$ (complex notation of equation (4.35)) and m defined as in equation (4.49), one can extract from equation (4.50) the following weakly viscous correction

$$i\varepsilon m^{(1)} = \mp\frac{i\varepsilon l}{2\alpha^3\sqrt{1-\alpha^2}}, \tag{4.51}$$

where $\alpha = \omega/N$. Hence, at an altitude z below the wave generation source, the weakly viscous streamfunction ψ_ν writes

$$\psi_\nu(z) = \psi(z)\exp(-\varepsilon m^{(1)}|z|). \tag{4.52}$$

According to equation (4.52), the typical vertical length of viscous damping $1/\varepsilon m^{(1)}$ depends on the frequency ω and is smaller at low frequencies than at high frequencies. These results will help understand experimental measurements of the wave field amplitudes when comparing them to the velocity amplitudes of the generator.

4.3 Experimental Results

We discuss here the ability and efficiency of the wave generator to produce radial modes. The resonance phenomenon, leading to high amplitude wave fields and non-linear effects, is also observed.

4.3.1 Radial Modes

As mentioned in sections 4.1 and 4.2, vertically propagating radial modes created from a top boundary forcing propagate downwards before being reflected at the bottom and propagating upwards. Hence we first focus on a regime before reflection happens.

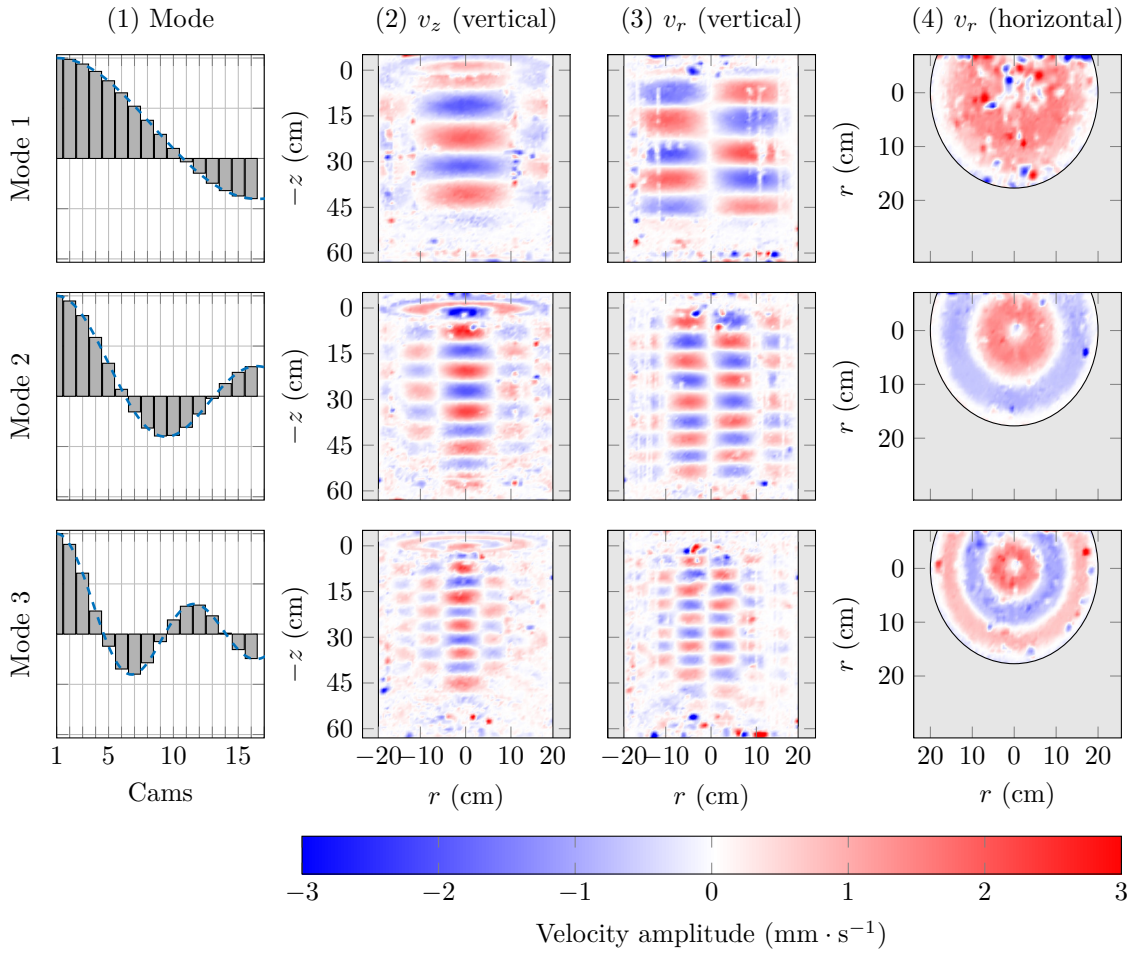

Figure 4.4: Radial modes 1, 2, and 3, as observed in PIV in the experiment. First column: generator configuration that sets the mode (see chapter 2). Second column: vertical velocity v_z in a vertical plane. Third and fourth columns: radial velocity v_r in a vertical and in a horizontal plane around mid-depth. Shaded areas are outside of the confining cylinder. For the purpose of visualisation, negative values of r are used in the vertical PIV plane, leading to antisymmetric radial velocities as predicted by equation (4.37).

Figure 4.4 presents a summary of the experimental PIV results for the generation of modes 1 through 3 in a linear stratification with $\omega/N = 0.6$ for modes 1 and 2 and $\omega/N = 0.65$ for mode 3, and a generator amplitude $a = 5$ mm. The generator plate configuration for each mode is illustrated in the left hand column, with n nodes for mode n. The vertical cross sectional plots of the vertical velocity, presented in column 2, possess the horizontal structure of the generator, increasingly intricate for the higher modes, with associated vertical sequences of maxima and minima. Columns 3 and 4 in figure 4.4 present vertical and horizontal cross sectional plots of

the radial velocity component. For every mode, the radial velocity structure possesses a left-right antisymetry in the vertical plane. The different nodes of radial velocity, which correspond to antinodes of vertical velocity, are also clearly visible in plots of the velocity in the horizontal plane, presented in column 4; these images also show the form of the generator being reproduced by the underlying wave field. No orthoradial velocity v_θ was observed in the horizontal plane.

In a previous study, Maurer *et al* [141] experimentally measured the internal wave dispersion relation for freely propagating waves generated by an axisymmetric wave generator with no lateral confinement, which was consistent with theoretical predictions. In the modal configuration, however, the dispersion relation does not explicitly contain an angle of propagation, only a statement of the vertical wave length as a function of the forcing frequency and horizontal wave number. The vertical wave number m was measured for different frequencies ω/N for the three modes in our experiments. Figure 4.5 compares the experimental values of m with the theoretical one extracted from equation (4.25) given the control parameters. Measurements were performed by looking at the spatial vertical period of the vertical velocity on PIV images. It shows a good agreement for the three modes considered in the study, though there is a slight deviation at low frequencies, probably because of the error in N which was about 10% for mode 1 experiment and 4% for mode 2 and mode 3 experiments.

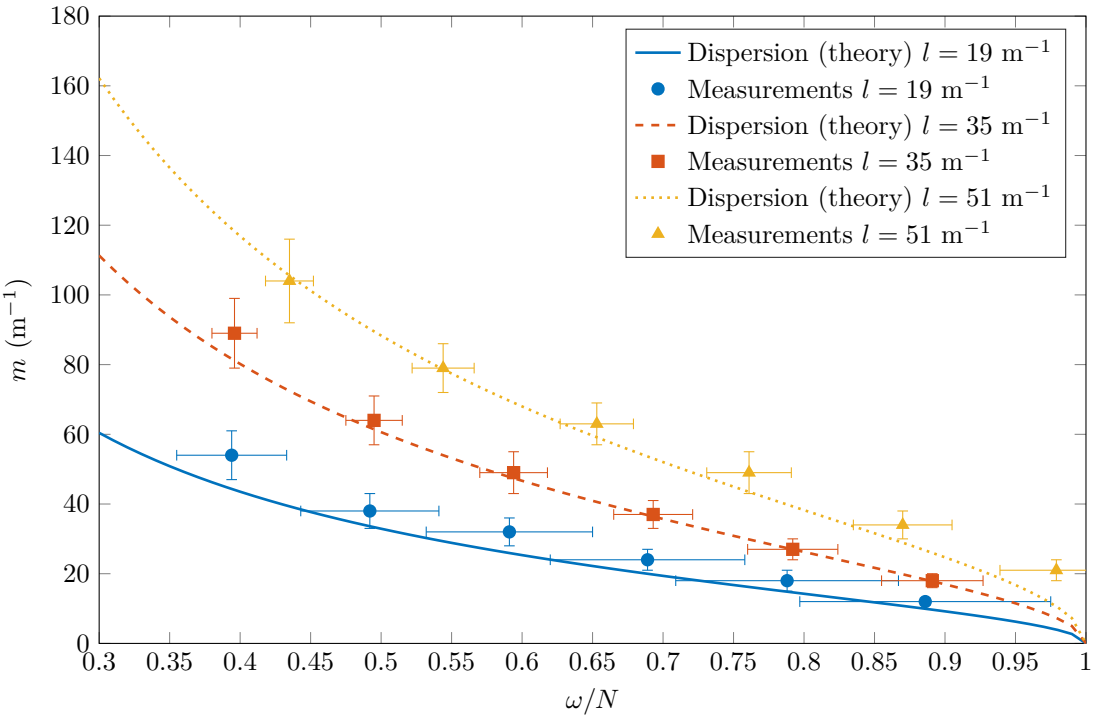

Figure 4.5: Measured values of the vertical wave number (data points) for modes 1, 2, and 3, compared to the theoretical expectations from equation (4.25) (lines). Vertical errors were determined using measurements of m at different times, and horizontal errors using the standard deviation on the buoyancy frequencies from the probe profiles.

To quantitatively investigate how close the experiments reproduce the theoretical modal Bessel profile, figure 4.6 presents radial profiles of v_z and v_r, fitted to the expected radial dependency of the Bessel mode, for mode 1, mode 2, and mode 3 configurations. For each tested profile, we looked for the best fit in amplitude to adjust the analytical Bessel profile. We see that $v_z(r) \propto J_0(lr)$ and $v_r(r) \propto J_1(lr)$, with $l = 19$ m^{-1}, 35 m^{-1}, or 51 m^{-1}, as expected; these horizontal structures are preserved through the vertical propagation of the wave field as nodes and antinodes almost coincide along vertical lines. Small deformations sometimes appear close to the boundaries at $r = 20$ cm, due to boundary layer effects, but remain localised over a few millimeters. The perturbation observed symmetrically around 12 cm $< |r| <$ 16 cm is actually caused by laser reflections in the cylinder, producing locally poor PIV visualisation. Mode 1 is the most accurately reproduced

compared to modes 2 and 3, which can be explained by the discretisation of the profile and a diminished number of plates between two nodes when inceasing the mode order.

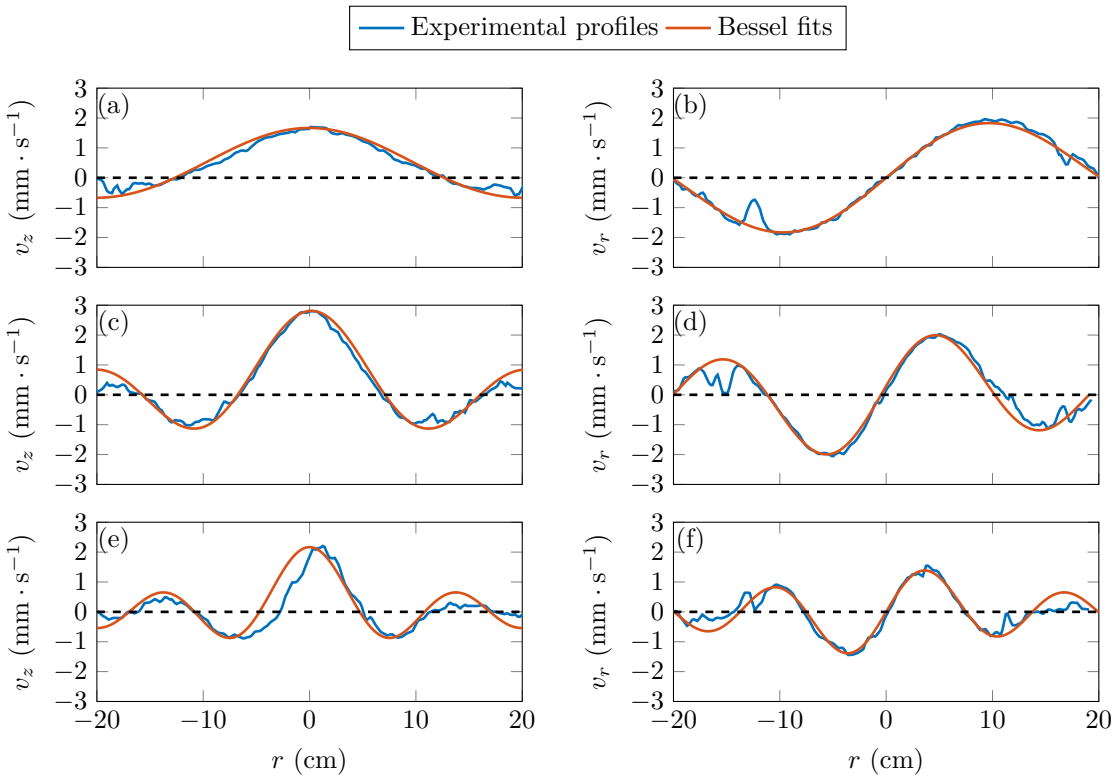

Figure 4.6: From top to bottom: examples of experimental velocity profiles (left) v_z and (right) v_r for mode 1, mode 2, and mode 3, taken at a given time and altitude, fitted by appropriate Bessel functions: $J_0(lr)$ for v_z and $J_1(lr)$ for v_r, with $l = 19$ m^{-1}, $l = 35$ m^{-1}, and $l = 51$ m^{-1} respectively.

4.3.2 Generator Efficiency

The efficiency of the wave generator, being the ratio of the amplitude of the waves produced to the amplitude of the generator motion, is investigated in order to characterize the quality of the produced wave field. Hence, it is essential to reliably measure the amplitude of the internal wave field which is, due to unavoidable reflections in closed domains, a delicate task and more challenging than measuring their frequency or wave length.

A few previous studies have made direct measurements of velocity amplitude, although these are typically done either at high frequencies or relatively high amplitudes. Mathur & Peacock [139] studied transmission and reflection of internal wave beams across a transmission region and took a Fourier transform of the reflected and transmitted wave fields along appropriately chosen transects, Maurer [140] measured wave amplitudes by looking at the maximum of the velocity over a given spatial area, and Supekar [219] utilized the distribution of maxima of amplitudes for a velocity field in a widespread two dimensional beam. In performing our experiments, it was necessary to more rigorously define our amplitude measurement methodology based on understanding of the group velocity of the wave fields we were studying.

The procedure to determine the wave amplitude was the following. In a first step, experimental amplitudes at a given time t_m were determined by fitting a Bessel function to the instantaneous horizontal profile at a given depth z_m of the vertical velocity, as illustrated in figure 4.6. The depth z_m chosen for this profile was selected to be 15 cm below the generator, as the wave field was properly developed at this depth. Since the stratification, the forcing frequency and the radial wave length are imposed, the only free parameter for the fit is the amplitude of the Bessel function.

Note that we used the vertical component of the velocity field for this fitting, since it has larger amplitudes than the radial velocity profile (which is characterized by a node at $r = 0$) and so was more amenable to fitting.

Measurements were repeated for all images over a time interval $t_m \in [t_i;\ t_f]$, with t_i being the time when the wave is expected to first cross the horizontal cross-section at $z = z_m$. The time t_f is the time when the reflected wave is predicted to reach $z = z_m$ after returning from the bottom of the tank, resulting in a disturbance of the wave field. Both t_i and t_f were estimated using the group velocity of the wave field established in equation (4.29). This series of measurements provided a time-series of local wave amplitudes at $z = z_m$. An example of such a time series is shown in figure 4.7. One would expect this time signal to be sinusoidal. As can be seen in this example, the growth of the wave amplitude due to the presence of other frequencies associated with the ramping up of the wave generator can be observed for the first few periods, and the decay after t_f is due to the interfering waves returning out in phase. This illustrates the difficulty of wave amplitude measurement in a finite size tank.

In a second step, in order to best estimate the wave amplitude of the steady state before the reflected wave returned (there is some uncertainty on the exact return time), we computed the RMS value of the time signal over three periods close to t_f half-covering each other, the middle one being just before theoretically seeing the reflected wave, the previous period covering the first half of this one, and the following period covering the second half of it (these measurement windows are illustrated by 3 rectangles in figure 4.7). The experimental global amplitude was determined as the mean value of the 3 RMS values obtained (multiplied by $\sqrt{2}$), and the standard deviation of these 3 measurements gives an estimate of the associated error. We checked that the method was sound by repeating some test measurements for other horizontal planes and obtaining consistent results.

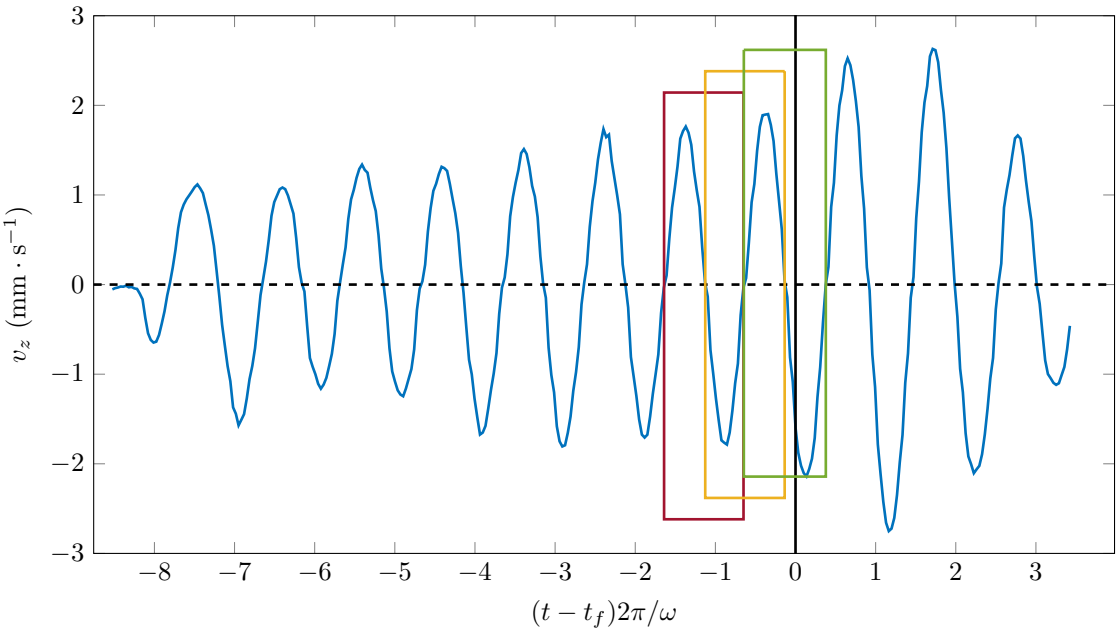

Figure 4.7: Example of time series of fitted instantaneous Bessel function amplitudes of the vertical velocity, measured at $z = z_m = -15$ cm for a mode 1 wave. After identifying t_f (solid vertical line), three periods half-covering each other (rectangles) are used to extract the global wave amplitude *via* RMS estimates.

The results of our efficiency experiments are presented in figure 4.8 for two different generator amplitudes. We plot the velocity amplitude normalised by the generator velocity amplitude $a\omega$. From equation (4.52), without dissipation effects, one expects this ratio to be 1 (straight line in figure 4.8). This proves correct in the high frequency range ($0.5 < \omega/N < 0.9$), except close to the buoyancy frequency as discussed further. The decrease at low frequency can be interpreted

by viscous effects. Indeed, when one includes viscous dissipation in the theoretical development, the expression of the stream function is given by equation (4.52). The curve corresponding to the vertical velocity extracted from this equation (at a depth of -15 cm since equation (4.52) depends on z) is plotted in figure 4.8, showing a similar bahaviour as the experimental data points for the two forcing amplitudes $a = 2.5$ mm and $a = 5$ mm. The difference in amplitude may be ascribed to boundary layer effects. Based on the approach of Beckebanze *et al* [19], an order of magnitude calculation of the damping on the boundaries gives an estimate comparable to the dissipation in the bulk. At very low frequencies (below $\omega/N = 0.05$), the amplitude is so low that measurements become impossible. Finally, for $\omega/N = 0.9$ to 1, we notice a decrease in amplitude that is expected, as shown by the theoretical curve, since the waves are evanescent for $\omega/N > 1$. However, this decrease comes sooner than expected.

To conclude, the generator efficiency was investigated and shows a similar behaviour as the theoretical prediction in all frequency ranges, providing one takes viscous effects into account. In addition, we identify a range of frequencies, from $\omega/N = 0.5$ to $\omega/N = 0.9$, where there is a very good agreement with the theory, making this range suitable for axisymmetric modes experiment and for resonant enhancement.

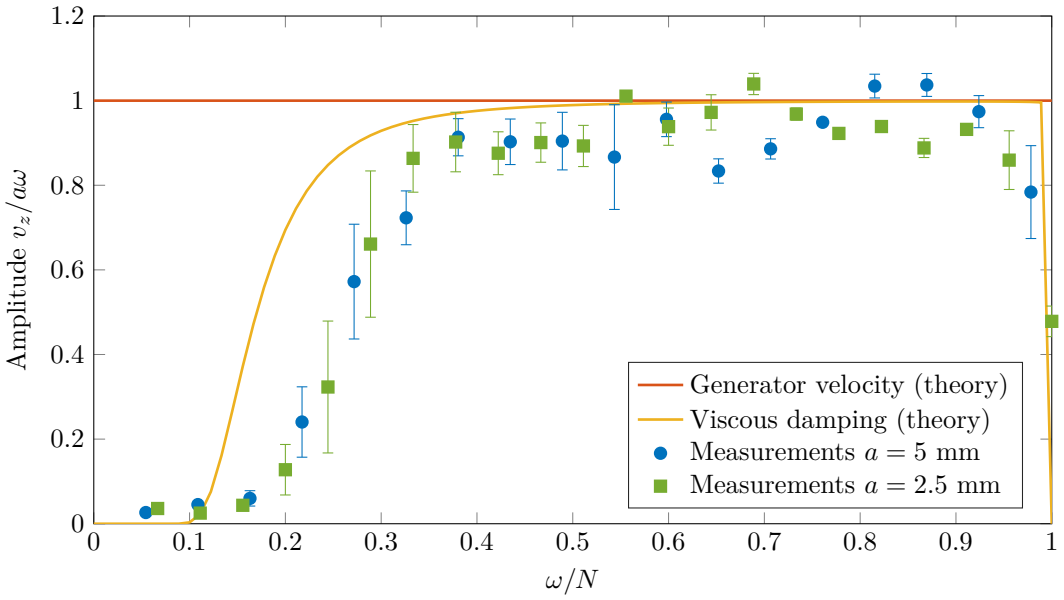

Figure 4.8: Generator efficiency measured at $z = -15$ cm, for two experiments with $a = 5$ mm and $a = 2.5$ mm. Results are compared to the theoretical predictions in the inviscid case and in the weakly viscous case (viscous damping curve, computed for $N = 0.9$ rad $\cdot$ s^{-1}).

4.3.3 Resonance

Having established the response of the stratification to the wave generator forcing, we then conducted experiments to detect resonance for a mode 1 excitation, due to the multiple reflections of the wave field at the top and bottom boundaries of the tank. These experiments consisted of measuring the amplitude of the wave by looking for the maximum value of vertical velocity in z and t at $r = 0$ (since $J_0(r = 0)$ is maximal and equal to 1). The time window for these measurements was chosen to ensure the establishment of the steady state resonant wave field. In order to allow a minimum of about 10 back and forth crossings, we chose this time window to be from 280 s after starting the forcing, based on the minimum value of the group velocity of the waves, to 300 s, end of the experiment duration.

Our experimental results are presented in figure 4.9, showing the measured velocity amplitude, normalised by the generator velocity amplitude $a\omega$. We performed two sets of experiments : one with $a = 2.5$ mm and $N \simeq 0.90$ rad $\cdot$ s^{-1} (blue circles) and another one with $a = 5$ mm and

$N \simeq 0.88$ rad $\cdot$ s^{-1} (red squares). The first set of experiments was mainly aimed at identifying the resonant peaks; the second set was more evenly spread over all frequencies (a hundred values of ω/N from 0.625 to 1 at a regular interval). In the latter case, however, because of the larger generator amplitude, all experiments where the frequency was too close to the resonance led to strong non-linear effects, making the measurement of an amplitude impossible. For this reason, the corresponding data points are not shown. The theoretical curve for the maximal amplitude of vertical velocity normalised by the generator, computed from equation (4.46), is also plotted in figure 4.9 as a solid line.

With the generator configured at low forcing amplitude ($a = 2.5$ mm), the peaks corresponding to the first resonant frequencies were observed as predicted by the theory (see table 4.1). The measured resonance peaks are not exactly centered on the predicted resonant frequencies, but this is not inconsistent with the characteristic 4% error on N. We see that in the vicinity of resonant frequencies the wave field reaches twice the amplitude of the generator, and even more for the highest frequencies. For non-resonant frequencies, however, the wave interaction is destructive and the measured amplitude is half the amplitude of the generator.

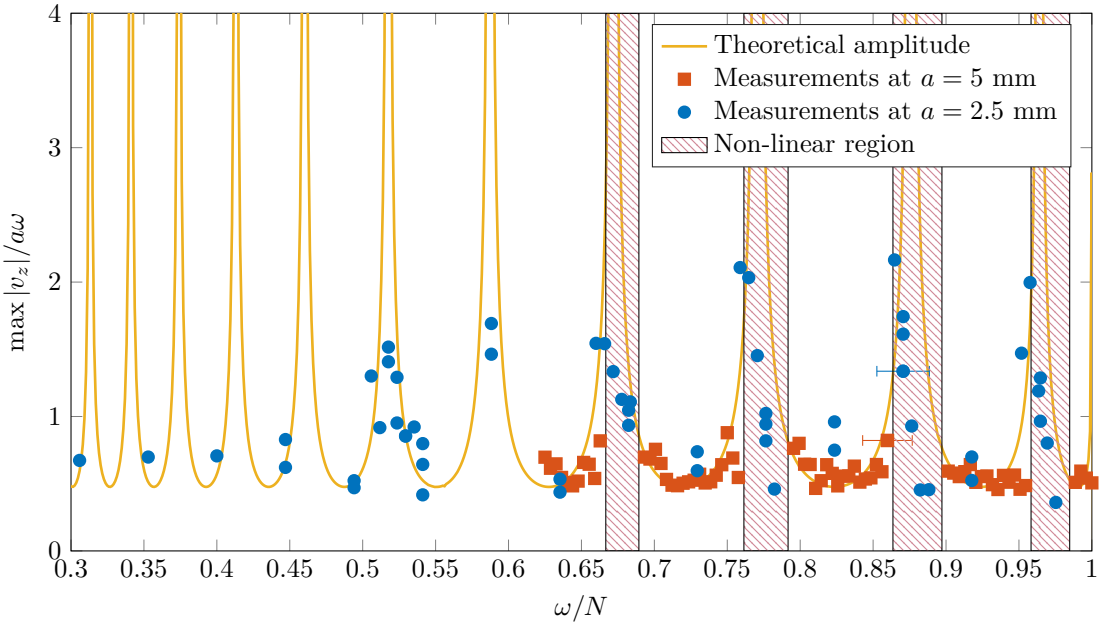

Figure 4.9: Amplitude measurements of the vertical velocity in the resonant cavity normalised by the generator velocity amplitude. Yellow line: theoretical amplitude for an infinite sum of waves as a function of the frequency ω/N. The dots are from three different sets of measurements run for different buoyancies or amplitudes. Red hatched regions show intervals of frequencies in which non-linear effects are clearly seen in the experiment for $a = 5$ mm.

In the vicinity of a resonant excitation frequency, we observed that the wave field amplitude kept strengthening until it triggered substantial non-linear effects. To illustrate this, figure 4.10 presents the temporal evolution of a horizontal profile of the vertical velocity component for $\omega/N = 0.73$ (figure 4.10(a), non-resonant), and $\omega/N = 0.77$ (figure 4.10(b), resonant). In the non-resonant case, each velocity profile has the shape of a Bessel profile, which is conserved during the whole experiment. No non-linear deformation of the wave field can be observed. The beating behaviour (i.e. low frequency fading amplitude) is because the reflected wave fields are not perfectly out of phase, due to the non-resonance condition. In the resonant case, such oscillations do not exist as all reflections are in phase and interfer constructively. These reflections, however, lead to an increasing amplitude that quickly triggers non-linear effects in which waves at other frequencies than ω are excited, after 80 seconds in the example in figure 4.10(b). The Bessel axisymmetric shape of the profile starts to disappear from the center of the tank due to emerging non-linear features, as the amplitude is maximum at $r = 0$. The non-linearities then propagate radially

towards the boundaries of the cylindrical tank, and the velocity field does not have a modal shape anymore (after 250 seconds in figure 4.10(b)).

By performing a similar analysis for all frequencies in the large amplitude case ($a = 5$ mm), we identified four frequency ranges in which all experiments led to non-linear effects. These ranges are marked with red hatched zones in figure 4.9. These intervals show a good agreement with the predicted resonance peaks (table 4.1) and with the increasing amplitude observed for the low amplitude measurements ($a = 2.5$ mm).

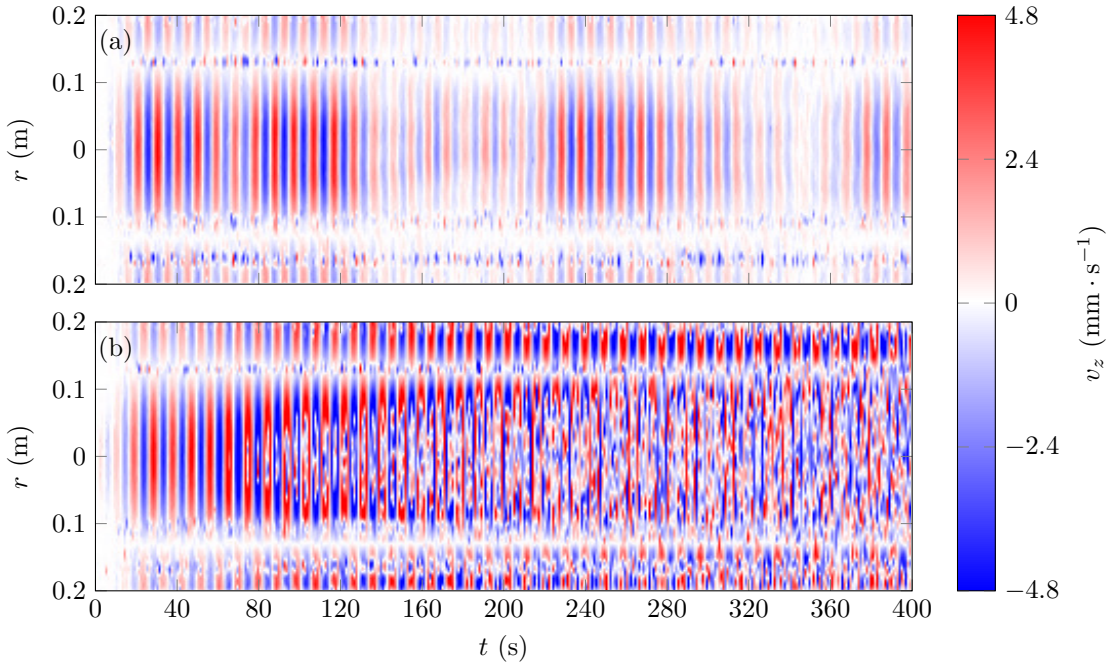

Figure 4.10: Temporal evolution of a horizontal profile of vertical velocity located at the center of the tank, for (a) $\omega/N = 0.73$ (non resonant case) and (b) $\omega/N = 0.77$ (resonance case). These profiles are measured at mid-depth in the tank for a mode 1 excitation, with $a = 5$ mm.

4.4 Conclusions and Discussion

We have presented the results of a combined theoretical and experimental study of axisymmetric internal wave modes, in which we first developed the theoretical framework of radial standing waves propagating vertically in uniform stratifications, incorporating both radial and vertical confinement and accounting for the impact of weak viscous damping. Then we presented the results of a laboratory experimental study of axisymmetric internal wave mode generation. The effect of rotation was not explored in our experiments, but the governing equations predict qualitatively similar behaviour as in the non-rotating case, the impact of rotation being foremost to influence the vertical wavenumber of the wave field for a given forcing frequency and buoyancy frequency [141, 169]. The experimental wave fields were produced using a novel configuration of internal wave generator technology that has previously been primarily used to excite nominally planar wave fields; in our experiments the arrangement directly excited the Bessel functions that are the natural basis of axisymmetric modes.

For the basic structure of the wave fields, there was very good qualitative and quantitative agreement between experiments and theory. Modes 1 through 3 were excited, leading to vertical and radial velocity profiles consistent with associated Bessel function forcing, and confirming the expected dispersion relation. As an additional component of these studies, we determined the efficiency of modal excitation by carefully studying the fluid system response to the generator forcing, fitting the PIV data to Bessel functions. A range of frequencies, from $\omega/N = 0.5$ to 0.9, was identified as being particularly suitable for studying axisymmetric modes as in this frequency

range the wave field is attenuated very little and has an almost full response to the forcing amplitude of the generator.

Having established the ability to excite vertical modes, the role of vertical confinement was then investigated. Such confinement has the potential to generate a resonance effect when reflected modes constructively interfere with each other. The resonance conditions for our system were determined and a series of experiments with different forcing amplitudes were performed. The experimental results on the wave field amplification aligned well with resonance predictions that incorporates weakly viscous correction for the wave field. Further refinement to account for the enhanced attenuation by boundary layers effects, or the effects of near surface and near bottom homogeneous fluid layers due to the filling process or diffusion could account for the minor discrepancies observed. Within the bounds of resonant peaks, the wave field was seen to amplify sufficiently to trigger non-linear effects that then eroded the linear wave field structure outwards from the centerline of the experimental domain, ultimately leading to a fully non-linear wave field throughout the experimental domain.

While there have been a number of nominally two-dimensional experimental studies comparing plane wave or mode behaviour with theoretical models, considering both their spatiotemporal form and transition to non-linear phenomena, there have been few such studies for axisymmetric geometries and most of them have been limited to the wave field excited by a vertically oscillating sphere. Axisymmetric wave fields are arguably more relevant as fundamental configurations for studying scenarios such as the excitation of atmospheric internal wave fields by storm cells [8] and the excitation of near-inertial wave fields in the ocean by surface storms [10]. This kind of laboratory experiments may also help to shed light on the resonance of seiches in appropriately shaped water basins, lakes, and estuaries [52, 94]. The experimental apparatus and consequent studies presented here demonstrate a new ability to excite axisymmetric wave fields and pure radial modes, opening the path to investigation of linear (e.g. internal wave transmission) and non-linear (e.g. TRI) internal wave phenomena in axisymmetric geometries. For example, inertial wave breaking and rotating turbulence, which was studied by Duran-Matute *et al* [66] using an oscillating torus, could be further investigated using our configuration with any desired combination of Bessel modes.

CHAPTER 5

Propagation in Non-Linear Stratifications

À la hâte coupez vos désirs trois-mâts échappés danseurs fous
La mer n'a plus de couleur venez voir la mer des algues
André Breton, Les Champs Magnétiques.

Inertia-gravity waves are known to be a significant vector for energy and momentum transfer in the ocean and atmosphere [220]. While a substantial amount of progress in understanding of their roles has been achieved via plane wave models, a planar geometry is not necessarily appropriate for studies pertaining to natural phenomena such as oceanic internal wave generation by hurricanes [113] and tropical cyclones [202], and atmospheric generation by thunderstorms [206]. Furthermore, Warren *et al.* [240] noted that a vertical disturbance of small spatial extent compared to the horizontal dimension of the system in a stably stratified fluid like the atmosphere leads to the emission of an axisymmetric perturbation. As such, and as discussed in some more details in chapter 3, axisymmetry is a reasonable approximation to consider for inertia-gravity waves generated by localised disturbances in either the atmosphere or the ocean.

When to consider energy transfer processes and wave propagation in the oceans and atmosphere, an important feature is the vertical form of the density-gradient, as shown in the works of King *et al.* [109] and Paoletti *et al.* [167] with numerical and in-situ studies of exponentially decaying buoyancy frequency. The influence of non-uniform stratifications has been studied for planar geometry, determining transmission and reflection coefficients for stratifications with sharp [158, 138] and smooth [45, 138] discontinuities. Numerical and experimental studies show good agreement with the theoretical predictions, considering two different scenarios: one with freely propagating incident waves [224, 138], a configuration relevant to the atmosphere, and another with parametric subharmonic instability in a forced, upper stratification layer [86], relevant to an ocean configuration. In the latter case, the finite extent of the upper layer leads to interferences between downard and upward waves reflected at the top and bottom boundaries, a phenomenon similar to resonant cavities as in optics [172] or Helmoltz cavities for sound waves [193, 153]. Such a resonant behaviour – by which we mean constructive interference[1] – has been observed by Sutherland and Yewchuck [224] and has been proven capable of triggering high amplitude wave fields [33].

Results from this chapter have been published in *Journal of Fluid Mechanics*[32].
Results from CPIES data are in preparation for *Geophysical Research Letters* [105].

[1]The use of the term *resonance* is ambiguous, as it can refer to two different phenomena in the physics of waves. Historically, resonance has been first used to describe cavities in which constructive interference occur due to reflection processes [172, 193, 153]. Later, it has been used to characterise the *Triadic Resonant Instability* (TRI) with a condition on the frequencies and wave vectors created through non-linearities [107, 27, 42, 140]. In this chapter, we refer to *resonance* in the sense of *constructive interference*.

5.1 A First Glance at Cartesian Wave Transmission

In non-rotating buoyant flows, the internal wave dispersion relation

$$\sin\beta = \pm\frac{\omega}{N}, \tag{5.1}$$

means that, for a given frequency ω, a change in buoyancy frequency N leads to a change in the angle of propagation β, as observed in various studies [86, 138]. As a consequence, a buoyancy interface creates wave beams with a different inclination, and propagation in non-linear stratifications leads to non-zero curvature of the wave beams as they follow the evolving gradient of density [140].

When dealing with modes, the problem is different because boundary conditions impose the wave field structure along given directions. In order to get a first intuition of the phenomenon, we run 2D DNS of downward propagating horizontal modes in Cartesian geometry, with $f = 0$ and linear and bi-linear stratification. DNS were run using Dedalus in a horizontal SinCos basis and vertical Chebyshev basis, with a 128×128 nodes resolution. A sinusoidal forcing is applied at the top boundary. Figure 5.1 presents snapshots of the results in two different stratifications: in figure 5.1(left), the stratification is linear with a constant N and the wave field is forced at $\omega/N = 0.1$; in figure 5.1(right), the stratification is bi-linear with layers of different buoyancy frequencies, N_1 and N_2, on top of each other, and a forced wave field at $\omega/N_1 = 0.5$ and $\omega/N_2 = 0.67$. After crossing the interface (dashed line in figure 5.1), the velocity field develops a horizontal structure in the bottom layer similar to the forcing in the top layer, but a different vertical structure. Note that, in these numerical simulations, the vertical wave length is badly defined in the whole domain (figure 5.1(left)) and in the top region (figure 5.1(right)) due to reflection of the wave field, at the bottom of the tank and at the interface, respectively.

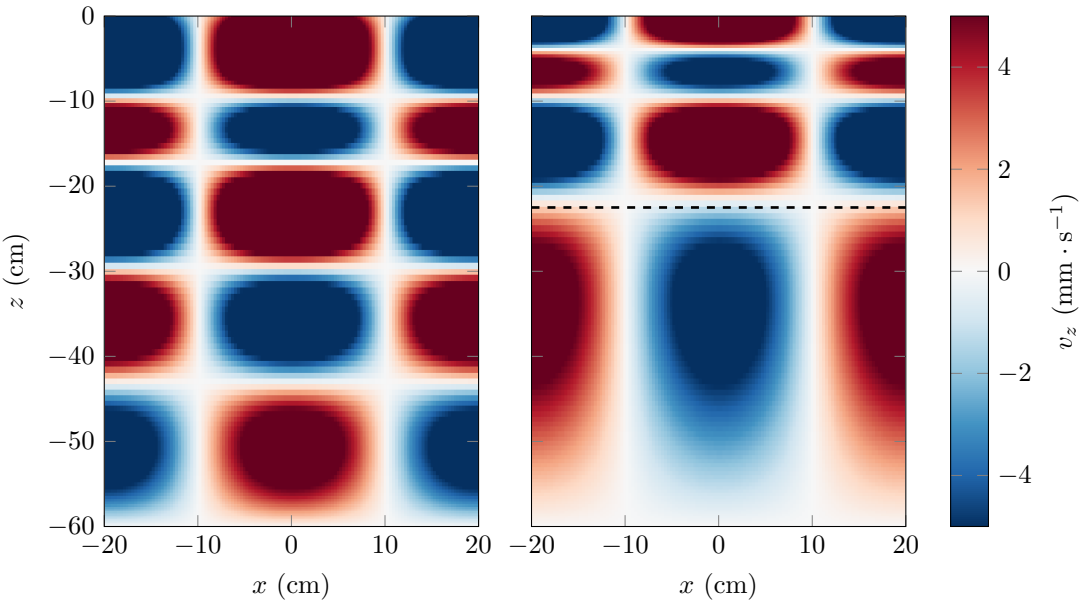

Figure 5.1: Snapshots of vertical velocity fields in a DNS of 2D Cartesian modes run using Dedalus. Left: in a linear stratification (at $\omega/N = 0.5$). Right: in a bi-linear stratification with N_1 for $z \in [0; -22]$ and N_2 for $z \in [-22; -60]$ (at $\omega/N_1 = 0.5$ and $\omega/N_2 = 0.67$). The dashed line shows the interface between N_1 and N_2.

The existence of reflected and transmitted wave beams at a buoyancy interface has been studied in 2D for planar wave fields [138, 219], but the dynamics of modes has not been deeply investigated. Furthermore, extending results from 2D Cartesian waves to 3D axisymmetric modes is not intuitive due to the geometry and non-uniform amplitudes. In the next sections, we delve further into transmission properties of axisymmetric wave fields with theoretical considerations and experimental evidence.

5.2 Axisymmetric Wave Transmission

Focusing on an inviscid Boussinesq fluid rotating at an angular velocity Ω, with a density stratification $\rho(z)$ where z is the ascendent vertical, small amplitude internal waves satisfy the following equation in cylindrical coordinates [33, 141]

$$\frac{\partial^2}{\partial t^2}\left(\frac{\partial^2\psi}{\partial z^2}+\frac{\partial}{\partial r}\left(\frac{1}{r}\frac{\partial(r\psi)}{\partial r}\right)\right)=-f^2\frac{\partial^2\psi}{\partial z^2}-N^2\frac{\partial}{\partial r}\left(\frac{1}{r}\frac{\partial(r\psi)}{\partial r}\right), \tag{5.2}$$

in which $f=2\Omega$ is the Coriolis frequency, and $N=\sqrt{(-g/\rho_0)\partial\bar{\rho}/\partial z}$ is the z-dependent buoyancy frequency, ρ_0 being the reference density. The stream function ψ is defined so that the radial and vertical velocities v_r and v_z are

$$v_r=-\frac{1}{r}\frac{\partial(r\psi)}{\partial z} \qquad \text{and} \qquad v_z=\frac{1}{r}\frac{\partial(r\psi)}{\partial r}. \tag{5.3}$$

In the configuration of a horizontal forcing in a linear stratification (N is a constant), the solutions of equation (5.2) can be expressed as a product of two decoupled functions: a radial part depending on the radius r, and a vertical part depending on the depth z. The cylindrical geometry leads to a natural decomposition over Bessel functions for the radial component and exponentials for the vertical component. Using a complex notation, as discussed in chapter 4, the stream function can therefore be written as a sum of cylindrical modes of the form [33]

$$\psi(r,z,t)=\psi_0 J_1(lr)e^{i(mz-\omega t)}, \tag{5.4}$$

with ψ_0 a constant amplitude, ω the wave frequency, and l and m its radial and vertical wavenumbers. The radial dependence is expressed through a first order Bessel function of the first kind J_1, corresponding to a non-divergent mode. In the case of either a free propagating or evanescent wave, the vertical dependence can be written with an exponential. For a more general framework in further sections, for example while considering vertically confined wave fields, the vertical component will be noted ϕ. As in cartesian geometry, the parameters ω, l, and m are linked through the internal wave dispersion relation [33, 141]

$$m=\pm l\left(\frac{\omega^2-N^2}{f^2-\omega^2}\right)^{1/2}, \tag{5.5}$$

derived from (5.2), (5.3) and (5.4).

In the next two sections, we discuss the two scenarios presented in figure 5.2, initially assuming a sharp interface (discontinuity between two different buoyancy frequencies N_1 and N_2, with $N_1 > N_2$). Figure 5.2(a) shows the transmission of a free incident wave ψ^I, which is more relevant to the modeling of atmospheric internal waves, whereas figure 5.2(b) shows the transmission of an incident wave confined from above, which is closer to an oceanic situation with a surface forcing.

5.2.1 Transmission of a Free Incident Wave

Sharp Interface

Linear vertical propagation of radial modes has been extensively studied by [33]. In this section, we consider a horizontal interface located at $z=0$ that splits the domain into two media of constant buoyancy frequency N: N_1 in the upper layer ($z>0$), N_2 in the lower layer ($z<0$), the density being continuous at the interface (figure 5.2(a)). We assume a larger buoyancy frequency in the upper layer so that $N_1 > N_2$. As depicted in figure 5.2(a), a free incident wave ψ^I reaching the interface leads to a reflected wave ψ^R in the upper region, and a transmitted wave ψ^T in the lower region. The total wavefield can be described by $\psi_1=\psi^I+\psi^R$ in the upper region, where ψ^I is known, and by $\psi_2=\psi^T$ in the lower region.

We define the transmission coefficients as the ratios of the velocities above and under the interface, as

$$T_{v_z}=\left|\frac{v_z^T}{v_z^I}\right| \qquad \text{and} \qquad T_{v_r}=\left|\frac{v_r^T}{v_r^I}\right|, \tag{5.6}$$

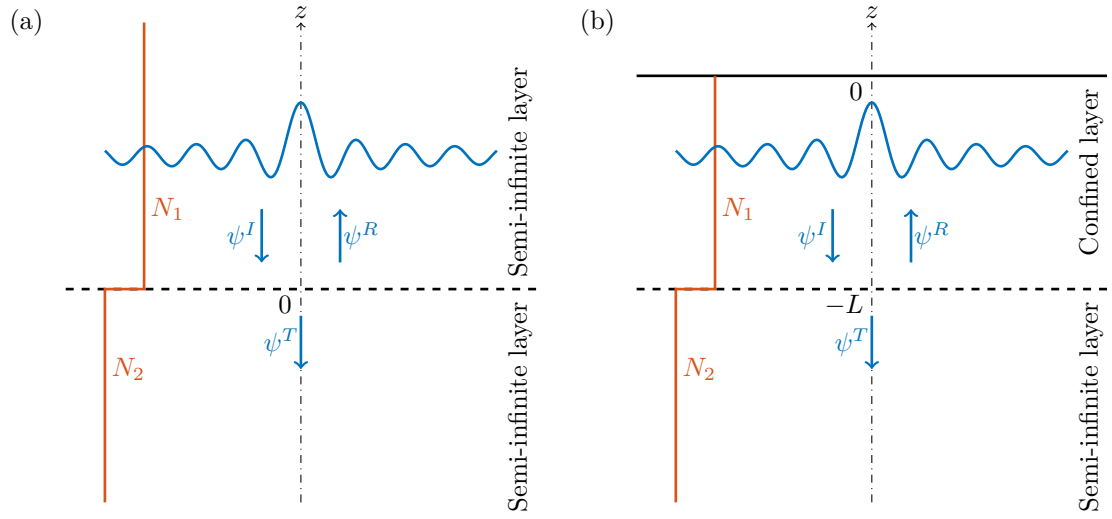

Figure 5.2: Transmission of a radial mode J_1 across a buoyancy frequency interface. The z axis is located at $r = 0$. In both cases, the interface is modeled by a sharp discontinuity in buoyancy frequency, and the blue pattern represents a Bessel shaped wave field. (a) free incident wave ψ^I reaching the interface, leading to a reflected wave ψ^R and a transmitted wave ψ^T. (b) a confined incident wave ψ^I, located between the surface at $z = 0$ and the interface at $z = -L$, is an infinite sum of waves being reflected at $z = 0$ and at $z = -L$, and leads to a transmitted wave ψ^T.

and

$$R_{v_z} = \left| \frac{v_z^R}{v_z^I} \right| \qquad \text{and} \qquad R_{v_r} = \left| \frac{v_r^R}{v_r^I} \right|, \tag{5.7}$$

where the notation I, R, and T, indicates that the vertical velocity v_z or the radial velocity v_r is computed from the stream function ψ^I, ψ^R, and ψ^T, respectively (see figure 5.2). These velocities are taken at the interface, which means in the limit $z \to 0$.

Transmission and reflection properties can be derived by applying boundary conditions at the interface: continuity of the total vertical velocity field v_z and the pressure p derived from ψ_1 and ψ_2 [138]. As in cartesian geometry, these quantities can be obtained using the linearised Navier-Stokes equations [13]. The transmission and reflection coefficients for the radial and vertical velocities v_r and v_z, and the flux of the energy $j = pv_z$ across the interface, can therefore be derived, respectively

$$T_{v_r} = \left| \frac{2m_2}{m_1 + m_2} \right|, \qquad T_{v_z} = \left| \frac{2m_1}{m_1 + m_2} \right|, \qquad \text{and} \qquad T_j = \left| \frac{4m_1 m_2}{(m_1 + m_2)^2} \right|, \tag{5.8}$$

and

$$R_{v_r} = \left| \frac{m_1 - m_2}{m_1 + m_2} \right|, \qquad R_{v_z} = \left| \frac{m_2 - m_1}{m_1 + m_2} \right|, \qquad \text{and} \qquad R_j = \left| \frac{(m_1 - m_2)^2}{(m_1 + m_2)^2} \right|, \tag{5.9}$$

where m_1 and m_2 are the vertical wavenumbers corresponding to regions 1 and 2, given by the dispersion relation (5.5). These coefficients are the same as in cartesian geometry for a plane wave beam crossing a density gradient interface [138], suggesting that the radial dependence does not affect wave properties at the interface though it still shapes the wavefield and the energy distribution. Colormaps of the transmission and reflection coefficient for the vertical velocity, T_{v_z} and R_{v_z}, are presented in figure 5.3 as functions of N_1/N_2 and ω/N_1. A maximum of transmission of vertical velocity appears for $\omega/N_1 = N_2/N_1$, when the wave just becomes evanescent in the lower region. This evanescence transition is clearly identified in the reflection coefficient, showing a total reflection of the wave field for $\omega/N_1 > N_2/N_1$. The high value of transmission of vertical velocity can be explained by the vertical co-oscillation imposed to the bottom layer by the interface.

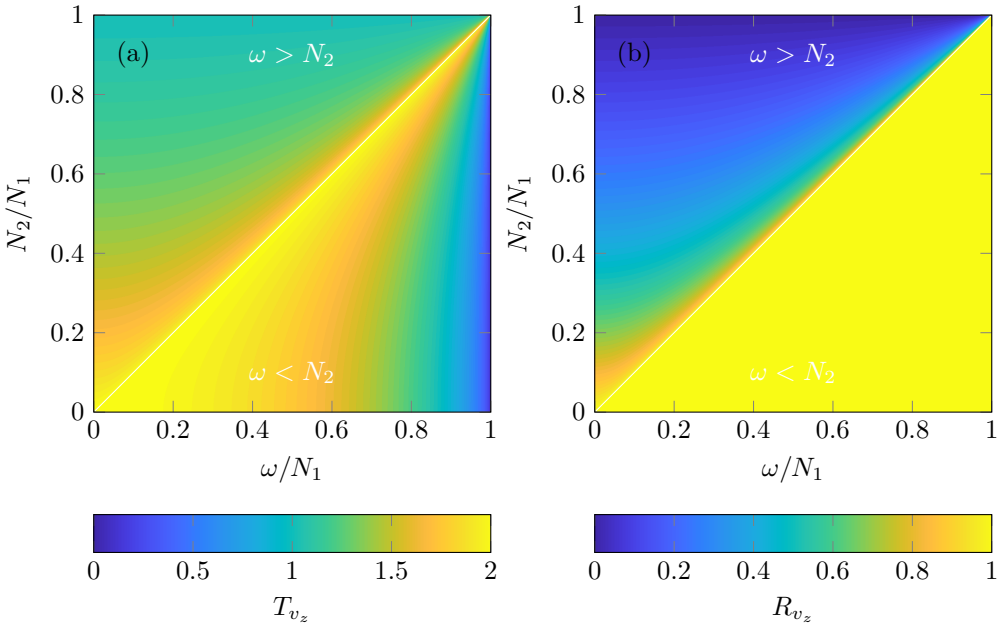

Figure 5.3: Colormaps of (a) the transmission coefficient T_{v_z} and (b) the reflection coefficient R_{v_z} in vertical velocity, in the plane $(\omega/N_1, N_1/N_2)$. The Coriolis frequency is set to be $f = 0$.

Smooth Interface

Following the approach of Mathur and Peacock [138], the propagation of the wave across a physical smooth interface of finite-width transition region δ is investigated using the buoyancy frequency profile

$$N^2(z) = \left(\frac{N_1^2 + N_2^2}{2}\right) + \left(\frac{N_1^2 - N_2^2}{2}\right) \tanh\left(\frac{z}{\delta}\right), \tag{5.10}$$

for which N is assumed to be constant far from the transition region and continuously going from N_1 to N_2 at the interface located at $z = 0$.

In a similar way as done by Mathur and Peacock [138] and Nault and Sutherland [158], the wave behaviour close to the interface is explored through a numerical approach. As the buoyancy frequency profile does only depend on z, the radial part is still described by a first order Bessel function J_1. We use an ansatz describing the stream function as

$$\psi(r, z, t) = \phi(z) J_1(lr) e^{i\omega t}, \tag{5.11}$$

where the vertical dependence is no longer described by an exponential as in (5.4) but by a z-dependent function ϕ. This function is found to satisfy the differential equation

$$\phi'' + \gamma(z)\phi = 0 \qquad \text{with} \qquad \gamma(z) = l^2 \left(\frac{\omega^2 - N^2(z)}{f^2 - \omega^2}\right), \tag{5.12}$$

where ϕ'' stands for the second order derivative of ϕ, and γ is a function of z that replaces the m wave number given in the sharp interface study. Far from the interface, the wave field is expected to behave vertically as a Fourier mode, which implies an asymptotic form

$$\tilde{\phi}(z) = \begin{cases} \phi_0^I e^{im_1 z} + \phi_0^R e^{-im_1 z} & \text{if} \quad z = z^+, \\ \phi_0^T e^{im_2 z} & \text{if} \quad z = z^-, \end{cases} \tag{5.13}$$

where ϕ_0^I, ϕ_0^R, and ϕ_0^T are constants describing the amplitudes of the incoming, reflected, and transmitted waves, m_1 and m_2 are the vertical wave lengths corresponding to the media of buoyancy frequencies N_1 and N_2 defined by (5.5), and z^+ and z^- are two locations far from the interface respectively above and below it. The asymptotic expression $\tilde{\phi}$ can be written as boundary conditions

for ϕ

$$\phi = \tilde{\phi} \qquad \text{at} \quad z = z^+, \tag{5.14a}$$

$$\phi' = im_2\tilde{\phi} \qquad \text{at} \quad z = z^-. \tag{5.14b}$$

Thus, we obtain a boundary value problem that can be solved numerically, giving the z-dependent function ϕ and allowing for the computation the transmission and reflection coefficients.

Weakly Viscous Correction

As discussed in chapter 4, viscous damping for radial modes has to be considered while using frequencies such as $\omega/N < 0.5$. The weakly viscous correction can be described by assuming that the first order correction in $\varepsilon = \nu l^2/\omega$ for a vertical dependence of the stream functions as $\phi(z) \propto e^{imz}$ takes the form [33]

$$m = m^{(0)} + i\varepsilon m^{(1)} + \mathcal{O}(\varepsilon^2), \tag{5.15}$$

with $m^{(0)}$ being the inviscid vertical wave number defined by equation (5.5), and $m^{(1)}$ the correction term

$$i\varepsilon m^{(1)} = \mp \frac{i\varepsilon l}{2(1-\gamma^2)\alpha^3\sqrt{1-\alpha^2}}, \tag{5.16}$$

where $\alpha = \omega/N$ and $\gamma = f/\omega$. Hence, after propagating over a distance z, the weakly viscous streamfunction ψ_ν is written

$$\psi_\nu(z) = \psi(z)\exp(-\varepsilon m^{(1)}|z|). \tag{5.17}$$

A more general calculation of the viscous correction, for arbitrary z-dependent stratifications, can be found in Kistovich and Chashechkin [110].

Using the above expressions, the transmission coefficient can be computed numerically and compared to the inviscid case. The problem is solved as a boundary value problem, using a similar system as proposed before (5.14). Yet, as ϕ is now driven by a fourth order differential equation [33], the boundary value problem requires four conditions to be closed

$$\phi = \tilde{\phi} \qquad \text{at} \quad z = L, \tag{5.18a}$$

$$\phi'' = -(m_1^{(0)} + \varepsilon m_1^{(1)})^2\tilde{\phi} \qquad \text{at} \quad z = L, \tag{5.18b}$$

$$\phi' = i(m_2^{(0)} + \varepsilon m_2^{(1)})\tilde{\phi} \qquad \text{at} \quad z = z^-, \tag{5.18c}$$

$$\phi'' = -(m_2^{(0)} + \varepsilon m_2^{(1)})^2\tilde{\phi} \qquad \text{at} \quad z = z^-. \tag{5.18d}$$

5.2.2 Transmission of a Confined Incident Wave

Sharp Interface

In the previous section, semi-infinite domains were implicitly assumed. Such situations can be found in the atmosphere, as discontinuities in the buoyancy frequency profile are likely to be far from a source of internal waves. In the oceans, however, strong stratifications are often found close to the surface [33], so the upper layer cannot be modeled by a region that extends vertically without boundaries.

We therefore consider a sharp interface between N_1 and N_2 at $z = -L$, and an upper rigid boundary (the ocean surface) at $z = 0$, as presented in figure 5.2(b). Analytically, this problem can be solved as in the case of a semi-infinite domain, except that the boundary conditions are different because the incoming wave ψ^I is not known. Instead, the total field at $z = -L$ is known and its vertical dependence satisfies: $\phi(z = -L) = \phi_0 = \phi_0^I e^{-iLm_1} + \phi_0^R e^{iLm_1}$. The following transmission coefficients are derived using the same continuity properties at the interface as in the

previous section

$$T_{v_r} = \left|\frac{v_r^T}{v_r^I}\right| = \left|\left[\cos(Lm_1) + i\left(\frac{m_1}{m_2}\right)\sin(Lm_1)\right]^{-1}\right|, \tag{5.19}$$

$$T_{v_z} = \left|\frac{v_z^T}{v_z^I}\right| = \left|\left[\cos(Lm_1) + i\left(\frac{m_2}{m_1}\right)\sin(Lm_1)\right]^{-1}\right|, \tag{5.20}$$

$$\text{and} \quad T_j = \left|\left[\cos(2Lm_1) + i\left(\frac{m_1^2+m_2^2}{2m_1m_2}\right)\sin(2Lm_1)\right]^{-1}\right|, \tag{5.21}$$

$$\text{with} \quad m_1 = \pm l\left(\frac{N_1^2}{\omega^2} - 1\right)^{1/2} \qquad \text{and} \qquad m_2 = \pm l\left(\frac{N_2^2}{\omega^2} - 1\right)^{1/2}. \tag{5.22}$$

where the v_r^T and v_z^T are the transmitted radial and vertical velocities respectively, and v_r^I and v_z^I are the incoming radial and vertical velocities for the total wavefield in the upper region (see figure 5.2). All velocities are taken at the interface, which means in the limit $z \to -L$. In equation (5.22) we recall the result from equation (5.5) in the non-rotating case ($f = 0$).

Expressions (5.19), (5.20), and (5.21), involve different experimentally tunable variables: the buoyancy frequencies of the two layers N_1 and N_2, the frequency of the wave ω, the depth L of the interface, and the radial wave number l. These parameters can be reduced to three non-dimensionalised parameters: $L \times l$, ω/N_1, and N_2/N_1. Figure 5.4 presents colormaps of the transmission coefficient for vertical velocity T_{v_z}, as a function of these different parameters. Clear peaks appear, with large amplitudes due to a constructive interference effect between upwards and downwards propagating waves in the upper layer. Figure 5.4(a) shows the transmission coefficient as a function of ω/N_1 and N_2/N_1 for a fixed value of $L \times l$ ($= 3.23$). Transmission is generally higher for cases where waves can propagate in both regions ($\omega < N_2 < N_1$) and drops off for evanescent frequencies in the lower region ($N_2 < \omega < N_1$). Maxima of transmission appear for well-defined values of ω/N_1 at a given N_2/N_1. The curves defining maxima of transmission are continuous between the evanescent and the propagating regions. Figure 5.4(b) shows the transmission coefficient as a function of ω/N_1 and $L \times l$ for a fixed value of N_2/N_1 ($= 0.74$). The cut-off between the propagating and evanescent regions is now observed at $\omega/N_1 = N_1/N_2 = 0.74$. The resonant interference peaks are expected to be less numerous as $N_2/N_1 \to 1$ or as $L \times l \to 0$. The study of the transmission coefficient in radial velocity T_{v_r} shows similar behaviour.

Smooth Interface

As in the freely incoming wave case, these results can be extended to the case of a smooth interface through the same method, simply by changing the boundary condition at the surface:

$$\tilde{\phi}(z) = \begin{cases} \phi_0 & \text{if} \quad z = L, \\ \phi_0^T e^{im_2 z} & \text{if} \quad z = z^-, \end{cases} \tag{5.23}$$

where z^- is a location far from the interface in the lower layer, leading to a new set of boundary conditions for the numerical computation.

Weakly Viscous Correction

The transmission mechanism involved in the confined configuration is supposed to result from an infinite number of reflection in the upper layer. Such a condition, however, is not truly satisfied in the case of a viscous fluid, as the amplitude of the wave field decreases and vanishes after a finite number of reflections. Once again, the problem is solved numerically after finding out the correct boundary conditions, using the first order developpement of the vertical wave number m [33].

5.3 Apparatus Configuration

The experiments did not involve rotation ($f = 0$), so the waves were purely internal gravity waves. Note that adding rotation at fixed values of N, ω, and l, would only change the vertical wave

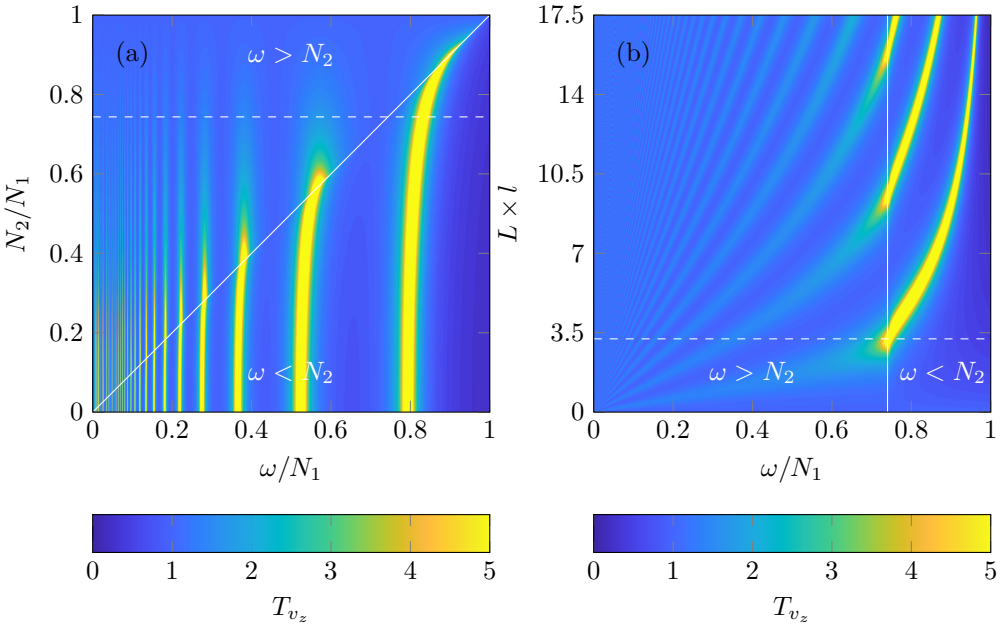

Figure 5.4: Colormaps of the transmission coefficient T_{v_z} as a function of (a) ω/N_1 and N_1/N_2 at a given $L \times l = 3.23$, and (b) ω/N_1 and $L \times l$ at a given $N_2/N_1 = 0.74$. Dashed lines show the cuts at (a) $N_2/N_1 = 0.74$ and (b) $L \times l = 3.23$. The Coriolis frequency is set to be $f = 0$.

number m and not the physics involved in the linear theory (see equation (5.5)).

We set the wave generator's configuration to be a mode 1 profile, with a radial wave length of $l = 19$ m^{-1}, as presented in chapter 2 figure 2.7. We use a generator amplitude $a = 2.5$ mm, which is low enough to limit non-linear effects (see chapter 7 on non-linear effects for more details).

The tank is filled with salt-stratified water in a bi-linear stratification, as described in chapter 2 figure 2.3(b), using a filling process based on the double bucket method [81, 164]. In order to obtain bi-linear stratifications, when required we stopped the filling, to change the filling tank density difference by removing salt water and adding fresh water without changing the density in the mixing tank. We then re-started the filling, which gave us a sharp but buoyancy frequency interface at the desired depth. In our experiments, we decided to use a stronger stratification in the upper layer ($N_1 > N_2$), as in the theory, because we wanted to look at transmission when the wave field in the lower layer was either propagating or evanescent. Such a configuration is also more common in the ocean, where the buoyancy frequency is larger in the pycnocline than deeper.

Experiments were conducted over a period of time up to 40 hours during which the interface becomes less sharp due to diffusive effects (we estimate the width of the interface to increase at a rate of about 1 cm/day). Due to the configuration of the apparatus, the stratification could not be measured at different times while running the experiment because the presence of the generator prevented access to the domain of interest by the conductivity probe. As detailed later in the result section, however, we conducted systematic repeated experiments showing that any evolution of the stratification did not impact the experimental results.

5.4 Experimental Results

5.4.1 Transmission of a Free Incident Wave

We first quantified the transmission coefficient for the vertical velocity field in the case of a freely incoming wave. To conduct this experiment, a two-layer stratification is used and a range of forcing frequencies is explored. For each frequency, the transmission coefficient is extracted from the PIV data by looking at the vertical velocity below the interface.

Figure 5.5 presents the stratification used to conduct this study. The first two plots show

the density profile $\rho(z)$ computed from the measurements of the C/T probe, and the buoyancy frequency profile $N(z)$ subsequently derived. The density curve shows two layers of linear stratification, one from 0 to 30 cm and one from 30 to 60 cm. The buoyancy frequency profile confirms this trend, showing two constant values for the density gradient: $N_1 = 0.94 \pm 0.02$ rad $\cdot$ s^{-1} and $N_2 = 0.62 \pm 0.05$ rad $\cdot$ s^{-1}. We indicate by a dashed line the interface between these two domains, and by a straight line the top of the tank. Two to three centimeters are missed in the measurements at the bottom of the tank, due to the configuration of the probe. On the buoyancy frequency curve, we fit the N profile with our models for a sharp and a smooth interface (equation (5.10)) with the same distance $L = 30$ cm from the generator, and a width $\delta = 1$ cm. No error is given on these lengths because it does not impact the transmission coefficient error, as we will discuss later. A small bump in the stratification is present at 42 cm below the generator: its width on the N profile is exaggerated because of the averaging process used to compute the buoyancy frequency and, as can be seen in figure 5.5(c), it does not affect the velocity field. However, to get the most accurate evaluation of N_2, we used the mean value and the standard deviation in the interval [31; 41] cm. The N_1 profile was estimated in the [3; 28] cm interval.

Figure 5.5(c) presents a PIV snapshot of the vertical velocity field after the wave field crossed the buoyancy frequency interface. The mode 1 shape of the generator in a horizontal plane is visible at the top due to a parallax effect. Through the interface, we see that the radial wave length, given by the horizontal nodes and antinodes of the field, is conserved. The vertical wave number, given by the vertical nodes and antinodes [33], changes when the wave field crosses the interface, and is lower in the bottom layer than in the top one. Such a behaviour is expected, as the vertical wave number m is fixed by the buoyancy frequency N and in our experiment we set $N_2 < N_1$.

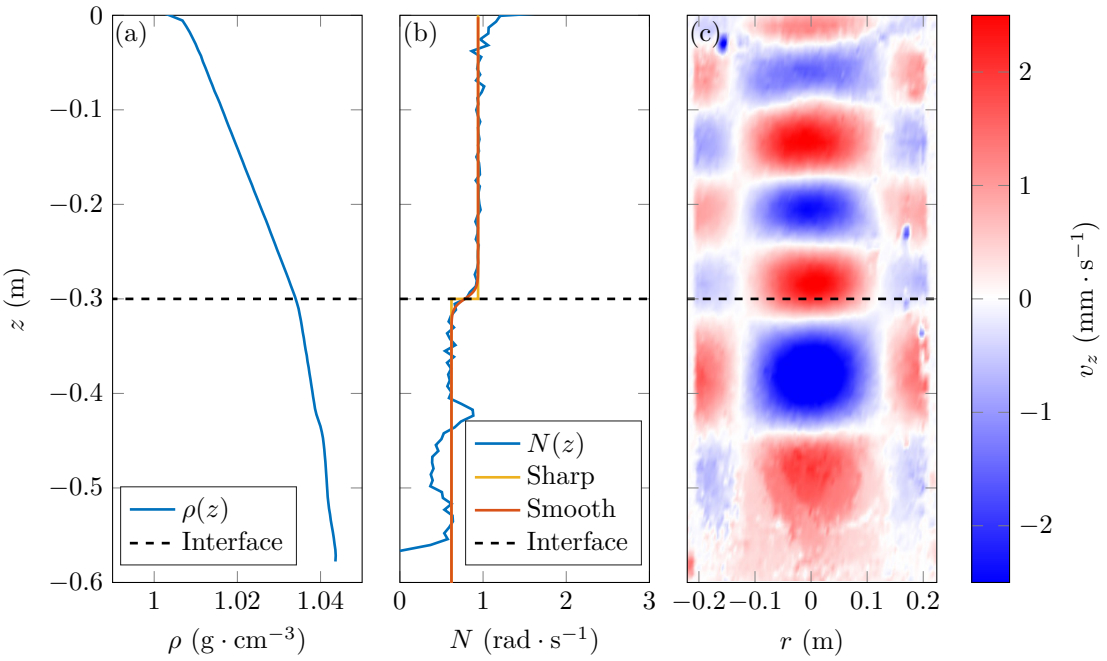

Figure 5.5: From left to right: (a) density profile $\rho(z)$, (b) buoyancy frequency profile $N(z)$ and fits (with $N_1 = 0.94 \pm 0.02$ rad $\cdot$ s^{-1}, $N_2 = 0.62 \pm 0.05$ rad $\cdot$ s^{-1}, $L = 30$ cm, width $\delta = 1$ cm), and (c) example of vertical PIV cross-section of the vertical velocity field ($\omega/N_1 \simeq 0.4$). The generator is located at the top ($z = 0$). The dashed line indicates the interface.

To ensure that the interface does not affect the modal shape of the field, we present in figure 5.6 horizontal profiles of the radial and vertical velocity fields in the upper layer and in the lower layer. Without any regard on the amplitude, as the profiles were taken at random times, we see that in both cases the fits with the expected Bessel functions respectively $J_0(lr)$ and $J_1(lr)$, with $l = 19$ m^{-1}, agree well with the experimental profiles.

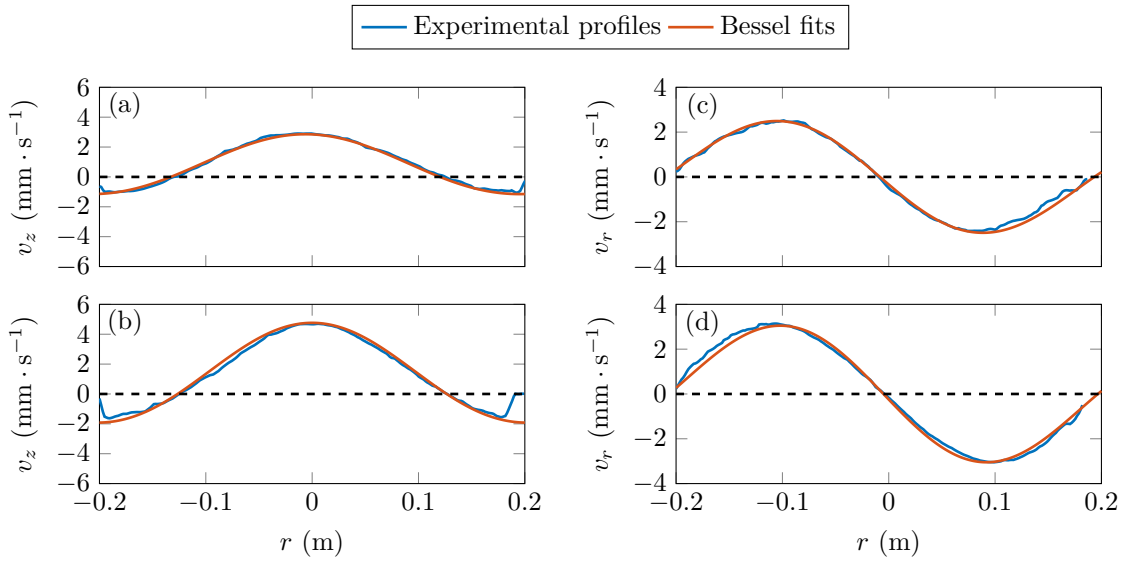

Figure 5.6: Experimental profiles and fits by Bessel functions: (a) vertical velocity in the upper layer, at $z \simeq -15$ cm; (b) vertical velocity in the lower layer, at $z \simeq -35$ cm; (c) radial velocity in the upper layer, at $z \simeq -15$ cm; (d) radial velocity in the lower layer, at $z \simeq -35$ cm. Profiles are taken at random times.

The transmission properties are investigated using the stratification from figure 5.5, by producing mode−1 wave fields first for increasing frequencies $\omega = 0.3$ to 0.98 rad · s^{-1} (labelled by $\omega_{\nearrow}$), then for decreasing frequencies $\omega = 0.96$ to 0.28 rad · s^{-1} (labelled by $\omega_{\searrow}$). As no direct measurement of the stratification can be performed inside the cylinder due to the lateral, top, and bottom boundaries, this protocol serves as a check that the stratification does not change while running the experiment. Because we only want to investigate the transmission of the wave field, short-time measurements are done with excitations of 100 s, at 20 min intervals each, to ensure that the fluid is initially at rest for each measurement. We measure the amplitude in the lower region, after the wave has crossed the interface. To this extent, the selection procedure described in [33] is adapted.

We consider the time series obtained by fitting horizontal cuts of vertical velocity for Bessel functions of radial number $l = 19$ m^{-1}. These cuts are taken at a depth z_m, a few centimeters below the interface. In this time series, we pick three different time windows of one-period width, starting at a time when $v_z = 0$, half-covering each other. The middle time window is chosen to be the last one before the wave reflected at the bottom returns at $z = z_m$. This returning time, t_f, is determined using the group velocity

$$\mathbf{v_g} = -\frac{ml^2N^2}{\omega k^4}\mathbf{e_z}, \tag{5.24}$$

computed in both layers. Figure 5.7 shows examples of (a) timeseries at $\omega/N_1 = 0.89$ and (b) timeseries at $\omega/N_1 = 0.50$, with the three different time windows used to estimate the amplitude in both cases. The wave field in figure 5.7(a) is evanescent in the lower region, so there is theoretically no reflected wave. In this case, the time t_f is taken just before seeing non-linearities. In the measurement region, the temporal evolution of the amplitude is nearly sinusoidal. In figure 5.7(b), the amplitude is still growing after the returning time. It can be due to the reflected wave, or to a non-fully established wave field.

For each of the three time windows defined, the RMS value of the time signal during the chosen time windows is computed. The wave amplitude is then defined as the average of the three values obtained, multiplied by $\sqrt{2}$ since the signal is fairly sinusoidal. The standard deviation between these three values gives an estimate of the measurement error. The need of such a process is justified by the fact that for some frequencies, the wave field is not fully developped when reaching

the interface (figure 5.7). Given this situation, measuring the right amplitude is difficult even when the profiles are well fitted by the theoretical Bessel functions.

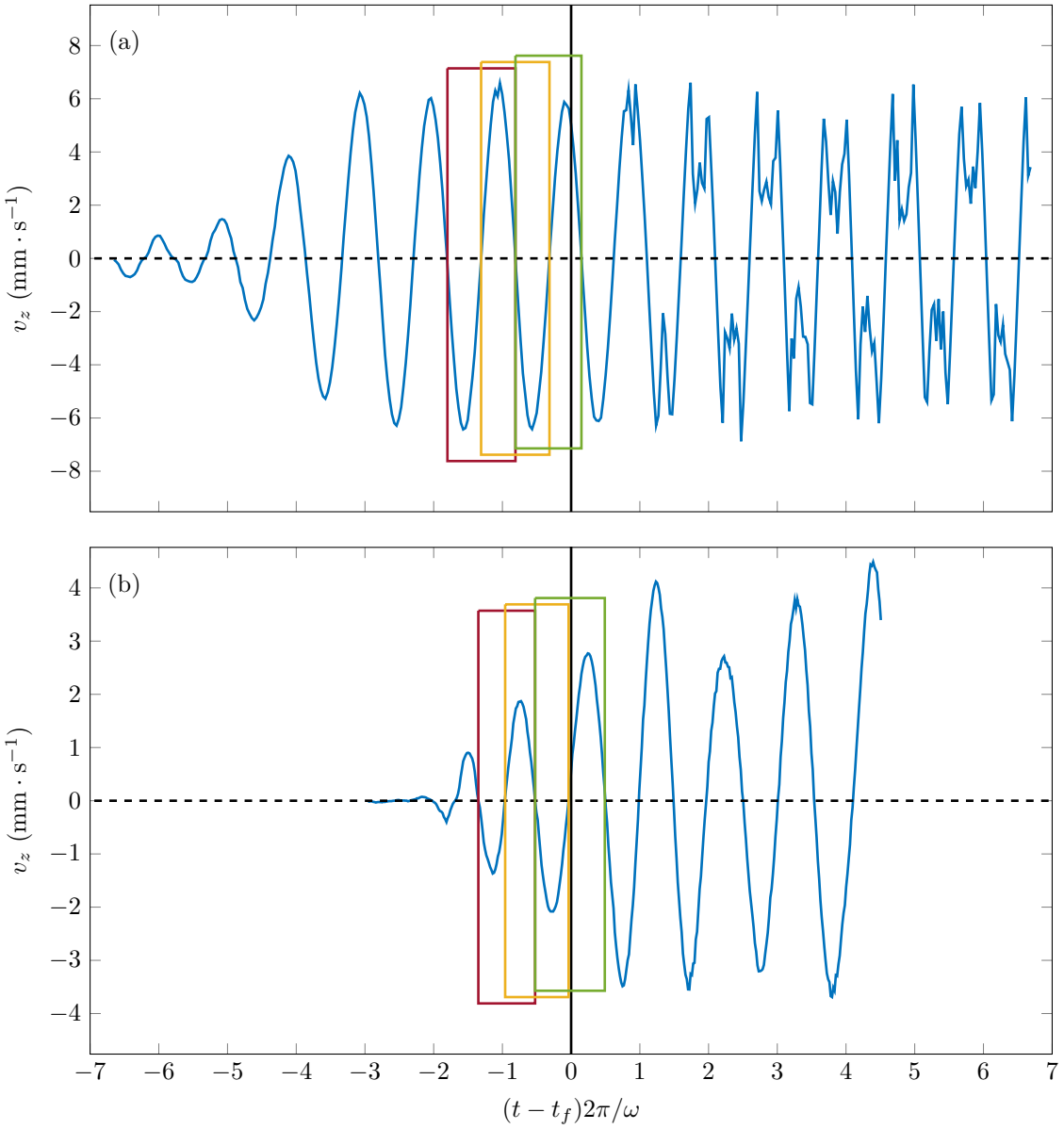

Figure 5.7: Timeseries of the amplitude of the vertical velocity over 100 s, (a) at $\omega/N_1 = 0.89$ and (b) at $\omega/N_1 = 0.50$. The black solid line indicates the time t_f used to compute the amplitude. Rectangles show the three periods used to estimate the wave amplitude from RMS.

Direct comparison between the amplitude of the wave field above and under the interface is not possible, because the multiple reflections within the relatively narrow top layer make it infeasable to extract the amplitude of the incident wave alone. However, we have shown in [33] that for frequencies above $\omega/N \simeq 0.3$, the experimental amplitude of an incident mode is well predicted by the generator amplitude $a\omega$, corrected with the theoretical viscous damping coefficient

$$v_{z,\mathrm{inc}} = a\omega \times \exp(-\varepsilon m_1^{(1)} L), \tag{5.25}$$

where $m_1^{(1)}$ is defined in section 5.2.1. Therefore, to estimate the transmission coefficient, we

compare the measured transmitted amplitude $v_{z,\mathrm{mes}}$ to the theoretical incident amplitude $v_{z,\mathrm{inc}}$.

$$T_{v_z} = \frac{v_{z,\mathrm{mes}}}{v_{z,\mathrm{inc}}} = \frac{v_{z,\mathrm{mes}}}{a\omega \times \exp(-\varepsilon m_1^{(1)} L)}. \tag{5.26}$$

The experimental transmission data points are presented in figure 5.8. To scale the frequencies as a non-dimensional parameter, we use the mean value of the buoyancy frequency N_1. We note that, as the two sets of measurements $\omega_{\nearrow}$ and $\omega_{\searrow}$ nicely follow the same trend, the influence of the forcing on the stratification can be considered as negligible. In order to draw comparisons with theoretical predictions, we must first make some considerations on the control parameters. The shape of the theoretical curves is controlled by various parameters: the position of the interface L, its width δ, and the buoyancy frequencies of the two layers N_1 and N_2. We studied the impact of these parameters by computing different curves for the smooth interface with a weakly viscous correction using the method explained in sections 5.2.1 and 5.2.1. We found out that the distance L mainly controls the viscous damping observed at low frequencies, as the amplitude of the wave is greatly attenuated for $\omega/N_1 < 0.5$, as discussed in [33]. The width δ changes the height of the peak in the transmission curve, located at $\omega/N_1 = N_2/N_1$. However, as the interface is really sharp in our experiment ($\delta = 1$ cm), its impact is negligeable. To investigate the influence of the boyancy frequencies, we looked at the ratio N_2/N_1. We found that the transmission curve is very sensitive to a slight change in the buoyancy frequencies, as it shifts the position of the transmission peak and defines the range of frequencies for which the wave is transmitted or fully reflected.

As discussed at the beginning of this section, we measured $N_1 = 0.94 \pm 0.02$ rad $\cdot$ s^{-1} and $N_2 = 0.62 \pm 0.05$ rad $\cdot$ s^{-1}. As a result, we have $N_2/N_1 = 0.66 \pm 0.06$. Due to the fairly large uncertainty on this value, however, we decided to compute numerically the transmission curves for a smooth interface with a weakly viscous correction, leaving the ratio N_2/N_1 as a free parameter that we adjust by ensuring that the position of the transmission peak in this curve corresponds to the data. This adjusted curve is shown in figure 5.8. The resulting fitted value of N_2/N_1 is 0.73, which is within the uncertainty of our experimental estimate for this ratio.

We can now discuss how the experimental data points compare with the theory for a smooth interface and weak viscous effects. The general trend is very similar, with an increased transmission as the frequency is increased, until one reaches a maximum of $T_{v_z} = 2$ at a frequency close to the buoyancy frequency of the lower layer, as expected since the waves then become evanescent in this region. Then, one observes a sharp decrease of the transmission. Above $\omega/N_1 \simeq 0.5$, which is the region of interest with the maximum of transmission, the experimental data points show good agreement with the theoretical curve. In contrast, in the region $0.3 < \omega/N_1 < 0.5$, the data points are below the theoretical prediction. We assume that this trend for low values of ω/N_1 is due to the poor efficiency of the apparatus at these frequencies, because of boundary layer damping effects on the cylinder [19, 33], which are not taken into account in our weakly viscous model. An order of magnitude of these effects gives, at low frequency, a damping in amplitude up to a factor 2, relevant to what is observed.

5.4.2 Transmission of a Confined Incident Wave

We now focus on the confined wave configuration. Figure 5.9 shows the experimental stratification used in this study, with (a) the density and (b) the buoyancy frequency profiles, computed as in the previous section. We use a two-layer stratification: the top layer is from 0 to 17 cm, with $N_1 = 1.17 \pm 0.07$ rad $\cdot$ s^{-1}, and the bottom layer is from 17 to 60 cm, with $N_2 = 0.85 \pm 0.03$ rad $\cdot$ s^{-1}. A dashed line indicates the location of the interface, and a straight line shows the water surface. The buoyancy frequency profile is fitted with a sharp interface curve and a smooth interface curve, with the same distance $L = 17$ cm, and a width $\delta = 3$ cm for the smooth interface. We see an important mixed layer at the surface, which is part of the upper layer and we make sure that N_1 is estimated outside this layer. We compute N_1 in the interval [2; 15] cm and N_2 using the interval [22; 53] cm. Figure 5.9(c) presents an example of a PIV field for the vertical velocity in this experiment. Between the generator, at the surface, and the interface, we can see that the wave field has a smaller vertical wave length than below the interface, consistent with $N_2 < N_1$, as in the previous experiment.

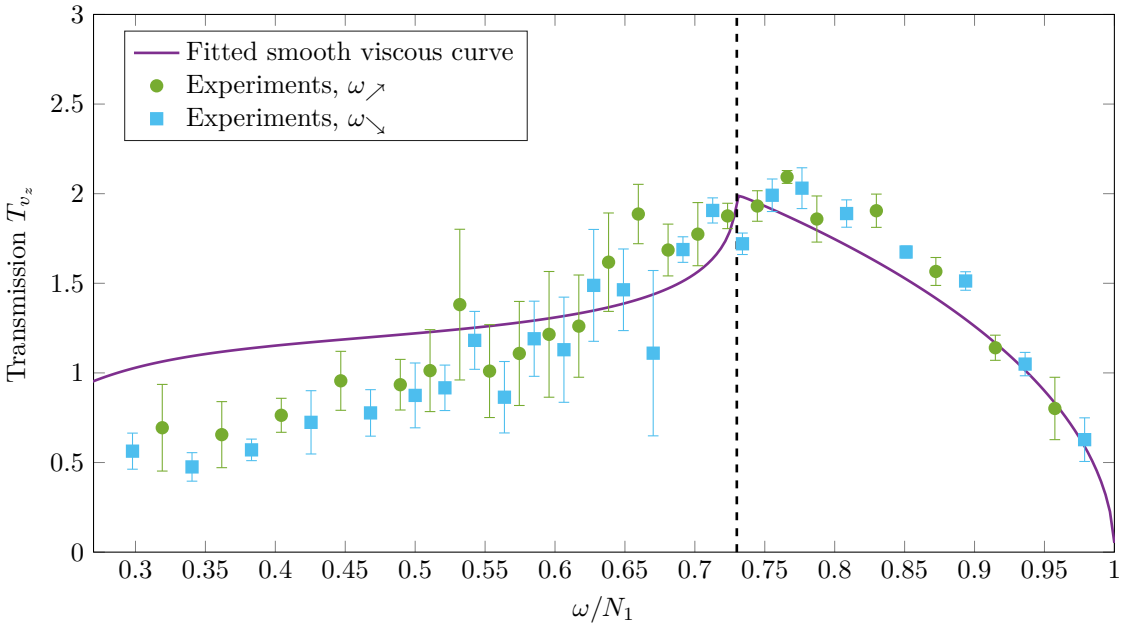

Figure 5.8: Experimental transmission curve. We fit the experimental data with a theoretical curve computed for a smooth interface with viscosity (straight line). The vertical dashed line shows the value $N_2/N_1 = 0.73$ used to fit the data.

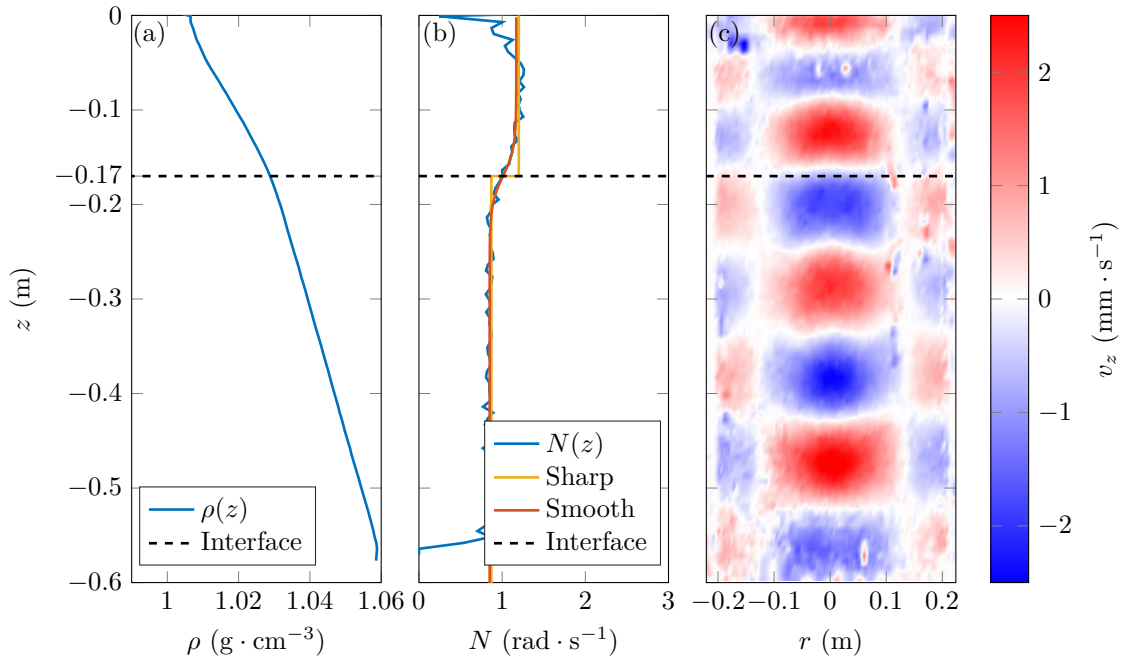

Figure 5.9: From left to right: (a) density profile $\rho(z)$, (b) buoyancy frequency profile $N(z)$ and fits (with $N_1 = 1.17 \pm 0.07$ rad · s^{-1}, $N_2 = 0.85 \pm 0.03$ rad · s^{-1}, $L = 17$ cm, width $\delta = 3$ cm), and (c) example of vertical PIV cross-section of the vertical velocity field ($\omega/N_1 \simeq 0.36$). The generator is located at the top ($z = 0$). The dashed line indicates the interface.

Mode−1 wave fields for 65 values of frequency from $\omega = 0.2$ to $1.09\ \mathrm{rad \cdot s^{-1}}$ are produced. Given the previous results on transmission in a non-resonant case, we assume that the stratification does not change in our experiment and we only perform the measurements by increasing the frequency. We also use short-time excitations of 100 s at 20 min interval each. Amplitudes are measured below the interface in a similar selection process as before, but the position of the interface closer to the generator allows for several back and forth reflections in the upper layer. Measurements are compared to the theoretical generator amplitude (5.25) to compute the transmission coefficient.

Results are presented in figure 5.10. Measurements of the transmission coefficient are plotted as a function of ω/N_1, using the mean value of N_1. As in the previous section, we must also investigate the influence of the different parameters L, δ, N_1, and N_2, on the theoretical transmission curve for a confined incident wave, a smooth interface and weekly viscous effects obtained following the method described in section 5.2.2. The length L contributes to the peak positions in the propagating region $\omega < N_2$. The width of the interface δ has little impact because the interface is relatively sharp. In contrast, the buoyancy frequencies N_1 and N_2 mainly control the shape of the curve, as they change the position of the peaks, their amplitude, as well as the limit between the propagating and evanescent transmissions. Using the C/T probe, we measure $N_1 = 1.17 \pm 0.07\ \mathrm{rad \cdot s^{-1}}$ and $N_2 = 0.85 \pm 0.03\ \mathrm{rad \cdot s^{-1}}$, which gives us a ratio N_2/N_1 going from 0.8 to 0.66. As a result, several theoretical curves for a smooth interface with viscosity, numerically computed, are presented in figure 5.10, one for the central value of N_2/N_1, namely 0.73, and two others for the extreme values of the ratio, 0.66 and 0.8. It shows that although the different theoretical curves always present the same trend, with various peaks, the position and height of the peaks can vary a lot by slightly varying the ratio N_2/N_1.

Experimental data display the same qualitative behaviour as theoretical predictions. For $\omega/N_1 \in [0.17;\ 0.74]$, the transmission coefficient increases non-monotonically with local extrema. As in the previous section, measurements at low frequencies show a smaller transmission than the expected value, also probably due to boundary layer damping effects [19, 33]. The most significant features, however, occur at higher frequencies and are therefore unaffected by this. For $\omega/N_1 > 0.74$ the transmission coefficient is globally decreasing as the waves become evanescent in the lower region. For a given range of frequencies $\omega/N_1 \in [0.77;\ 0.84]$, however, non-linear effects are triggered and no amplitude can be measured as the wave field is no longer described by our model. This area is indicated by a shaded area in figure 5.10 and corresponds to the expected resonant interference peak of the theoretical curves. Snapshot examples of the vertical velocity field are given in figure 5.11 for three different situations after 34 periods of excitation: figure 5.11(a) shows propagating waves in both layers at $\omega/N_1 = 0.7$, while in figure 5.11(b) and 5.11(c) waves are evanescent in the lower layer at $\omega/N_1 = 0.8$ and $\omega/N_1 = 0.9$, respectively. In contrast to the images presented in figures 5.11(a) and 5.11(c), the image presented in figure 5.11(b) shows small-scale disturbances of the wave field resulting from non-linear effects due to constructive interference in the upper layer, representing the typical behaviour observed within the hatched region identified in figure 5.10.

5.5 Applications to Ocean

In this section, we present applications of our study to real oceanic stratifications by first using the two-layer model previously developped, and then extending the boundary value problem solving tool to more complex non-linear stratifications.

5.5.1 An Ideal Bi-Linear Stratification in the Arctic

An interesting application of our confined layer studies is to relate our findings to a scenario that has a strong upper ocean stratification overlying a weaker deep ocean stratification. Figure 5.12 presents an example of density and buoyancy frequency profiles taken at 159°57.111′ W, 73°32.439′ N during the Stratified Ocean Dynamics of the Arctic (SODA) research cruise, on the R/V Sikuliaq, in September 2018. A very simple model can be used to describe this stratification at first order: a Melting Layer (ML) at the surface issued from ice melting with a strong density gradient, and a bi-linear stratification with two buoyancy frequencies N_1 and N_2 below.

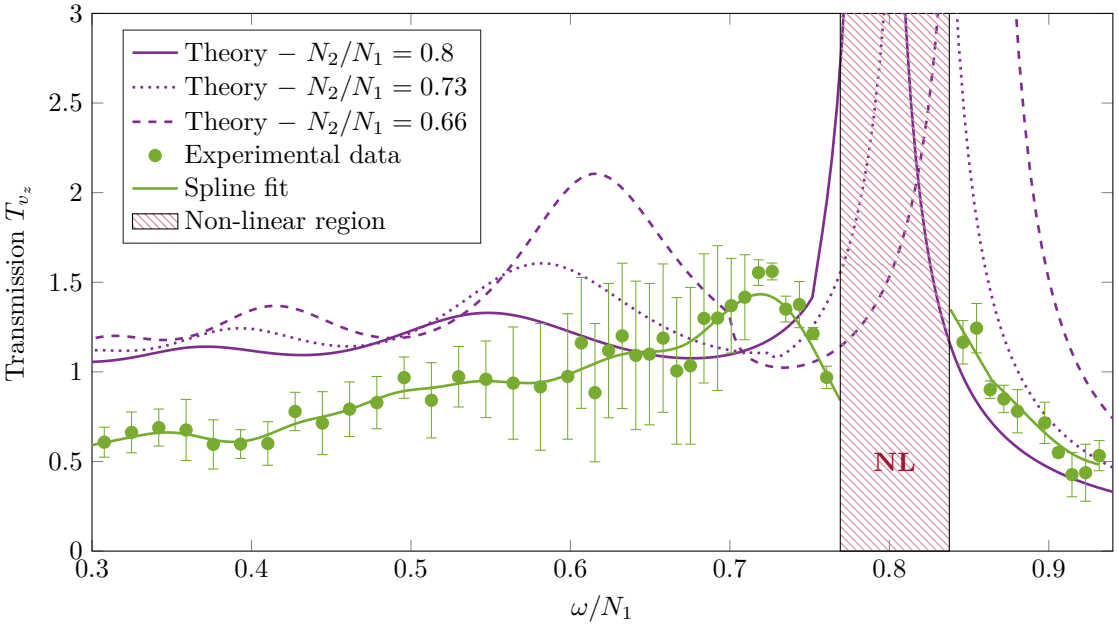

Figure 5.10: Experimental transmission curve for a forced upper layer. Theoretical curves computed for the maximal, mean, and minimal values of N_2/N_1 are plotted. A spline fit (dashed green line) is added to guide the eye on the experimental curve.

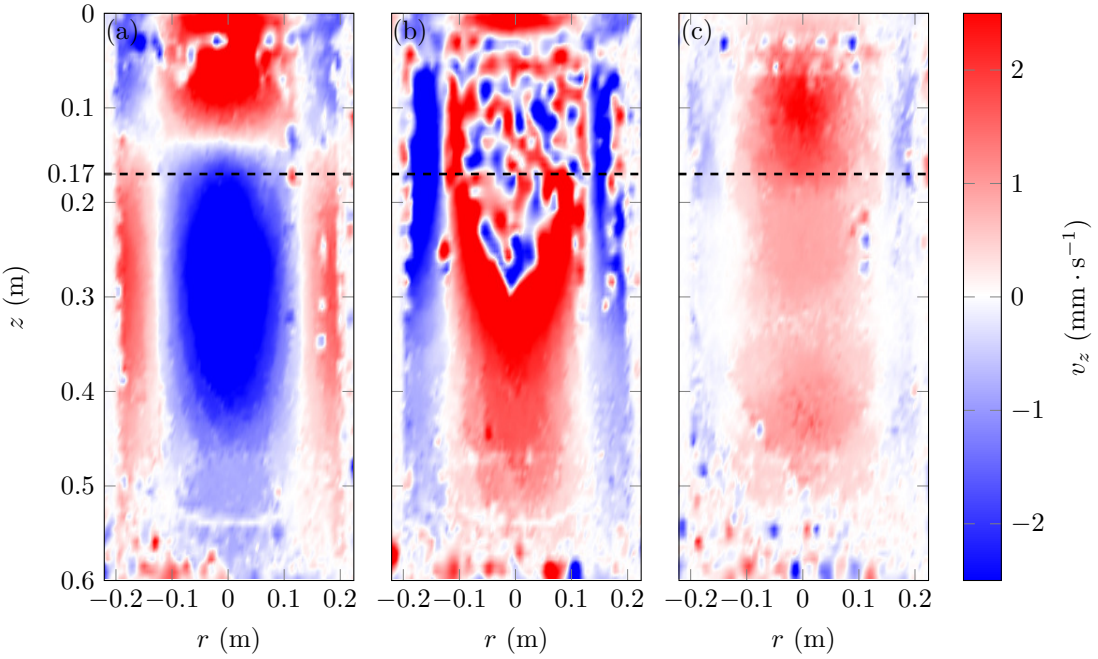

Figure 5.11: Snapshots of the vertical velocity field in three different cases: (a) $\omega < N_2 < N_1$ and $\omega/N_1 = 0.7$; (b) $N_2 < \omega < N_1$ and $\omega/N_1 = 0.7$; and (c) $N_2 < \omega < N_1$ and $\omega/N_1 = 0.8$. All pictures are taken at 34 periods of excitation.

Using equation (5.10), such a profile can be fitted with $N_1 \simeq 0.011$ rad $\cdot$ s^{-1} in the upper layer, $N_2 \simeq 0.001$ rad $\cdot$ s^{-1} in the lower layer, $L \simeq 250$ m from the Melting Layer (ML) to the center of the Interface Region (IR) which has a width $\delta \simeq 150$ m. Note that such parameters cannot be obtained in our experiments, due to its size and to the range of buoyancy frequencies we are able to produce (here, N_1 and N_2 are of the same order of magnitude), but the physics involved remains the same.

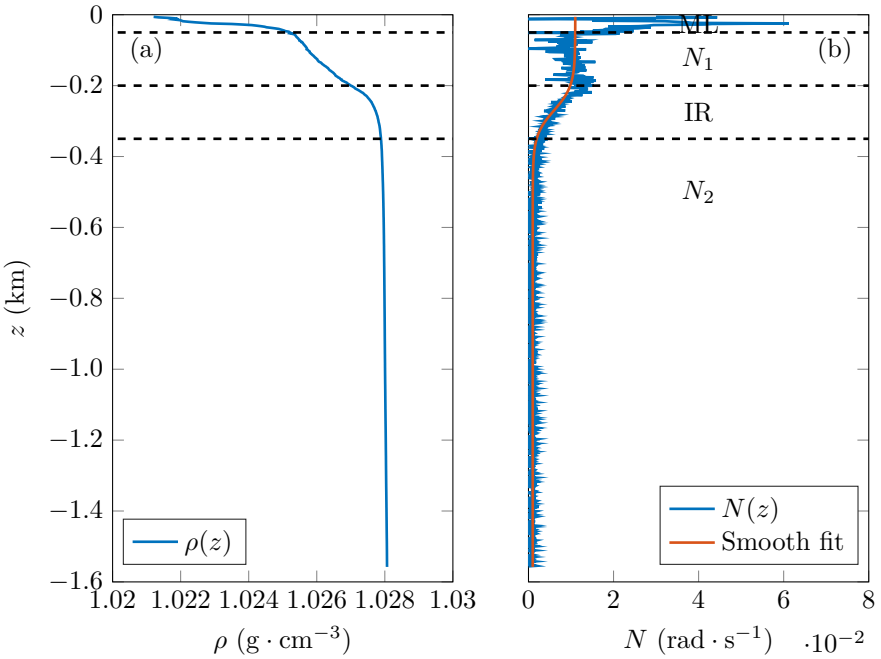

Figure 5.12: Example of (a) density profile and (b) buoyancy profile, from in-situ measurements. Different layers can be identified between dashed lines, from top to bottom: Melting Layer (ML), N_1 linear layer (N_1), Interface Region (IR), and N_2 linear layer (N_2).

As shown by our study, constructive interference effects may appear and produce high transmission coefficient value for confined internal waves. These effects, however, arise only when the vertical wave length $2\pi/m_1$ is larger than the interface width [138]. Upon the contrary, the interface acts as a smooth density change for the wave and internal waves pass through relatively unaffected. Re-writing equation (5.5) in terms of the radial wave length $2\pi/l$ as

$$\frac{2\pi}{m_1} = \frac{2\pi}{l}\left(\frac{\omega^2 - f^2}{N_1^2 - \omega^2}\right)^{1/2}, \tag{5.27}$$

we explore the range of parameters $(\omega;\ 2\pi/l)$ by plotting the quantity $\log(2\pi/m_1)$ for propagating waves in the upper layer, which means $f < \omega < N_1$, in figure 5.13. The Coriolis frequency is set to be $f = 1.24 \cdot 10^{-4}$ rad $\cdot$ s^{-1}, a typical value in this region [56].

Near-inertial wave generation, with frequencies close to f are found to be easily excited in the Arctic Ocean [56], with a small vertical wave length as illustrated in figure 5.13. In this configuration, the factor $\omega^2 - f^2$ is of the order of f^2 (10^{-8} rad$^2 \cdot$ s^{-2}). Since $N_1 \gg \omega$, the factor $N_1^2 - \omega^2$ is of the order of N_1^2 (10^{-4} rad$^2 \cdot$ s^{-2}), yielding $l/m_1 \simeq 10^{-2}$. Hence, to obtain vertical wave lengths of the order of 100 m, the radial wave length has to be of the order of 10 km, which can be produced by storms of large extent. Higher frequency waves can also be produced [20, 53, 184], with a frequency of the same order of magnitude than the buoyancy frequency N_2. Hence, the term $\omega^2 - f^2$ is of the order of N_2^2 (10^{-6} rad$^2 \cdot$ s^{-2}), yielding $l/m_1 \simeq 10^{-1}$. As a result, resonant interference waves with vertical wave length of the order of 100 m can have small radial wave length (of the order of 1 km).

Following the approach of Ghaemsaidi *et al.* [86], we present in figure 5.14 numerical computation of the transmission coefficient for the Arctic stratification (figure 5.12) for three different

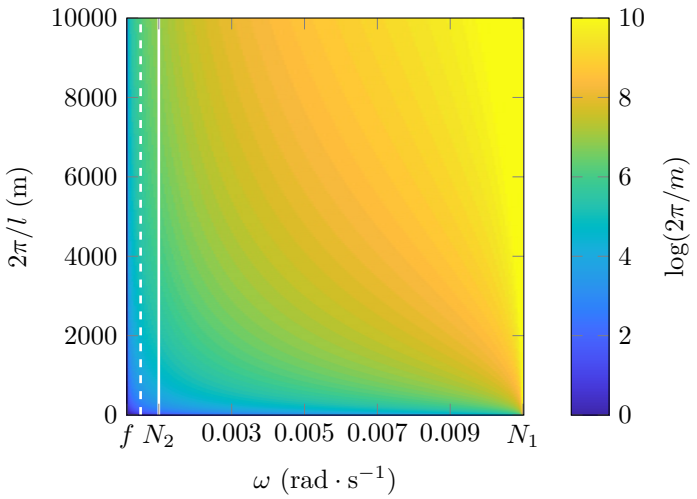

Figure 5.13: Logarithmic colormap of the vertical wave length in the upper layer (with $N_1 = 0.011$ rad · s^{-1}) as a function of the frequency ω (from f to N_1) and the radial wave length $2\pi/l$. The white solid line represents $\omega = N_2$, and the white dashed line represents $\omega = N_2/2$.

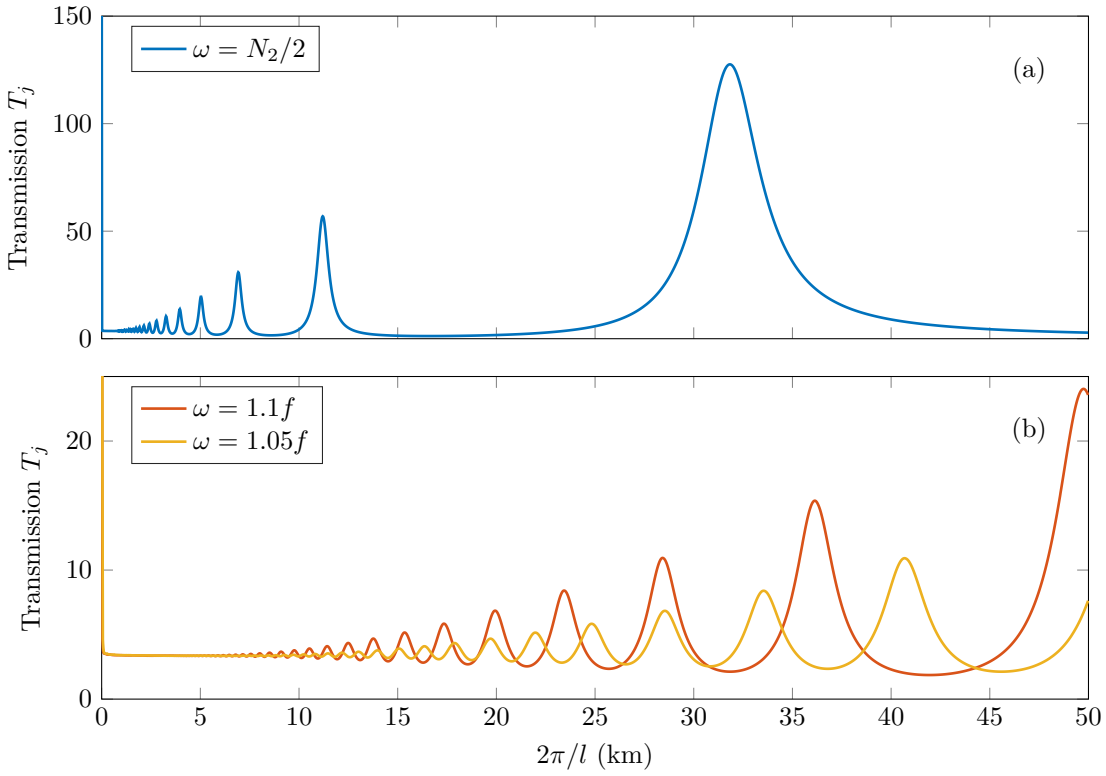

Figure 5.14: Numerical computation of the transmission coefficient as a function of the radial wave length, for three different frequencies $1.05f$, $1.1f$, and $N_2/2$, after normalisation by the incoming energy at the surface.

frequencies, two of them being near-inertial at $\omega = 1.05f$ and $\omega = 1.1f$, and the third one corresponding to a higher frequency with $\omega = N_2/2$. A resonant cavity effect, in the sense of constructive interference with sequential peaks of high transmission rate of internal waves, occurs for $\omega = N_2/2$, for both small or large radial wave lengths. For near-inertial waves, however, the transmission coefficient is almost constant until the vertical wave length is larger than 10 km, meaning that this enhancement is only relevant for large wave length storms. In both scenarios the enhancement can be several times, even over an order of magnitude.

5.5.2 In-situ Measurements: CTD and PDS-CPIES

In late summers 2017 and 2018, Current-and-Pressure recording Inverted Echo Sounders (CPIES) with embedded Popup Data Shuttles (PDS) were deployed during research campaigns in the Arctic on the R/V Aaron and R/V Sikuliaq (see Jeon *et al.* [105]).

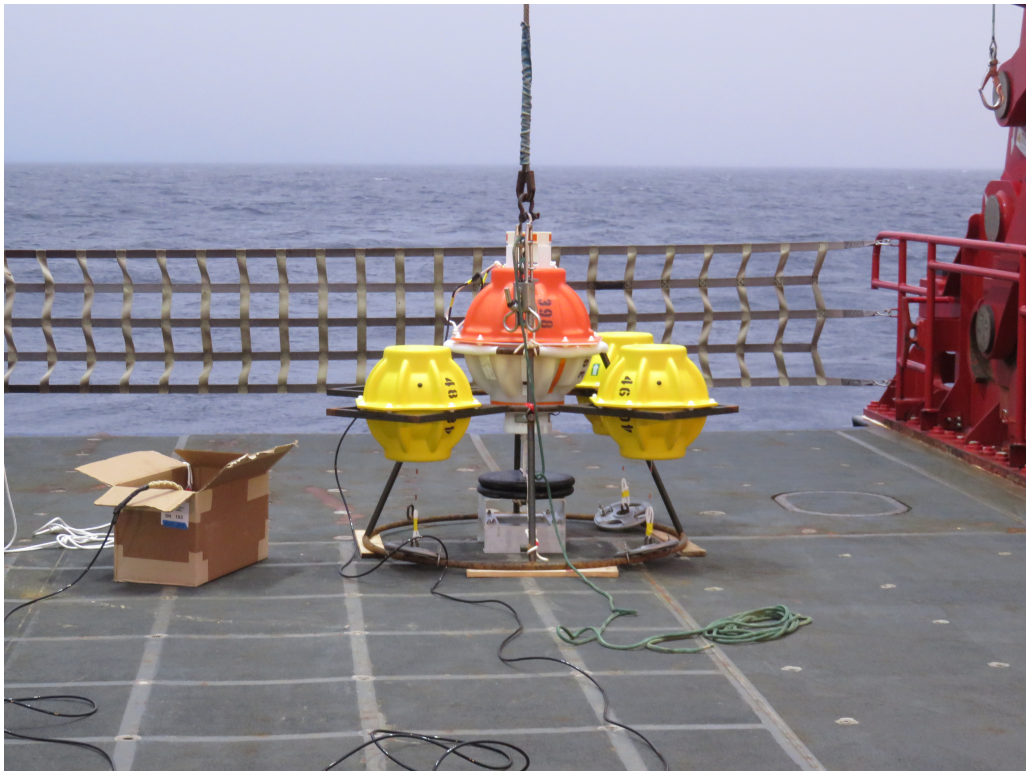

Figure 5.15: Photography of a PDS-CPIES ready to be deployed, on the R/V Sikuliaq rear deck.

CPIES are moorings dropped on the oceanic floor with a scheduled date of release and recovery, about two years after deployment. They record temperature, salinity, pressure, sea-surface activity (echo sounder), and horizontal currents (velocimeter). A PDS-CPIES is an updated version of the CPIES equipped with four data shuttles (PDS) used to retrieve data at scheduled dates earlier than the usual recovery date of the main CPIES mooring (for furter details on the PDS-CPIES measurements, see [105]). A photography of the device is presented in figure 5.15. We refer to PDS-CPIES using the acronym AES (Arctic Echo Sounder).

A total of six AES have been deployed in the Arctic in 2017 and 2018, in the Northwind Abyssal Plain (AES 1 through 3) and in the South-West edge of the Canada Basin (AES 4 through 6), as shown in figure 5.16. The AES are located near rough topographies in order to investigate near-inertial wave (NIW) generation in the Arctic Ocean. At deployment locations, Conductivity-Temperature-Depth (CTD) casts were performed to know the stratification properties in the vicinity of the mooring.

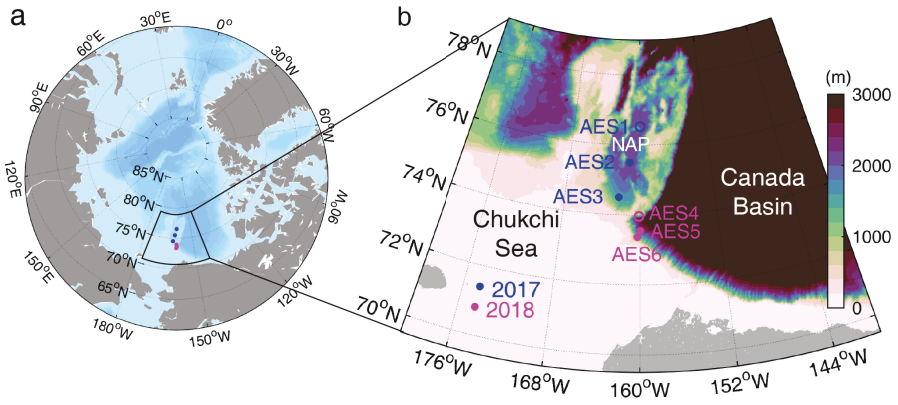

Figure 5.16: Arctic PDS-CPIES with (a) large-scale map, and (b) close look at the Chukchi Sea and Canada Basin with AES deployment locations. From [105].

5.5.3 PDS-CPIES and Near-Inertial Waves Transmission

Internal wave signals have been recorded by AES with different amplitudes [105]. Through a power-spectrum analysis, their frequency can be estimated and are presented for AES 3, 5, and 6, in table 5.1 in terms of the local Coriolis frequency. As explained in chapter 3, using the f-plane approximation, the local Coriolis frequency f is a function of the latitude and this variability must be taken into account.

AES #	3	5	6
Local f ($\times 10^{-4}$ rad $\cdot$ s^{-1})	1.405	1.399	1.397
NIW frequency	$1.02f$	$1.03f$	$1.06f$

Table 5.1: Near-inertial wave frequency recorded at location of AES 3, 5, and 6, in terms of the local Coriolis frequency.

Not only the Coriolis frequency may differ betwen two moorings, but also the density stratification and the buoyancy frequency N. In the previous section, we explored the capability of our model to describe the Arctic stratification as a two-layer system, independently of of small features. The bottom part of it, below 400 m depth, was approximated to be at constant $N_2 \simeq 0.001$ rad $\cdot$ s^{-1}, though many small features exist and can impact wave transmission, motivating a separate study. Figure 5.17 presents density (left pannel) and buoyancy (right pannel) profiles at AES 3, 5, and 6. Though mostly similar, these profiles shows small differences in terms of vertical extent (AES 6 stops sooner) and fluctuations.

The boundary value problem solver developed for bi-linear stratification has been improved to investigate a wide variety of non-linear stratification, so that a smoothed profile of the stratifications in figure 5.17 can be used directly in the code. This process gives us, for given Coriolis and NIW frequencies (table 5.1), a numerical estimate of the transmission coefficient for radial velocity between 400 m depth and the bottom of the water column. Our results, presented in figure 5.18, show a weak variability between the three AES, and a resonant behaviour that may be caused by small scale layered patterns in the stratification. Such a study is a first step in the understanding of wave transmission in the Arctic Ocean, and will, in future work, be compared to actual AES measurements of internal wave amplitudes and estimates of forcing from atmospheric activity using, for example, a slab model [58].

5.6 Conclusions and Discussion

We have presented an experimental study of the propagation of axisymmetric internal wave modes across a buoyancy interface in stratified non-rotating flows. To support our laboratory experiments,

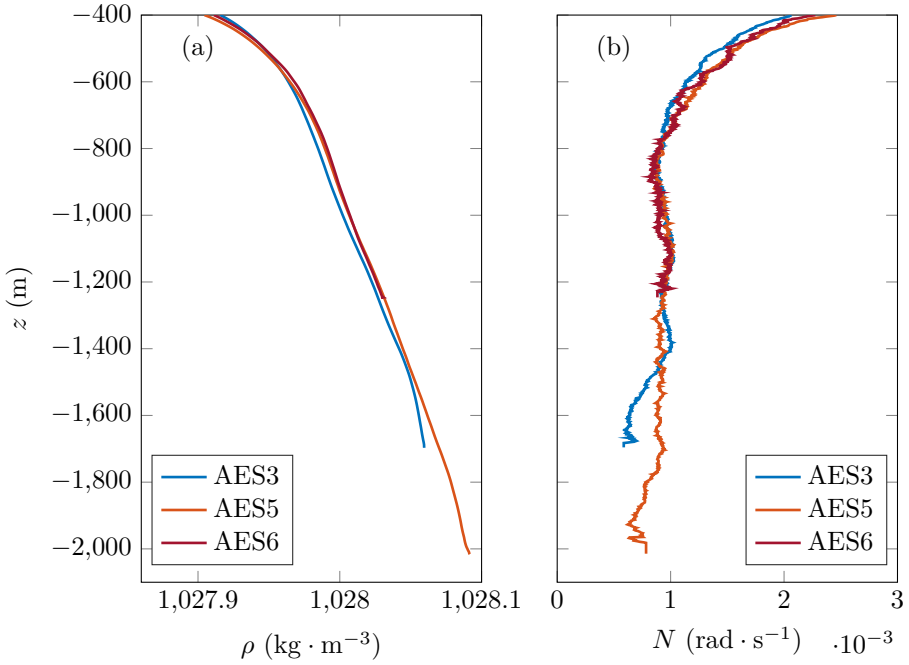

Figure 5.17: Stratifications measured at AES3, AES5, and AES6 locations, with (a) density profiles and (b) buoyancy frequency profiles. The top part of the stratifications is not shown.

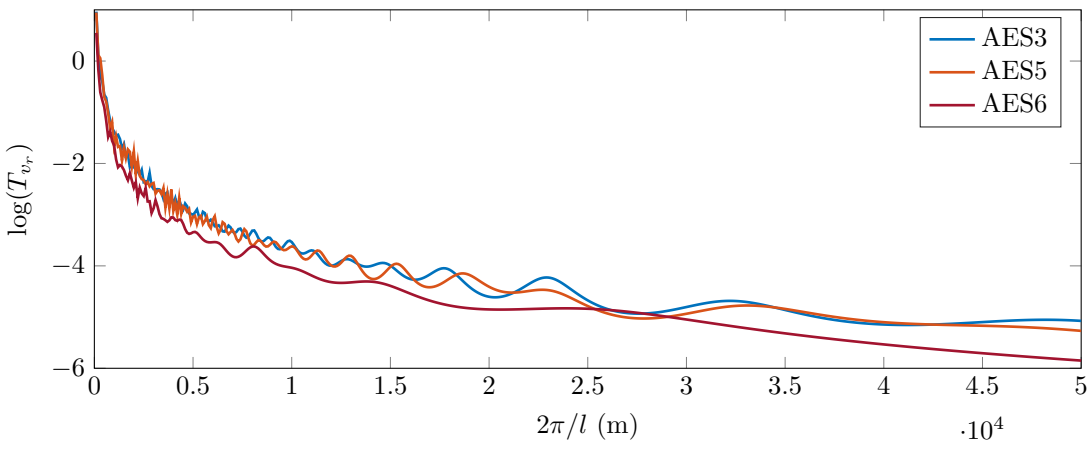

Figure 5.18: Logarithm of the transmission coefficient in radial (horizontal) velocity T_{v_r} as a function of the radial wave length $\lambda = 2\pi/l$ for near inertial waves ($\omega_3 = 1.02f_3$, $\omega_5 = 1.03f_5$, and $\omega_6 = 1.05f_6$). The transmission coefficient is computed using the real stratification measured at AES3, AES5, and AES6 locations, as shown in figure 5.17.

we develop a theoretical framework for freely incoming waves and for confined waves, as they represent qualitatively two different scenarios that have relevance to the atmosphere and ocean, respectively.

In this study we find that, despite the additional geometric complexity, with associated features such as inhomogeneous spatial distribution of energy flux, results for plane waves can be generalised to axisymmetric wave fields. For a free incident wave, we show that the maximum of transmission (shown by a maximum of vertical displacement) occurs when the frequency of the wave is equal to the buoyancy frequency of the lower layer. For a confined incident wave, we identify the existence of a constructive interference effect in the upper layer, leading to larger transmission coefficients and potentially non-linear effects. For both scenarios, theory and experiments show excellent qualitative, and good quantitative, agreement, especially within the range of frequencies containing the resonant interference peaks and the enhanced transmission.

This kind of study can help to shed light on in-situ measurements of internal waves signals, for example near-inertial waves in strongly stratified regions such as the Arctic Ocean. Different scenarios can be investigated, such as high frequency internal waves generated by storms at the ocean surface and travelling downwards, or near-inertial waves produced by tides and topography in the deep ocean and travelling upwards. In particular, this latter type of waves can therefore be enhanced through transmission processes and lead to strong signals though the generation process might be of very low amplitude.

Via a similar mechanism that small-extent staircase stratifications can create selective transmission of internal waves [86], we show that surface forced non-linear stratifications can potentially give rise to enhanced transmission due to resonant interference effect of internal waves to the deep ocean. Nevertheless, for small scale waves of wave length below 10 km, these effects seem to be limited to high frequencies, while no effect is observed for near-inertial waves. For the latter type of waves, enhanced transmission can however also be observed in the case of very large size disturbances of wave length above 20 km. We notice that the process involves higher amplification factors as frequency increases, while becoming more selective in terms of wave length.

These studies could be extended to more complex cases with various layers of different buoyancy frequencies, as long as the thickness of the interfaces remains small compared to the vertical wave length [158, 86]. For a given wave, generated by a storm and observed near the ocean surface, it could help predict the amount of energy that will be carried down towards the deep ocean, as well as the ranges of wave lengths more likely to be transmitted. Such a selection process would lead to a change in the wave features as it travels downwards. Enhanced amplitudes generated by such constructive interference behaviours can also trigger non-linear effects [33] producing smaller scale waves. The mechanisms involved are still to be explained for axisymmetric geometry, and could lead to mixing events, changing the stratification, with subsequent feed-back effects on the wave propagation.

CHAPTER 6

Internal Wave tunneling

La realidad no suele coincidir con las previsiones; con lógica perversa, prever un detalle circunstancial es impedir que este suceda.
Jorge Borges, FICCIONES.

In the previous chapter, we derived the theory of axisymmetric internal wave transmission accross buoyancy interfaces, and showed experimental evidence of this phenomenon. In oceanic stratifications, however, constant density layers can exist, especially near the surface in the wind-mixed layer, in which waves are evanescent. Such layers can be either at the very bottom of the stratification in the deep ocean [105], or inserted in the stratification such as, for example, staircase stratifications observed in the Arctic [86]. These layers may have non-zero buoyancy frequency, but the stratification can be so weak that the wave field becomes evanescent.

For non-rotating fluids, unstratified regions should be, in theory, wave-free, and an incoming wave should be damped quickly. Nevertheless, due to the decaying amplitude of the exponential term, the waves are actually damped over a given length scale and still penetrate the layer. As a result, if the layer is thin enough, a downward propagating incoming wave field arriving from the top can still be seen below, and may propagate through with a lower amplitude: this phenomenon is called *tunnel effect* and its counterpart in quantum mechanics has been widely studied.[1]

In this chapter, we expand previous results from Sutherland and Yewchuk [224] who first saw evidence of internal wave tunneling in laboratory experiments, with Cartesian plane waves, as detailed in section 6.1. We then derive the theory of axisymmetric internal wave tunneling in section 6.2 and show experimental realisations of this phenomenon in section 6.3. Section 6.4 presents our conclusions and discussion.

Results from this chapter are in preparation for *Physical Review Fluids* [37].

6.1 Evidence of Cartesian Internal Wave tunneling

If we consider a density stratified fluid without rotation, internal waves can only be excited if their frequency ω is smaller than the buoyancy frequency N: according to the dispersion relation, waves are propagating below, and evanescent above. The experiments on wave transmission presented in chapter 5, however, show that the transmission coefficient measured below the interface in the evanescent region is non-zero because we can still measure an amplitude, which means that the

[1] Although it is often associated to quantum mechanics, the tunnel effect is not confined to this application. It is, in fact, a property of wave fields and can therefore be applied to various problems in physics.

wave velocity is not zero and that part of the wave field can penetrate. Due to evanescent damping, it quickly dissipates and, as the dispersion relation writes

$$m^2 = l^2 \left(\frac{N^2}{\omega^2} - 1 \right), \tag{6.1}$$

with m and l the vertical and horizontal wave numbers, the characteristic length for this evanescent dissipation can be estimated to be

$$L_d = \frac{1}{m} = \frac{1}{l} \frac{\omega}{\sqrt{\omega^2 - N^2}}, \tag{6.2}$$

when $\omega > N$. In chapter 5, we considered a semi-infinite bottom layer. Measurements at a distance from the interface larger than L_d would then show a wave amplitude that is almost zero, and waves no longer exist. Would the stratification change further below, it would remain unperturbed. But in the case of a thin layer of vertical extension smaller than L_d in which $\omega > N$, the amplitude of the wave field is not zero at the bottom boundary of this layer. In the bottom layer, the problem can be formulated as if the non-zero evanescent wave field acts as a forcing located at the top, of same frequency and wave lengths, but of reduced amplitude. Such a forcing may repeat through multiple layers in staircase stratification [45, 222]. Performing experiments in 2D geometry with a vertically oscillating cylinder in a salt-stratified fluid, Sutherland and Yewchuk [224] have shown evidence that, in agreement with theoretical and numerical predictions, downward propagating wave beams can tunnel through evanescent layers.

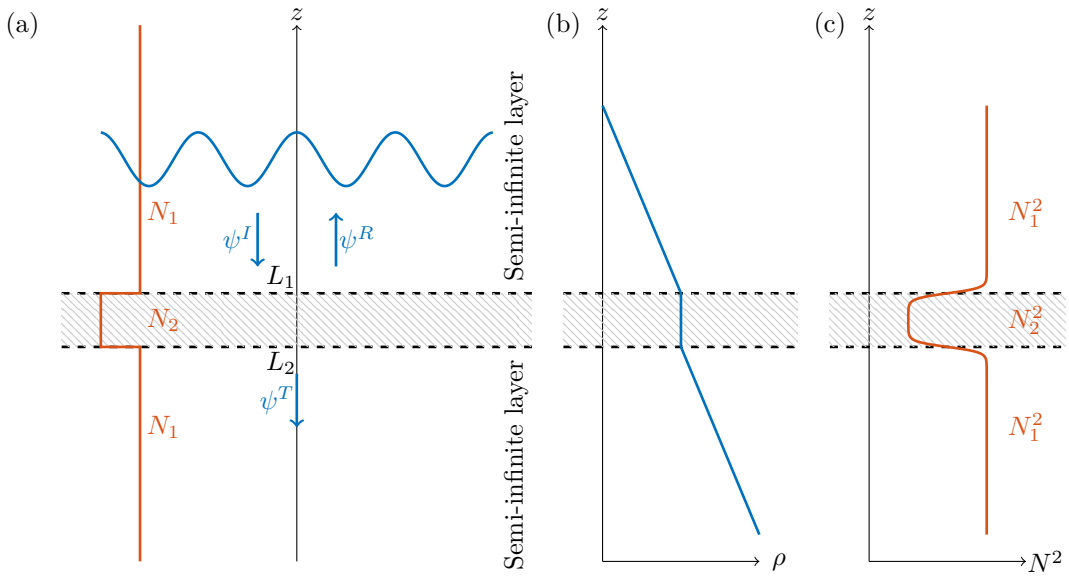

Figure 6.1: tunneling of a horizontal cosine mode across a layer of constant density, represented by the hatched region between L_1 and L_2: (a) schematic of the phenomenon, where the blue pattern represents a cosine shaped wave field, with a free incident wave ψ^I reaching the interface, leading to a reflected wave ψ^R and a transmitted wave ψ^T; (b) density profile; (c) buoyancy profile modeled using two hyperbolic tangents.

A schematic of the phenomenon is presented in figure 6.1(a), where a 2D cosine horizontal mode is propagating downwards, reaching the layer of constant density (hatched region), to be reflected and transmitted. Idealised density and buoyancy profiles are shown in figures 6.1(b) and 6.1(c). A corresponding two-dimensional inviscid DNS showing internal wave tunneling is presented in figure 6.2. As before, the DNS were run using Dedalus in a horizontal SinCos basis and vertical Chebyshev basis, with a 128×128 nodes resolution. A sinusoidal forcing is applied at the top boundary, corresponding to a mode 1 in figure 6.2(left) and to a mode 2 in figure 6.2(right). We set the Coriolis frequency $f = 0$, and we choose the buoyancy frequency profile to be constituted

of three layers

$$N = \begin{cases} N_1 = 0.8 \text{ rad} \cdot \text{s}^{-1} & \text{for } z \in [-60;\ -30] \cup [-30;\ 0], \\ N_2 = 0.1 \text{ rad} \cdot \text{s}^{-1} & \text{for } z \in [-30;\ -20]. \end{cases} \tag{6.3}$$

For numerical purposes and to take into account the finite width of the interfaces, we choose to use a sum of two hyperbolic tangents to model the stratification. The forcing frequency is set at $\omega/N_1 = 0.75$ and, as a consequence, $\omega/N_2 = 6$. In both figures, the dashed lines identify the limits of the domain with $N = N_2$ where waves are evanescent. Above and below, in the regions where $N = N_1$, waves are propagating. In these two DNS, the mode develops in the top region and propagates downwards until it reaches the first interface and becomes evanescent. Then, accordingly, we can see a very clear decaying amplitude from the boundary at $z = -20$ cm to the boundary at $z = -60$ cm. Below, the wave can propagate downwards again and its amplitude remains constant, as expected for inviscid flows. In the three layers, the horizontal structure is preserved (same nodes), but the vertical structure is not. As described by Sutherland and Yewchuk [224], the waves are not stopped at the top interface but go through the evanescent layer until they reach the bottom propagating region, in which their original structure is re-established at a lower amplitude.

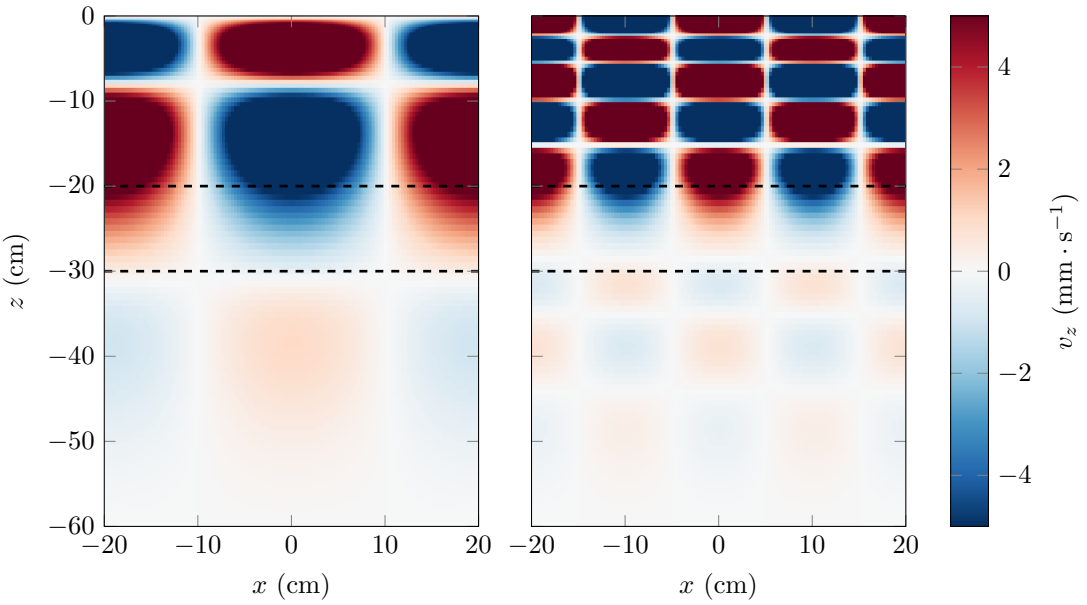

Figure 6.2: Snapshots of vertical velocity fields in a DNS of 2D Cartesian modes run using Dedalus. Left: mode 1 forcing. Right: mode 2 forcing. The dashed lines show the interfaces between N_1 for $z \in [-60;\ -30] \cup [-30;\ 0]$ and N_2 for $z \in [-30;\ -20]$.

In the next sections, we will extend these results analytically (section 6.2) and experimentally (section 6.3) to the case of axisymmetric waves.

6.2 tunneling Effect for Axisymmetric Waves

6.2.1 Governing Equations

As previously discussed in chapters 1, 4, and 5, the linear differential equation for internal waves, in a rotating density stratified fluid, writes in axisymmetric coordinates

$$\frac{\partial^2}{\partial t^2}\left(\frac{\partial^2 \psi}{\partial z^2} + \frac{\partial}{\partial r}\left(\frac{1}{r}\frac{\partial (r\psi)}{\partial r}\right)\right) = -f^2 \frac{\partial^2 \psi}{\partial z^2} - N^2 \frac{\partial}{\partial r}\left(\frac{1}{r}\frac{\partial (r\psi)}{\partial r}\right), \tag{6.4}$$

where ψ is the stream function, f the Coriolis frequency, and N the buoyancy frequency which is assumed to be a function of z. We consider, in this section, that N is constant by steps. Over one of these sections, the solution of equation (6.1) writes

$$\psi(r, z, t) = \psi_0 J_1(lr) e^{i(mz - \omega t)}, \tag{6.5}$$

with

$$m^2 = l^2 \left(\frac{\omega^2 - N^2}{f^2 - \omega^2} \right). \tag{6.6}$$

As previously mentioned, in the case where $f < N$, the dispersion relation (6.3) describes two kinds of waves: either $\omega \in [f;\ N]$ and the waves are propagating, or $\omega \notin [f;\ N]$ and the waves are evanescent. A similar result is obtained in the case $f > N$. From now, we will set $f = 0$ and only consider non-rotating fluids, but our results naturally extend to the case $f \neq 0$.

6.2.2 Three-Layered Problem

We consider the following density profile, in which the buoyancy frequency N is function of depth

$$N^2(z) = N_0^2 \left[\tanh\left(\frac{z - L_1}{\delta} \right) + \tanh\left(\frac{L_2 - z}{\delta} \right) \right] + N_2^2, \tag{6.7}$$

where N_0 and N_2 are reference buoyancy frequencies, L_1 and L_2 are (positive) locations of interfaces, and δ is a small length scale corresponding to the width of the interface. Such a profile is constituted of three layers, labeled I, II, and III, from top to bottom: a stratified layer at $N = N_1 \equiv \sqrt{N_0^2 + N_2^2}$ for $z > -L_1$, a weakly stratified layer at $N = N_2$ for $z \in [-L_2;\ -L_1]$ of vertical extension $\Delta L = L_2 - L_1$, and another stratified layer at $N = N_1$ for $z < -L_2$. For theoretical convenience, although it may not be true in the experiments, we consider that the two stratified layers have the same buoyancy frequency N_0 and that the interfaces have the same width δ. Note that the additional constant term N_2 could also be set to zero this profile to model zero buoyancy frequency in the central region.

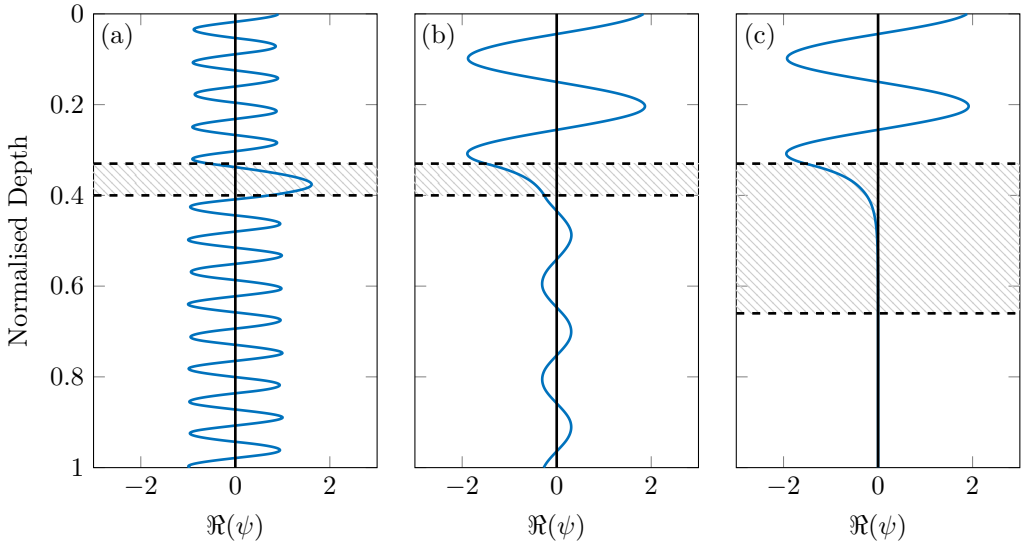

Figure 6.3: Real part of the streamfunction obtained by solving the uni-dimensional boundary value problem derived from equation (6.9) in a three-layered stratification, with (a) $\omega < N_2 < N_1$ and (b) and (c) $N_2 < \omega < N_1$. The dashed lines indicate the interfaces between the different layers, and the hatched region the evanescent layer. Total depth is normalised to be 1.

Solutions of the wave equation (6.4) can be found by a separation of variables method (see chapter 4) and we write them using a function ϕ that contains the vertical dependence in z as

$$\psi(r, z, t) = \phi(z) J_1(lr) e^{i\omega t}. \tag{6.8}$$

As stated in chapter 5, ϕ satisfies the following second order differential equation that involves a z-dependent parameter

$$\phi'' + \gamma(z)\phi = 0 \qquad \text{with} \qquad \gamma(z) = l^2\left(\frac{N^2(z)}{\omega^2} - 1\right). \tag{6.9}$$

In a model case of sharp interfaces between $N = N_1$ and $N = N_2$ regions, this equation can be solved independently in each layers and then reconnected thanks to continuity relations (see chapter 5 and [65, 224]). The study of smooth interfaces could be done using numerical boundary value problem solvers.

As two values of buoyancy frequency are involved in the problem, the solution will change depending on the value of ω. As summarised in table 6.1, if $\omega < N_2 < N_1$, the wave is always propagating, whereas if $N_2 < N_1 < \omega$ the wave is always evanescent and cannot even be excited by the generator. An illustration of the first two cases is shown in figure 6.3, with the real part of the stream function computed by finding the numerical solution of a boundary value problem based on equation (6.9), using the method described in chapter 5. In the three regions delimited by the dashed lines, the buoyancy frequencies are $N_1 = 1$ rad $\cdot$ s^{-1} in the top and bottom layers, and $N_2 = 0.6$ rad $\cdot$ s^{-1} in the middle layer. In figure 6.3(a), the wave frequency $\omega = 0.4$ rad $\cdot$ s^{-1} leads to propagating waves in both regions. On the contrary, in figure 6.3(b) and (c), $\omega = 0.8$ rad $\cdot$ s^{-1} and the wave is evanescent in the intermediate layer. In this inviscid model, the transmitted amplitude is not affected in the first situation in figure 6.3(a), but a significant decay is observed after the wave tunnels in figure 6.3(b). In figure 6.3(c), the evanescent layer is too large for the wave to go through, and no amplitude is detected below. Note that these results are not specific to the axisymmetric configuration and also apply to the Cartesian case.

Frequency ω	Layer I	Layer II	Layer III
$\omega < N_2 < N_1$	Propagating	Propagating	Propagating
$N_2 < \omega < N_1$	Propagating	Evanescent	Propagating
$N_2 < N_1 < \omega$	Evanescent	Evanescent	Evanescent

Table 6.1: Different kinds of solutions for the three-layered problem, depending on the value of ω compared to the buoyancy frequencies N_1 and N_2.

We now focus on the intermediary case, $N_2 < \omega < N_1$, for which the wave field is propagating in both the top and the bottom layer, but evanescent in between.

Solution in the Top Layer

The top layer of buoyancy frequency N_1, from $z = 0$ to $z = -L_1$, corresponds to the forcing layer: the wave generator, on top, excites the wave field as described in chapters 2, 4, and 5. In the case of propagating wave fields in a semi-infinite layer, forced at frequency $\omega < N_1$, the axisymmetric stream function ψ_{I} is described by a Bessel function from equation (6.8) in the case of a mode, and by decomposition over the basis of Bessel functions in the case of a conical wave field.

As detailed in chapter 5, the interface at depth L_1 produces a transmitted wave field, which is discussed later, as well as a reflected wave field. The complete solution ψ_{I} in the top layer, is therefore a sum of a downward propagating incoming wave and of an upward propagating reflected wave, so that

$$\psi_{\mathrm{I}}(r,z,t) = \psi_{\mathrm{I}}^I J_1(l_{\mathrm{I}}^I r)\exp(i(\omega_{\mathrm{I}}^I t - m_{\mathrm{I}}^I z)) + \psi_{\mathrm{I}}^R J_1(l_{\mathrm{I}}^R r)\exp(i(\omega_{\mathrm{I}}^R t - m_{\mathrm{I}}^R z)), \tag{6.10}$$

where l_{I}^I and m_{I}^I are the radial and vertical wave numbers of the incoming wave, $\omega_{\mathrm{I}}^I = \omega$ its frequency, ψ_{I}^I its amplitude, and l_{I}^R, m_{I}^R, ω_{I}^R, and ψ_{I}^R the same quantities for the reflected wave. Results from the previous chapter allow us to drop the I and R exponents for all quantities except the amplitudes. Note that in the case of a confined incident wave, the model will be different as shown by the study presented in chapter 5 for transmission of internal waves across a buoyancy frequency interface.

Solution in the Transient Layer

The wave transmitted from the top layer to the transient layer is assumed to be evanescent. Introducing the dissipative length scale L_d (see equation (6.2)), the solution ψ_{II} writes

$$\psi_{\mathrm{II}}(r,z,t) = \psi^0_{\mathrm{II}} J_1(l_{\mathrm{II}} r)\exp(i\omega_{\mathrm{II}} t)e^{z/L_d}, \tag{6.11}$$

where l_{II} is the radial wave number, ω_{II} the frequency, and ψ^0_{II} is defined as the transmitted amplitude from the top layer (see chapter 5).

It is important to discuss the effect of the width of this layer, called L_{II}. As explained in section 6.1, if $L_d \ll L_{\mathrm{II}}$, then the wave will be entirely dissipated when it reaches the interface between regions II and III, and there would not be tunneling effect. In the opposite situation, the wave will reach the interface with a decreased amplitude and be transmitted to region III, but also be reflected exactly as occurs in the top layer. This reflected wave, however, is assumed to be of sufficiently small amplitude to be neglected in our calculation.

Solution in the Bottom Layer

In the bottom layer we consider, in this model, a semi-infinite domain so that the wave can propagate freely from a forcing at the interface. There is no returning wave and the solution ψ_{III} writes

$$\psi_{\mathrm{III}}(r,z,t) = \psi^0_{\mathrm{III}} J_1(l_{\mathrm{III}} r)\exp(i\omega_{\mathrm{III}} t - m_{\mathrm{III}} z), \tag{6.12}$$

where l_{III} and m_{III} are the radial and vertical wave numbers, ω_{III} the frequency, and ψ^0_{III} the wave amplitude.

Continuity Relations and Complete solution

Vertical velocity and pressure field are continuous at the interfaces (see chapter 5 and [65, 224]), which gives continuity relations on the derivatives of the stream functions. These relations are satisfied for all spatial point of the interface and for all times, so they must be independent of the radial coordinate r and time t. Hence, we obtain that

$$\omega_{\mathrm{I}} = \omega_{\mathrm{II}} = \omega_{\mathrm{III}}, \tag{6.13}$$

and

$$l_{\mathrm{I}} = l_{\mathrm{III}}, \tag{6.14}$$

from what follows, using the dispersion relation recalled in equation (6.6), the relation on vertical wave numbers is

$$m_{\mathrm{I}} = m_{\mathrm{III}}, \tag{6.15}$$

since the buoyancy frequency is the same in regions I and III.

Using these relations, the complete solution can be written as

$$\psi_{\mathrm{I}}(r,z,t) = J_1(lr)e^{i\omega t}\left(\psi^R_{\mathrm{I}} e^{-imz} + \psi^I_{\mathrm{I}} e^{imz}\right), \tag{6.16}$$

$$\psi_{\mathrm{II}}(r,z,t) = J_1(lr)e^{i\omega t}\psi^0_{\mathrm{II}} e^{z/L_d}, \tag{6.17}$$

$$\psi_{\mathrm{III}}(r,z,t) = J_1(lr)e^{i\omega t}\psi^0_{\mathrm{III}} e^{-imz}. \tag{6.18}$$

The transmission coefficient T of the wave field across the buoyancy frequency gap, defined as the ratio $\psi^0_{\mathrm{III}}/\psi^I_{\mathrm{I}}$, can be obtained using the continuity relations of vertical velocity and pressure at the two interfaces. In this model, we obtain

$$T_{\omega>N_2} = \left|\frac{2mL_d}{mL_d - 1}\right| \exp\left(-\frac{|\Delta L|}{L_d}\right), \tag{6.19}$$

valid for $N_2 < \omega < N_1$. This coefficient is identical whether considering the transmission of ψ, v_z, and v_r. If the forcing frequency is such that $\omega < N_2 < N_1$, meaning that the wave is propagating in the three regions, this model leads to a different result

$$T_{\omega<N_2} = \left|\frac{2m_1}{m_1 + m_2}\right|, \tag{6.20}$$

where m_1 and m_2 are the vertical wave numbers associated to N_1 and N_2 respectively. In this unconfined inviscid model, when waves are propagating in the three regions, the second interface has no influence on the amplitude of the wave field as the transmission coefficient is the same as derived in chapter 5 for the vertical velocity. An explanation for that is that there should be a reflected wave propagating upwards in the layer at N_2 that cannot be neglected if the wave is propagating.

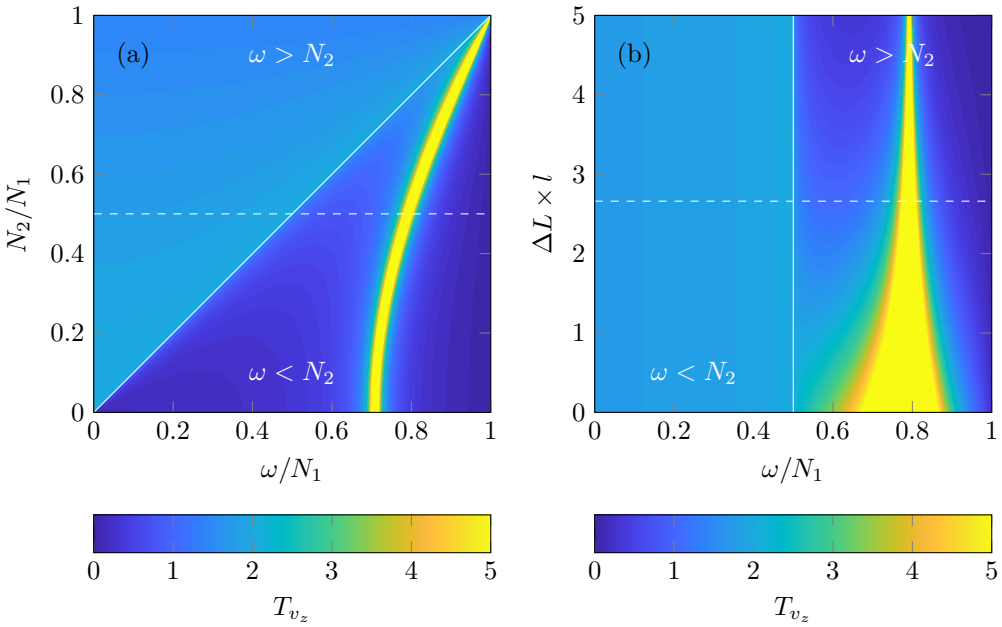

Figure 6.4: Colormaps of the transmission coefficient T_{v_z} as a function of (a) ω/N_1 and N_1/N_2 at a given $\Delta L \times l = 2.66$, and (b) ω/N_1 and $\Delta L \times l$ at a given $N_2/N_1 = 0.5$. Dashed lines show the cuts at (a) $N_2/N_1 = 0.5$ and (b) $\Delta L \times l = 2.66$.

The transmission coefficient for vertical velocity $T_{v_z} = T_{\omega > N_2}$ defined by equation (6.19) depends on various parameters that can be tuned in the experiments: the two buoyancy frequencies N_1 and N_2, the forcing frequency ω, the radial wave number l, and the vertical dimension of the evanescent region ΔL. These parameters collapse into three dimensionless variables ω/N_1, N_2/N_1, and $\Delta L \times l$ and we can plot colormaps of the transmission coefficient to study their influence, similarly to chapter 5 and [32]. They are presented in figure 6.4 with T_{v_z} as a function of (a) ω/N_1 and N_1/N_2 at a given $\Delta L \times l = 2.66$, and (b) ω/N_1 and $\Delta L \times l$ at a given $N_2/N_1 = 0.5$. A solid white line indicates the transition between fully propagating ($\omega < N_2 < N_1$) and tunneling ($N_2 < \omega < N_1$) regions. Due to the divergence of the ratio in equation (6.19), an increased transmission amplitude appears when ω/N comes closer to given values set by the buoyancy frequencies, for example when $\omega/N_1 \to 0.8$ in figure 6.4(b) for $\Delta L \times l = 2.66$. This peak is shifted to lower frequencies ω when the ratio N_2/N_1 decreases, and its width and amplitude increase for lower values of $\Delta L \times l$.

6.3 Experimental Realisation

We perform experiments of internal wave tunneling in axisymmetric geometry in two different configurations. In one case, we use the wave generator in an unconfined domain to produce a conical wave beam that remains close to the plane waves studied in [224]. In the other case, we reuse the setup from chapters 4 and 5 to study internal wave mode tunneling. The same stratification has been realised for both configurations.

6.3.1 Stratification

Thanks to the filling process based upon the double-bucket method and described in chapter 2, we produced a non-linear stratification constituted of different layers, as presented in figure 6.2, with density profile 6.2(a) and buoyancy profile 6.2(b). The top and the bottom layers are stratified, with $N = 0.80 \pm 0.05$ rad $\cdot$ s^{-1} and $N = 0.92 \pm 0.07$ rad $\cdot$ s^{-1} respectively. In between, over $\Delta L \simeq 10$ cm from $z = 23$ cm to $z = 33$ cm, is a weakly stratified region with $N = 0.48 \pm 0.08$ rad $\cdot$ s^{-1} evidenced by the hatched region in figure 6.2.

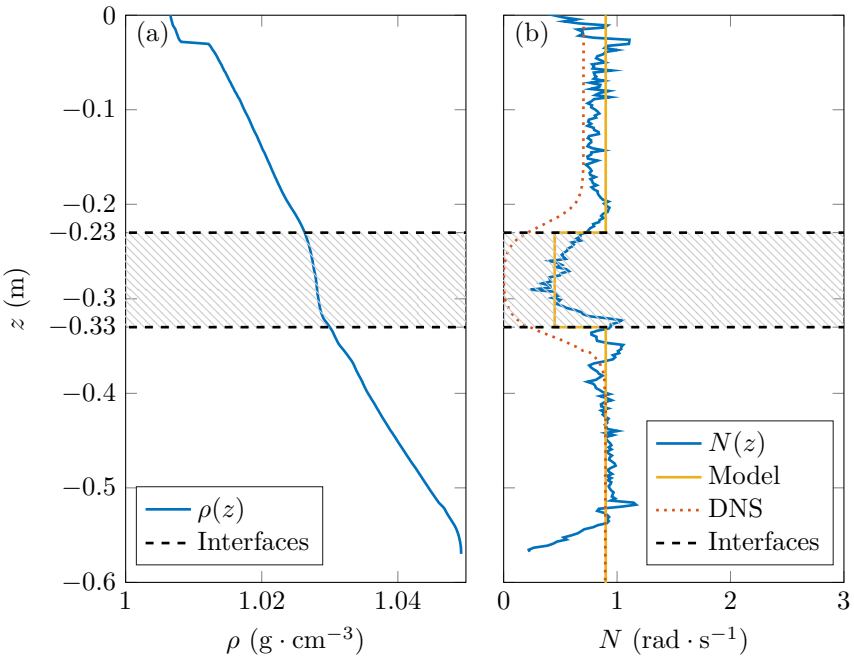

Figure 6.5: Example of a non-linear stratification with a constant density layer. Left (a): density profile. Right (b): buoyancy frequency profile in the experiment and in the DNS. The hatched region between $z = 23$ cm and $z = 33$ cm corresponds to the almost constant density layer in which we can approximate $N \simeq 0$.

Although the ideal stratification to perform internal wave tunneling experiments would be with $N_2 = 0$, here the density is still increasing with depth between the two interfaces. In figure 6.2(b), probe measurement of the buoyancy profile shows two constant buoyancy layers at the top and at the bottom, but a non-linear and non-zero buoyancy in between. This is due to the filling process, but can also be due to probe errors as the densitymeter measured nearly equal densities at the boundaries of this layer while filling the tank. With such a stratification, the range of frequencies for which tunneling is predicted to happen is $\omega \in [0.48;\ 0.8]$.

6.3.2 Wave tunneling: Case of Conical Beam

The first series of experiments mimmic the Cartesian plane wave works from Sutherland and Yewchuk [224]. The wave generator is not confined, and therefore produces a conical wave field propagating downards. Our results are presented in figure 6.6 in the first row (vertical velocity) and third row (radial velocity) where each column is a different forcing frequency, from left to right, $\omega = 0.304$ rad $\cdot$ s^{-1}, $\omega = 0.464$ rad $\cdot$ s^{-1}, and $\omega = 0.624$ rad $\cdot$ s^{-1}.

Second and fourth rows in figuree 6.6 present the vertical and the radial velocity obtained from Direct Numerical Simulations made in axisymmetric geometry, for comparison purposes. These DNS were run by Bruce Sutherland, solving the 2D axisymmetric equations for vorticity and buoyancy on a finite-difference staggered grid. The stream function is then found from the vorticity by performing a Fourier-Bessel transform, solving the Laplacian and then inverting in spectral space. The forcing is applied to the buoyancy field, which is a proxy for vertical displacement as

$b \propto v_z \propto J_0(lr)e^{i(\omega t - mz)}$ in the linear regime. It is applied at a depth $z = 0$ in a domain ranging vertically from $z = -H$ to $z = +H$. For $z > 0$, viscosity increases linearly from 0.01 $\text{cm}^2 \cdot \text{s}^{-1}$ to 1 $\text{cm}^2 \cdot \text{s}^{-1}$ at the top. In this way, upward propagating waves in this artificial half of the domain are damped, and so do not reflect back into the lower half of the domain that corresponds to the experimental region. The dimensions used in the simulation are the same as the experimental tank, with 128 grid points in the radial direction and 256 in the vertical lower half direction. The Bessel transform is performed using 50 zeros of the Bessel function. The time step was 0.001 s, small enough to deal with the high viscosity in the upper domain. In all three simulations presented in figure 6.6 rows 2 and 4, the amplitude of the forcing to the vertical displacement was $a = 5$ mm and the total running time was about 30 minutes.

6.3.3 Wave tunneling: Case of Axisymmetric Modes

We now focus on internal wave tunneling in the case of axisymmetric modes. Figure 6.7 presents similar results to the ones in figure 6.6, but in a radially confined case. The generator is set in a mode 1 configuration at low amplitude ($a = 2.5$ mm) and the forcing frequencies are, from left to right: $\omega = 0.304$ rad $\cdot$ s^{-1}, $\omega = 0.464$ rad $\cdot$ s^{-1}, and $\omega = 0.624$ rad $\cdot$ s^{-1}. In the three cases, we see that the mode is established in the top region and tunnels through the intermediate region to propagate in the bottom layer. As predicted by the theory, the mode structure is preserved in both layers but the amplitudes have decreased in the bottom region due to the evanescent transit in the middle region.

The tunneling phenomenon reduces the amplitude of the mode, as the velocity is smaller in the bottom layer than in the top layer, but the shape of the mode itself is not affected. In figure 6.8 are presented horizontal profiles of the vertical and radial velocity fields above and below the evanescent region, in the experiment at $\omega = 0.624$ rad $\cdot$ s^{-1}, corresponding to the third column of figure 6.7. On the profiles, taken at $z \simeq -10$ cm and at $z \simeq -40$ cm for the above and below cuts, are superimposed the fits from the expected Bessel functions, respectively $J_0(lr)$ for the vertical velocity and $J_1(lr)$ for the radial velocity, with $l = 19$ m^{-1} as set by the generator. Qualitatively, the fits agree well with the experimental profiles in both regions.

6.3.4 Amplitude Measurements

To investigate in some more details the effect of the buoyancy gap on the amplitude, we run a set of 39 experiments from $\omega = 0.160$ rad $\cdot$ s^{-1} to $\omega = 0.768$ rad $\cdot$ s^{-1} and we adapt the method presented in chapters 4 and 5 to measure the amplitude of the transmitted wave in our experimental setup. Horizontal cuts of vertical velocities at various times are fitted by a Bessel function (as in 6.8(b)) a few centimeters below the tunneling region, giving amplitude measurements as a function of time. The timeseries obtained by this process are quasi-sinusoidal and can be used to determine the amplitude of the wave field. The wave being reflected at the bottom boundary, measurements have to be performed before a returning time, noted t_f, determined using the group velocity in the top layer

$$\mathbf{v_g} = -\frac{ml^2 N_1^2}{\omega k^4}\mathbf{e_z}. \tag{6.21}$$

This returning time is therefore underestimated as the group velocity is lower in the evanescent region. Estimates of the vertical velocity amplitude are obtained from three overlaping periods, the last one containing t_f. We compute Root Mean Square (RMS) values over each of these periods and the amplitude is then given by the mean value of the three RMS and the error by the standard deviation. Figure 6.9 shows an example of a timeseries at $\omega = 0.624$ rad $\cdot$ s^{-1}, with the returning time indicated by the vertical solid line and the three different time windows used to get an estimate of the amplitude. Later times of the experiment are not considered as constructive or destructive interference may give wrong estimates and non-linearities may arise.

Transmission coefficient measurements are presented in figure 6.10, where the amplitude of the vertical velocity measured in the experiment has been normalised by its amplitude at the generator $a\omega$. The experimental data (green dots), obtained thanks to the process previously described, are superimposed to the theoretical prediction (solid purple line). The parameters have been adjusted to $N_1 = 0.9$ rad $\cdot$ s^{-1}, $N_2 = 0.45$ rad $\cdot$ s^{-1}, and $\Delta L = 14$ cm to find the best fit to the data points,

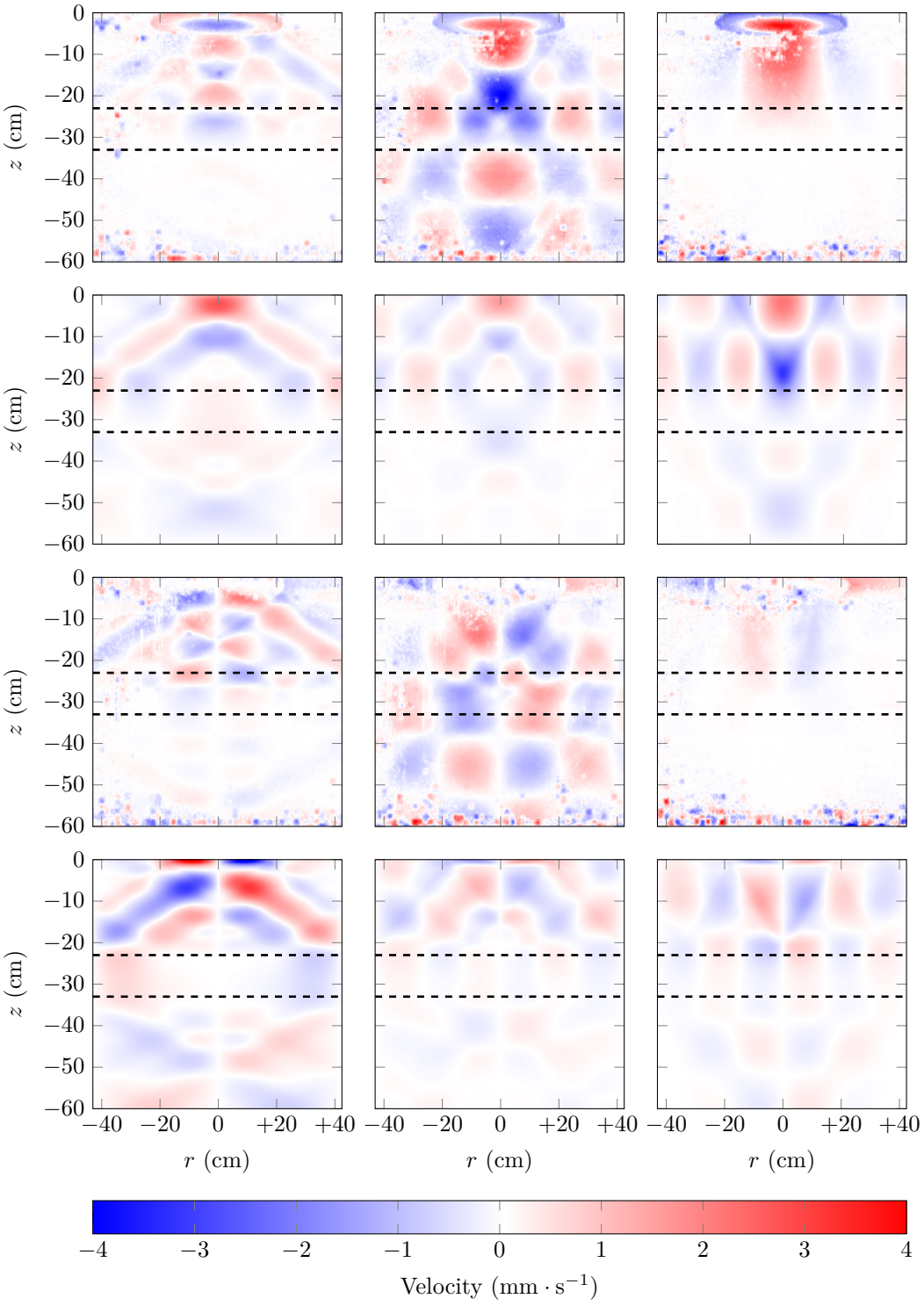

Figure 6.6: Examples of velocity fields for, from left to right: $\omega = 0.304\ \mathrm{rad \cdot s^{-1}}$, $\omega = 0.464\ \mathrm{rad \cdot s^{-1}}$, and $\omega = 0.624\ \mathrm{rad \cdot s^{-1}}$. First row is the vertical velocity and third row is the radial velocity, from PIV fields filtered at the forcing frequency. Second row is the vertical velocity and fourth row is the radial velocity obtained in DNS. Fields are taken 120 s after the generator has been started.

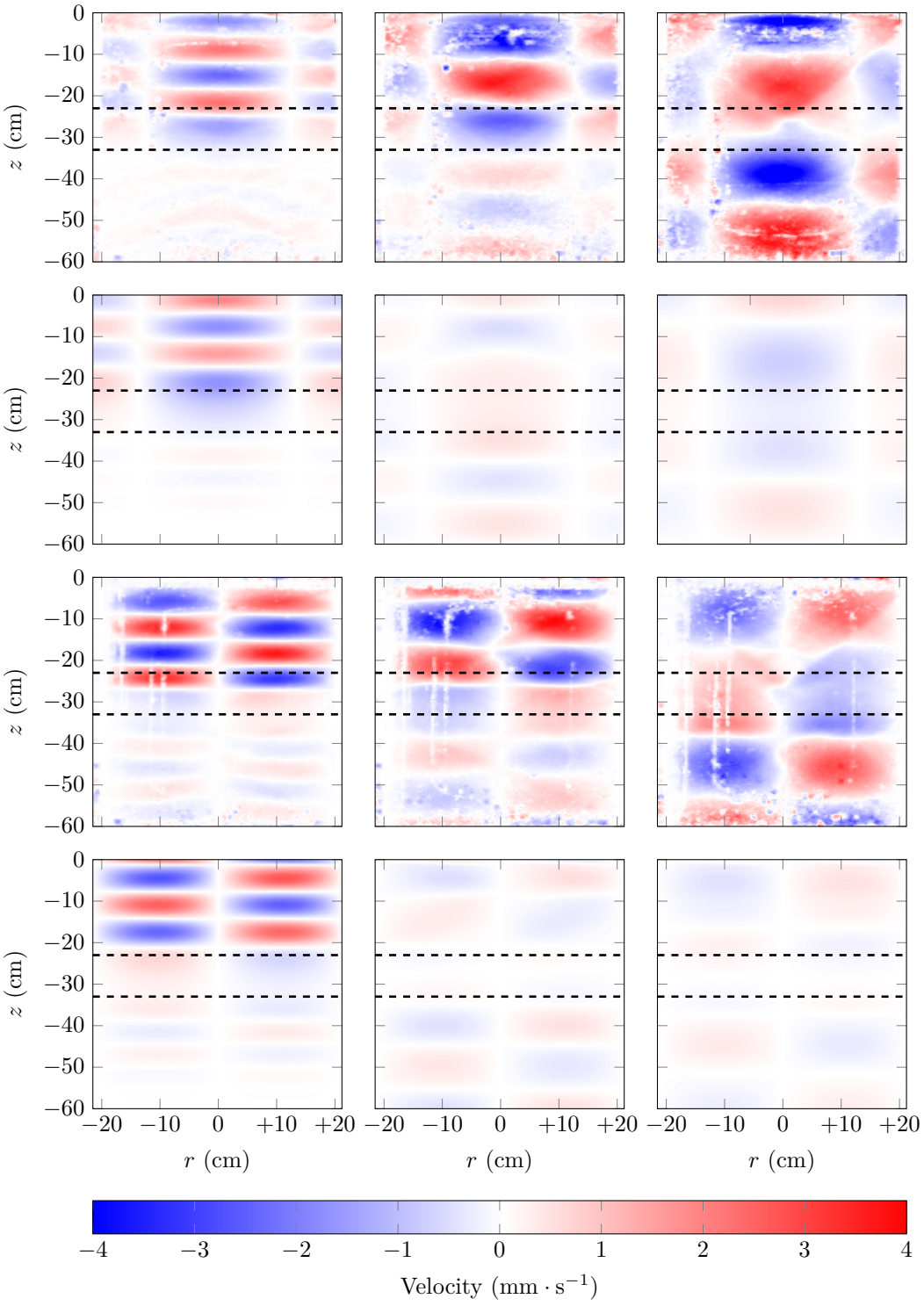

Figure 6.7: Examples of velocity fields for, from left to right: $\omega = 0.304\ \mathrm{rad \cdot s^{-1}}$, $\omega = 0.464\ \mathrm{rad \cdot s^{-1}}$, and $\omega = 0.624\ \mathrm{rad \cdot s^{-1}}$. First row is the vertical velocity and third row is the radial velocity, from PIV fields filtered at the forcing frequency. Second row is the vertical velocity and fourth row is the radial velocity obtained in DNS. Fields are taken 120 s after the generator has been started.

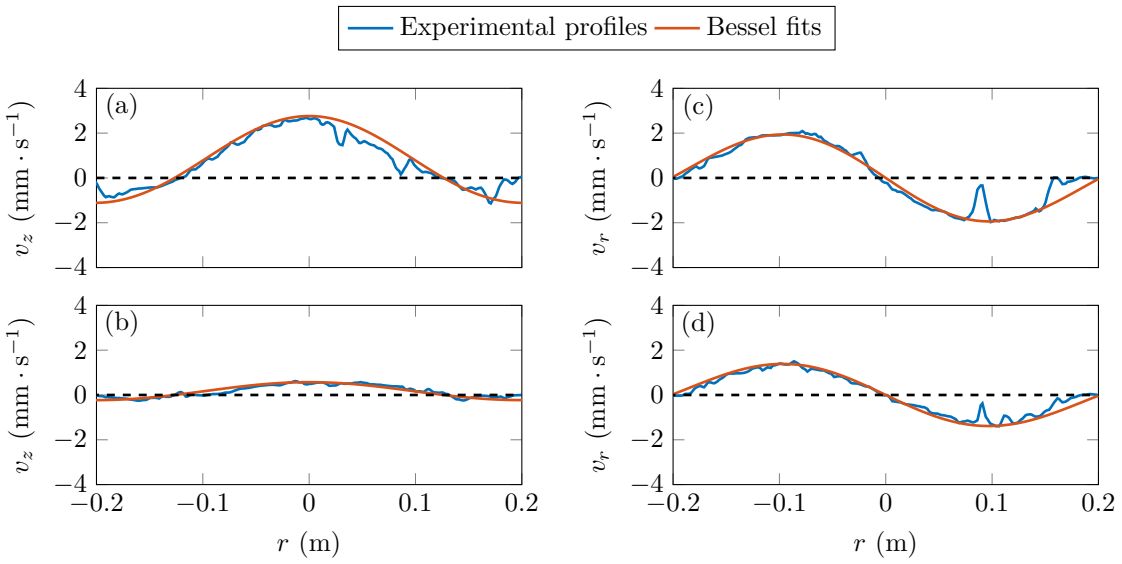

Figure 6.8: Experimental profiles and fits by Bessel functions for $\omega = 0.624$ rad $\cdot$ s^{-1}, with: (a) vertical velocity in the top layer, at $z \simeq -10$ cm; (b) vertical velocity in the bottom layer, at $z \simeq -40$ cm; (c) radial velocity in the top layer, at $z \simeq -10$ cm; (d) radial velocity in the bottom layer, at $z \simeq -40$ cm. Profiles are taken 70 s after the generator was started.

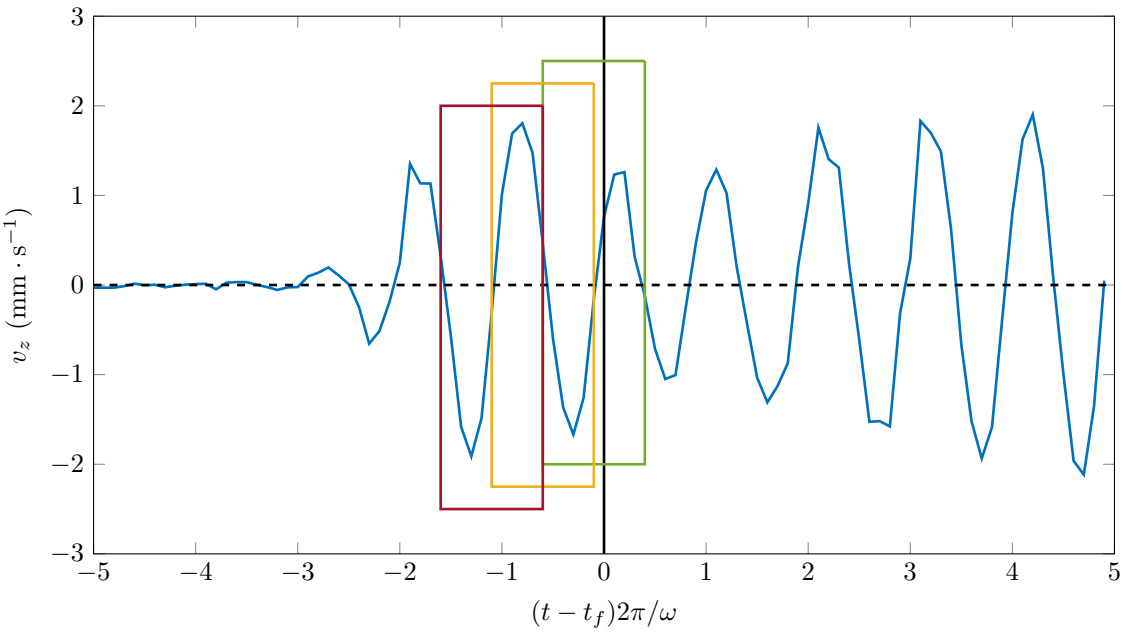

Figure 6.9: Timeseries of the amplitude of the vertical velocity over 100 s at $\omega = 0.624$ rad $\cdot$ s^{-1}. The black solid line indicates the time t_f used to compute the amplitude. The three rectangles show the periods that are used to estimate the wave amplitude from RMS.

and are all consistent with the stratification showed in figure 6.5. The use of a slightly larger value of the gap ΔL between the two layers can result from the fact that no viscous damping effects are taken into account in the model. A vertical dashed line indicates the value of N_2/N_1. Results for $\omega < N_2$ are not considered because the theory does not apply and, as observed in [32, 33] and chapters 4 and 5, measurements are not satisfying for small frequency ratios. In the range of frequency going from N_2 to N_1, the values of transmission coefficient estimated in the experiment agree well with the theoretical curve and qualitatively validate our model.

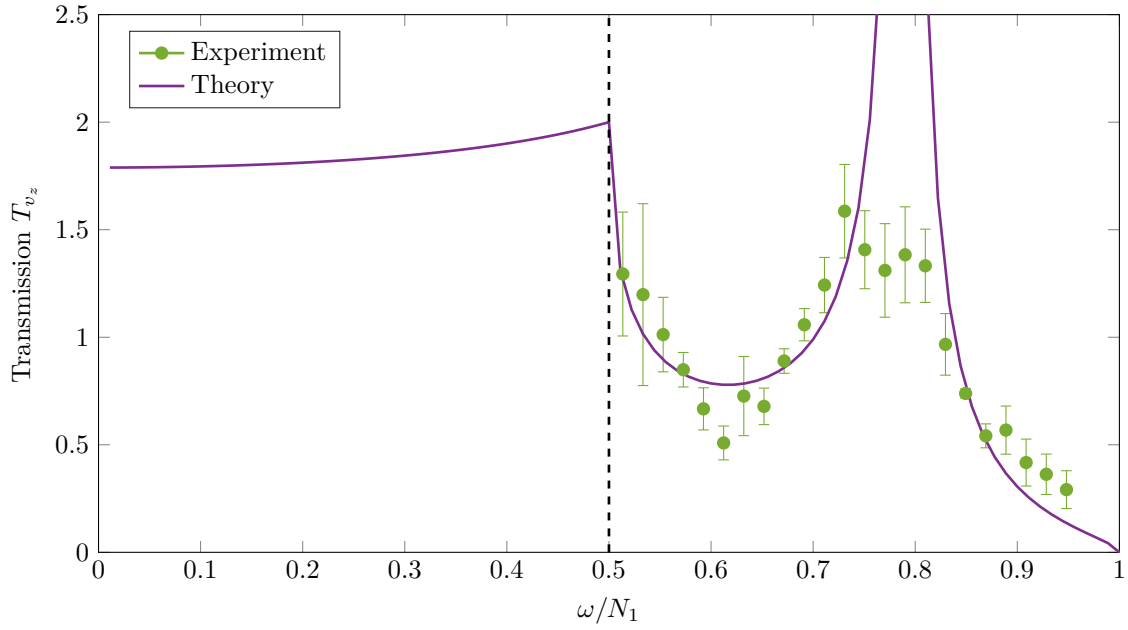

Figure 6.10: Comparison between the transmission coefficient T_{v_z} measured in the experiment (green dots) and its theoretical prediction (solid purple line) obtained from equation (6.19) with $N_1 = 0.9\text{rad} \cdot \text{s}^{-1}$, $N_2 = 0.45$ rad $\cdot \text{s}^{-1}$, and $\Delta L = 14$ cm.

Despite the qualitative agreement of the experiment with our model, some discrepancies are visible, the most important one being the truncated peak around from $\omega/N_1 = 0.75$ to 0.82, where the amplitude saturates although the theory predicts a peak.

Various reasons can explain such a difference between the theory and the experiment. First of all, the theory can be improved by taking into account the forced upper layer configuration (see chapter 5), as the first interface is close to the generator and the wave can be reflected several times in the top layer before being transmitted. A similar phenomenon could be considered in the evanescent layer as well, especially for frequencies for which the dissipative length L_d becomes larger than the tunneling layer vertical extension ΔL. These two phenomena could lead to either increased or descreased amplitudes due to constructive or destructive interference, and possibly to non-linear behaviours that saturate the wave amplitude at finite value as observed in previous experiments from chapters 4 and 5, although we were not able to state it clearly from the raw velocity fields. In addition, taking a close look at the stratification, the values of N_1 and especially N_2 are difficult to estimate and it is very likely that the range of frequency for which the waves are evanescent in the middle layer is smaller or larger than stated above.

6.4 Conclusions and Discussion

We have presented, in this section, preliminary results on internal wave tunneling in axisymmetric geometry. We first derived a simple model of transmission across a three-layered stratification in the case of an intermediary evanescent layer, and we have found that experimental measurements of the transmission coefficient agree well with the theoretical prediction.

Some disagreements can be pointed out. The most important one is the existence of a peak in transmission at a given forcing frequency between N_2 and N_1, predicted by the theory and barely observed in the experiments. Moreover, the parameters used for the theoretical prediction do not exactly correspond to the stratification, although they are still close, and additional viscous decrease in amplitude should be taken into account to get a better estimate of the transmission coefficient at a given depth.

As mentioned in [86, 224, 221], incursions of weakly stratified regions exist in oceanic stratifications, from isolated layers to staircases stratifications. Such density profiles can result from processes such as double diffusion [200] in a salt and temperature stratified media, sometimes coupled to non-linear wave-wave interactions [101]. Examples of these stratifications have been observed both in warm regions (e.g. in the Tyrrhenian Sea [106, 152] and in the Caribbean Sea [117, 143, 201]) and cold regions (in the Arctic Ocean [191, 233, 231, 247]). As discussed in chapter 3, the shrinking ice coverage of the Arctic leads to enhanced generation of inertia-gravity waves by wind-driven events at the ocean surface, that can propagate through the stratification [105, 191, 192, 189]. This work is therefore complementary to the study of axisymmetric internal wave transmission across buoyancy interfaces [32] and helps understand the complexity of the Arctic Ocean and possible impacts of climate change on its re-stratification.

Further work can be undertaken to complement this study. Direct Numerical Simulations such as those presented in figure 6.7 can be used to provide additional measurements of the transmission coefficients at various frequencies, using the same method, to check the relevance of the model. The difference between a confined and an unconfined top layer could also be explored, as well as possible resonant interference in the middle region, to determine whether this behaviour contributes significantly to the transmision coefficient (as was the case for a buoyant interface, see chapter 5 and [32]) or not. And, lastly, the transition between the intervals $\omega < N_2 < N_1$ and $N_2 < \omega < N_1$ could be discussed, with a theory involving doubly-confined layers and constructive-destructive interference behaviours in the top two layers of the stratification.

Part III

Non-Linear Effects and Axisymmetry Breaking

CHAPTER 7

Challenging Non-Linear Effects

Le città come i sogni sono costruite di desideri e di paure,
anche se il filo del loro discorso è segreto, le loro regole assurde,
le prospettive ingannevoli, e ogni cosa ne nasconde un'altra.
Italo Calvino, Le Città Invisibili.

In two-dimensional stratified fluids, wave-wave interaction has been proven capable to produce higher frequency harmonics, either through the forced interaction of two different waves [101], or through the self-interaction of the wave itself [221, 16]. Extending these works to three-dimensional wave fields, however, remains challenging, and poorly studied experimentally. Closed domains, such as the resonant cavity described in [33], are capable of producing enhanced amplitude wave fields and non-linear interactions either in linear or non-linear stratifications [33, 32], and could possibly lead to Triadic Resonant Interactin (TRI) or Super-Harmonic Generation (SHG).

In the previous chapters, we always focused on the linearised wave equations. In this process, we set the Jacobians and other product terms equal to zero, leading to the following linear system of equations

$$\partial_t \Delta_h \psi = \partial_r b, \tag{7.1}$$
$$\partial_t v_\theta = 0, \tag{7.2}$$
$$\partial_t b = -N^2 \frac{1}{r} \partial_r (r\psi). \tag{7.3}$$

Equation (7.2) is self-consistent, and gives an orthoradial velocity that does not evolve in time. Cross-derivatives of equations (7.1) and (7.3) give a linear equation on ψ that writes

$$\mathcal{L}[\psi] = 0, \tag{7.4}$$

where $\mathcal{L}$ is defined as

$$\mathcal{L}[\psi] = \partial_t^2 \Delta_h \psi + N^2 \partial_r \left(\frac{1}{r} \partial_r (r\psi) \right). \tag{7.5}$$

As discussed in Maurer *et al.* [141] and in Boury *et al.* [33], the linear solution of equations (7.2) and (7.4) that fulfills the boundary conditions imposed by an axisymmetric forcing at the surface and zero velocity normal to the other sides, with no orthoradial velocity, is described by Bessel functions of zeroth and first order, respectively J_0 for the vertical velocity and J_1 for the radial velocity. The frequency ω is linked to the radial and vertical wave numbers l and m through the dispersion relation for gravity waves, which is a direct consequence of the linear operator $\mathcal{L}$.

The non-linear terms, however, are of primary importance to describe stratified mixing processes. To date, non-linear interactions have been extensively studied in two-dimensionnal cartesian

geometry (for instance in [107, 251, 43, 221, 235]) but three-dimensional studies remain marginal (for example, see the recent work of [208]). More relevant to geophysics, as they mimic the geometry of the wave source in unconfined domains, 3D and, more particularly, axisymmetric wave fields are still challenging to study when dealing with linear and non-linear phenomena. Classical generation mechanisms, such as vertically oscillating spheres [154, 74], prevent from studying 3D non-linearities in their whole complexity as they usually generate localised 3D wave fields. Instead, Maurer *et al.*'s axisymmetric wave generator [141], built upon the technology of Gostiaux *et al.*'s planar generator [92], has been proven capable of exciting pure axisymmetric wave fields shaped as Bessel functions [33], that can lead to more targeted studies of non-linear effects.

Based upon this new generator technology and preliminary studies of non-linearities in axisymmetric geometry [140], we explore in this chapter two phenomena observed in our experimental setup: Super-Harmonic Generation (SHG) and Triadic Resonant Instability (TRI).

Results from the first half of this chapter are in preparation for *Physical Review Fluids* [34].
Results from its second half are in preparation for *Journal of Fluid Mechanics* [31].

7.1 A Criterion for Linearity vs. Non-Linearity

To begin with, we use a scale analysis to derive a qualitative criterion allowing us to discriminate whether the forcing amplitude is low enough to delay the growth of non-linearities.

In the previous chapters, all non-linear terms in the internal wave equation were neglected and the study only focused on the linear equation. The complete equation, including both linear and non-linear terms, can be obtained starting from the following set of equations

$$\partial_t \Delta_h \psi + \mathcal{J}^{\odot}\left(r\psi, \frac{\Delta_h \psi}{r}\right) = -\left(\frac{2v_\theta}{r} + f\right)\partial_z v_\theta + \partial_r b, \tag{7.6}$$

$$\partial_t v_\theta + \frac{1}{r^2}\mathcal{J}^{\odot}(r\psi, rv_\theta) = f\partial_z \psi, \tag{7.7}$$

$$\partial_t b + \frac{1}{r}\mathcal{J}^{\odot}(r\psi, b) = -N^2 \frac{1}{r}\partial_r(r\psi), \tag{7.8}$$

coupling the axisymmetric stream function ψ to the azimuthal velocity v_θ and the buoyancy field b. As discussed in chapter 1, the Laplacian $\Delta_h \psi$ is defined by

$$\Delta_h \psi = \frac{\partial^2 \psi}{\partial z^2} + \frac{\partial}{\partial r}\left(\frac{1}{r}\frac{\partial (r\psi)}{\partial r}\right) = \frac{\partial^2 \psi}{\partial z^2} + \frac{\partial^2 \psi}{\partial r^2} + \frac{1}{r}\frac{\partial \psi}{\partial r} - \frac{\psi}{r^2}, \tag{7.9}$$

and the cylindrical Jacobian $\mathcal{J}^{\odot}$ of two functions f and g is a non-linear operator given by

$$\mathcal{J}^{\odot}(f, g) = \frac{\partial f}{\partial r}\frac{\partial g}{\partial z} - \frac{\partial g}{\partial r}\frac{\partial f}{\partial z}. \tag{7.10}$$

After some calculus, these equations collapse into

$$\partial_t^2 \Delta_h \psi + N^2 \partial_r\left(\frac{1}{r}\partial_r(r\psi)\right) + f^2 \partial_z^2 \psi = \mathcal{N}[\psi, v_\theta, b], \tag{7.11}$$

where $\mathcal{N}$ denotes the non-linear terms

$$\mathcal{N}[\psi, v_\theta, b] = -\partial_t \mathcal{J}^{\odot}\left(r\psi, \frac{\Delta_h \psi}{r}\right) - f\partial_z \frac{1}{r^2}\mathcal{J}^{\odot}(r\psi, rv_\theta) - \partial_r\left(\frac{1}{r}\mathcal{J}^{\odot}(r\psi, b)\right) - \frac{1}{r}\partial_t \partial_z v_\theta^2. \tag{7.12}$$

Let's now consider a scale analysis. The stream function amplitude ψ_0 is a relevant scaling to be considered. As all frequencies are of the same order of magnitude, ω, N, and f, are assumed to have the same scaling in $1/T$ with T the period of the forcing. Disregarding boundary layer effects, the r and z derivatives are also assumed to have the same scaling in $1/L$, with L a given lengthscale. Under these assumptions, the linear part of the equation scales as

$$\frac{\psi_0}{T^2 L^2}, \tag{7.13}$$

and all non-linear terms scale as

$$\frac{\psi_0^2}{TL^4}. \tag{7.14}$$

Non-linear terms have to be taken into account as soon as both scalings are of the same order of magnitude, but they can be neglected if

$$\frac{\psi_0}{T^2L^2} \gg \frac{\psi_0^2}{TL^4}, \tag{7.15}$$

which means

$$\frac{L^2}{\psi_0 T} \gg 1. \tag{7.16}$$

The lengthscale L can be set so that $L \sim 1/l$, l being the radial wave number. Given that ψ_0 is the amplitude of the stream function, the amplitude of the vertical velocity is $\psi_0 l$ with l the radial wave number and the amplitude of the vertical displacement is $\psi_0 l/\omega \sim \psi_0 lT$. Setting a the amplitude of the wave generator, a criterion stating that non-linear effects are small is

$$a \ll 1/l. \tag{7.17}$$

For example, in our classical experimental setup, we have $l = 19$ m^{-1} ($1/l = 5$ cm). The generator amplitude should be one order of magnitude lower to prevent non-linear effects to appear too early so that they can be neglected compared to the linear wave field, which means a few millimeters. As we usually have $a = 2.5$ mm, this condition is satisfied.

7.2 Non-Linearities in Cartesian Geometry

We first focus on the case of non-linearities in Cartesian geometry. In a two-dimensional geometry, the non-linear equations, recalled from chapter 1, are

$$\begin{aligned}
\partial_t \Delta\psi + \mathcal{J}(\psi, \Delta\psi) &= -f\partial_z v_y + \partial_x b, &(7.18)\\
\partial_t v_y + \mathcal{J}(\psi, v_y) &= f\partial_z \psi, &(7.19)\\
\partial_t b + \mathcal{J}(\psi, b) &= -N^2 \partial_x \psi. &(7.20)
\end{aligned}$$

The Jacobians, cross-products of derivatives of the stream function and of the buoyancy field, contain all the non-linear physics. These terms can be computed using the plane wave solution of the linearised equations, written as

$$\begin{aligned}
\psi(x,z,t) &= \psi_0 e^{i(\omega t - \mathbf{k}\cdot\mathbf{x})}, &(7.21)\\
v_y(x,z,t) &= -\frac{fm\psi_0}{\omega} e^{i(\omega t - \mathbf{k}\cdot\mathbf{x})}, &(7.22)\\
b(x,z,t) &= -\frac{N^2 l\psi_0}{\omega} e^{i(\omega t - \mathbf{k}\cdot\mathbf{x})}, &(7.23)
\end{aligned}$$

leading to

$$\begin{aligned}
\mathcal{J}(\psi, \Delta\psi) &= 0, &(7.24)\\
\mathcal{J}(\psi, v_y) &= 0, &(7.25)\\
\mathcal{J}(\psi, b) &= 0, &(7.26)
\end{aligned}$$

As a result, in a linear stratification (constant N) and homogeneously rotating fluid (constant f), all self-interacting[1] terms for 2D Cartesian wave fields are zero. Note that a direct consequence of this result is that there is no non-linear behaviour due to self-interaction in a linearly stratified fluid, and Cartesian self-interaction are only observed in non-linear stratifications [16]. Non-linear interactions, however, can still exist in linear stratifications in two-dimensonal Cartesian geometry if they involve different waves, as in triadic interaction [21, 107].

[1] From now on, we will use the term "self-interaction" in a very specific way. A wave field can locally self-interact with itself, meaning that it virtually interacts with a wave field of same amplitude, same frequency, and same wave numbers (in magnitude). In Cartesian geometry, a plane wave can self-interact, as can a standing wave field (described by cosine or sine functions); but a wave beam (described by a sum of plane waves of varying wave lengths in the transerse direction) will not self-interact *per se* as there would be additional cross-interactions between the plane waves of different transverse wave lengths.

7.3 Experimental Configuration

In the following sections, we explore non-linear phenomena in a linear stratification and axisymmetric geometry. All experiments were conducted with the generator set into a radial mode 1 profile, at low amplitude ($a = 2.5$ mm), low enough to delay non-linearities from appearing and allowing for weakly non-linear study of the wave field.

Different sets of experiments were undertaken, for two ranges of ω/N: a first study at low ω/N (between 0.3 and 0.5) to delve into self-interaction and the generation of super-harmonics (section 7.4), and a second study at high values of ω/N (between 0.8 and 1) to explore triadic resonant instability (section 7.5).

7.4 Super-Harmonic Generation by Self Interaction

Through the use of an oscillating sphere and the study of the radiated conical wave field, Ermanyuk *et al.* [74] have shown that the first harmonic created by non-linear interaction is likely to present a non-trivial structure with a symmetry breaking, e.g. dipolar or quadripolar. In their study, however, the radiated wave field cannot be decomposed over a single Bessel function and the different components of the wave field, which can be extracted through a Fourier-Hankel transform [141], can interact together *via* the non-linear terms of the wave equation. In the present study, we consider a pure axisymmetric wave field shaped as a radial standing wave, called a mode, and discuss what is, to our knowledge, the first experimental observation of superharmonic generation through self-interaction of axisymmetric gravity waves.

7.4.1 Non-Linear Problem

Back to equations (7.6), (7.7), and (7.8), the same cross derivation that led to the linear system can be used to derive the full non-linear equation

$$\mathcal{L}[\psi] = \mathcal{N}[\psi, v_\theta, b], \tag{7.27}$$

where $\mathcal{L}$ is still defined by equation (7.5) and $\mathcal{N}$ is the non-linear operator

$$\mathcal{N}[\psi, v_\theta, b] = -\partial_t \mathcal{J}^\odot\left(r\psi, \frac{\Delta_h \psi}{r}\right) - \partial_r\left(\frac{1}{r}\mathcal{J}^\odot(r\psi, b)\right) - \frac{1}{r}\partial_t \partial_z v_\theta^2. \tag{7.28}$$

As discussed in section 7.1, when the velocity amplitudes become too large, these non-linear terms cannot be neglected. If we consider the axisymmetric linear solution previously derived, we note that $v_\theta = 0$ so $\mathcal{N}[\psi, v_\theta, b] = \mathcal{N}[\psi, b]$. The non-linear right-hand side of equation (7.27) therefore becomes only dependent on two Jacobians that can be evaluated. Using that [163]

$$\frac{\partial(J_0(lr))}{\partial r} = -lJ_1(lr), \qquad \frac{\partial(rJ_1(lr))}{\partial r} = lrJ_0(lr), \qquad \text{and} \qquad \frac{\partial(r^{-1}J_1(lr))}{\partial r} = -lr^{-1}J_2(lr), \tag{7.29}$$

and the linear solution for ψ and b, the non-linear terms write

$$\partial_t \mathcal{J}^\odot\left(r\psi, \frac{\Delta_h \psi}{r}\right) = C\frac{[J_1(lr)]^2}{r}\cos(2\omega t - 2mz), \tag{7.30}$$

$$\partial_r\left(\frac{1}{r}\mathcal{J}^\odot(r\psi, b)\right) = C\left[\cos^2(\omega t - mz)J_0(lr)\partial_r J_0(lr) + \sin^2(\omega t - mz)J_1(lr)\partial_r J_1(lr)\right], \tag{7.31}$$

with

$$C = 2\omega(l^2 + m^2)m\psi_0^2. \tag{7.32}$$

As a result, the right-hand side of equation (7.27) writes

$$\mathcal{N}[\psi, b] = CJ_1(lr)\left[J_2(lr)\sin^2(\omega t - mz) - J_1(lr)\cos^2(\omega t - mz)\right] \neq 0 \tag{7.33}$$

In the general case, inspired by the work of Thorpe [227], we write ψ as a sum over possible solutions of various frequencies ω_j as

$$\psi(r,z,t) = \sum_j \chi_j(r,z)\cos(\omega_j t), \tag{7.34}$$

very much like a Fourier Transform, with χ_j, $j \in \mathbb{Z}$, a spatial function. The linear part of equation (7.27) therefore writes

$$\mathcal{L}[\psi] = \sum_j \left[(N^2 - \omega_j^2)\frac{\partial}{\partial_r}\left(\frac{1}{r}\frac{\partial(r\chi_j)}{\partial_r}\right) - \frac{\partial^2\chi_j}{\partial z^2}\right]\cos(\omega_j t). \tag{7.35}$$

As the non-linear terms are only second order products of the stream function, we assume the following development

$$\mathcal{N}[\psi] = \sum_{g,h} C_{g,h}(r,z)\cos((\omega_g + \omega_h)t), \tag{7.36}$$

where ω_g and ω_h are frequencies, and $C_{g,h}$ is a spatial fonction. Projection of equation (7.28) over frequencies leads to

$$\forall j \in \mathbb{Z},\ (N^2 - \omega_j^2)\frac{\partial}{\partial_r}\left(\frac{1}{r}\frac{\partial(r\chi_j)}{\partial_r}\right) - \frac{\partial^2\chi_j}{\partial z^2} = C_j, \tag{7.37}$$

where C_j is defined as the function $C_{g,h}$ where g and h verify $\omega_j = \omega_g + \omega_h$. The C_j functions act over the modes as forcing terms produced by non-linear wave-wave interactions. The impact of this forcing term can be further explored in theory using the Green functions (see appendix) and an expansion of the stream function, or with Direct Numerical Simulations, which is beyond the scope of this study.

7.4.2 Non-Linear Forcing and Green Functions

Inspired by the approach of [237, 74, 238], we compute the Green function of the linear operator $\mathcal{L}$ in cylindrical coordinates (for more details on the calculus, see [4, 163]). In the axisymmetric case, without θ-dependence, this Green function can be written as follows

$$G(\mathbf{r},t;\mathbf{r}',t') = \frac{G_0}{4\pi^2}\int_{-\infty}^{+\infty} e^{i\omega(t-t')}\int_{-\infty}^{+\infty} e^{im(z-z')}[J_1(lr_<)Y_1(lr_>)]\mathrm{d}m\mathrm{d}\omega, \tag{7.38}$$

where G_0 is a normalisation coefficient, and ω, l, and m satisfy the dispersion relation for internal waves. The radial dependence is expressed through the first order Bessel functions J_1 and Y_1, two analytical solutions of the radial part of the wave equation [33]. The variables are noted t, $\mathbf{r} = (r,\theta,z)$, t', and $\mathbf{r}' = (r',\theta',z')$, and we use the notation $r_< = \min(r,r')$ and $r_> = \max(r,r')$.

From the wave equation and the top boundary forcing, the linear wave field can be obtained as a solution of the problem

$$\begin{cases} \mathcal{L}[\psi,b] = 0 & \text{for } \mathbf{r} \in \mathcal{C} \\ \psi = \delta(z)J_0(lr)\cos(\omega t) & \text{for } \mathbf{r} \in \partial\mathcal{C}, \end{cases} \tag{7.39}$$

where $\mathcal{C} = \{(r,\theta,z) \in [0;\ R] \times [0;\ 2\pi] \times [0;\ -L]\}$ is the cavity domain and $\partial\mathcal{C}$ stands for its boundaries. The forcing at the top boundary is expressed by a Dirac distribution $\delta(z)$. Equation 7.39 admits for solution

$$\psi(z,r,t) = \int_{\partial\mathcal{C}\times\mathbb{R}} \delta(z')J_0(lr')\cos(\omega t')\frac{\partial G}{\partial \mathbf{n}}(\mathbf{r},t;\mathbf{r}',t')\mathrm{d}S'\mathrm{d}t', \tag{7.40}$$

while integrating over the boundary $\partial\mathcal{C}$.

A small parameter $\varepsilon = \psi_0 T/L^2$ characterizing the contribution of non-linear terms can be defined from the derivation proposed in chapter 7 section 7.1 as well as in [35], allowing to write the stream function with a similar development as in Husseini *et al.* [101] in the following expansion

$$\psi = \varepsilon\psi^{(1)} + \varepsilon^2\psi^{(2)} + \mathcal{O}\left(\varepsilon^3\right), \tag{7.41}$$

where $\psi^{(1)}$ is the solution to the linear problem previously discussed. Considering that the second order terms come from the non-linear term

$$\mathcal{N}[\varepsilon\psi^{(1)}, \varepsilon b^{(1)}] = \varepsilon^2 C J_1(lr) \left[J_2(lr)\sin^2(\omega t - mz) - J_1(lr)\cos^2(\omega t - mz) \right], \tag{7.42}$$

at lowest order, the weakly non-linear correction $\psi^{(2)}$ can be found by defining a new Green problem where the non-linear self-interaction of the linear term acts as a forcing field over the whole domain

$$\begin{cases} \mathcal{L}[\varepsilon^2\psi^{(2)}, \varepsilon^2 b^{(2)}] = \varepsilon^2 \mathcal{N}[\psi^{(1)}, b^{(1)}] & \text{for } \mathbf{r} \in \mathcal{C} \\ \psi = 0 & \text{for } \mathbf{r} \in \partial\mathcal{C}, \end{cases} \tag{7.43}$$

whose solution is found analytically as

$$\varepsilon^2\psi^{(2)}(r, z, t) = \varepsilon^2 \int_{\mathcal{C}\times\mathbb{R}} \mathcal{N}[\psi^{(1)}, b^{(1)}] G(\mathbf{r}, t; \mathbf{r}', t') \mathrm{d}r' \mathrm{d}z' \mathrm{d}t'. \tag{7.44}$$

This expression predicts that the wave created through self-interaction is a first harmonic at 2ω, or a mean flow at zero frequency. The spatial dependence, however, being coupled between l and m, cannot be directly infered.

7.4.3 Wave Resonator and Mode Selection

Cylindrical cavities have been demonstrated to produce enhanced modal wave fields in Boury *et al.* [33], likely to trigger instabilities at high frequencies. In such a confined configuration, radial and vertical modes can be excited if they satisfy the boundary condition, namely a zero orthogonal velocity at the boundaries. A cavity mode is therefore described by a stream function

$$\psi(r, z) = \psi^0 J_1(lr)\sin(mz). \tag{7.45}$$

As we will see next, the radial confinement sets the possible values of l, and so does the vertical confinement for the values of m.

Radial Confinement

The cylinder imposes a radial confinement within a radius R. As such, modes of radial wave number l_p, $p \in \mathbb{N}^*$, are selected with the boundary condition stating that the radial velocity is zero at the boundary

$$v_r(r = R, z, t) = \left(-\frac{1}{r}\frac{\partial(r\psi)}{\partial z} \right)_{r=R} = 0, \tag{7.46}$$

equivalent to

$$J_1(l_p R) = 0. \tag{7.47}$$

If $j_{1,p}$ is the p^{th} zero of the 1^{st} order Bessel function J_1, then the values of l_p are given by

$$\forall p \in \mathbb{N}^*,\ l_p = \frac{j_{1,p}}{R}. \tag{7.48}$$

Table 7.1 presents the first zeros of the J_1 Bessel function, extracted from [17], and the corresponding radial wave numbers for a cylindrical confinement of radius $R = 20$ cm. An experimental visualisation of these radial modes for $p = 1$, 2, and 3, can be seen in figure 4.4 and found in Boury *et al.* [33].

p	1	2	3	4	5
$j_{1,p}$	3.83	7.02	10.17	13.32	16.47
l_p	19.15	35.10	50.85	66.60	82.35

Table 7.1: First zeros of the J_1 Bessel function and associated radial wave number for $R = 20$ cm.

Vertical Confinement

The upper and lower boundaries, set, respectively, by the bottom of the tank and the wave generator, impose a vertical confinement (cavity) over a given height L. The vertical modes are found by stating that, at $z = 0$ – neglecting the generator motion which is at low amplitude – and at $z = -L$, the vertical velocity is zero

$$v_z(z=0) = \left(\frac{1}{r}\frac{\partial(r\psi)}{\partial r}\right)_{z=0} = 0 \quad \text{and} \quad v_z(z=-L) = \left(\frac{1}{r}\frac{\partial(r\psi)}{\partial r}\right)_{z=-L} = 0, \tag{7.49}$$

which justifies that the vertical dependence of ψ is described by a sine function, and which also means

$$\sin(mL) = 0. \tag{7.50}$$

As a consequence, vertical modes should have a half-integer number of vertical wave lengths in the cavity. It follows that the vertical wave number $m_q,\ q \in \mathbb{N}^*$, is given by

$$\forall q \in \mathbb{N}^*,\ m_q = \frac{\pi q}{L}. \tag{7.51}$$

Table 7.2 gives the smallest vertical wave numbers that can be found in a resonant cavity of height $L = 60$ cm.

q	1	2	3	4	5	6	7	8	9
m_q	5.23	10.47	15.70	20.93	26.17	31.40	36.63	41.87	47.1

Table 7.2: Lowest vertical wave numbers m_q for $L = 60$ cm.

Cavity Modes

Each mode in the cavity is designated by a couple $(p, q) \in \mathbb{N}^{*2}$, so that its radial wave number is l_p and its vertical wave number is m_q. A mode (p, q) has a given frequency $\omega_{p,q}$ fixed by the linear dispersion relation for internal waves as

$$\frac{\omega_{p,q}}{N} = \left(\frac{l_p^2}{l_p^2 + m_q^2}\right)^{1/2}. \tag{7.52}$$

We present in table 7.3 the values of $\omega_{p,q}/N$ corresponding to modes (p, q) in a cavity of radius $R = 20$ cm and height $L = 60$ cm.

$\omega_{p,q}/N$	$p=1$	$p=2$	$p=3$	$p=4$	$p=5$
$q=1$	0.9647	0.9891	0.9948	0.9969	0.9980
$q=2$	0.8774	0.9583	0.9795	0.9879	0.9920
$q=3$	0.7733	0.9128	0.9555	0.9733	0.9823
$q=4$	0.6750	0.8589	0.9247	0.9540	0.9692
$q=5$	0.5905	0.8017	0.8892	0.8307	0.9530
$q=6$	0.5207	0.7453	0.8509	0.9045	0.9344
$q=7$	0.4633	0.6919	0.8114	0.8762	0.9137
$q=8$	0.4159	0.6424	0.7720	0.8466	0.8914
$q=9$	0.3766	0.5975	0.7336	0.8165	0.8680

Table 7.3: Values of $\omega_{p,q}$ corresponding to modes (p, q) of radial wave number l_p and vertical wave number m_q for $R = 20$ cm and $L = 60$ cm.

As shown in equation (7.36), a non-linear wave-wave interaction produces a wide range of waves that can be projected over the appropriate basis of linear solutions (7.45). With non-zero non-linear terms, as shown in equation (7.33), harmonic modes can be fed by an excitation mode. A

mode at frequency ω is therefore in resonance with the n^{th} harmonic, $n \in \mathbb{N}^*$, if there exists a couple of non-zero integers (p, q) such that

$$n\omega = \omega_{p,q}. \tag{7.53}$$

In particular, a mode excited at frequency ω is in non-linear resonance with its first harmonic if twice the forcing frequency 2ω is close to a frequency $\omega_{p,q}$ that corresponds to a mode (p, q). We will verify that in the following sections.

7.4.4 Axisymmetric Non-Linear Wave Generation

We run a set of nine experiments indexed from 0 to 9, with forcing frequency from $\omega/N = 0.305$ to 0.449, using a mode 1 configuration at the generator [33]. For each frequency, long term forcing of the cavity, up to 10 minutes, leads to non-linear wave-wave interactions, where higher frequency waves are created. This phenomenon is illustrated in figure 7.1, showing frequency spectrum from experiment number 9 at $\omega/N = 0.449$. The spectrum contains not only the forcing frequency at ω/N, but also a mean flow at $\omega = 0$ and harmonics at $2\omega/N$, $3\omega/N$, and so on. Here, the first harmonic would be propagating as $\omega/N < 0.5$ and therefore $2\omega/N < 1$. This behaviour is observed for all frequencies, regardless of any resonant cavity aspect identified in Boury *et al.* [33]. In the performed experiments, due to the range of frequencies choosen, the first harmonic at $2\omega/N$ is always propagating and, except for experiments 1 and 2, the second harmonic at $3\omega/N$ is evanescent.

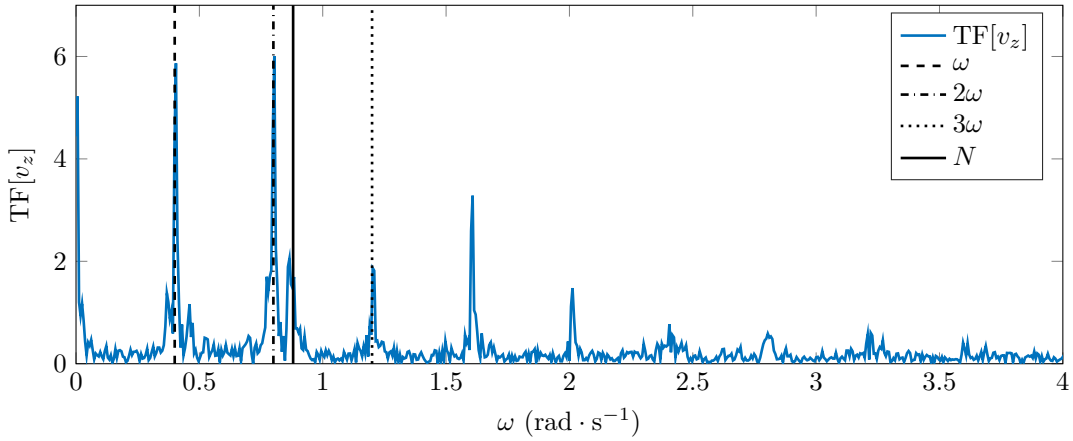

Figure 7.1: Example of Fourier transform performed over the last two minutes of the experiment with a forcing at $\omega/N = 0.449$. The solid line shows the cut-off frequency at N. Dashed, dashed-dotted, and dotted lines show ω, 2ω, and 3ω frequencies.

Figure 7.2 gives snapshot examples of such an experiment, for a forcing at $\omega/N = 0.449$ corresponding to the spectrum presented in figure 7.1. The first row shows the wave field filtered at the forcing frequency ω with, from left to right, v_z and v_r in the vertical plane, and v_r and v_θ in the horizontal plane. The excited wave field corresponds to a mode 1 and presents all features of an axisymmetric wave field [33]: right-left symmetry of v_z and right-left antisymmetry of v_r in the vertical plane, invariance by rotation of center $(0, 0)$ for v_r in the horizontal plane, and a negligible orthoradial velocity v_θ when observed in the horizontal plane (v_r dominates v_θ by a factor ~ 10 in magnitude).

The first harmonic created at $2\omega/N$ is filtered and shown in the second row of figure 7.2. Though no spatial wave lengths can be directly infered from the wave field, we notice that the created harmonic field shares the same axisymmetric properties as the excitation wave field. The right-left symmetry/antisymmetry of v_z and v_r in the vertical plane is also consistent with an axisymmetric description of the wave field. More specifically, a zero of radial velocity is observed at the center of the experimental domain whereas filtered wave fields in Triadic Resonant Instability (TRI) [140] have shown, in some cases, non-zero velocity, breaking the axisymmetry of the system.

The orthoradial velocity v_θ is, as compared to the excitation wave field, a noisy signal and does not show either any symmetry breaking.

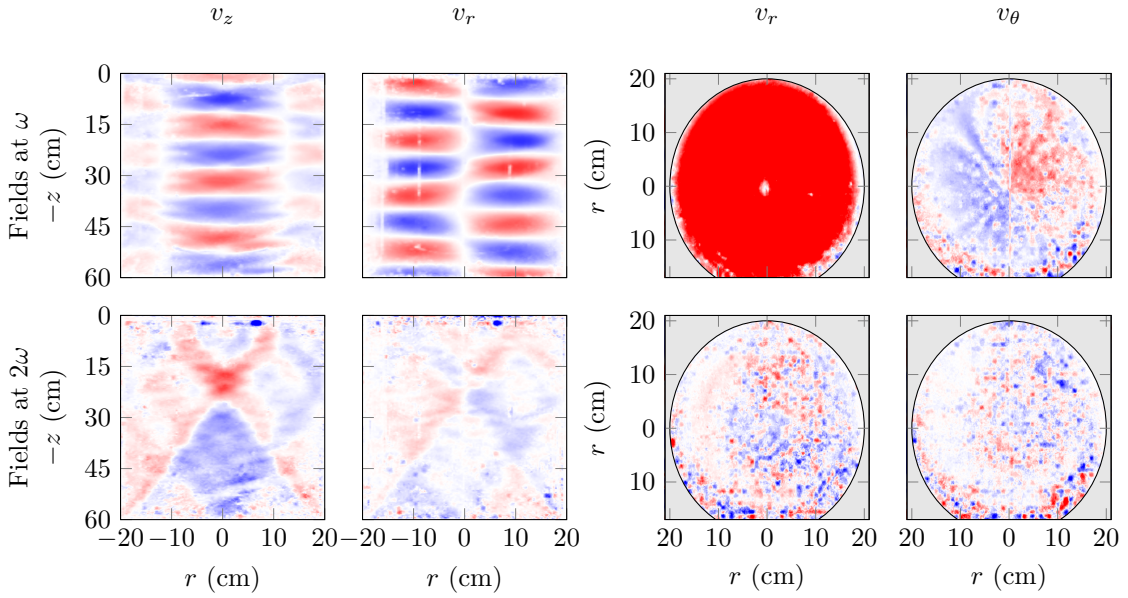

Figure 7.2: Velocity fields in experiment 9, at forcing frequency $\omega/N = 0.449$. The first row shows the filtered wave field at ω and the second row shows the filtered wave field at 2ω. From left to right: v_z, v_r in a vertical cross-section, and v_r, v_θ in a horizontal cross section. Visualisation time is about 9 minutes after the generator started to excite the wave field.

7.4.5 Proper Orthogonal Decomposition

In order to describe quantitatively the wave field at a given frequency and, more particularly, the wave field created in the harmonic at twice the forcing frequency, we used a Proper Orthogonal Decomposition (POD) method to fit our needs. As we know which basis to use (see previous sections and table 7.3), the POD process simply consists in projecting the experimental wave field over an orthogonal basis built accordingly.

The series of $\{r \mapsto J_0(l_p r) \mid p \in \mathbb{N}^*\}$ and $\{z \mapsto \sin(m_q z) \mid q \in \mathbb{N}^*\}$ forms an orthogonal basis in axisymmetric geometry, which are of relevance for this study. A direct consequence is that the stream function can be written in terms of normalised modes (p, q), denoted $\psi_{p,q}$, in the axisymmetric domain $(r, \theta, z) \in \mathcal{C} = [0;\ R] \times [0;\ 2\pi] \times [0;\ -L]$, defined as

$$\psi_{p,q}(r,z) = \psi^0_{p,q} J_1(l_p r)\sin(m_q z), \qquad \text{with} \qquad \psi^0_{p,q} = \frac{1}{J_1'(l_p R)}\sqrt{\frac{2}{L\pi}}, \tag{7.54}$$

satsifying the condition

$$\int_{\mathcal{C}} \left[\psi_{p,q}(r,z)\right]^2 r\mathrm{d}r\,\mathrm{d}\theta\,\mathrm{d}z = 1, \tag{7.55}$$

from which we can derive the vertical and radial velocities associated to a mode (p, q) as

$$v_z^{p,q}(r,z) = \frac{1}{r}\frac{\partial(r\psi_{p,q})}{\partial r} = -l_p \psi^0_{p,q} J_0(l_p r)\sin(m_q z), \tag{7.56}$$

$$v_r^{p,q}(r,z) = -\frac{1}{r}\frac{\partial(r\psi_{p,q})}{\partial z} = m_q \psi^0_{p,q} J_1(l_p r)\cos(m_q z). \tag{7.57}$$

Hence, the kinetic energy contained in one mode (p, q) is given by

$$K_{p,q} = \left[\int_{\mathcal{C}} v_z(r,z)\cdot v_z^{p,q}(r,z) r\mathrm{d}r\,\mathrm{d}\theta\,\mathrm{d}z\right]^2 + \left[\int_{\mathcal{C}} v_r(r,z)\cdot v_r^{p,q}(r,z) r\mathrm{d}r\,\mathrm{d}\theta\,\mathrm{d}z\right]^2, \tag{7.58}$$

which, accounting for the discretisation of our domain, can be written as follows

$$K_{p,q} = \left[\sum_{r,z} 2\pi r v_z(r,z) \cdot v_z^{p,q}(r,z)\right]^2 + \left[\sum_{p,q} 2\pi r v_r(r,z) \cdot v_r^{p,q}(r,z)\right]^2 . \tag{7.59}$$

As a result, if we note K_0 the kinetic energy of the total wave field, the fraction of energy in a mode (p,q) is given by the scalar product (7.59) normalised by K_0. The higher the quantity, the more dominant the mode is in the observed field. Note that the prefactors for $v_{z,p,q}$ and $v_{r,p,q}$ can differ if the normalisation process is directly applied to the stream function or to the velocities.

The left panel of figure 7.3 shows an example of such a POD decomposition using the excitation wave field previously presented in the top part of figure 7.2, and the right panel of figure 7.3 shows the decomposition of the first harmonic wave field, respectively at $\omega/N = 0.449$ and $2\omega/N = 0.898$. Figure 7.3 (top) depicts the colormap of the energetic distribution onto different modes and figure 7.3 (bottom) plots the kinetic energy contained in every tested mode as a function of the quantity $p.q$, defined as $p.q = p + 0.1q$, used to identify the different modes with a single number or, in other words, to transform the 2D plot of the top row of figure 7.3 into the more easily quantifiable 1D plot of the bottom of figure 7.3. As expected, figure 7.3 (left) shows that nearly all the energy of the wave field produced by the generator lies in a radial mode 1 wave, more exactly a $(1,7)$ mode, that can be clearly identified in figure 7.2 with 7 zeros along the vertical direction and one along the horizontal direction. In addition, while the filtered wave field at $2\omega/N$ in figure 7.2 does not explicitly displays a mode, we see from figure 7.3 (right) that the energy is mostly split into mode $(1,2)$ (47%), mode $(3,5)$ (32%), and mode $(5,8)$ (8%), the other contributions being negligible. The first harmonic generated in experiment 9 can therefore be described as a sum of modes $(1,2)$, $(3,5)$ and $(5,8)$ with given prefactors to account for the distribution of energy between the three modes.

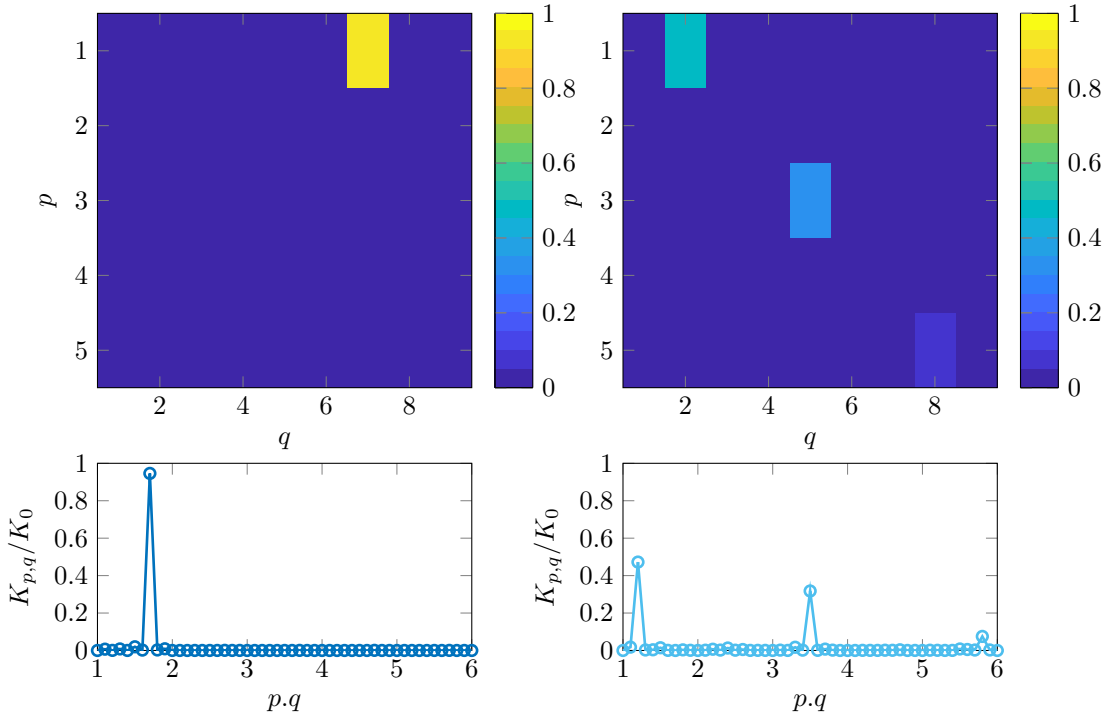

Figure 7.3: POD performed on experiment number 9. Top row is the colormap of the energy distribution in the different modes in the (p,q) plane, and the bottom row is the transposition of this 2D plot into a 1D plot of axis $p.q = p + 0.1q$. Left: POD over the filtered wave field at the excitation frequency $\omega/N = 0.449$. Right: POD over the filtered wave field at the first harmonic $2\omega/N = 0.898$.

7.4.6 Observation of Super-Harmonics

The POD discrimination process is applied to experiments 1 to 9 and its results are summarised in tables 7.4 and 7.5.

In some cases, the first harmonic generated by the non-linear wave-wave interaction can be clearly identified by eye as a single mode (p, q), as shown for two experiments at $2\omega/N = 0.755$ and $2\omega/N = 0.791$, respectively in figures 7.4 and 7.5, with the generation of a mode $(1, 3)$ and a mode $(2, 6)$ respectively. In these cases, this clearly observed mode is the one identified as the most energetic in the POD decomposition. Figure 7.6 illustrates this point with experiment 5 and 6, showing a single mode containing about 80 to 90% of the total kinetic energy of the first harmonic. The remaining fraction of energy, from 10 to 20%, is sparsely distributed into lower modes that only contain less than 5% energy each and do not contribute to the general aspect and behaviour of the wave field. In other cases, as described in the previous section for experiment 9, the energy is more evenly distributed between several modes.

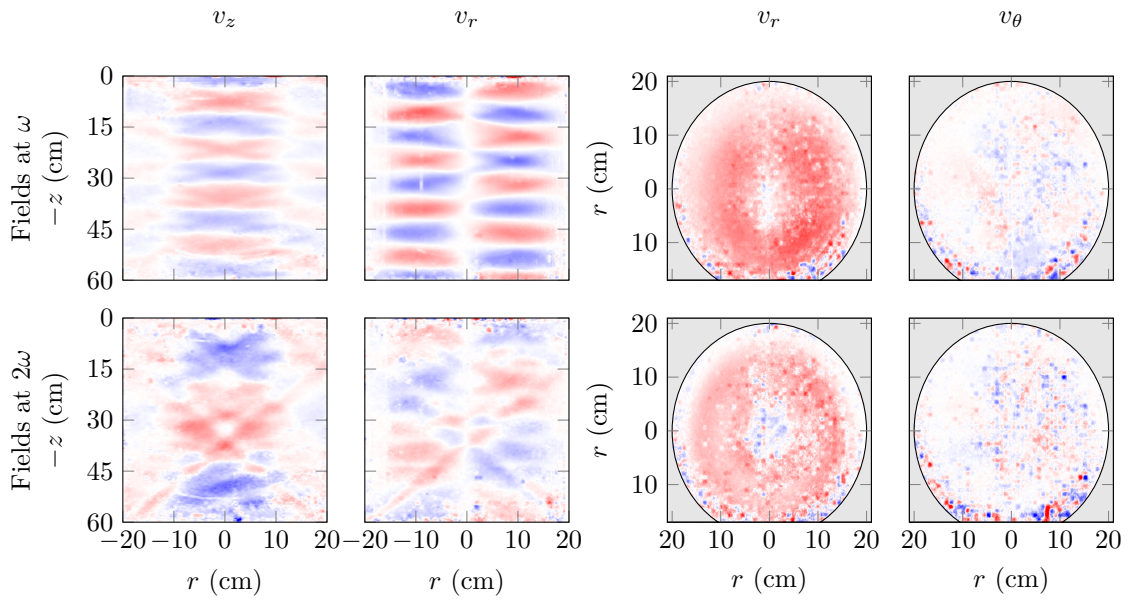

Figure 7.4: Velocity fields in experiment 6, with $2\omega/N = 0.791$, with generation of a mode $(1, 3)$.

The structure of the generated harmonic modes does not always match the one of the excitation mode. For example, experiments 3 and 6 lead to generation of a dominant mode with a radial structure similar to the excitation wave field ($l_1 = 19\ \mathrm{m}^{-1}$), whereas experiments 2, 5, and 8 generate a dominant higher order radial structure ($l_2 = 35\ \mathrm{m}^{-1}$). For a given radial structure, we note that the vertical wave number increases with the frequency $2\omega/N$, consistently with the dispersion relation. Interestingly, the mode frequencies are not ordered by lower p or lower q but seem randomly distributed: for example, by increasing ω, the harmonics can be dominated by a radial mode 1, then a radial mode 2, and then a radial mode 1 again.

Table 7.5 reproduces the theoretical results of table 7.3, highlighting the frequencies corresponding to the observed modes of experiments 1 to 9, which can be compared to the values in table 7.4. This comparison shows that, when a dominant mode (p, q) is observed, the frequency of the harmonic (third column in table 7.4) is close to the frequency of the same mode (p, q) stated by the dispersion relation (table 7.5). For instance, in experiment 6, 78% of the energy of the super-harmonic is in a mode $(1, 3)$, which is the mode observed in figure 7.4, and the frequency predicted for such a mode is $\omega_{1,3}/N = 0.773$ according to table 7.4, close to the harmonic frequency observed in the experiment $2\omega/N = 0.791$ (table 7.4). Similarly, in experiment 5, 82% of the energy of the super-harmonic is in a mode $(2, 6)$, which is the mode observed in figure 7.5, and the frequency predicted for such a mode is $\omega_{2,6}/N = 0.745$, also close to the harmonic frequency observed in the experiment $2\omega/N = 0.755$.

To generalize this observation, we summarized our results in figure 7.7. The blue circles show,

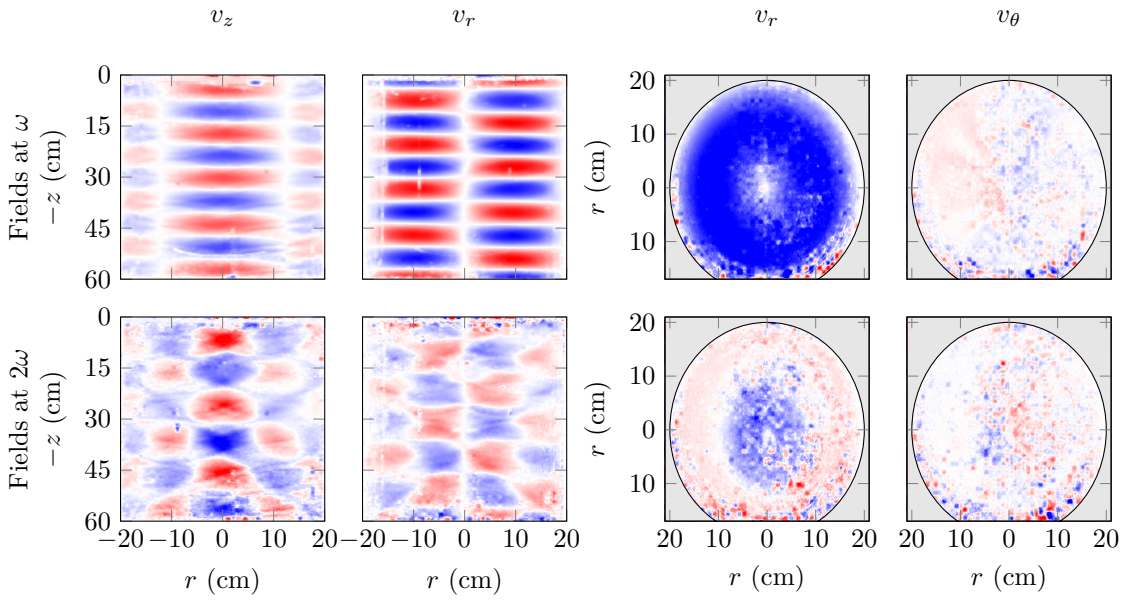

Figure 7.5: Velocity fields in experiment 5, with $2\omega/N = 0.755$, with generation of a mode $(2, 6)$.

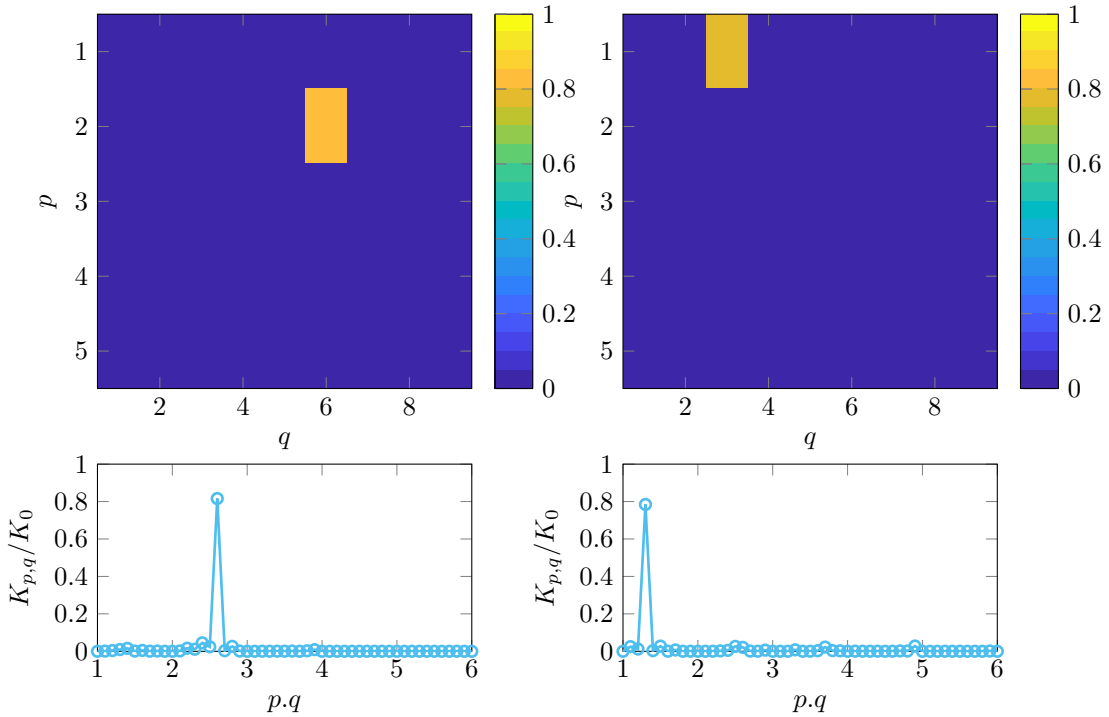

Figure 7.6: POD projection for experiments 5 (left) and 6 (right).

Experiment	ω/N	$2\omega/N$	(p,q) [%]		
1	0.309	0.618	$(1,5)$ [61%]	$(2,9)$ [18%]	
2	0.327	0.654	$(2,8)$ [61%]	$(1,4)$ [10%]	
3	0.345	0.690	$(1,4)$ [89%]		
4	0.364	0.728	$(1,4)$ [22%]	$(2,7)$ [21%]	
5	0.382	0.764	$(2,6)$ [82%]		
6	0.400	0.800	$(1,3)$ [78%]		
7	0.418	0.836	$(2,5)$ [35%]	$(1,3)$ [14%]	$(3,7)$ [8%]
8	0.436	0.872	$(2,4)$ [69%]	$(3,6)$ [9%]	
9	0.456	0.912	$(1,2)$ [47%]	$(3,5)$ [32%]	$(5,8)$ [8%]

Table 7.4: Forcing frequencies and their first harmonics, with identified dominating modes (in % of kinetic energy) using POD.

$\omega_{p,q}/N$	$p=1$	$p=2$	$p=3$	$p=4$	$p=5$
$q=1$	0.9647	0.9891	0.9948	0.9969	0.9980
$q=2$	**0.8774** [9]	0.9583	0.9795	0.9879	0.9920
$q=3$	**0.7733** [6,7]	0.9128	0.9555	0.9733	0.9823
$q=4$	**0.6750** [2,3,4]	**0.8589** [8]	0.9247	0.9540	0.9692
$q=5$	**0.5905** [1]	**0.8017** [7]	**0.8892** [9]	0.8307	0.9530
$q=6$	0.5207	**0.7453** [5]	**0.8509** [8]	0.9045	0.9344
$q=7$	0.4633	**0.6919** [4]	**0.8114** [7]	0.8762	0.9137
$q=8$	0.4159	**0.6424** [2]	0.7720	**0.8914** [9]	0.8914
$q=9$	0.3766	**0.5975** [1]	0.7336	0.8165	0.8680

Table 7.5: Reproduction of table 7.3, showing the modes (p,q) identified in the POD. Bold red values of $\omega_{p,q}/N$ are the theoretical frequencies corresponding to the modes observed in the experiments. The associated experiments are indicated between brackets.

in the phase space ($x = \omega/N, y = p.q$), all the theoretical cavity modes that can be created according to table 7.3 (for $p = 1$ through 5 and $q = 1$ through 9). In parallel, each first harmonic frequency for experiment 1 to 9 is represented by a vertical dashed line at constant ω/N. At each of these frequencies, modes extracted from the POD projection of the filtered harmonic wave fields are represented by red dots in the phase space, where the colour intensity shows the energetic contribution of each dominant mode. To guide the eye, black rectangles link together an experimentally observed mode with its theoretical counterpart whose frequency is within 1 to 7% of the experimental frequency in all cases. This margin is of the order of the error on the buoyancy frequency N measured with the probe (about 4%). On a vertical dashed line, when a single red dot is plotted (see for example experiment 5), it means that the harmonic wave field looks like a single mode which, as shown by the linking rectangle, corresponds to the mode selected by the non-linear interaction. On the contrary, when several dots appear for a given harmonic frequency (see for example experiment 1), resonant conditions stated by the dispersion relation are not exactly fulfilled and the harmonic wave field is a combination of two or more modes, the system being unable to select a proper one.

Modes of lowest radial wave numbers seem likely to be selected through this weakly non-linear interaction and, indeed, the most energetic modes are for $p = 1$ and $p = 2$, whereas the few contributions observed at $p = 3$ and beyond are usually small. This behaviour can be explained by the resistance of the stratification against vertical motions, which makes the transfer of energy more efficient to lower radial modes and, especially, to a mode $p = 1$ whose structure is already forced by the wave generator. Higher modes, for $p > 5$ and $q > 9$, could also exist in the harmonic wave field, but, for clarity, they are not displayed in figure 7.7. When sounded, all of these modes show very little contribution to the overall kinetic energy (about a few percents maximum).

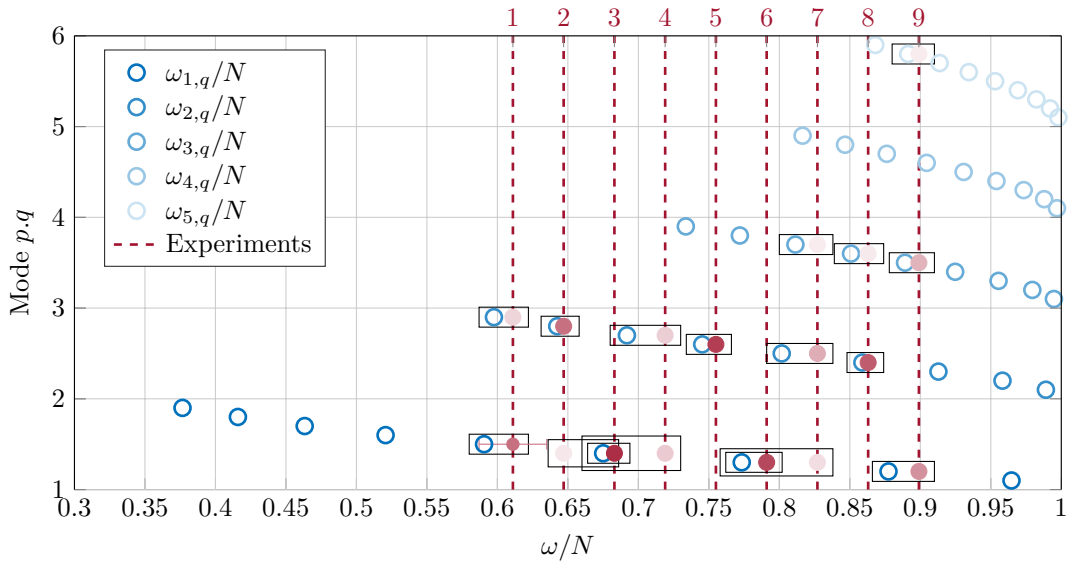

Figure 7.7: Selected modes vs. frequency. The blue circles show the frequencies and mode numbers of the cavity modes (p, q) (from table 7.3). The vertical red dashed lines show the first harmonics $(2\omega/N)$ seen in the 9 conducted experiments, which numbers are indicated above. On each line, red dots indicate the modes identified with POD, darker red meaning a more energetic mode. The correspondence between theory (circles) and experiments (dots) is shown by black rectangles.

7.4.7 Discussion

This study presents, to our knowledge, the first experimental evidence of internal wave harmonics created by weakly non-linear internal wave self-interaction in a linear stratification. As the excited wave field has a frequency below $N/2$, the first harmonic created can always propagate and the experimental PIV velocity fields display coherent structures when filtered at the harmonic frequency $2\omega/N$. With a simple analytical argument, we show that the confined domain provides restrictive boundary conditions so that the non-linear wave field has to satisfy a given set of constraints, leading to a discrete collection of radial and vertical wave numbers that can be predicted. The modes, or standing waves, defined by these relations constitute an excellent description of the first harmonic field in terms of a sum of several contributions.

Interestingly, and as recalled in section 7.2, self-interacting non-linear terms (the Jacobians) are null when computed using plane waves in Cartesian geometry. Hence, such a non-linear interaction cannot exist in linearly stratified fluids and, to obtain super-harmonics as in [16], a non-linear buoyancy frequency profile is required. This study shows that in axisymmetric geometry, however, self-interaction and super-harmonics generation is a common process even with linear stratifications. From a theoretical point of view, the exact generation process is not fully understood yet. A more detailed study, using Green functions, could be undertaken to derive the exact forcing terms that generate super-harmonics, but falls beyond the scope of this work.

Through a Proper Orthogonal Decomposition technique, we show that a mode selection occurs in the generation process the harmonic wave field. For some frequencies, the first harmonic reproduces almost perfectly a mode, both in the vertical and in the radial directions and, in other cases, the first harmonic is a sum of modal wave fields. Moreover, in all cases, the newly generated wave field remains axisysmmetric. Modes of lowest radial wave numbers seem likely to be selected through this weakly non-linear interaction and, indeed, the most energetic modes are for $p = 1$ and $p = 2$, whereas the few contributions observed at $p = 3$ and beyond are usually small. This behaviour can be explained by the resistance of the stratification against vertical motions, which makes the transfer of energy more efficient to lower radial modes and, especially, to a mode $p = 1$ whose structure is already forced by the wave generator. Higher modes, for $p > 5$ and $q > 9$, could also exist in the harmonic wave field, but, for clarity, they are not displayed in figure 7.7. When

tested using the POD decomposition, all of these modes show very little contribution to the overall kinetic energy (about a few percents maximum).

In such an experiment, other non-linear phenomena such as wave breaking or Triadic Resonant Instability (TRI), might occur. The underlying mechanisms, however, are likely to be different as, for example, they yield to the generation of sub-harmonics in the case of TRI, or they may involve a symmetry breaking [140] and a fully developped cylindrical wave field with potential orthoradial velocities, as we will discuss in the next section.

7.5 Sub-Harmonics and Triadic Resonant Instability

The dual phenomenon of the Super-Harmonic Generation (SHG) investigated in the previous section is a sub-harmonics generation mechanism called Triadic Resonant Instability (TRI). As previously observed in various configurations [21, 145, 146, 213, 228], and shown in figure 7.8 reproduced from Joubaud *et al.* [107], TRI is characterised by the non-linear breaking of an energetic internal wave (usually called *mother wave*) into two waves of smaller frequency (*daughter waves*). A key feature of TRI is that the triad of waves is in resonance, which means their frequencies ω and wave vectors $\mathbf{k}$ are linked through a linear relation

$$\omega_0 = \omega_1 + \omega_2, \tag{7.60}$$

$$\mathbf{k_0} = \mathbf{k_1} + \mathbf{k_2}, \tag{7.61}$$

where ω_0 and $\mathbf{k_0}$ (respectively ω_1, ω_2 and $\mathbf{k_1}$, $\mathbf{k_2}$) are related to the mother wave (respectively the daughter waves). Snapshots of density gradient presented in figure 7.8 (top row) at different times show an example of such a non-linear interaction, for a vertical mode horizontally propagating in Cartesian two-dimensional geometry (from [107]). The filtered wave fields after 40 periods of forcing at the three resonant frequencies (figure 7.8 (bottom row)) show different wave patterns corresponding to the mother and daughter wave fields. Interestingly, although the excitation wave field is a vertical mode, the two sub-harmonics do not have any modal structure.

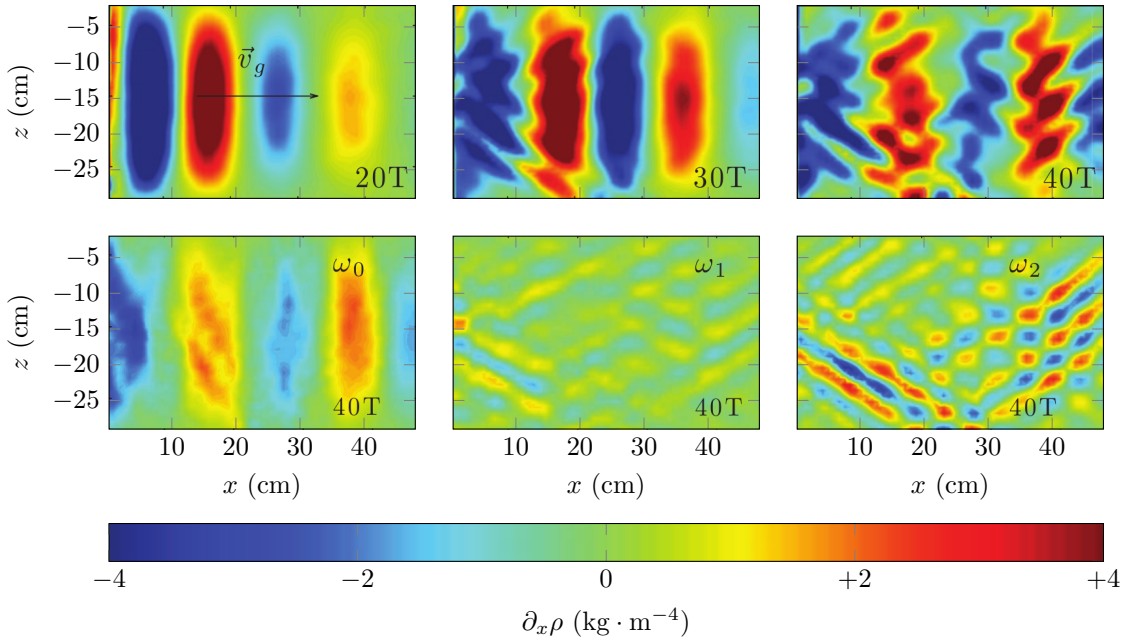

Figure 7.8: Snapshots of vertical density gradient, showing non-linear triadic interaction fed by a vertical mode horizontally propagating in Cartesian two-dimensional geometry. Top row: instantaneous field at different times, after 20, 30, and 40 forcing periods. Bottom row: filtered fields at the forcing frequency ω_0 and at the sub-harmonics frequencies ω_1 and ω_2, taken after 40 periods of forcing. Extracted from [107].

Numerous studies have been conducted on this non-linear phenomenon in 2D geometries [28, 107, 21], either experimental or theoretical. The cylindrical counterpart, however, is poorly documented. The existence of resonant triads in cylindrical geometry has been explored in the case of the elliptic instability and later extended to the Kelvin mode of azimuthal wave number $p = 1$ (see chapter 1 and appendix E), issued from the elliptic instability or from a precessional forcing [5, 6, 72, 88, 116, 115, 150]. Recent works have shown that TRI occurs in 3D geometries with axisymmetric excitations [140, 208], and that its characteristics are likely to be similar to the Cartesian case but they only focus on wave fields of small spatial extension. Although they both show evidence of symmetry breaking, these experimental studies show different results on the resonance condition: the equalities on frequencies and vertical wave numbers are satisfied, but while Maurer [140] did not measure a resonance condition on the radial wave number, Shmakova and Flór [208] managed to measure a condition on the horizontal wave number and found that they satisfy the resonant condition $m_0 = \pm m_1 \pm m_2$. In both cases the wave field is described by a combination of truncated Bessel functions that can be asymptotically approximated by plane wave beams, leaving open the question of exact resonance condition in cylindrical geometry. To date, 3D TRI has only been experimentally observed and studied locally and no exact derivation of cylindrical TRI has been undertaken.

In the present section, we first derive the theory for Cartesian 2D TRI and we extend it to axisymmetric and cylindrical geometry. Then, we present an experimental study of the generation of sub-harmonics in confined domains (the cavity) and in unconfined domains. The triadic resonant relations are further discussed, as well as the influence of the boundary conditions imposed by the horizontal (top and bottom) and cylindrical walls on the sub-harmonic properties.

7.5.1 Cartesian Two-Dimensional TRI

Triadic Resonant Interaction is depicted as the interaction of three waves, the mother wave at $(\omega_0, \mathbf{k_0})$, excited by the generation mechanism, and two daughter waves at $(\omega_1, \mathbf{k_1})$ and $(\omega_2, \mathbf{k_2})$, that grow out of noise. To investigate the TRI problem, we therefore assume that the total wave field is a sum of three interacting propagative waves with time-varying amplitudes

$$\psi(x,z,t) = \sum_{p=0}^{2} \psi_p^0(t) e^{i(\omega_p t - \mathbf{k_p}\cdot\mathbf{r})} + \text{c.c.}, \tag{7.62}$$

$$v_y(x,z,t) = \sum_{p=0}^{2} v_{y,p}^0(t) e^{i(\omega_p t - \mathbf{k_p}\cdot\mathbf{r})} + \text{c.c.}, \tag{7.63}$$

$$b(x,z,t) = \sum_{p=0}^{2} b_p^0(t) e^{i(\omega_p t - \mathbf{k_p}\cdot\mathbf{r})} + \text{c.c.}. \tag{7.64}$$

Resonance Condition

Isolating the linear and non-linear contributions in equations (7.18), (7.19), and (7.20), we can write these three equations under the form

$$\underbrace{\sum_{p=0}^{2} A_p e^{i(\omega_p t - \mathbf{k_p}\cdot\mathbf{r})}}_{\text{Linear terms}} = \underbrace{\sum_{m=0}^{2}\sum_{n=0}^{2} B_{mn} e^{i((\omega_m+\omega_n)t - (\mathbf{k_m}+\mathbf{k_n})\cdot\mathbf{r})}}_{\text{Non-linear terms}}, \tag{7.65}$$

where A_p and B_{mn} are amplitudes independent on spatial variables, but eventually time-dependent if we are studying the growth of the instability. As discussed in 7.2, $B_{mm} = 0$ because of the antisymmetry of the jacobian $\mathcal{J}$. Note that the result still holds if we consider the viscous equations ($\nu \neq 0$) as follows. The coefficients A_p and B_{mn} can be computed exactly as, on the first hand,

the computation of the linear terms gives

$$\begin{aligned}
\mathcal{J}(\Delta\psi,\psi) &= -\partial_t\Delta\psi - f\partial_z v_y + \partial_x b + \nu\Delta^2\psi && (7.66)\\
&= \sum_{p=0}^{2}\left(k_p^2(\dot{\psi_p^0} + i\omega_p\psi_p^0) + ifm_p v_{y,p}^0 - il_p b_p^0 + \nu k_p^4\psi_p^0\right)e^{i(\omega_p t - \mathbf{k_p}\cdot\mathbf{r})} + \text{c.c.}, && (7.67)\\
\mathcal{J}(v_y,\psi) &= -\partial_t v_y + f\partial_z\psi + \nu\Delta v_y && (7.68)\\
&= \sum_{p=0}^{2}\left(-\dot{v_{y,p}^0} - i\omega_p v_{y,p}^0 - ifm_p\psi_p^0 - \nu k_p^2 v_{y,p}^0\right)e^{i(\omega_p t - \mathbf{k_p}\cdot\mathbf{r})} + \text{c.c.}, && (7.69)\\
\mathcal{J}(b,\psi) &= -\partial_t b - N^2(z)\partial_x\psi && (7.70)\\
&= \sum_{p=0}^{2}\left(-\dot{b_p^0} - i\omega_p b_p^0 + iN^2 l_p\psi_p^0\right)e^{i(\omega_p t - \mathbf{k_p}\cdot\mathbf{r})} + \text{c.c.}, && (7.71)
\end{aligned}$$

and, on the other hand, the direct calculus of the non-linear terms writes

$$\begin{aligned}
\mathcal{J}(\Delta\psi,\psi) &= \sum_{p=0}^{2}\sum_{q=0}^{2} -(m_p l_q - l_p m_q)k_p^2\psi_p^0\psi_q^0 e^{i((\omega_p+\omega_q)t - (\mathbf{k_p}+\mathbf{k_q})\cdot\mathbf{r})} + \text{c.c.}, && (7.72)\\
\mathcal{J}(v_y,\psi) &= \sum_{p=0}^{2}\sum_{q=0}^{2}(m_p l_q - l_p m_q)v_{y,p}^0\psi_q^0 e^{i((\omega_p+\omega_q)t - (\mathbf{k_p}+\mathbf{k_q})\cdot\mathbf{r})} + \text{c.c.}, && (7.73)\\
\mathcal{J}(b,\psi) &= \sum_{p=0}^{2}\sum_{q=0}^{2}(m_p l_q - l_p m_q)b_p^0\psi_q^0 e^{i((\omega_p+\omega_q)t - (\mathbf{k_p}+\mathbf{k_q})\cdot\mathbf{r})} + \text{c.c.}. && (7.74)
\end{aligned}$$

For each equality, the j^{th} coefficient of the Fourier transform ($j = 0$, 1, or 2) can be rigorously identified by multiplying the equation by $e^{i(\omega_j t - \mathbf{k_j}\cdot\mathbf{r})}$ and by integrating the obtained equation over the space-time domain. Such an integral backs on the following property of a mathematical basis of a linear vectorial space

$$\int_{\mathbb{R}^4} e^{i(\omega_j t - \mathbf{k_j}\cdot\mathbf{r})}\cdot e^{i(\omega_p t - \mathbf{k_p}\cdot\mathbf{r})}\mathrm{d}t\,\mathrm{d}\mathbf{r} = \delta(\omega_j - \omega_p)\delta^3(\mathbf{k_j} - \mathbf{k_p}). \tag{7.75}$$

Therefore, the integration over the linear terms gives only the corresponding Fourier coefficient. The contribution on a single mode ω_0 can be written

$$A_0 = \sum_{m=0}^{2}\sum_{n=0}^{2} B_{mn}\delta(\omega_m + \omega_n - \omega_0)\delta(\mathbf{k_m} + \mathbf{k_n} - \mathbf{k_0}). \tag{7.76}$$

As $m \neq n$ and $\omega_p \neq 0$, the unique solution that allows an interaction between the waves is given by the resonance condition

$$\begin{aligned}
\omega_0 &= \omega_1 + \omega_2, && (7.77)\\
\mathbf{k_0} &= \mathbf{k_1} + \mathbf{k_2}, && (7.78)
\end{aligned}$$

and we obtain, using the notations of equation (7.76), coupled equations of the form

$$A_0 = B_{12}, \tag{7.79}$$

that are, explicitly

$$\begin{aligned}
-k_0^2(\dot{\psi_0^0} - i\omega_0\psi_0^0) - ifm_0 v_{y,0}^0 + il_0 b_0^0 - \nu k_0^4\psi_0^0 &= (m_1 l_2 - l_1 m_2)k_1^2\psi_1^0\psi_2^0, && (7.80)\\
-\dot{v_{y,0}^0} - i\omega_0 v_{y,0}^0 - ifm_0\psi_0^0 - \nu k_0^2 v_{y,0}^0 &= (m_1 l_2 - l_1 m_2)v_{y,1}^0\psi_2^0, && (7.81)\\
-\dot{b_0^0} - i\omega_0 b_0^0 + iN^2 l_0\psi_0^0 &= (m_1 l_2 - l_1 m_2)b_1^0\psi_2^0. && (7.82)
\end{aligned}$$

Similar equations can be obtained on $(\psi_1^0, v_{y,1}^0, b_1^0)$ and $(\psi_2^0, v_{y,2}^0, b_2^0)$, by a circular permutation of the indices 0, 1, and 2. Following the approach used in [28, 27, 140], we neglect the forcing term applied at a boundary (wave generator) in order to derive these equations.

When TRI occurs, the previous relations are verified between the primary wave (mother wave) and the secondary ones (daughter waves). As shown from experiments, the three waves respect both the temporal and the spatial resonance for the planar Cartesian case [27, 107, 140, 142]. Note that these results can be obtained whether considering exponential propagative waves or sine and cosine modes.

Polarisation Relations

For slow varying amplitudes, we can write $\dot{\psi}_p^0 \ll \omega_0 \psi_p^0$ (and similarly for $v_{y,p}^0$ and b_p^0), i.e. the characteristic time of the variation of the field amplitude is small compared to the temporal period of the waves. Therefore, in the inviscid limit, equations (7.80), (7.81), and (7.82) lead to the polarisation relations

$$v_{y,p}^0 = \frac{f m_p}{\omega_p} \psi_p^0 \qquad \text{and} \qquad b_p^0 = -\frac{N^2 l_p}{\omega_p} \psi_p^0, \tag{7.83}$$

from which we can recover the dispersion relation for internal waves after re-injecting the amplitudes $v_{y,p}^0$ and b_p^0 in the wave equations.

Growth Rate

Using the same time scale separation, we can write

$$\dot{v}_{y,p}^0 = \frac{f m_p}{\omega_p} \dot{\psi}_p^0 \qquad \text{and} \qquad \dot{b}_p^0 = -\frac{N^2 l_p}{\omega_p} \dot{\psi}_p^0, \tag{7.84}$$

in order to find the temporal evolution equation for the wave field. These equations are obtained by injecting the expression for $v_{y,p}^0$ and b_p^0 from equation (7.83), and $\dot{v}_p^0$ and $\dot{b}_p^0$ from equation (7.84), into equations (7.80), (7.81), and (7.82). The complete calculus leads to a second order differential equation on ψ_p^0 whose solutions are growing and decaying exponentials, such as

$$\psi_{1,2} = \psi_{1,2}^+ e^{+\sigma^+ t} + \psi_{1,2}^- e^{-\sigma^- t}, \tag{7.85}$$

where $\psi_{1,2}^+$ and $\psi_{1,2}^-$ are growing and decaying amplitudes for the two daughter waves, and σ^+ is the growth rate. The coefficient σ^- stands for decaying wave fields, and is not to be taken into account for the growth of the instability. The non-rotating ($N \neq 0$ and $f = 0$) solution has been explored by Bourget *et al.* [28] and the non-stratified ($N = 0$ and $f \neq 0$) solution by Bordes *et al.* [26]. In the more general case of inertia-gravity waves ($N \neq 0$ and $f \neq 0$), the growth rate has been computed by Maurer *et al.* [142]. For further details on the calculus and on the onset of the instability, the reader is refered to [140]. Note that the size of the interaction region also matters, which is discussed in more detail in [27, 140].

7.5.2 Axisymmetric TRI

As evidenced by Maurer [140] and Shmakova and Flór [208], Triadic Resonant Interaction occurs in cylindrical geometry. In both cases, although the forcing is axisymmetric (cylindrical wave generator [140] and vertically oscillating torus [208]), which ensures that the forcing mother field is axisymmetric, there are no prescriptions on the daughter waves to be axisymmetric. Experimental observations themselves are contradictory: if Shmakova and Flór [208] observed an axisymmetric wave field, the focusing configuration with the wave generator showed symmetry breaking highlighted by a non-zero radial velocity at the center in Maurer's experiments [140]. In this subsection, we assume that the wave field remains axisymmetric and we derive the corresponding theory for Triadic Resonant Instability using a similar method as in Cartesian. We also extend the results to the case of cylindrical wave fields (Kelvin modes) with an azimuthal wave number.

Resonance Condition

The set of equations (1.59), (1.60), and (1.61), derived in chapter 1, governing inertia-gravity wave dynamics, can be split into a linear left-hand side and a non-linear right-hand side, so that we write when taking into account the viscous terms

$$\partial_t \Delta_h \psi + f\partial_z v_\theta - \partial_r b - \nu\Delta_h^2\psi = -\mathcal{J}^\odot\left(r\psi, \frac{\Delta_h\psi}{r}\right) - \frac{2v_\theta}{r}\partial_z v_\theta, \tag{7.86}$$

$$\partial_t v_\theta - f\partial_z\psi - \nu\Delta_h v_\theta = -\frac{1}{r^2}\mathcal{J}^\odot(r\psi, rv_\theta), \tag{7.87}$$

$$\partial_t b + N^2\frac{1}{r}\partial_r(r\psi) = -\frac{1}{r}\mathcal{J}^\odot(r\psi, b). \tag{7.88}$$

We consider a wave field composed of three axisymmetric components as follows

$$\psi(r,z,t) = \sum_{p=0}^{2}\psi_p^0(t)J_1(l_p r)e^{i(\omega_p t - m_p z)} + \text{c.c.}, \tag{7.89}$$

$$v_\theta(r,z,t) = \sum_{p=0}^{2}v_{\theta,p}^0(t)J_1(l_p r)e^{i(\omega_p t - m_p z)} + \text{c.c.}, \tag{7.90}$$

$$b(r,z,t) = \sum_{p=0}^{2}b_p^0(t)J_0(l_p r)e^{i(\omega_p t - m_p z)} + \text{c.c.}. \tag{7.91}$$

solution of the linear equations. Using the same approach as for Cartesian TRI, we explicitly calculate the linear and non-linear terms in order to do the projection over the axisymmetric basis of exponentials and Bessel functions. The computation of the linear terms on the left-hand side yields

$$\mathcal{J}^\odot\left(r\psi, \frac{\Delta_h\psi}{r}\right) + \frac{2v_\theta}{r}\partial_z v_\theta = -\partial_t\Delta_h\psi - f\partial_z v_\theta + \partial_r b + \nu\Delta_h^2\psi, \tag{7.92}$$

$$= \sum_{p=0}^{2}\left(k_p^2(\dot{\psi_p^0} + i\omega_p\psi_p^0) + ifm_p v_{\theta,p}^0 - il_p b_p^0 + \nu k_p^4\psi_p^0\right) \tag{7.93}$$

$$\times J_1(l_p r)e^{i(\omega_p t - m_p z)} + \text{c.c.}, \tag{7.94}$$

$$\frac{1}{r^2}\mathcal{J}^\odot(r\psi, rv_\theta) = -\partial_t v_\theta + f\partial_z\psi + \nu\Delta_h v_\theta, \tag{7.95}$$

$$= \sum_{p=0}^{2}\left(-\dot{v_{\theta,p}^0} - i\omega_p v_{\theta,p}^0 - ifm_p\psi_p^0 - \nu k_p^2 v_{y,p}^0\right) \tag{7.96}$$

$$\times J_1(l_p r)e^{i(\omega_p t - m_p z)} + \text{c.c.}, \tag{7.97}$$

$$\frac{1}{r}\mathcal{J}^\odot(r\psi, b) = -\partial_t b - N^2\frac{1}{r}\partial_r(r\psi). \tag{7.98}$$

$$= \sum_{p=0}^{2}\left(-\dot{b_p^0} - i\omega_p b_p^0 + iN^2 l_p\psi_p^0\right) \tag{7.99}$$

$$\times J_0(l_p r)e^{i(\omega_p t - m_p z)} + \text{c.c.} \tag{7.100}$$

and, for the non-linear terms on the right-hand side

$$\mathcal{J}^{\odot}\left(r\psi, \frac{\Delta_h \psi}{r}\right) + \frac{2v_\theta}{r}\partial_z v_\theta = \sum_{p=0}^{2}\sum_{q=0}^{2}\left[l_q m_p J_1(l_p r)J_2(l_q r) - l_p m_q J_0(l_p r)J_1(l_q r)\right] \quad (7.101)$$

$$\times \psi_p^0 \psi_q^0 k_q^2 e^{i((\omega_p+\omega_q)t-(m_p+m_q)z)}, \quad (7.102)$$

$$\frac{1}{r^2}\mathcal{J}^{\odot}(r\psi, rv_\theta) = \sum_{p=0}^{2}\sum_{q=0}^{2}\left[m_p l_q J_1(l_p r)J_0(l_q r) - l_p m_q J_0(l_p r)J_1(l_q r)\right] \quad (7.103)$$

$$\times i\psi_p^0 v_{\theta,q}^0 e^{i((\omega_p+\omega_q)t-(m_p+m_q)z)}, \quad (7.104)$$

$$\frac{1}{r}\mathcal{J}^{\odot}(r\psi, b) = \sum_{p=0}^{2}\sum_{q=0}^{2}\left[m_p l_q J_1(l_p r)J_1(l_q r) - m_q l_p J_0(l_p r)J_0(l_q r)\right] \quad (7.105)$$

$$\times i\psi_p^0 b_q^0 e^{i((\omega_p+\omega_q)t-(m_p+m_q)z)}. \quad (7.106)$$

We now generalise the projection method used in the previous subsection for Cartesian TRI. The Fourier-Hankel scalar product allows for the identification of the coefficients thanks to the mathematical identity of orthogonality of exponentials and Bessel functions. Using the notation $\psi_{nj}(r,z,t) = J_n(l_j r)e^{i(\omega_j t - m_j z)}$, we have

$$\langle \psi_{nj}, \psi_{np}\rangle = \frac{1}{R^2}\int_0^R J_n(l_j r)J_n(l_p r)r\,\mathrm{d}r \int_{\mathbb{R}^2} e^{i(\omega_j t - m_j z)}\cdot e^{i(\omega_p t - m_p z)}\mathrm{d}t\,\mathrm{d}z, \quad (7.107)$$

$$= \frac{1}{2}\left[J_n'(l_j R)\right]^2 \delta(l_j - l_p)\delta(\omega_j - \omega_p)\delta(m_j - m_p), \quad (7.108)$$

where R is the radius of the cylinder (hence, by construction, $l_j R$ are zeros of the Bessel functions). From the projection, we obtain two conditions for resonance on the frequencies and on the vertical wave numbers, identical to the ones displayed in equations (7.77) and (7.78) using plane wave Cartesian formulation

$$\omega_0 = \omega_1 + \omega_2, \quad (7.109)$$

$$m_0 = m_1 + m_2. \quad (7.110)$$

The radial dependence, however, is more complex. Integration over the radial coordinates yields

$$k_0^2(\dot{\psi_0^0} + i\omega_0\psi_0^0) + ifm_0 v_{\theta,0}^0 - il_0 b_0^0 + \nu k_0^4 \psi_0^0 = \frac{2\psi_1^0\psi_2^0 k_2^2}{\left[J_1'(l_0 R)\right]^2}\left[m_1 l_2 \Xi_{112} - m_2 l_1 \Xi_{101}\right], \quad (7.111)$$

$$-\dot{v_{\theta,0}^0} - i\omega_p v_{\theta,0}^0 - ifm_0\psi_0^0 - \nu k_0^2 v_{\theta,0}^0 = \frac{2i\psi_1^0 v_{\theta,2}^0}{\left[J_1'(l_0 R)\right]^2}\left[m_1 l_2 \Xi_{110} - m_2 l_1 \Xi_{101}\right], \quad (7.112)$$

$$-\dot{b_0^0} - i\omega_0 b_0^0 + iN^2 l_0 \psi_0^0 = \frac{2i\psi_1^0 b_2^0}{\left[J_0'(l_0 R)\right]^2}\left[m_1 l_2 \Xi_{011} - m_2 l_1 \Xi_{000}\right], \quad (7.113)$$

where we define

$$\forall (h,i,j) \in \mathbb{N}^3,\ \Xi_{hij} = \frac{1}{R^2}\int_0^R J_h(l_0 r)J_i(l_1 r)J_j(l_2 r)r\,\mathrm{d}r. \quad (7.114)$$

Hence, a sufficient condition for radial resonance is that the right-hand side of equations (7.111), (7.112), and (7.111) is non-zero, so that a forcing is exerted on the linear equation. This is ensured if the terms Ξ_{hij} for $(h,i,j) \in \mathbb{N}^3$ involved in these equations are non-zero. According to previous works on TRI in Cartesian geometry, and based on the observations of Shmakova and Flór [208], the solution given by the resonance relation $l_0 = l_1 + l_2$ is likely to satisfy this condition. Its unicity, however, is still to be verified.

Numerical Investigation of the Radial Condition

The coefficients Ξ_{hij} involed in equations (7.111), (7.112), and (7.113), can be numerically investigated. Figure 7.9 presents colormaps of the normalised absolute value of these coefficients (i.e.

the ratio $|\Xi_{hij}|/\max(|\Xi_{hij}|)$ for: (a) $|\Xi_{112}|$; (b) $|\Xi_{110}|$; (c) $|\Xi_{011}|$; (d) $|\Xi_{101}|$; (e) $|\Xi_{000}|$. The last colormap (f) shows the product of the first three quantities, also normalised. All quantities are plotted as a function of l_1/l_0 and l_2/l_0, with l_1/l_0 and l_2/l_0 going from 0 to 2. The plots can be extended by symmetry and one can get the complete diagram for l_1/l_0 and l_2/l_0 going from -2 to $+2$. We can see that, although the five coefficients $|\Xi_{112}|$, $|\Xi_{110}|$, $|\Xi_{011}|$, $|\Xi_{101}|$, and $|\Xi_{000}|$, have different behaviours at a random location in the parameter space $(l_1/l_0, l_2/l_0)$, they generally show maximum values on the diagonals such that $\pm l_1 \pm l_2 = l_0$. Their product is even more eloquent, as there is a clear maximum for $\pm l_1 \pm l_2 = l_0$ whereas the product is almost zero everywhere else. From these observations, we conjecture that the most likely values for radial wave numbers in TRI, for which relations (7.111), (7.112), and (7.113) have non-zero right-hand sides, satisfy the relation $l_0 = l_1 + l_2$, as shown experimentally by [208] and as already observed for Cartesian plane waves where it can be analytically demonstrated that $\pm l_1 \pm l_2 = l_0$ is a necessary condition (see equation (7.78)).

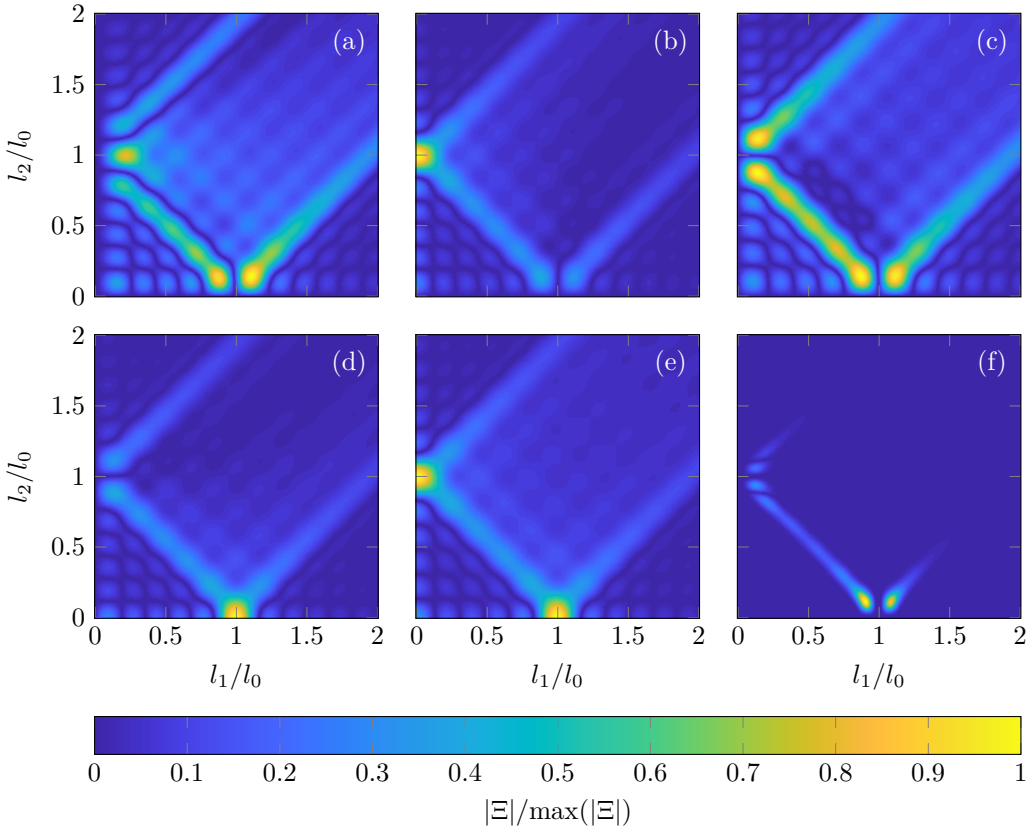

Figure 7.9: Colormaps of the normalised coefficients $|\Xi_{hij}|$ as a function of wave number ratios l_1/l_0 and l_2/l_0 with: (a) $|\Xi_{112}|$; (b) $|\Xi_{110}|$; (c) $|\Xi_{011}|$; (d) $|\Xi_{101}|$; (e) $|\Xi_{000}|$; (f) product of the five previous quantitites.

Asymptotics

A possible way to investigate further the radial resonance condition is to use an asymptotic development of the Bessel functions. At a given radial wave number l, for large values of lr, the functions J_n can be approximated by the functions $\tilde{J}_n$ defined as follows [163]

$$\forall n \in \mathbb{N},\ \forall r \in \mathbb{R}^*,\ \tilde{J}_n(lr) = \sqrt{\frac{2}{\pi lr}} \cos\left(lr - \frac{\pi}{2}\left(n + \frac{1}{2}\right)\right), \tag{7.115}$$

from what we deduce

$$\forall r \in \mathbb{R}^*,\ \tilde{J}_0(lr) = \sqrt{\frac{2}{\pi lr}}\cos\left(lr - \frac{\pi}{4}\right) \qquad \text{and} \qquad \tilde{J}_1(lr) = \sqrt{\frac{2}{\pi lr}}\sin\left(lr - \frac{\pi}{4}\right). \tag{7.116}$$

These approximations are presented in figure 7.10 for (a) $n = 0$ and (b) $n = 1$. As can be seen in these plots, the values of lr for which the approximation (7.115) is valid is $lr > 1$ for J_0 and $lr > 3$ for J_1, thus, in general, this constitutes a good approximation of the Bessel functions. Compared to our experimental configuration of a radial mode 1 with $l = 19\ \mathrm{m}^{-1}$, this means that the profile is very well approximated by this decaying cosine for $r > 15$ cm, and sooner for higher order radial modes.

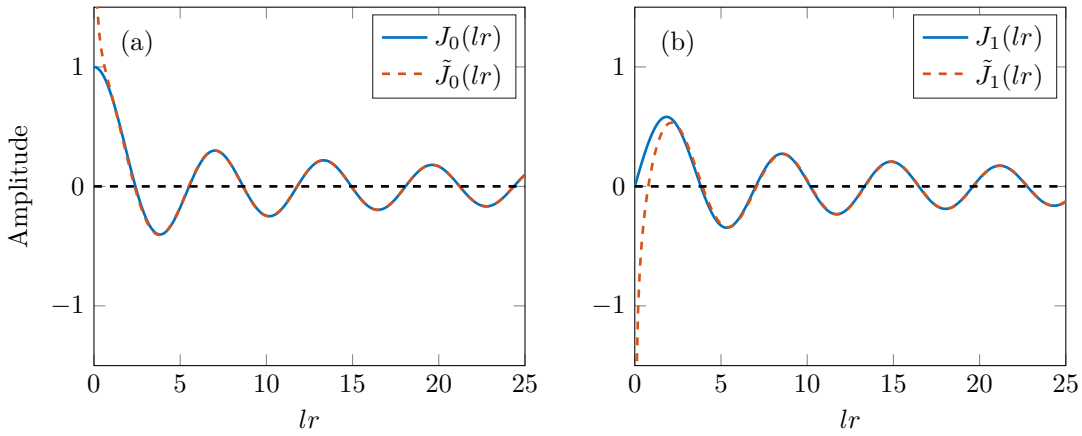

Figure 7.10: Plots of the functions (a) J_0 and (b) J_1 (solid line) with the asymptotics approximation $\tilde{J}_0$ and $\tilde{J}_1$ (dashed lines).

The coefficient Ξ_{hij} previously defined in equation (7.114) can be rewritten, using this asymptotic formulation, as

$$\forall (h,i,j) \in \mathbb{N}^3,\ \Xi_{hij} \simeq \lim_{\varepsilon \to 0} \frac{1}{R^2} \int_{\varepsilon}^{R} \tilde{J}_h(l_0 r)\tilde{J}_i(l_1 r)\tilde{J}_j(l_2 r) r \,\mathrm{d}r. \tag{7.117}$$

Using the definition from equation (7.115) and trigonometric relations, we find that the coefficient Ξ_{hij} can be expressed as a sum of integrals over approximated Bessel functions

$$\forall (h,i,j) \in \mathbb{N}^3,\ \Xi_{hij} \simeq \Gamma(1,h,i,j) + \Gamma(0,h,i,-j) + \Gamma(0,h,-i,j) + \Gamma(-1,h,-i,-j), \tag{7.118}$$

where, given $(a,b,c,d) \in \mathbb{Z}^4$, we write

$$\Gamma(a,b,c,d) = \lim_{\varepsilon \to 0} \frac{1}{R^2} \int_{\varepsilon}^{R} \frac{1}{2\pi} \sqrt{\frac{l_{bcd}}{l_0 l_1 l_2}} \tilde{J}_{a+b+c+d}(l_{bcd} r)\,\mathrm{d}r, \tag{7.119}$$

with, using the sign function, the radial interaction wave number l_{abc} defined by

$$l_{bcd} = \mathrm{sign(b)}l_0 + \mathrm{sign(c)}l_1 + \mathrm{sign(d)}l_2. \tag{7.120}$$

Note that the four Γ integrals are linked to four different radial interaction wave number l_{abc} as shown in table 7.6. Interestingly, the cases $l_{bcd} = 0$ correspond to the four possible triads that can be obtained.

$\Gamma(a,b,c,d)$	$\Gamma(1,h,i,j)$	$\Gamma(0,h,i,-j)$	$\Gamma(0,h,-i,j)$	$\Gamma(-1,h,-i,-j)$
l_{bcd}	$l_0 + l_1 + l_2$	$l_0 + l_1 - l_2$	$l_0 - l_1 + l_2$	$l_0 - l_1 - l_2$

Table 7.6: Radial interaction wave number l_{bcd} corresponding to the different Γ integrals.

Thanks to trigonometric relations and change of variables, these Γ integrals can be explictly described by a sum of Fresnel integrals C and S (see appendix D and [163]) as follows

$$\Gamma(a,b,c,d) = \Gamma^{\mathsf{C}}(a,b,c,d) + \Gamma^{\mathsf{S}}(a,b,c,d), \tag{7.121}$$

with

$$\Gamma^{\mathsf{C}}(a,b,c,d) = \sqrt{\frac{2}{\pi^3 R^3 l_0 l_1 l_2}} \cos\left(\frac{\pi}{2}\left(a+b+c+d+\frac{1}{2}\right)\right) \frac{\mathsf{C}\left(l^*_{bcd}\right)}{l^*_{bcd}}, \tag{7.122}$$

and

$$\Gamma^{\mathsf{S}}(a,b,c,d) = \sqrt{\frac{2}{\pi^3 R^3 l_0 l_1 l_2}} \sin\left(\frac{\pi}{2}\left(a+b+c+d+\frac{1}{2}\right)\right) \frac{\mathsf{S}\left(l^*_{bcd}\right)}{l^*_{bcd}}, \tag{7.123}$$

where, for the sake of clarity, we use the notation

$$l^*_{bcd} = \sqrt{\frac{2R|l_{bcd}|}{\pi}}, \tag{7.124}$$

for the reduced interaction radial wave number l^*.

If l_0, l_1, and l_2 are linked by a triadic relation so that $l_{bcd} = 0$ for given $(b,c,d) \in \mathbb{Z}^3$, then one of the four Γ integrals has a reduced interaction radial wave number l^*_{bcd} equal to zero whereas the three other have non-zero reduced interaction radial wave numbers. The corresponding disjonctive case study is presented in table 7.7. The reduced interaction radial wave numbers l^* are therefore

Triadic relations: If...	$l_0+l_1+l_2=0$	$l_0+l_1-l_2=0$	$l_0-l_1+l_2=0$	$l_0-l_1-l_2=0$
Then $l_0+l_1+l_2=$	0	$2l_2$	$2l_1$	$2l_0$
Then $l_0+l_1-l_2=$	$-2l_2$	0	$2l_0$	$2l_1$
Then $l_0-l_1+l_2=$	$-2l_1$	$2l_0$	0	$2l_2$
Then $l_0-l_1-l_2=$	$2l_0$	$-2l_1$	$-2l_2$	0

Table 7.7: Disjunctive case study showing the values of $l_0 \pm l_1 \pm l_2$ when a triadic relation between the radial wave numbers is satisfied.

either 0 or have relatively high values ($l^* \gg 1$) as, for example, typical values for l_0, l_1, and l_2 are 19, 35, or 51 m^{-1} for cavity modes. By studying the limits of $x \mapsto \mathsf{C}(x)/x$ and $x \mapsto \mathsf{S}(x)/x$, we deduce that Γ^{S} always goes to zero (and exactly zero if $l^* = 0$) and that Γ^{C} is equal to 1 if $l^* = 0$ and goes to zero for the three others. Hence, the only contributing Γ integral is the one for which $l^* = 0$, and we can write

$$|\Xi_{hij}| \simeq \frac{1}{\sqrt{\pi^3 R^3 l_0 l_1 l_2}}, \tag{7.125}$$

for $(hij) = (112)$, (110), (011), (101), and (000) (that correspond to Ξ_{hij} involved in equations (7.111), (7.112), and (7.113)). The five Ξ integrals are therefore non-zero, and have approximatively the same norm. It can also be shown that they are maximal since $\mathrm{d}[C(x)/x]/\mathrm{d}x = 0$ for $x = 0$ (see appendix D). In this case, when the three radial wave numbers are linked by a linear relation of the form $l_0 = \pm l_1 \pm l_2$, the system of equations (7.111), (7.112), and (7.113) reduces to a system similar to (7.80), (7.81), and (7.82), allowing for the same resolution method as in Cartesian geometry. Although the result is approximate, this is an interesting finding that may contribute to the derivation of the resonance relation.

Polarisation Relations and Growth Rate

A similar method as previously explained for Cartesian plane waves can be used in axisymmetric geometry to derive the following polarisation relations

$$v^0_{\theta,p} = \frac{f m_p}{\omega_p}\psi^0_p \qquad \text{and} \qquad b^0_p = -\frac{N^2 l_p}{\omega_p}\psi^0_p, \tag{7.126}$$

as already predicted by the linear theory (see chapter 1) and identical to the ones derived for plane waves in equation (7.83). The time scale separation method, not derived in the present manuscript,

can be applied to derive the growth rate of the instability. A difference can be highlighted, as the growth rate here depends on the coefficients Ξ_{hij} and is therefore not identical to the growth rate in Cartesian coordinates.

7.5.3 Sub-Harmonics Generation in Confined Domain

We performed experiments for values of ω/N from 0.82 to 0.92, with a low amplitude ($a = 2.5$ mm) mode 1 configuration at the generator [33]. In several experiments, towards the end of the 10 minutes forcing one can observe the creation of sub-harmonics as presented in the spectrum in figure 7.11 computed using the last two minutes of the acquisition. Two daughter waves are created at frequencies smaller than the imposed forcing ($\omega_1/N = 0.36$ and $\omega_2/N = 0.55$) that satisfy the triadic resonant condition $\omega_1 + \omega_2 = \omega_0$, as $\omega_1 = 0.4\,\omega_0$ and $\omega_2 = 0.6\,\omega_0$.

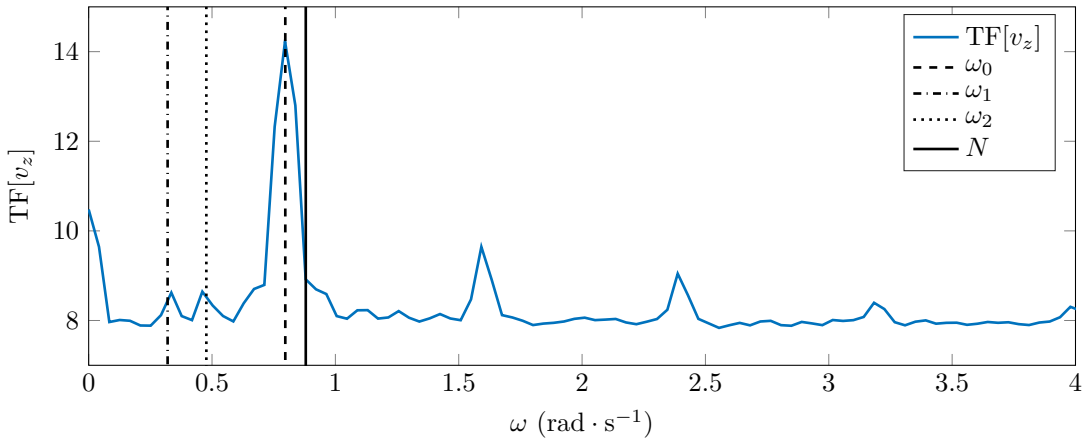

Figure 7.11: Fourier transform performed over the last two minutes of the experiment with a forcing at $\omega/N = 0.91$. From left to right: the dash-dotted line shows ω_1, the dotted line shows ω_2, both sub-harmonics, and the dashed line shows the forcing frequency ω_0, and the solid line shows the buoyancy frequency N

Filtered wave fields at the three frequencies ω_0, ω_1, and ω_2, are presented in figure 7.12, with the vertical velocity on top of the radial velocity. On the left, the mother wave shows high amplitude of about 4 mm · s^{-1}, and is close to be a cavity mode $(1, 2)$. The center and left columns are the two daughter waves identified from the spectrum 7.11, at ω_1 and ω_2 respectively. We identify 1 vertical wave length in the fields at ω_0, 5 in the fields at ω_1, and 5 in the fields at ω_2: hence the resonance condition is not satisfied for the vertical wave numbers, as we have $m_0 \pm m_2 \pm m_1 \neq 0$. Nevertheless, this is not observed in all our experiments with sub-harmonic generation as sometimes we have $m_0 = m_1 + m_2$ consistent with experimental data of Maurer [140] and Shmakova *et al.* [208]. As regards the radial direction, we see different patterns in the filtered wave fields: the fields at ω_0 and ω_1 look like a radial mode 1, but the field at ω_2 looks like a radial mode 2. This behaviour, however, is not a strong feature of the sub-harmonics generation *via* TRI, as some experiments only show radial mode 1 patterns.

In general, we observe that in this confined configuration, the resonant conditions are not satisfied. The reason could be that the selected frequencies and wave lengths are likely to be linked to the boundary conditions. As can be seen in figure 7.12, in the vertical plane, the sub-harmonics can be identified as cavity modes. For example, in figure 7.12, the field at ω_1 is a mode $(1, 10)$ and the field at ω_2 is a mode $(2, 10)$. Results from section 7.4 on SHG can be extended to this problem: the frequencies associated to these cavity modes $(1, 10)$ and $(2, 10)$ are $\omega_{1,10}/N = 0.34$ and $\omega_{2,12}/N = 0.56$, close to the experimental values of $\omega_1/N = 0.36$ and $\omega_2/N = 0.55$.

Contrary to the observations of Maurer [140] in his focusing experiments, but in agreement with Shmakova and Flór [208], we did not see any axisymmetry breaking in our experimental wave fields. Due to the poor visualisation in the horizontal plane, however, this statement could not be further explored. Our conjecture is that the presence of a cylindrical boundary at fixed radius might prevent the daughter waves from breaking the symmetry in a similar way as in Maurer's

observations in which non-zero radial velocity was detected [140]: such velocities, indeed, could not be described by the Bessel functions we used and could be contradictory to the condition of zero radial velocity at the cylindrical bound.

The mother and daughter waves are not always satisfying the TRI relations on the wave numbers, particularly the radial wave number, which means that the boundary conditions that set the cavity mode are, in that sense, "stronger" than the resonance conditions. In addition, part of the velocity fields are blurred, for example the vertical velocity at ω_1 and ω_2 close to $r = 0$ cm at the top and at the bottom of the tank (figure 7.12). This is likely due to the presence of other modes or to exchanges between the cavity mode and another wave field set by the TRI conditions. Similarly to Super-Harmonic Generation, the existence of resonance conditions in TRI may prescribe the cavity modes allowed for non-linear interaction.

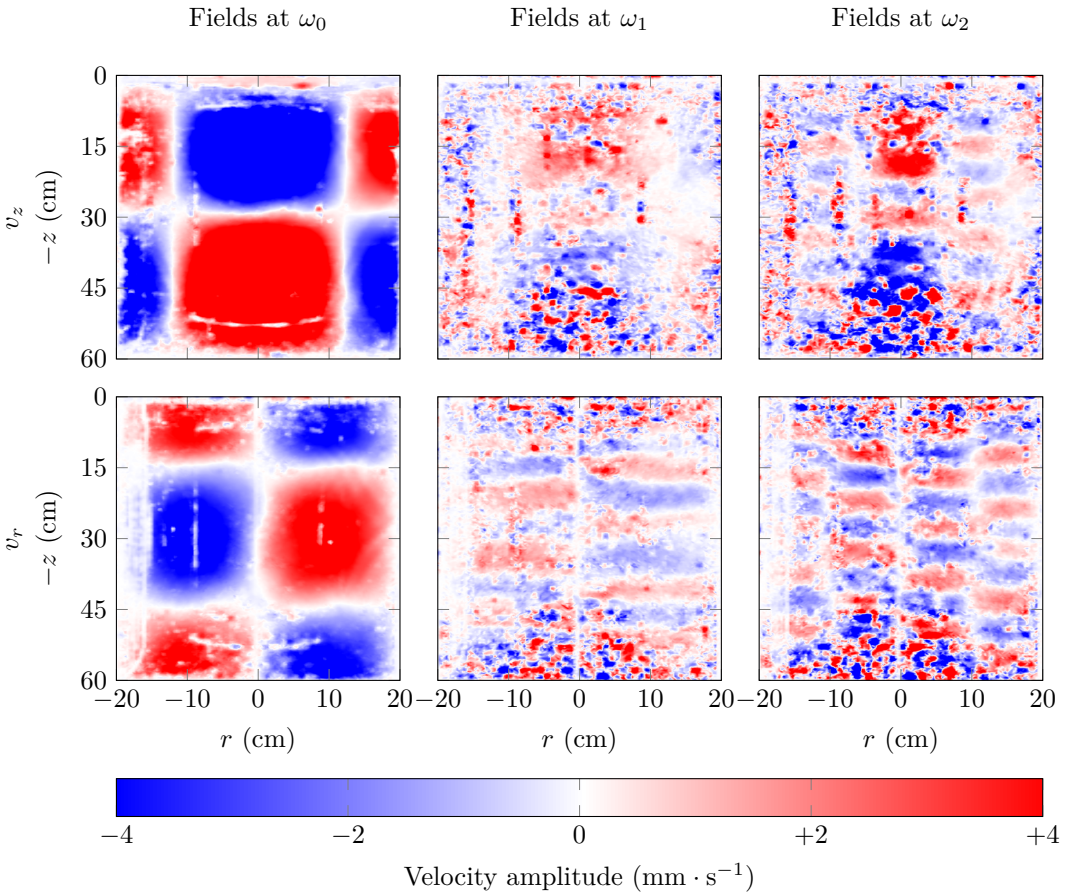

Figure 7.12: Vertical velocity (top row) and radial velocity (bottom row) after 9 minutes of forcing in the experiment. From left to right, fileds are filtered at ω_0, $\omega_1 = 0.4\,\omega_0$, and $\omega_2 = 0.6\,\omega_0$.

7.5.4 Unconfined Wave Fields, Rotation, and Symmetry Breaking

At the end of his PhD [140], Paco Maurer did some experiments involving density stratified and rotating fluid, generating axisymmetric inertia-gravity waves in an unconfined domain. The aim of these preliminary experiments was to trigger TRI with high sensitivity in the regime $(\omega/f, \omega/N)$ in which it is the most likely to occur [142]. Incidently, some of his experiments have shown resonant triads in cylindrical geometry, with a symmetry breaking. This subsection focuses on the analysis of one of these experiments, run at buoyancy frequency $N = 0.97$ rad · s^{-1} and Coriolis frequency $f = 0.294$ rad · s^{-1}. The forcing imposed at frequency $\omega_0 = 0.80$ rad · s^{-1} is a truncated Bessel function with a wave number $l_0 = 42$ m^{-1} and an amplitude $a = 15$ mm.

In order to discuss the frequency content and the transition between the linear and the non-

linear regime, we can compute the time-frequency diagram S_K [79] of the kinetic energy in the vertical plane $K = \rho_0(v_r^2 + v_z^2)/2$, given by

$$S_K(\omega, t) = \left\langle \left| \int_{-\infty}^{+\infty} K(r, z, t) e^{i\omega u} h(t-u)\, \mathrm{d}u \right|^2 \right\rangle, \tag{7.127}$$

where h is a Hamming window whose length can be tuned. On this diagram, presented in figure 7.13, we can see a peak at the forcing frequency $\omega_0 = 0.80$ rad $\cdot$ s^{-1} almost from the beginning of the experiment. After 200 s of forcing, two peaks appear and start growing at smaller frequencies, respectively $\omega_1 = 0.30$ rad $\cdot$ s^{-1} and $\omega_2 = 0.50$ rad $\cdot$ s^{-1}. Hence, these three frequencies satisfy the triadic resonant condition $\omega_0 = \omega_1 + \omega_2$.

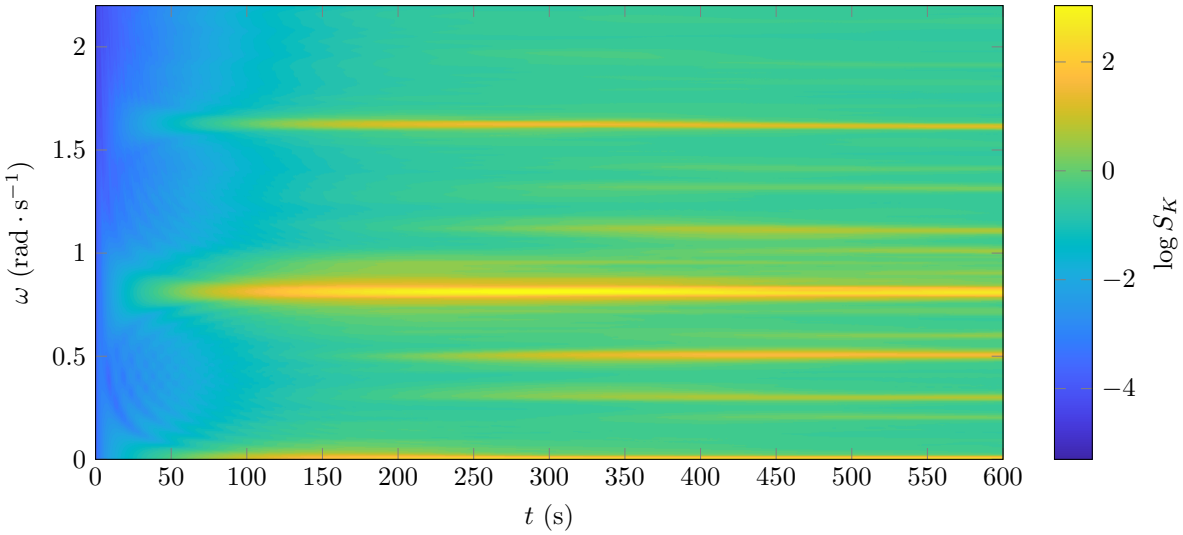

Figure 7.13: Time-frequency diagram computed for the experiment. The buoyancy frequency is $N = 0.97$ rad $\cdot$ s^{-1} and the Coriolis frequency $f = 0.294$ rad $\cdot$ s^{-1}. Forcing was imposed at a frequency $\omega_0 = 0.80$ rad $\cdot$ s^{-1}.

Velocity fields filtered at the frequencies associated with the observed TRI satisfying the resonance condition are presented in figure 7.14. In the vertical cross-section, we can estimate the vertical wave length and associated wave number m_j for $j \in \{0, 1, 2\}$. These values are presented in table 7.8. From our estimates, we verify the resonance condition on the vertical wave number as we have $m_0 \simeq m_1 - m_2$.

Field at frequency ω_j	ω_0	ω_1	ω_2
Vertical wave length (m)	0.40 ± 0.04	0.10 ± 0.02	0.13 ± 0.02
Corresponding wave number m_j (m^{-1})	15.7	62.8	48.4

Table 7.8: First zero r_j measured in the experiment and corresponding radial wave number l_j for the radial velocity fields filtered at ω_j, with $j \in \{0, 1, 2\}$.

The radial wave fields are described by Bessel functions of the first kind J_1 and are therefore of the form $J_1(l_j r)$ for $j \in \{0, 1, 2\}$. According to Beattie [17], the first zero of this Bessel function is equal to 3.83. For each value of j, the location r_j of the first zero can be identified in these velocity fields, and the corresponding wave number l_j can then be deduced ($l_j = 3.83/r_j$). These numbers are presented in table 7.9 for the three frequencies identified in figure 7.14. The radial wave number $l_0 = 42$ m^{-1} obtained for the mother wave is consistent with the imposed forcing. The two radial wave numbers for the daughter waves are close to satisfy the resonance relation $l_0 \simeq l_1 + l_2$.

Furthermore, there is a clear symmetry breaking as the velocity fields for the daughter waves at ω_1 and ω_2 start rotating clockwise and anti-clockwise respectively, meaning that there is an

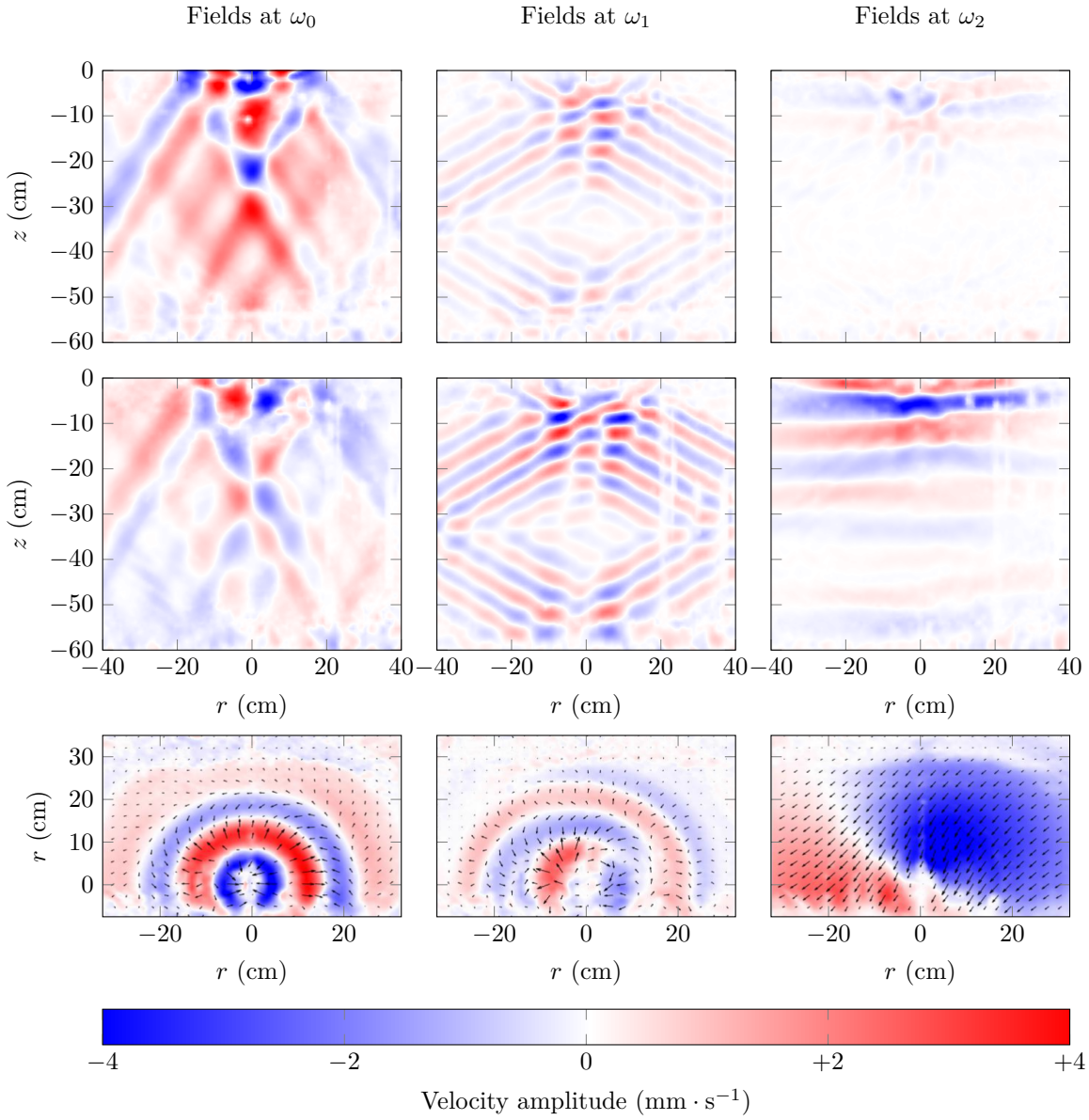

Figure 7.14: Radial velocity fields in an experiment run by Paco Maurer, with no confining cylinder, buoyancy frequency $N = 0.97$ rad · s^{-1} and Coriolis frequency $f = 0.294$ rad · s^{-1}. From left to right: mother wave at $\omega_0 = 0.80$ rad · s^{-1}, and daughter waves at $\omega_1 = 0.50$ rad · s^{-1} and $\omega_2 = 0.30$ rad · s^{-1}. The first two rows show the vertical and the radial velocities in the vertical cross-section, and the third row shows the radial velocity in the horizontal cross-section.

Field at frequency ω_j	ω_0	ω_1	ω_2
First zero identified r_j (m)	0.09 ± 0.01	0.12 ± 0.01	0.33 ± 0.03
Corresponding wave number l_j (m^{-1})	42	32	12

Table 7.9: First zero r_j measured in the experiment and corresponding radial wave number l_j for the radial velocity fields filtered at ω_j, with $j \in \{0, 1, 2\}$.

azimuthal wave number $p_1 = +1$ and $p_2 = -1$ respectively. The natural conjecture from this result is that a similar resonant condition would exist on the azimuthal wave number, as $p_0 = 0$, such that $p_0 = p_1 + p_2$. Using the cylindrical formalism derived in chapter 1, and a similar approach for TRI theory, this condition would be a direct consequence of the scalar product over the orthoradial coordinate θ.

7.5.5 Discussion and Further Work

We have derived the equations for Triadic Resonant Interaction (TRI) in axisymmetric geometry, following a similar method as used to deal with Cartesian plane waves. We have shown that, analytically, the resonance condition is the same in both geometries for the frequencies and the vertical wave numbers. A numerical study, supported by previous laboratory experiments [140, 208], led us to the conclusion that the resonance condition in axisymmetric geometry is likely to be the same in axisymmetric geometry, and we write

$$\omega_0 = \omega_1 + \omega_2, \tag{7.128}$$
$$m_0 = m_1 + m_2, \tag{7.129}$$
$$l_0 \simeq l_1 + l_2, \tag{7.130}$$

where the indices 0, 1, and 2, stand for the mother wave and the two daughter waves respectively.

Our experimental study of TRI in confined axisymmetric domain, however, shows that the cavity sets the spatial shape of the wave field and that the daughter waves are cavity modes. A similar behaviour may likely be found for Cartesian waves, although it has not been tested yet. Hence, in the confined case, only the resonance condition on the frequencies is satisfied. Interestingly, though Shmakova and Flór verified the resonance condition in their experiment [208], Maurer could not verify it and observed instead a symmetry breaking [140]. Adding rotation, the daughter wave fields are not axisymmetric anymore but cylindrical, with an azimuthal periodicity. The observation and understanding of TRI in large axisymmetric unconfined domains with and without rotation is, therefore, still a challenge.

7.6 Beating Behaviour

We now focus on the remaining frequency information that can be identified in the experiments. As mentioned in chapter 4 while studying confined modes in the wave resonator created by the cylindrical boundary, the bottom of the tank, and the wave generator at the top, a beating phenomenon may appear (see figure 4.10(a)). This periodically fading velocity is associated with a modulated amplitude, as can be seen in the time series of the vertical velocity v_z, presented in figure 7.15(a), computed over the whole experimental domain, when excited with a radial mode 1 forcing at low amplitude ($a = 2.5$ mm $\cdot$ s^{-1}) in a linear stratification ($N = 0.91$ rad $\cdot$ s^{-1}).

The spectral information of this experiment is shown in figure 7.15(b). It reveals a strong peak at $\omega_0 = 0.797$ rad $\cdot$ s^{-1}, corresponding to the forcing frequency. As expected from the non-linear theory discussed in section 7.4, super-harmonics are generated and appear at integer multiples of the forcing frequency past the solid line indicating the buoyancy frequency N. Close to ω_0, and still below N, a smaller peak can be seen at a frequency of 0.88 rad $\cdot$ s^{-1}. Although the harmonics correspond to evanescent waves, these two peaks at 0.797 and 0.88 rad $\cdot$ s^{-1} are related to propagating waves, and are responsible for the beating beahaviour observed in figure 7.15(a). According to table 7.3, the secondary peak is identical to a cavity mode at $\omega_{1,1}$. This phenomenon is observed in all experiments (see, for example, the two small peaks observed close to the forcing frequency in figure 7.1 on SHG), which means that the wave field adjusts itself to the cavity and, as the experiment is conducted, energy is transfered between the forcing frequency and the cavity mode. This is illustrated by the time-frequency spectrum presented in figure 7.16, showing the temporal evolution of the frequency content in the vertical velocity field.

The existence of the frequency $\omega_{1,1}$ can be confirmed by a quick calculation using the modulation frequency ω_{mod}. From figure 7.1(a), the modulation period of the beating pattern is $T_{\text{mod}} = 75$ s, meaning that $\omega_{\text{mod}} = 2\pi/T_{\text{mod}} = 0.084$ rad $\cdot$ s^{-1}. This frequency corresponds to the frequency

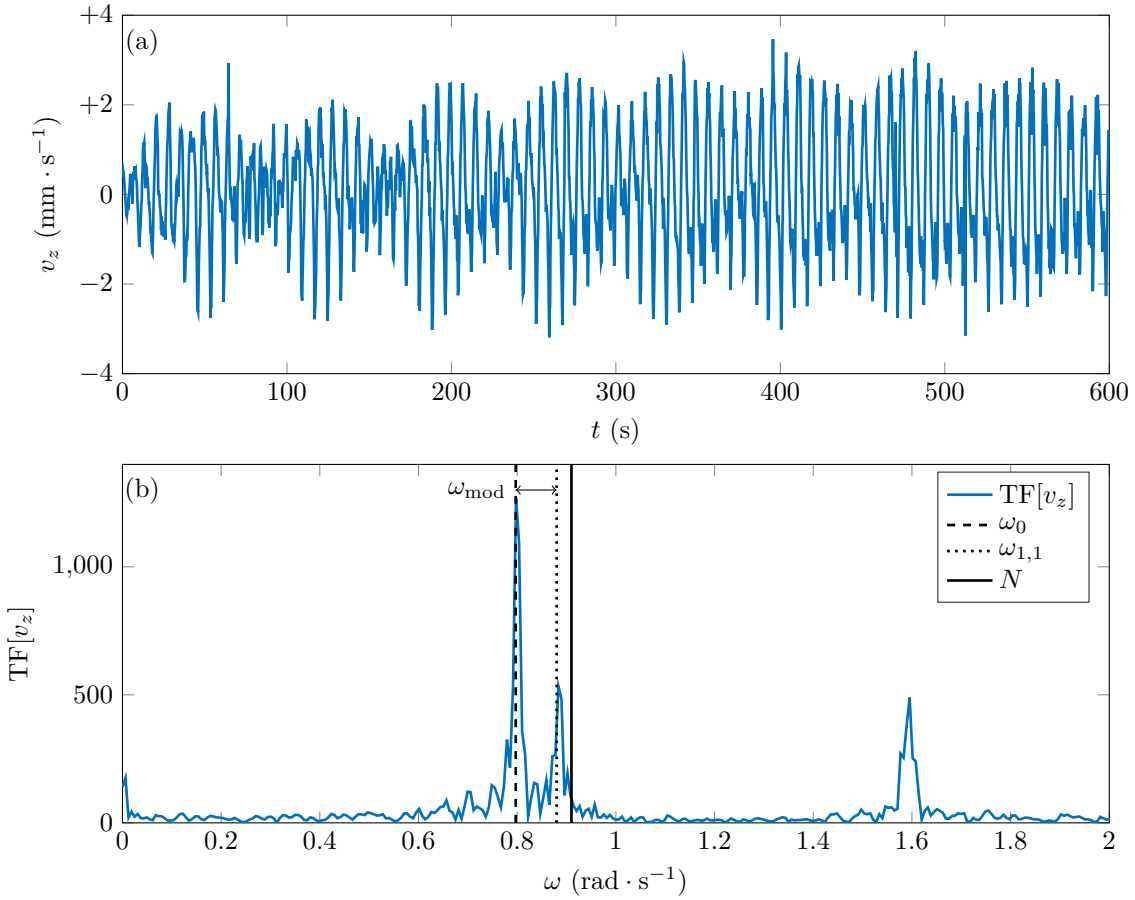

Figure 7.15: (a): Time series of the vertical velocity field over the whole experimental domain. (b): Fourier transform of the time series shown above, with the forcing frequency ω_0 (dashed line), the cavity mode frequency $\omega_{1,1}$ (dotted line), and the buoyancy frequency N (solid line). The modulation frequency ω_{mod} is highlighted by an arrow between ω_0 and $\omega_{1,1}$.

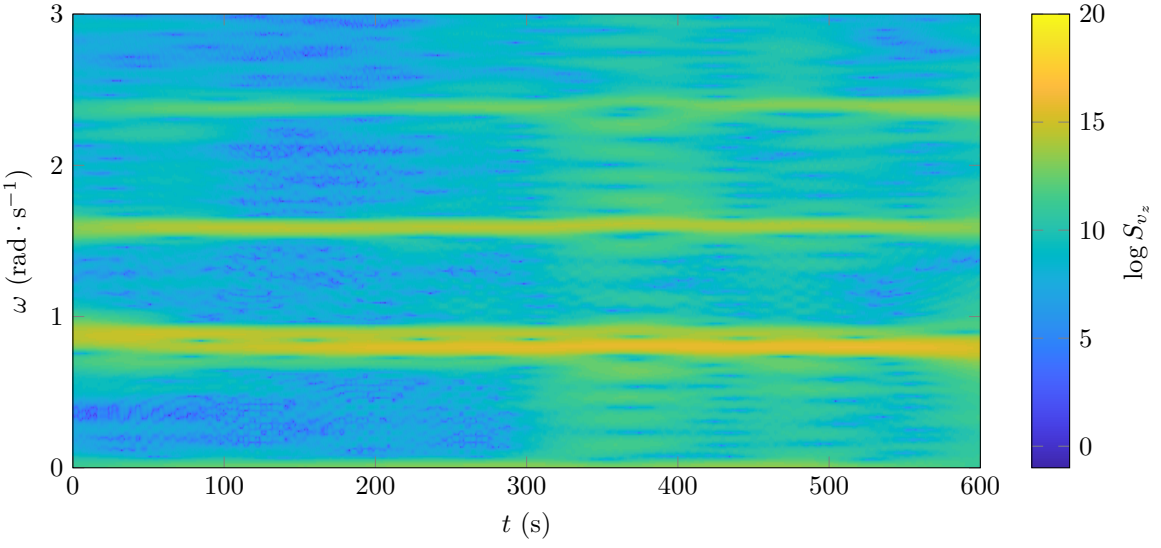

Figure 7.16: Time-frequency diagram of the vertical velocity field in the experiment.

shift between the forcing frequency and the cavity resonant frequency, as observed in figure 7.15(b). Accordingly, we obtain that $\omega_{\text{mod}} = \omega_{1,1} - \omega_0 = 0.074\text{rad} \cdot \text{s}^{-1}$.

We interpret the presence of a mode $(1,1)$ as follows. To satisfy the boundary conditions, the chosen radial profile is a radial mode 1 as it already corresponds to the excitation wave field. The vertical profile, which has to agree with the boundary conditions, can be shifted to either a mode with an odd or an even number of half vertical wave lengths. The reflection at the bottom, however, introduces a phase shift in the wave field, meaning that an even number of half wave lengths, although it satisfies the boundary conditions at the bottom and at the top, leads to destructive interference, and the odd wave number that leads to constructive interference is then more likely to be selected. As an example, in figure 7.15(b), the frequency $\omega_{1,1}$ corresponding to a mode $(1,1)$ appears instead of the frequency $\omega_{1,2}$ that would be associated to a non-resonant mode $(1,2)$.

7.7 Conclusions and Discussion

As pictured in figure 7.17, two phenomena are likely to appear during non-linear interactions and are used to describe the total wave field, namely Super-Harmonic Generation (SHG) and Triadic Resonant Instability (TRI). In the SHG case, the self-interaction of an internal wave at ω_0 creates super-harmonics, which means waves at $n\omega_0$ with $n \in \mathbb{N}$. In the TRI case, starting from an internal wave at ω_0, non-linear processes create two waves at lower frequency, ω_1 and ω_2, such that $\omega_1 + \omega_2 = \omega_0$. These two non-linear interactions can occur simultaneously.

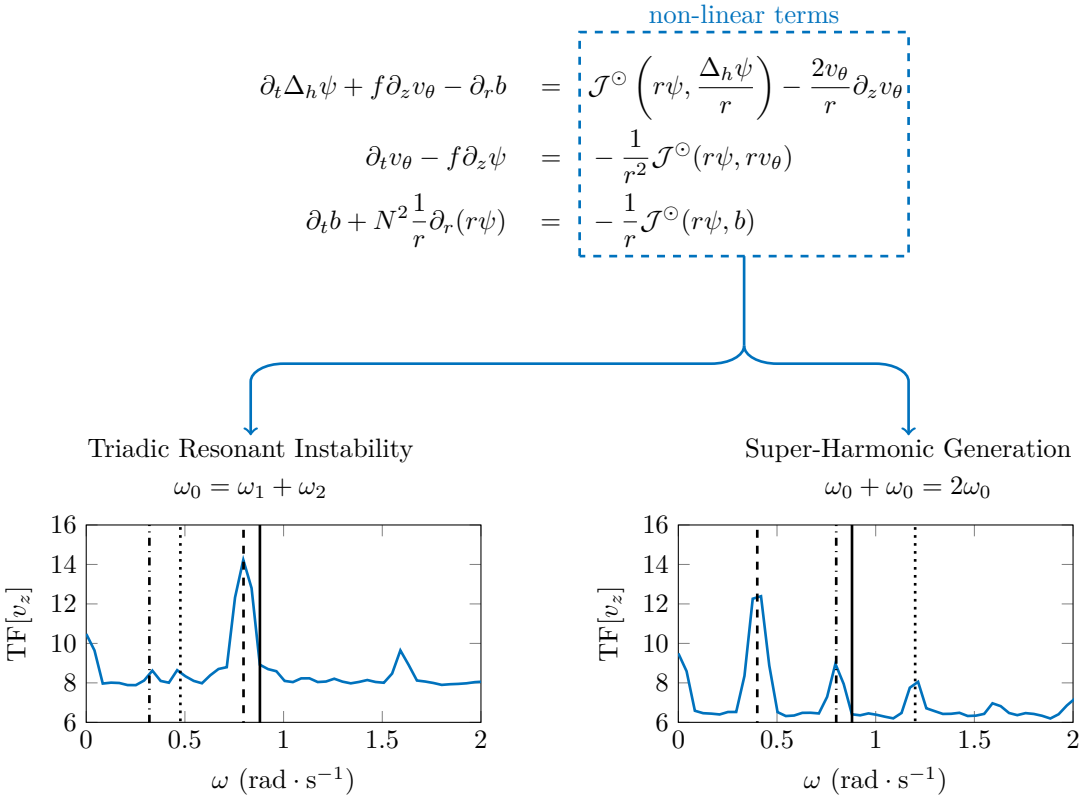

Figure 7.17: Schematic of the non-linear interaction from the set of internal wave equations, leading to either a three wave interaction (Triadic Resonant Instability (TRI)) or self-interaction (Super-Harmonic Generation (SHG)).

The prevalence of a phenomenon over the other can be explained by simple considerations. SHG is better observed at low forcing frequencies, for which the primary wave field and at least the first super-harmonic are propagating. In such a configuration, $\omega_0/N < 0.5$, and the excited

waves at ω_0 are more horizontal than vertical (in the non-rotating stratified case), producing shear on the different layers of the stratification. On the contrary, TRI only occurs at high frequencies, with $\omega_0/N > 0.7$. The excited wave field is then more vertical than horizontal and is penetrating more into the stratification, bending the layers of the stratification and producing instabilities at larger scales. From the criterion derived in section 7.1, as the vertical and the horizontal velocities depend on the frequency, we infer that SHG is better generated by non-linearities on the horizontal velocity, whereas TRI is generated by non-linearities coming from the vertical velocity.

It is important to note that these two non-linear mechanisms are not unique to axisymmetric internal waves. Triadic Resonant Instability (TRI) and Parametric Sub-harmonic Instability (PSI) have been first observed experimentally in two-dimensional Cartesian setups, and were therefore expected to be detected in our three-dimensional setup. Super-Harmonic Generation (SHG), however, is more specific to the axisymmetric configuration as the excitation of super-harmonics in linear stratification cannot occur with Cartesian plane waves, but directly comes to existence due to non-zero self-interaction terms with cylindrical wave fields. Nonetheless, although we have shown that the confined configuration (cavity) imposes the spatial shape of the wave field in TRI as in SHG, the relationship between the wave vectors in the unconfined geometry is still unclear as we have no exact proof of the resonant condition on the radial wave numbers.

The importance of SHG and TRI can henceforth be discussed. On the one hand, TRI is considered to be a key step in the non-linear cascade that would transfer energy from scale to scale [21, 253, 235]. Ongoing works on wave attractors have, indeed, proven experimentally the existence of an internal wave cascade [42]. On the other hand, SHG has recently been proposed as a step from which energy transfer can then downscale to reach the dissipation scale [239]. In the ocean, tidal excitation of semidiurnal modes could excite super-harmonics from near-inertial waves [62, 257]. In both TRI and SHG, waves at various frequencies are created out of non-linear interactions and energy is transferred between frequencies and scales, preliminary to mixing and dissipation events at small scales.

CHAPTER 8

Inertial Wave Attractors

C'est la tempête et le tonnerre. Pourquoi pas le silence
Du déluge, car nous avons en nous tout l'espace rêvé
Pour le plus grand silence et nous respirerons
Comme le vent des mers terribles, comme le vent
Qui rampe lentement sur tous les horizons.
Paul Éluard, Capitale de la douleur.

In the previous chapters, we have shown that the dispersion relation sets the angle of propagation of internal wave beams, and we have performed experimental studies of this phenomenon in non-rotating stratified fluids, where the angle of propagation β with respect to the vertical axis is given by

$$\sin\beta = \frac{\omega}{N}. \tag{8.1}$$

For non-stratified rotating fluids, a dual relation exists and the angle β is then given by the ratio of the wave frequency ω to the Coriolis frequency f as

$$\cos\beta = \frac{\omega}{f}. \tag{8.2}$$

Due to this relation, and as partially explored in the previous chapters, a rich variety of wave motions is encountered in rotating and stratified fluids as identified in early pioneering studies, and explored in details in subsequent literature: normal modes in bounded domains of simple geometry (sphere, cylinder, rectangular box) [7, 144, 145, 127, 23, 118, 24, 248], wave beams emanating from isolated oscillatory sources [91, 99, 225, 155], and webs of wave beams (wave attractors) in bounded domains with sloping walls [214, 40, 216, 217, 131, 129, 134], the latter configuration being the focus of the present chapter.

The propagation angle β being fixed only by a ratio of frequencies, a very specific law emerges for internal wave reflection upon a solid wall [173, 73, 135, 128]. In two-dimensional domains, a focusing-defocusing effect has been predicted and observed [59] and, in closed domains, the iteration of reflections leads to limit cycles called *wave attractors*. The branches of the attractor show increased density of energy that may trigger instabilities and, enventually, wave breaking and energy cascade [42]. In three-dimensional geometries, the variety of possible configurations is significantly enriched involving the possibility of wave-energy trapping upon limit cycle [97, 181]. In the case of a rotating spherical layer, theory predicts the formation of attractors in the meridional plane [130, 188] and the literature on the linear dynamics of inertial wave attractors in such layers usually considers the motions in the ring-shaped meridional slices [83, 63, 195, 194, 197] and disregards the azimuthal coordinate. The proposed study aims at triggering an instability in the

horizontal cross-section of an inertial wave attractor to study the azimuthal destabilisation and to delve into the symmetry breaking that occurs in the non-linear regime.

This chapter starts by a brief reminder on the general theory of internal wave attractors in section 8.1. Section 8.2 presents the experimental configuration used to perform this study, adapted from the cylindrical domain presented in chapter 2. Our results are detailed in section 8.3, with the study of the linear and non-linear regimes of the inertial wave attractor. Conclusions and discussion on the experiment are presented in section 8.4.

Results from this chapter are in preparation for *Journal of Fluid Mechanics* [36].

8.1 Theory of Internal Wave Attractors

8.1.1 Reflection of Internal Wave Beams

In optics and acoustics, wave reflection is governed by the well-known Snell-Descartes law, defining *specular reflection*. Considering the normal $\mathbf{n}$ of the material surface, the angle between $\mathbf{n}$ and the incoming wave beam is the same as between $\mathbf{n}$ and the reflected beam. As detailed in chapters 1 and 4, however, internal wave beams propagate along particular directions whose angles are set by the dispersion relation. These angles may differ from the one predicted by the Snell-Descartes law for a reflected wave beam. As detailed in [42, 171, 174], reflection of internal wave beams leads to two phenomena, the first one being non-specular reflection, and the second one being focusing-defocusing (see illustration in figure 8.1).

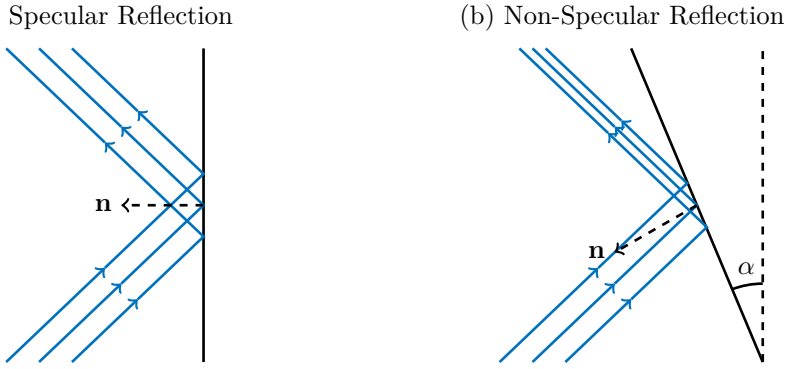

Figure 8.1: Left: specular reflection (Snell-Descartes law) of an internal wave beam on a vertical wall, where incidence and reflection angle are equal. Right: non-specular reflection of an internal wave beam, where the propagation angles before and after reflection are set by the dispersion relation.

Let us consider a material boundary, or a wall, inclined by an angle α with respect to the vertical (see figure 8.1(b)), and an incoming wave beam and a reflected wave beam, respectively described by the stream functions ψ_i and ψ_r. In Cartesian coordinates, they write

$$\psi_i(x,z,t) = \psi_i^0 e^{i(\omega_i t - \mathbf{k_i}\cdot\mathbf{x})}, \tag{8.3}$$
$$\psi_r(x,z,t) = \psi_r^0 e^{i(\omega_r t - \mathbf{k_r}\cdot\mathbf{x})}, \tag{8.4}$$

with ψ_i^0 and ψ_r^0 two constant amplitudes, ω_i and ω_r the wave frequencies, and $\mathbf{k_i}$ and $\mathbf{k_r}$ the wave vectors. Hence, the velocity field can be derived from the total stream function $\psi = \psi_i + \psi_r$.

On the wall, the non-penetration boundary condition imposes that the normal velocity $\mathbf{u}\cdot\mathbf{n}$ must be zero, where $\mathbf{n} = -(\cos\alpha, \sin\alpha)$. By defining coordinates attached to the wall $(\tilde{x}, \tilde{z})$, corresponding velocity components $(\tilde{u} = -\partial_{\tilde{z}}\psi, \tilde{w} = \partial_{\tilde{x}}\psi)$, and wave vector $\mathbf{k} = (k_{\tilde{x}}, k_{\tilde{z}})$, the boundary condition writes $\tilde{u} = 0$ at $\tilde{x} = 0$ which means, in terms of stream function

$$k_{\tilde{z},i}\psi_i^0 e^{i(\omega_i t - \mathbf{k_i}\cdot\mathbf{x})} + k_{\tilde{z},r}\psi_r^0 e^{i(\omega_r t - \mathbf{k_r}\cdot\mathbf{x})} = 0. \tag{8.5}$$

This relation must be satisfied at $\tilde{x} = 0$ for all $\tilde{z}$ and at all times t, leading to the following set of relations between the incoming and reflected quantities

$$\omega_i = \omega_r, \tag{8.6}$$
$$k_{\tilde{z},i} = k_{\tilde{z},r}, \tag{8.7}$$
$$\psi_i^0 = \psi_r^0, \tag{8.8}$$

and, by geometrical construction, the horizontal along-slope components of the wave vectors are given by [42]

$$k_{\tilde{x},i} = k_{\tilde{z},i} \tan(\beta - \alpha), \tag{8.9}$$
$$k_{\tilde{x},r} = k_{\tilde{z},r} \tan(\beta + \alpha). \tag{8.10}$$

Hence, we define the focusing-defocusing coefficient γ to be the ratio between the norms of the two wave vectors $\mathbf{k_i}$ and $\mathbf{k_r}$

$$\gamma = \frac{k_r}{k_i} = \left| \frac{\cos(\beta - \alpha)}{\cos(\beta + \alpha)} \right|. \tag{8.11}$$

From an energetic point of view, we can compute the density of kinetic energy in the incoming wave beam

$$K_i = \frac{1}{2}\left(u_i^2 + w_i^2\right) = \frac{1}{2}\left((\partial_z \psi_i)^2 + (\partial_x \psi_i)^2\right) = \frac{1}{2} k_i^2 \left|\psi_i^0\right|^2, \tag{8.12}$$

and in the reflected wave beam

$$K_r = \frac{1}{2}\left(u_r^2 + w_r^2\right) = \frac{1}{2}\left((\partial_z \psi_r)^2 + (\partial_x \psi_r)^2\right) = \frac{1}{2} k_r^2 \left|\psi_r^0\right|^2. \tag{8.13}$$

Therefore, the densities of kinetic energy are linked by the relation

$$K_r = \gamma^2 K_i, \tag{8.14}$$

leading to focusing ($\gamma > 1$) or defocusing ($\gamma < 1$) effect as the wave beam is reflected over the slope boundary. This phenomenon is illustrated in figure 8.1. In the case of a vertical wall (figure 8.1(a)), $\alpha = 0$ and $\gamma = 1$, corresponding to a specular reflection with no focusing effect. For $\alpha \neq 0$ (figure 8.1(b)), the reflection is non-specular with focusing or defocusing effect. The present calculation can be derived for an inclination of any of the four walls on which reflection occurs.

8.1.2 Limit Cycles

The study of internal wave reflection on an inclined boundary shows that reflections on horizontal or vertical walls are always specular, whereas reflections on inclined walls are non-specular. In the case of a confined trapezoidal domain, the subsequent reflections may lead to a closed limit cycle in which the focusing effect will increase the density of energy: such cycles are called *attractors*. Figure 8.2 shows examples of these limit cycles for inertial waves ($N = 0$ and $f \neq 0$) with: figure 8.2(a) $\omega/f = 0.406$, (b) $\omega/f = 0.224$, and (c) $\omega/f = 0.680$. Depending on the frequency, the limit cycle can be constituted of four reflections or more.

The variety of shapes of internal wave attractors in a closed trapezoidal domain of width L and maximum height H depends on the following three non-dimensional parameters: the aspect ratio L/H of the domain, the angle α of the inclined wall, and the angle β of propagation of waves (with $\tan^2\beta = (\omega^2 - f^2)/(N^2 - \omega^2)$). Maas *et al.* [129] have shown that the control parameters of such a system can be actually reduced to two non-dimensional numbers $d = 1 - (2L/H)\tan\alpha$ and $\tau = (2L/H) \times 1/\tan\beta$. They have summarised the variety of shapes of the attractors in the (d, τ) diagram reproduced in figure 8.3, where the greyscale shows the logarithm of $-\Lambda$, with Λ the Lyapunov exponent of the trajectories, as defined in [131]. High values of $|\Lambda|$ correspond to regions where attractors exist. These regions are labelled by two numbers $(p, q) \in \mathbb{N}^2$, where p indicates the number of reflections at the top boundary and q the number of reflections on the vertical boundary. For example, figure 8.2(a) corresponds to a $(1, 1)$ attractor, figure 8.2(b) to a $(3, 1)$ attractor, and figure 8.2(c) to a $(1, 2)$ attractor. From now, we only consider $(1, 1)$ attractors with pure inertial waves.

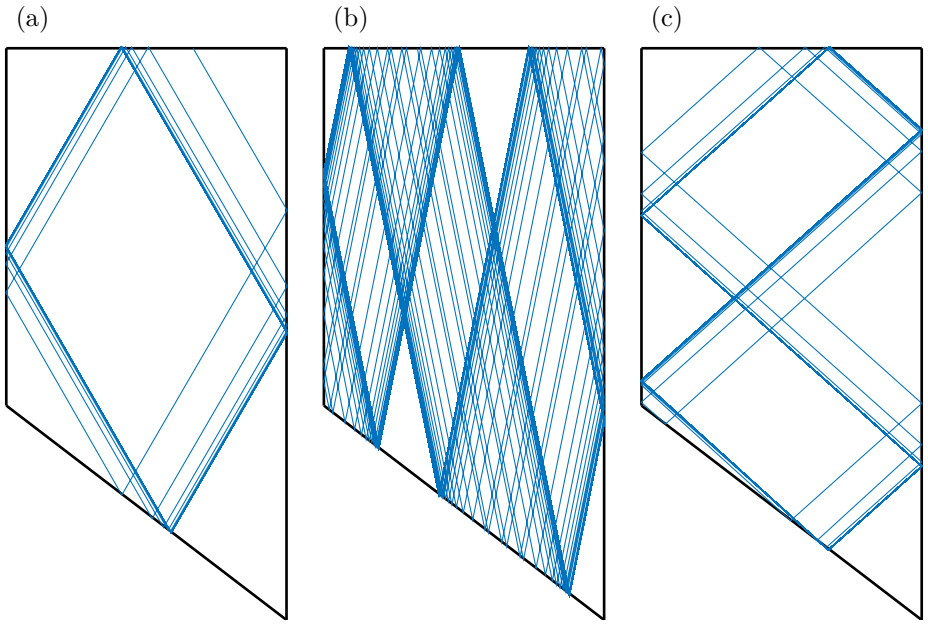

Figure 8.2: Examples of limit cycles obtained by ray tracing converging towards inertial wave attractors, with a $(1,1)$ attractor at (a) $\omega/f = 0.406$, a $(3,1)$ attractor at (b) $\omega/f = 0.153$ and a $(1,2)$ attractor at (c) $\omega/f = 0.650$. Bottom slope is at $\alpha = 45°$, in a domain of $L = 20$ cm width by $H = 40$ cm height, corresponding to the experimental apparatus described later.

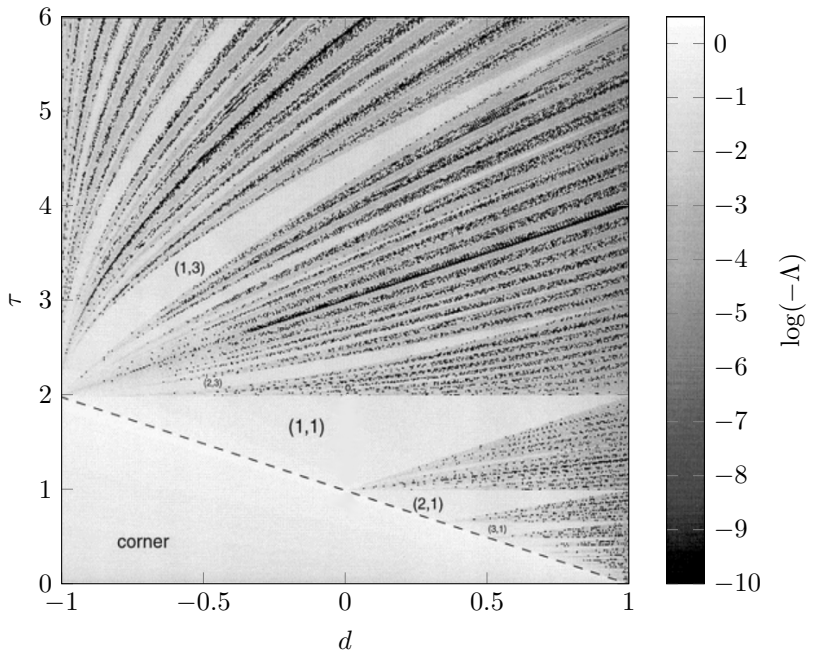

Figure 8.3: Reproduction of the (d, τ) diagram extracted from [129]. The greyscale shows $\log(-\Lambda)$ with Λ the Lyapunov exponent of the trajectories. The white regions correspond to high values of $|\Lambda|$, meaning that attractors can exist for these values of (d, τ). The different labels on the attractive regions $(1,3)$, $(1,1)$, $(2,1)$, etc, correspond to the shape of the attractor. See [42, 129] for more details.

8.1.3 Instability of Wave Attractors

Triadic Resonant Instability (TRI), as previously described in chapter 7, has been proven to be efficiently triggered in the attractor branches as the energy density gradually increses after a few focalising cycles [42, 203]. The non-linear fate of the two-dimensional $(1, 1)$ attractor, and subsequent feedback, has been explored experimentally and numerically in density stratified fluids in trapezoidal domains [44, 203] and in rotating tilted square domains [108]. Recently, scaling laws in terms of Reynolds and Rossby numbers for the amplitude of the attractor branches have been proposed and tested experimentally in both the linear and non-linear regimes [47], providing better understanding of their dynamics.

Of particular interest are wave attractors to study non-linear phenomena and internal wave breaking. The instability that develops in the most energetic branches has been shown capable of feeding a triadic cascade, bringing energy from the forcing scale down to smaller scales and, eventually, to the scale of turbulence [42, 43]. These processes, however, may be different in three-dimensional axisymmetric geometry: although instabilities are still predicted, geometric effects might re-stabilise the attractor and delay the onset of the cascade.

8.2 Experimental Configuration

To conduct the experiments, the apparatus used in the previous chapters has been slightly modified and is presented in figure 8.4. The experimental fluid domain is bounded by two vertical acrylic cylinders, by the wave generator at the top, and by an acrylic conical surface at the bottom. The outer and inner radii of the domain are $R_1 = 20.2$ cm and $R_0 = 5$ cm, respectively. The generatrix of the conical bottom surface has an inclination of 45°, and the apex of the cone can point either upwards or downwards.

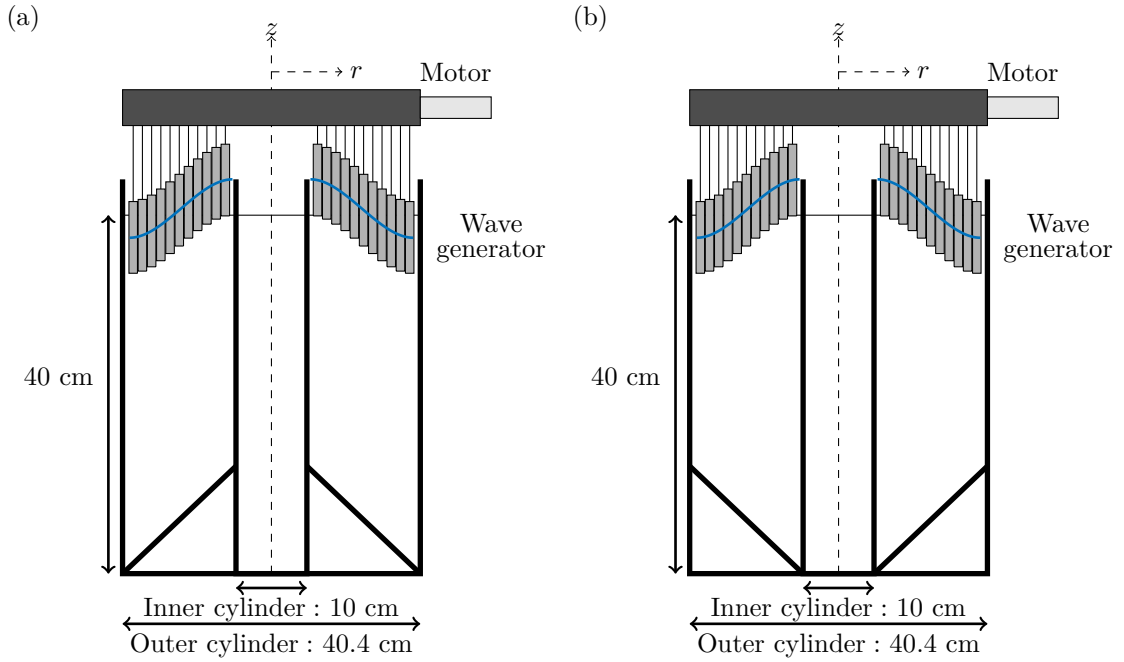

Figure 8.4: Schematic illustration of the experimental apparatus configuration: (a) upside-oriented cone, (b) downside-oriented cone. Note that the amplitude of the wave generator is greatly exagerated and the upper bound of the fluid domain is nearly flat.

In a vertical (meridional) cross-section of the setup, two trapezoidal domains are facing each other as shown in figure 8.4. The depth of fluid measured along the generatrix of the outer cylinder is $H = 40$ cm. In a horizontal (equatorial) cross-section, the experimental domain is a ring of width $L = R_1 - R_0$. The whole setup is inserted into a square acrylic tank of 100 cm $\times$ 100 cm horizontal

section and 65 cm height, as used in [33]. Each part of the facility is rigidly fixed to prevent any parasitic vibration when the whole setup mounted on the rotating table is brought to rotation at angular velocity Ω. The axis of rotation of the table coincides with the symmetry axis of the setup.

The axisymmetric wave generator was set into a cubic profile configuration of low amplitude, and the cylinders have been lowered down with extensions made of 20 cm long aluminium rods. These 20 cm reduce the experimental domain to a 40 cm tall region, so that the tank is only partially filled with water in order to prevent water from going out of the experiment by centrifugal force even at the highest rotation rates of 30 rpm. As discussed in chapter 2, the cubic profile has been chosen because it is the closest to a radial mode 1 confined between two cylinders, still satisfying the zero radial velocity boundary condition and the volume conservation condition.

Experiments were run with fresh water ($N = 0$ rad $\cdot$ s^{-1}) in rotation at relatively high Coriolis frequency, from $f = 2\pi/3$ rad $\cdot$ s^{-1} (20 rpm) to $f = \pi$ rad $\cdot$ s^{-1} (30 rpm). As a result, the Ekman number in the experiments is reasonably low ($E = \nu/2\Omega L^2 \simeq 10^{-5}$) so the impact of viscosity on the non-linear energy transfer can be neglected.

8.3 Experimental Results

The setup is designed to allow for the non-linear coupling between inertial wave attractors in vertical (meridional) cross-sections, and two-dimensional manifold in horizontal (equatorial) cross-sections. This coupling and its strength as well as the location of the onset of instabilities are linked to the axisymmetric geometry of the experiment and to the two configurations of the inclined boundary that can be oriented in two different ways (upside-oriented cone or downside-oriented cone).

We first note that a radial focusing-defocusing effect occurs, inherent to the cylindrical geometry of the system: when propagating inwards (smaller r), the energy density increases whereas, when propagating outwards (larger r), the energy density decreases. This phenomenon has been shown efficient to trigger instabilities in this geometry, in the case of an oscillating torus [208] or with a ring shaped wave generator [140]. This geometrical convergence of waves propagating from larger to smaller radial coordinate is superimposed to the focusing or defocusing reflection on the cone at the bottom boundary of the domain. Figure 8.5 illustrates the phenomenon of (a) focusing reflection and (b) defocusing reflection for waves propagating towards the center of the domain $r = 0$. In the focusing case in figure 8.5(a), the width of the beam is larger before reflection than after ($\delta_i > \delta_r$) while it is the opposite in the defocusing case in figure 8.5(b). In our setup, for a $(1, 1)$ attractor, two branches have a radial focusing and two branches have a radial defocusing and, depending of the orientation of the bottom cone, either focusing or defocusing effect is added by the bottom slope reflection.

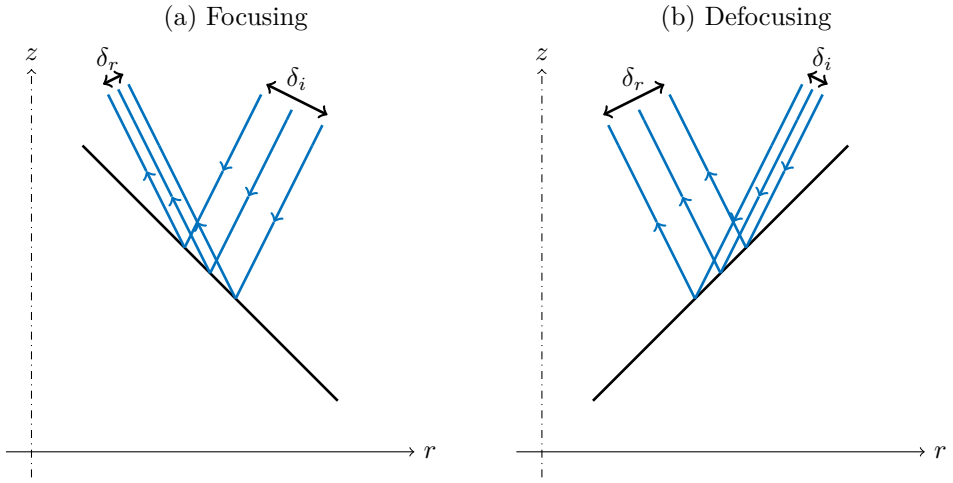

Figure 8.5: Reflections on the bottom cone in (a) focusing case, and (b) defocusing case for beams propagating inwards, showing its width before and after reflection, δ_i and δ_r. In the experiment, either one configuration or the other is used.

To prove the existence of an axisymmetric inertial wave generator in the linear regime, we use both configurations presented in figure 8.4. To study the non-linear behaviour of the attractor, however, we only focus on the configuration in which the cone is oriented so that the apex points upwards (figure 8.4(a)), leading to an additional focusing of the wave beam as it goes inwards. On the contrary, if the appex points downwards, the radial focusing and reflexion defocusing effects act in opposition, creating a more uniform distribution of energy in the experimental domain and less localised instabilities.

8.3.1 Linear Regime: Existence of an Axisymmetric Attractor

After a few forcing periods T (with $T = 2\pi/\omega_0$, where ω_0 is the forcing frequency), the attractor establishes itself in the linear regime. The focusing effect downscales the wave motion from the global forcing scale L to the scale associated with the width of the wave beams, called λ_h and defined by $\lambda_h = 2\pi/k_h$, k_h being the horizontal wave number [195, 98, 93]. This scale λ_h can be predicted from the geometry of the system and measured in attractor experiments [44, 203]. Due to the double focusing effect that increases the forced wave amplitude, waves at smaller frequencies appear even in the first cycles of the attractor due to Triadic Resonant Instability but their amplitude is weak compared to the forcing and they are therefore neglected in the first stages of the experiment.

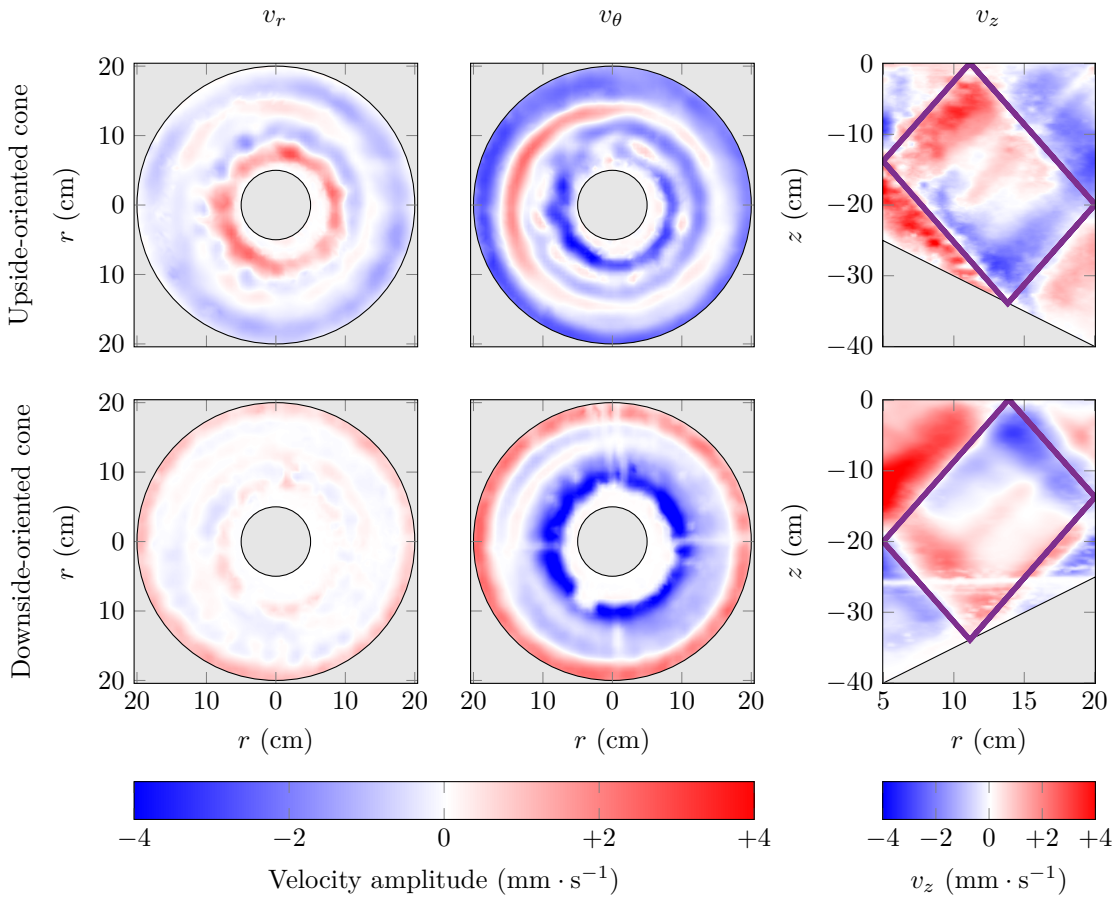

Figure 8.6: Experimental velocity fields observed in PIV after 17 periods of forcing at $\omega_0 = 1.7$ rad · s^{-1}, filtered over 4 periods at $\omega = \omega_0$. Gray shaded area is out of the experimental domain. From left to right: v_r, v_θ, and v_z. Straight lines on the right plot show the theoretical attractor. First row: upside-oriented cone (figures 8.4(a) and 8.5(a)). Second row: downside-oriented cone (figures 8.4(b) and 8.5(b)).

Figure 8.6 shows a typical wave pattern observed in the quasi-linear regime: the wave motion has a high amplitude about 4 mm $\cdot$ s^{-1} while the small-amplitude daughter waves generated at the initial stage of TRI are filtered out. We observe thus only the motion corresponding to the forcing frequency $\omega = \omega_0$. The radial and azimuthal velocities, observed in the horizontal plane, depict a nearly axisymmetric wave pattern. In the vertical plane, the structure of a classical two-dimensional attractor is seen (e.g. see [47]), with superimposed geometrical prediction obtained by ray tracing (trapezoidal cycles in solid line, righthand-side of figure 8.6). The observed attractor is consistent with Direct Numerical Simulations run previously to the experimental study by Ilias Sibgatullin *et al.* [209]. Note that the white lines observed in the configuration in which the cone points downward are due to the boundaries of the cone and have no physical meaning.

8.3.2 Non-Linear Regime: Instability and Coherent Structures

When the fluid is forced steadily, the attractor soon reaches a saturated regime and becomes unstable. The temporal evolution of the kinetic energy E_k of the attractor filtered at the forcing frequency, computed in a vertical cross-section and normalised by its overall mean value $\overline{E_k}$, is shown in figure 8.7. The kinetic energy starts growing and, after a few forcing periods (about $5T$), the saturated regime appears. Until the end of the experiment, the energy keeps oscillating around its mean value. This mean value is fluctuating at a larger time scale, both at low and high frequencies, pointing towards highly non-linear phenomena.

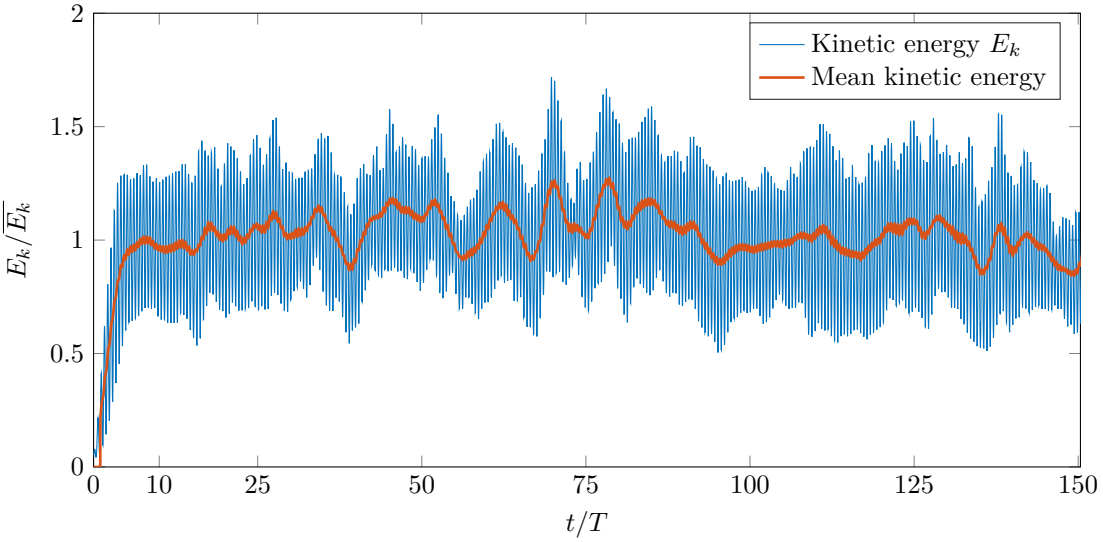

Figure 8.7: Temporal evolution of the kinetic energy of the inertial wave attractor filtered at the forcing frequency, computed in the vertical cross-section. The instantaneous fluctuations are shown by the blue curve, and the mean energy (sliding average computed over 4 periods) is shown in orange.

This unstable and non-linear behaviour can be seen in the frequency analysis presented in figure 8.8, showing time-frequency spectra [79] (top row) and frequency spectra at different times of the experiment (bottom row), both in the vertical cross-section (left) and in the horizontal cross-section (right).

At the begining of the experiment, a clear peak is identified at the forcing frequency ω_0, and remains approximatively at the same amplitude. Soon, the frequency content is more important almost everywhere but quickly saturates. At very low frequency, close to zero, a peak appears and increases during the experiment, reaching saturation at about 100 forcing periods, of similar magnitude as the forcing frequency peak in the horizontal plane. We note that a small peak is present in the horizontal plane at the rotation frequency but we believe this comes from the rotating table. Super-harmonics also appear in the spectra and are likely due to the wave-wave self-interaction described in chapter 7, but we did not investigate this further. These spectra can

be understood in more details by filtering the wave fields at the main frequencies appearing in figure 8.8, i.e. the forcing frequency $\omega = \omega_0$, and the very low frequency, as follows.

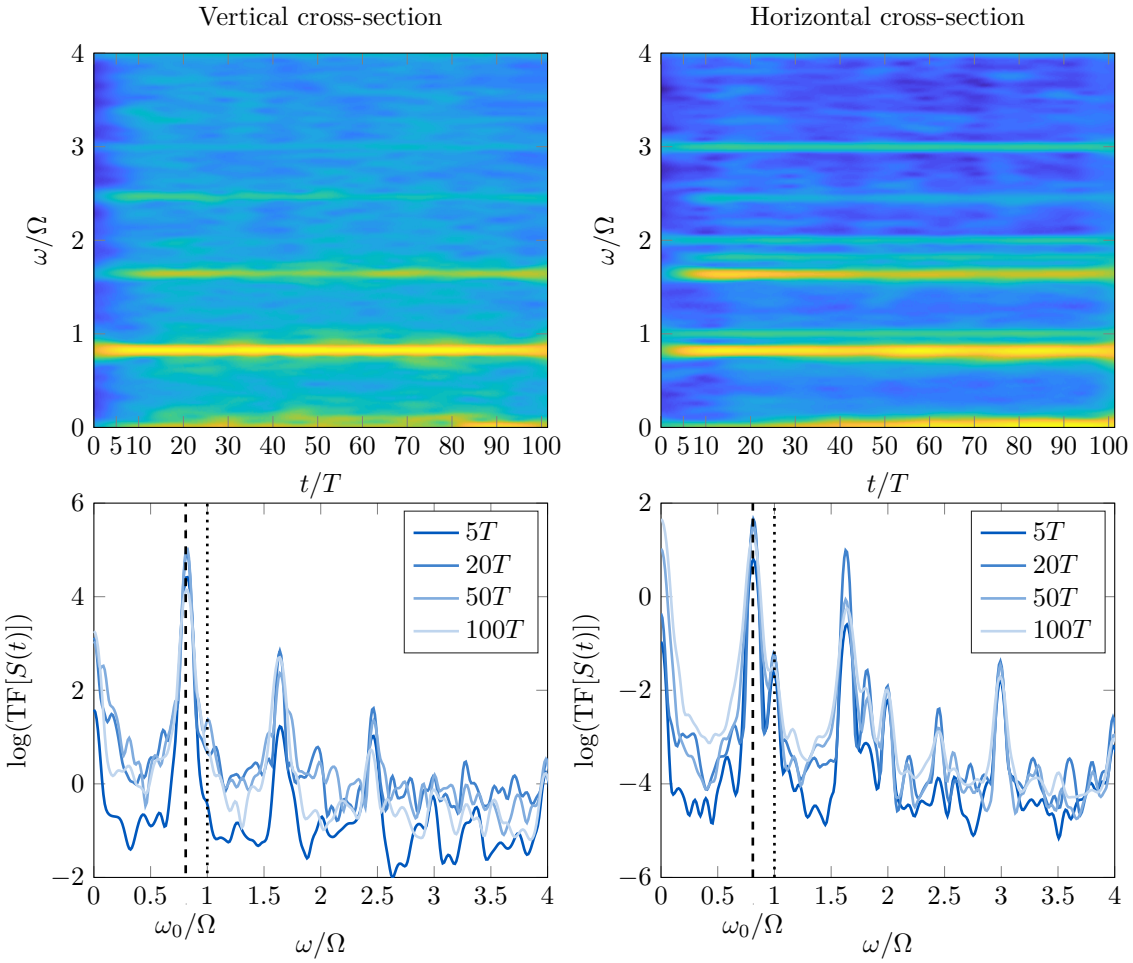

Figure 8.8: Top: time frequency spectra. Bottom: cuts at different times in the time frequency spectra above. Left: data from the vertical cross-section. Right: data from the horizontal cross-section. In the bottom pannel, the dashed line indicates the forcing frequency ω_0 and the dotted line marks the rotation rate Ω.

Figure 8.9 presents snapshots of the velocity fields filtered at the forcing frequency with, from left to right, radial velocity v_r, azimuthal velocity v_θ, and vertical component of the vorticity ξ_z, in the horizontal plane, and vertical velocity v_z in the vertical plane. The three rows present three different times in the experiment. In the first row, at $17T$, the attractor is in a quasi-linear regime and the velocity fields are the ones presented in figure 8.6. Almost all kinetic energy injected by the generator is feeding the forcing mode, shown in 8.9, with the structure of the $(1, 1)$ attractor in the vertical plane and a nearly axisymmetric pattern in the horizontal plane shown by rings of opposite signs. Concentric rings of vorticity, remnent of the oscillating branches of the attractor, can be seen. As expected, we observe that the magnitude of the velocities is higher close to the inner cylinder than close to the outer cylinder, due to the radial geometric focusing effect. The second row, at $50T$, shows the destabilisation of the inertial wave attractor that is no longer axisymmetric as discretised patterns gradually appear around the inner cylinder. Filtering out the other frequencies created through non-linear interaction, we still observe the structure of the $(1, 1)$ attractor in the vertical velocity field in the vertical cross-section. Close to the outer cylinder, in the horizontal cross-section, the velocity and vorticity fields remain qualitatively axisymmetric as the amplitude is weaker. In the last row, at $150T$, close to the end of the experiment, we note the presence of a θ-periodic structure in the horizontal plane with eight patterns in the velocity and

vorticity fields. The shape of the attractor is less clear but still visible in the vertical plane. As already stated for the velocity fields taken at $50T$, the outer region remains quasi-axisymmetric and the two branches of the attractor that it contains are still well defined.

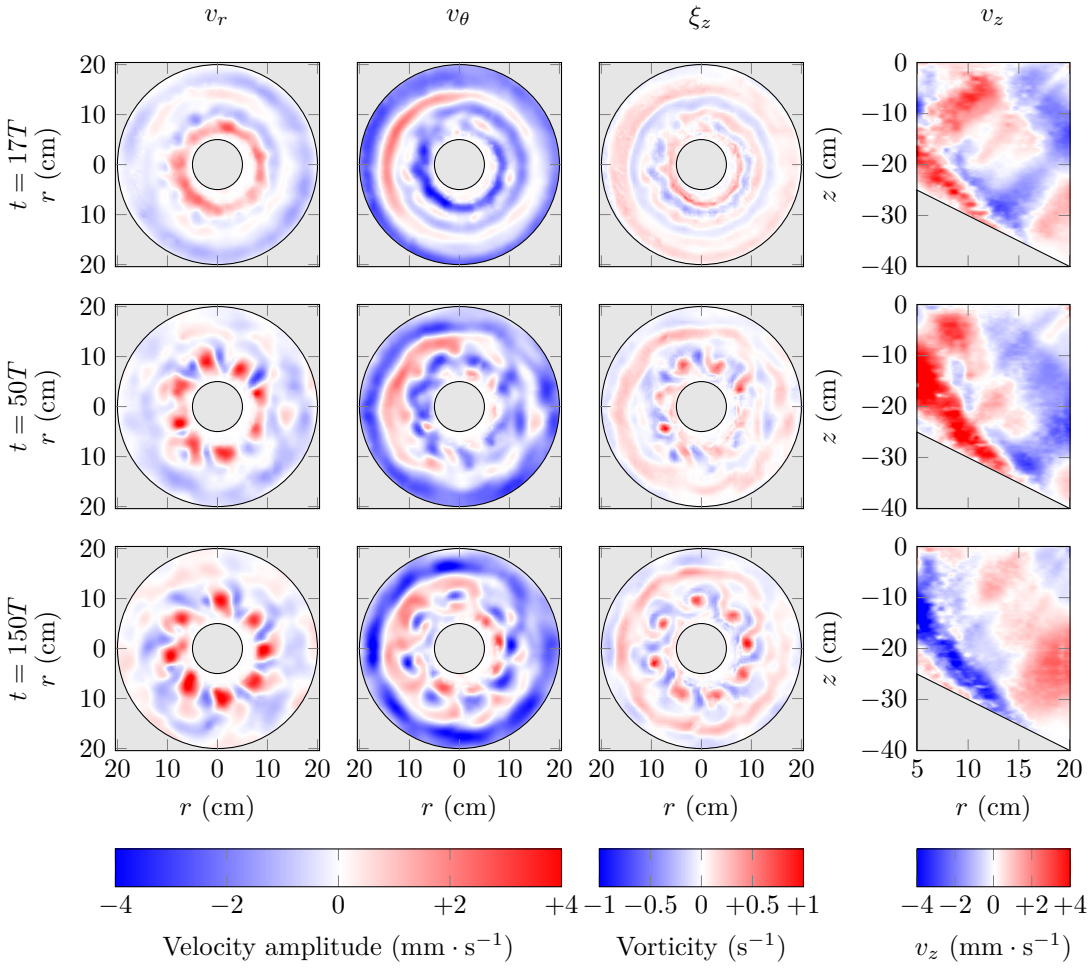

Figure 8.9: Velocity fields filtered at $\omega = \omega_0$. First three columns, from left to right: vertical velocity, azimuthal velocity, and vertical component of the vorticity, in the horizontal cross-section; fourth column: vertical velocity in the vertical cross-section. Top row to bottom show different times, at $17T$, $50T$, and $150T$.

The zero frequency component is investigated in some more details in figure 8.10, presenting, from left to right, radial velocity v_r, azimuthal velocity v_θ, and vertical component of the vorticity ξ_z, in the horizontal plane, and vertical velocity v_z in the vertical plane, filtered at $\omega = 0$, each row corresponding to a different time in the experiment (at $17T$, $50T$, and $150T$, as in figure 8.9, for purpose of comparison). As highlighted by the first row, in the linear regime of the wave attractor, only noise is visible at zero frequency at the begining of the experiment. A vertical flow, however, starts to develop in the vertical plane. Later on, at $50T$, we observe a clear transient regime with patches gradually appearing in the horizontal plane from the top-left corner. At the end of the experiment, in the bottom row at $150T$, a well-established manifold can be seen. The pattern observed in the horizontal plane and seen in the last row of figure 8.10 is constituted of an ensemble of eight self-organised vortices, fully established after about 100 periods of forcing, and stable for the remaining duration of acquisition. These vortices are stable in time, always characterised by a positive vorticity and therefore rotating in the same direction, with a magnitude that does not fluctuate in time. Interestingly, these structures have a different dynamics from inertial waves that is to be further explored and even more intriguing since they are not exactly at zero frequency:

the filtering process, indeed, has a frequency band width of $5\,10^{-2}$ rad $\cdot$ s^{-1}. From the second and third rows in figure 8.10, we observe that the locations of the center of the vortices is not always the same: the whole structure seems to have rotated (either clockwise or anti-clockwise) as, for example, the cores of the vortices almost align with the $r = 0$ axis at $150T$ but not at $50T$. This is also visible on the radial velocity plots, as the colours for corresponding patches are inversed for $50T$ and $150T$.

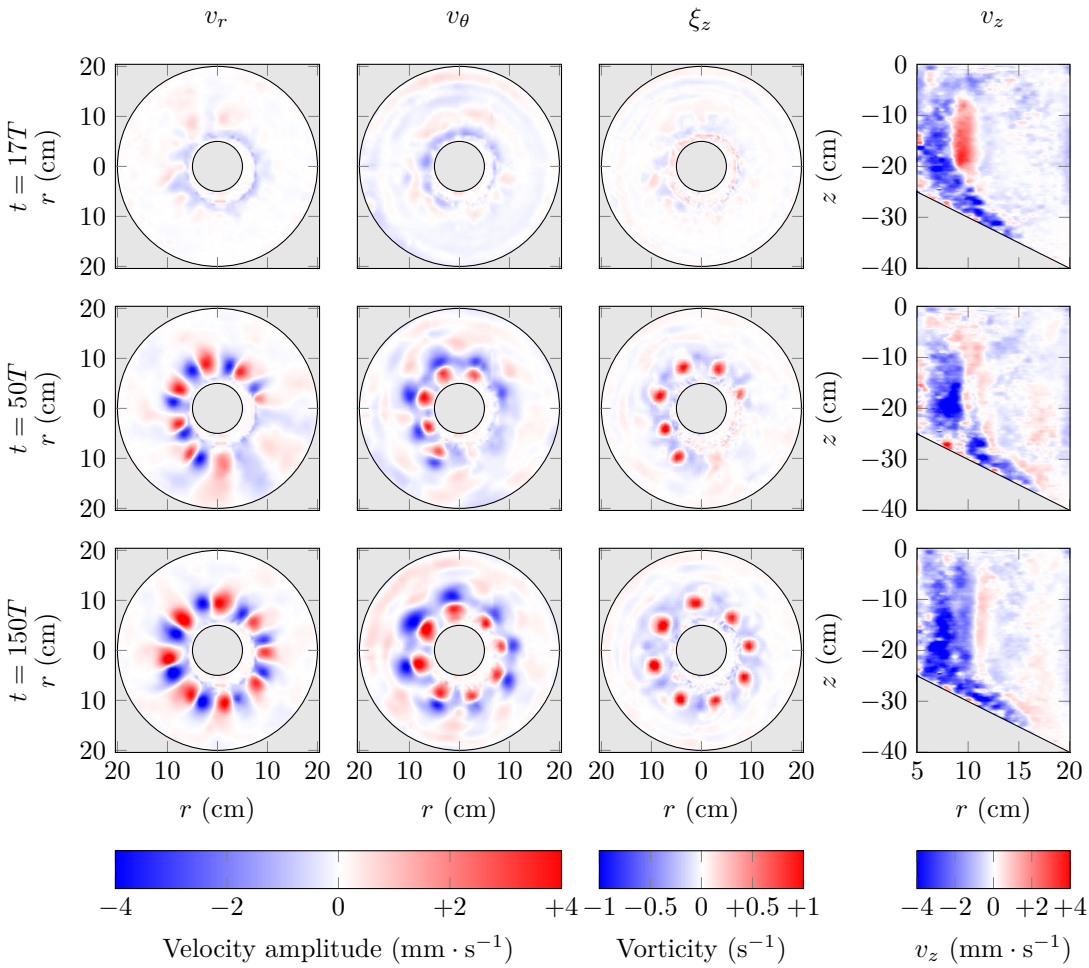

Figure 8.10: Velocity fields filtered at $\omega = 0$. First three columns, from left to right: vertical velocity, azimuthal velocity, and vertical component of the vorticity, in the horizontal cross-section; fourth column: vertical velocity in the vertical cross-section. Top row to bottom show different times, at $17T$, $50T$, and $150T$.

The structures observed in the vertical plane are reminiscent of the Taylor columns. There is, however, an important distinction, as the Taylor columns are formed as a consequence of a slow motion of perturbation imposed to the rotating fluid, whereas the coherent structures seen in figure 8.10 arise due to a non-linear process that drains energy from the wave field towards the two-dimensional manifold observed at very low frequency.

8.3.3 Temporal Evolution of the Instability

The manifold observed in the horizontal plane gradually appear while inertial waves are being excited. At a given time, the structure may not be entirely present in the domain as shown in the second row of figures 8.9 and 8.10. Another example is presented in figure 8.11, with the instantaneous radial velocity field in the horizontal cross-section at $75T$. The structure is mostly

present in the top-left corner, whereas it is less clear in the bottom-right corner.

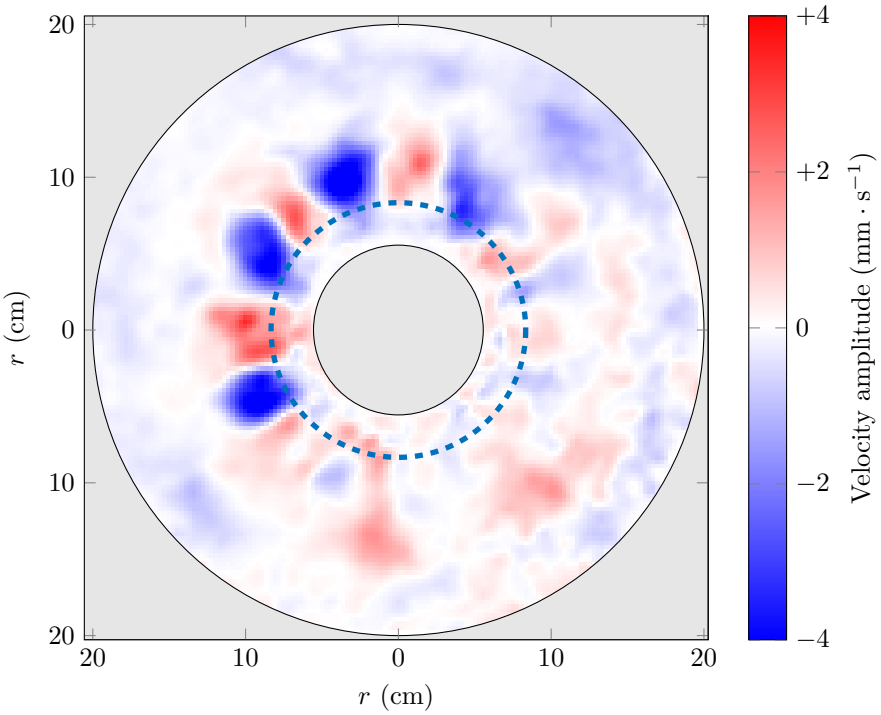

Figure 8.11: Unfiltered radial velocity field in a horizontal cross-section, during the formation of coherent structures at $t = 75T$. The dashed circle indicates the location of the sampling pattern used in figure 8.12.

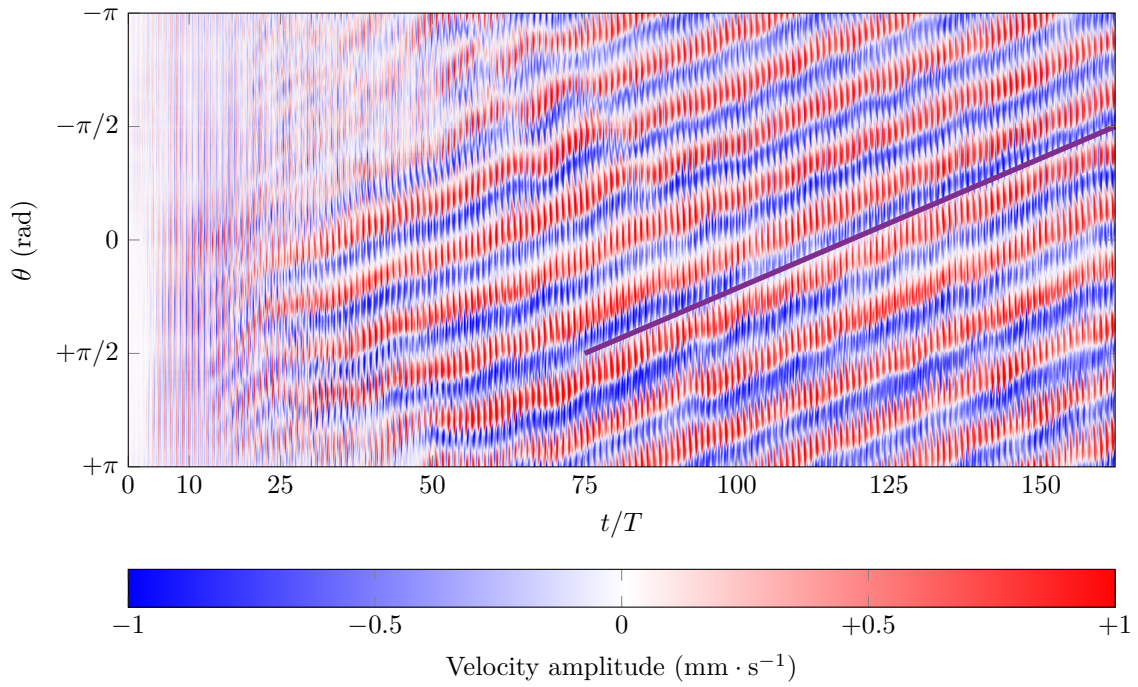

Figure 8.12: Temporal evolution of the radial structure obtained by taking profiles of radial velocity at a given radius in the horizontal plane. To guide the eye, a solid line shows the drift experienced by the structures.

Visual evidence of the transient regime can be seen in figure 8.12, which presents the temporal evolution of the radial structure measured by sampling the pattern at constant radius between R_0 and R_1, as shown by the dashed line superimposed to the radial velocity field at $t = 75T$ in figure 8.11. The eight vortices observed in figure 8.10 at the end of the experiment start to grow from one side of the inner cylinder and self-organise until being stably structured along a circle. After $100T$, the whole system of vortices is fully established and shows a clear anticyclonic rotation at $1.05\,10^{-2}$ rad $\cdot$ s^{-1}. The solid line added to figure 8.12 helps the reader see the constant drift of the radial velocity paterns as the experiment is run. Hence, the fields seen in figure 8.9 are likely not at zero frequency, but their frequency is too low to be distinguished from a zero frequency in the filtering process.

The evolution of the azimuthal velocity, complementary to the behaviour of the radial velocity, can be further explored. A surface plot of the zonally-averaged azimuthal velocity $\hat{v_\theta}$, corresponding to

$$\hat{v_\theta}(r,t) = \frac{1}{2\pi}\int_0^{2\pi} v_\theta(r,\theta,t)\mathrm{d}\theta, \tag{8.15}$$

is presented in figure 8.13 as a function of relative radial location $(r - R_0)/(R_1 - R_0)$ and dimensionless time t/T. This spatio-temporal plot shows that, at the begining of the experiment, a peak of positive azimuthal velocity appears close to the inner cylinder at $(r - R_0)/(R_1 - R_0) \simeq 0.2$, closely followed by a small peak of negative vorticity at $(r - R_0)/(R_1 - R_0) \simeq 0.4$. Then, these two peaks move away from the center of the domain as, during the growth of the instability, a dual circulation establishes with cyclonic velocity close to the inner cylinder and anticyclonic velocity a bit further out. This pattern seems to be very stable in time, and the extrema of the zonally-averaged azimuthal velocity remain at constant radius over the last 100 forcing periods of the experiment.

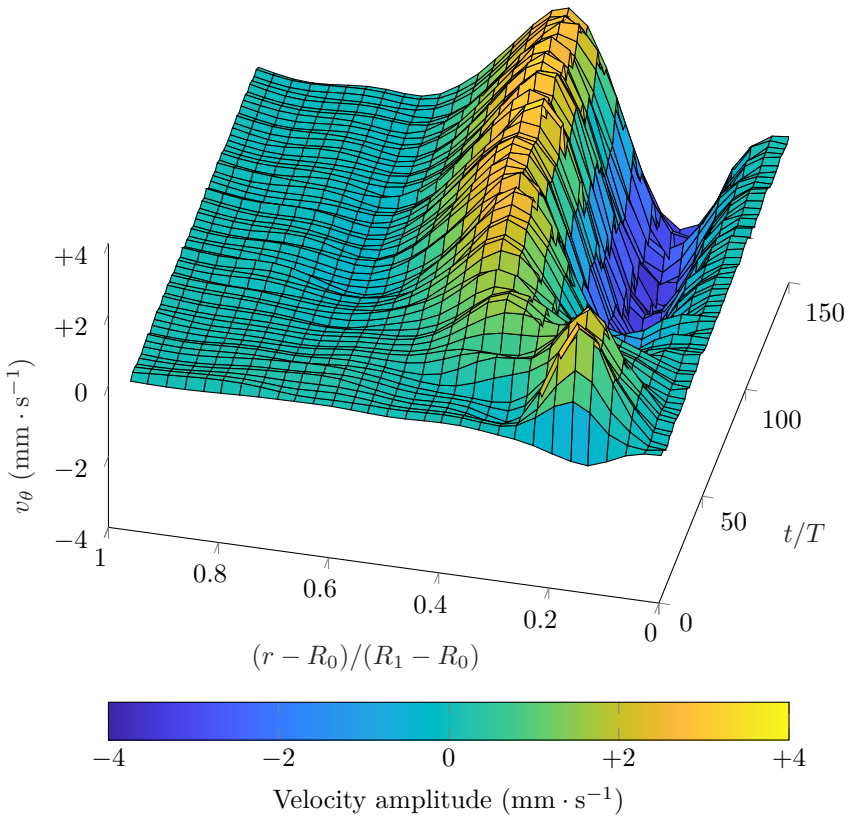

Figure 8.13: Spatio-temporal surface plot of the zonally-averaged azimuthal velocity, as a function of dimensionless time t/T and relative radial location $(r - R_0)/(R_1 - R_0)$.

For better insight into the dynamics of the process, we consider the time-evolution of the zonally-averaged enstrophy-based Rossby number Ro^{ens}, defined by

$$Ro^{\text{ens}} = \frac{\langle \xi_z \rangle}{2\Omega}, \tag{8.16}$$

where the zonally average vorticity $\langle \xi_z \rangle$ is a proxy for the entrophy. The corresponding spatio-temporal surface plot is presented in figure 8.14 as a function of dimensionless time t/T and relative radial location $(r - R_0)/(R_1 - R_0)$. For $(r - R_0)/(R_1 - R_0) \simeq 0.26$ ($r \simeq 9$ cm), a peak of Rossby number up to 0.04 is clearly observed after ~ 75 forcing periods and, as the previous quantities presented in figures 8.12 and 8.13, the structure remains stable after 100 periods of forcing. This distance from the center of the experiment corresponds to the location of the centers of the vorticies identified in the PIV fields shown in figure 8.10. The value of the enstrophy-based Rossby number is consistent with the estimate that can be computed from the velocity of the radial structures by comparing the characteristic frequency of the structures to the Coriolis frequency

$$Ro^{\text{struct}} = \frac{\text{structure frequency}}{\text{Coriolis frequency}} = \frac{U_{\max} \frac{n}{2\pi r^*}}{2\Omega} \sim 10^{-2}, \tag{8.17}$$

where $U_{\max}$ is the maximal velocity amplitude measured in the horizontal plane, $r^* = 9$ cm is the radial location of the center of the vortices, and $n = 8$ is the number of structures (vortices) observed in the experiment.

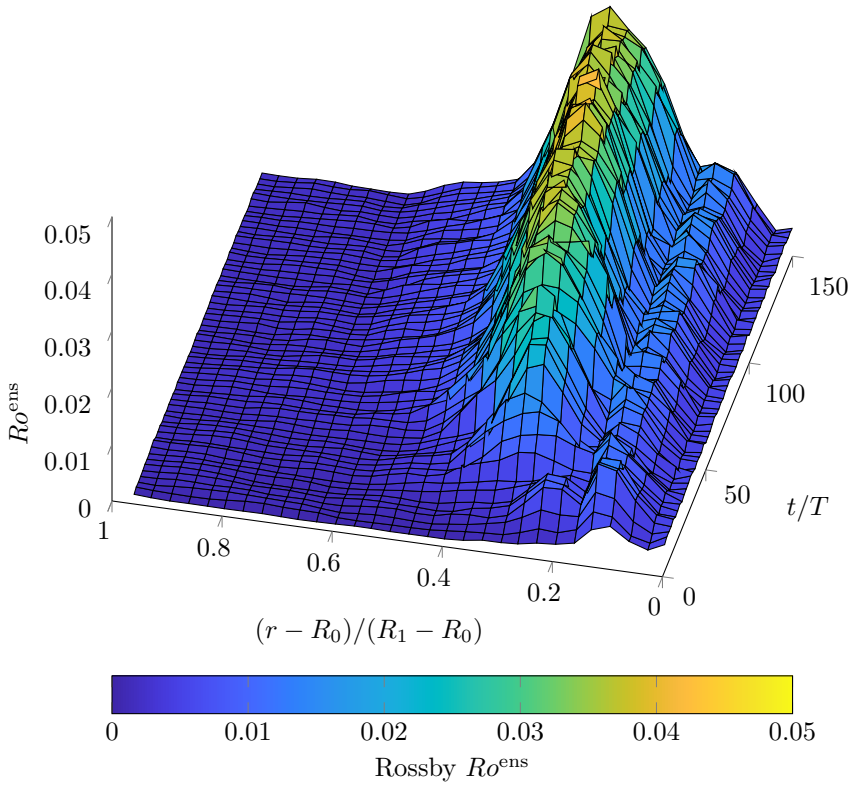

Figure 8.14: Spatio-temporal surface plot of the zonally averaged enstrophy-based Rossby number, as a function of dimensionless time t/T and relative radial location $(r - R_0)/(R_1 - R_0)$.

Figure 8.15 shows typical PDFs of $\xi_z/(2\Omega)$ at different stages of the development of the coherent vortex structures, computed over the wave field filtered at the forcing frequency $\omega = \omega_0$ in figure 8.15(a), and filtered at zero frequency $\omega = 0$ in figure 8.15(b). The PDFs at the forcing

frequency (figure 8.15(a)) are slighlty skewed with higher values of positive vorticity than negative vorticity, due to the presence of the instability close to the inner cylinder. For the PDFs computed with the wave field filtered at zero frequency (figure 8.15(b)), however, a clear skewness is visible at late times pointing towards a significant symmetry breaking. This skewness is related to the creation of the eight vortices as seen in figure 8.10. For these PDFs, we see an increased distribution of negative and positive vorticities with a large tail that quickly develops up to $\xi_z/f \simeq 0.3$ as soon as the vortices are formed, and that remains stable afterwards. Note that, initially, the PDF at zero frequency has a sharp peak at zero, contrary to the PDF at the forcing frequency.

There exists a literature work on the conditions corresponding to the cyclonic-anticyclonic symmetry breaking, starting with pioneering works of [38, 170]. The literature is briefly reviewed in [89], with the conclusion that instability of anticyclonic vortices appears if $\xi_z/(2\Omega) \simeq -1$, i.e. when the vorticity in the vortex core is comparable to 2Ω and has the opposite sign. As can be seen in figure 8.15, however, our experimental data yield $|\xi_z/(2\Omega)| < 0.4$. In our experiment, the overall symmetry breaking is manifested in the data filtered at zero frequency, with the asymmetric PDFs of relatively large tail in positive vorticities compared to negative vorticites (figure 8.15(b)), and with a slow cyclonic precession of the whole pattern of coherent structures (see figure 8.12 on temporal drift of the radial structures).

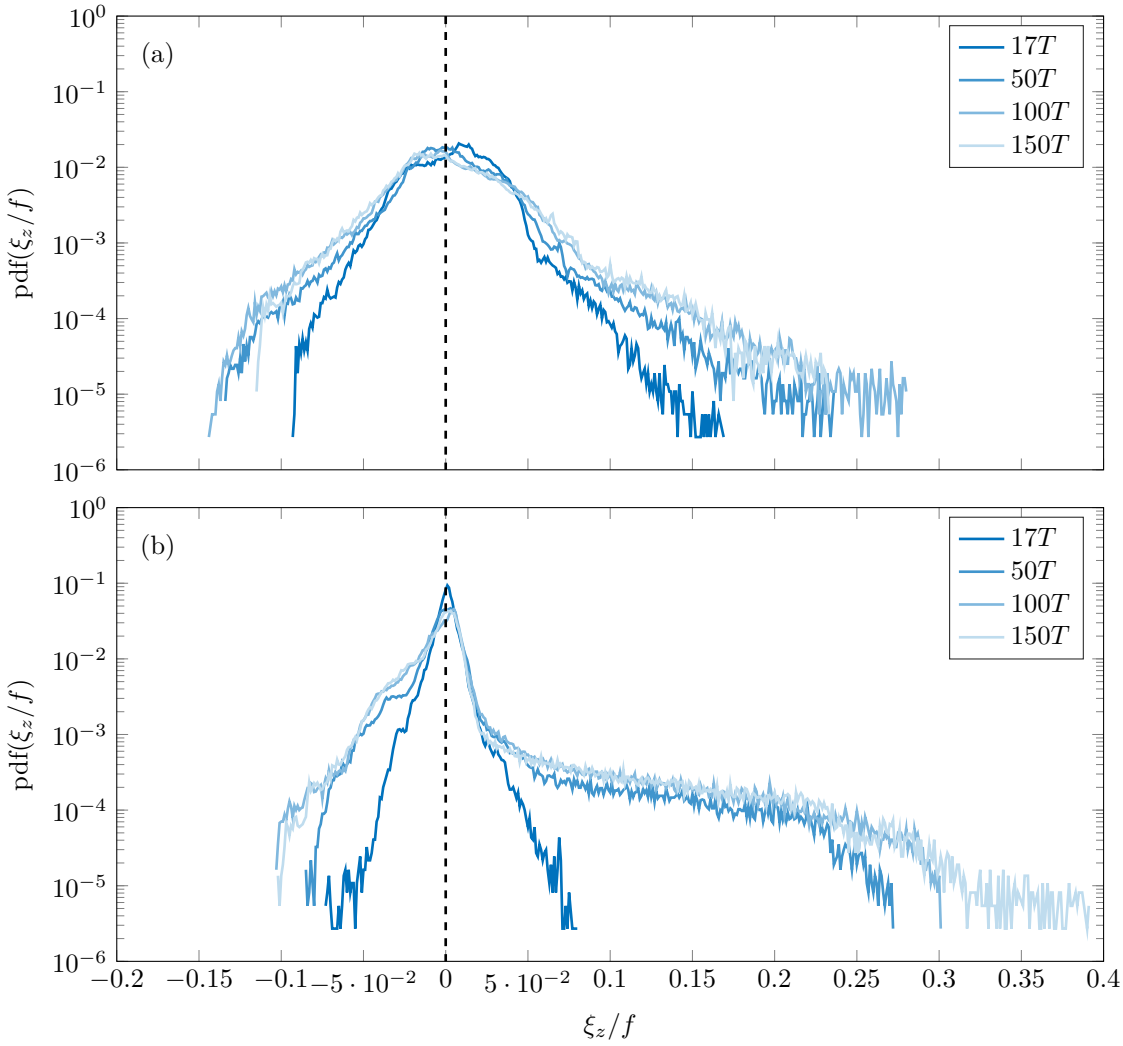

Figure 8.15: PDFs of vorticity at different times in the experiment (at $17T$, $50T$, $100T$, and $150T$) computed over the experimental domain in the horizontal cross-section for the wave field (a) filtered at $\omega = \omega_0$, and (b) filtered at $\omega = 0$.

8.3.4 Variability of the Number of Vortices

In our experiment, 8 vortices were observed equally spaced around the central cylinder. If this seems to be a consistent behaviour in our setup, the number of vortices, however, depends on the geometry and of the forcing amplitude. Direct Numerical Simulations run by Ilias Sibgatullin with Nek5000 open solver based code, help shed light on this phenomenon. Figure 8.16 shows the vorticity field in the outputs of two different simulations at a time when the steady state is reached. In figure 8.16(a), the configuration is the same as in the experimental setup ($R_0 = 5$ cm, $R_1 = 20$ cm and $a = 2.5$ mm), and we can see the development of six vortices. In figure 8.16(b), the domain is slightly larger ($R_0 = 10$ cm and $R_1 = 30$ cm), and the forcing amplitude is also higher ($a = 6$ mm), but the ratio ω_0/Ω remains unchanged. We can see, in this second picture, four vortices equally distant from each other and the vortices themselves are bigger than in the latter case. The number of structures observed shows therefore some variability depending on the geometric configuration and the forcing, but the non-linear regime is always characterised by the growth of several vortices and an azimuthal symmetry breaking. At this stage, no precise characterisation of this variability has been found.

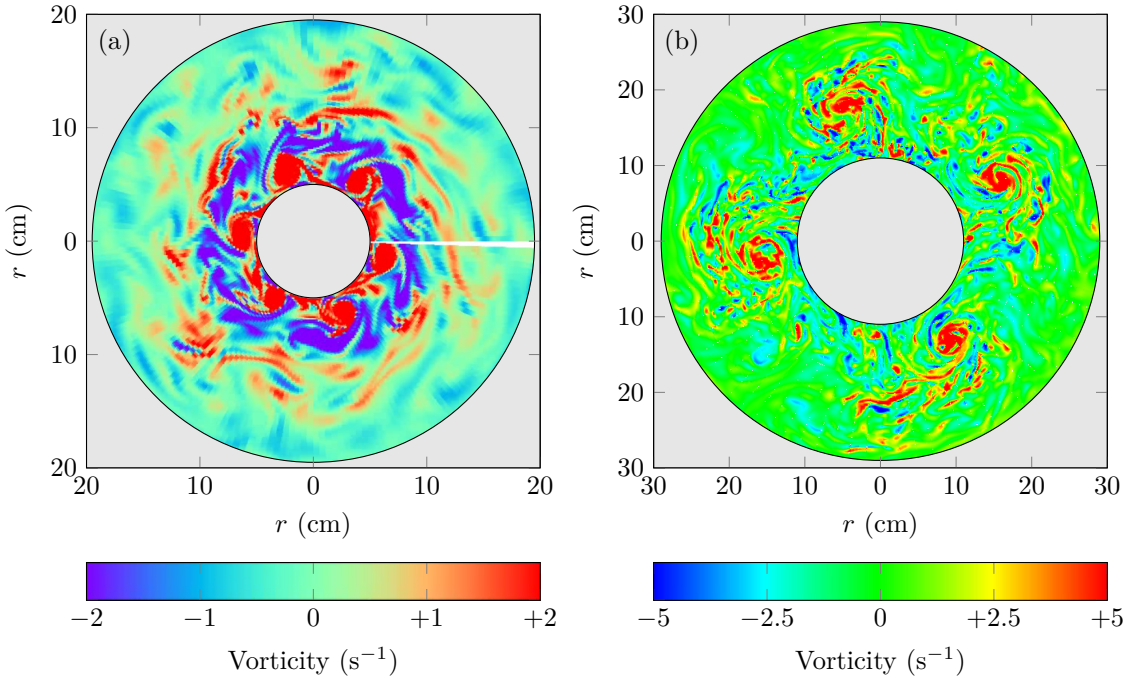

Figure 8.16: Snapshots adapted from DNS run by Ilias Sibgatullin. Left: configuration with $R_1 = 5$ cm, $R_1 = 20$ cm, $a = 2.5$ mm. Right: configuration with $R_1 = 10$ cm, $R_1 = 30$ cm, $a = 6$ mm.

8.4 Conclusions and Discussion

This experimental study provides evidence of the existence of three-dimensional axisymmetric inertial wave attractors, in agreement with Direct Numerical Simulations and two-dimensional ray tracing theory. Two configurations are explored, depending on the orientation of the bottom slope: a radially and reflection focusing configuration and a less energetic radially focusing and reflection defocusing configuration. As predicted from DNS run by Ilias Sibgatullin, the attractor establishes in the linear regime and remains axisymmetric until its destabilisation.

In the doubly-focusing configuration, the non-linear regime is reached soon after the begining of the experiment, triggering instability close to the center of the cylindrical domain. The onset of instabilities leads to symmetry breaking as the θ-invariance is lost, and vortices at very low

frequency gradually appear to constitute a ring of equally distant coherent structures. Depending on the amplitude, the number of structures present in the system varies, but our results always show an even number of them.

The existence of such azimuthal structures, which had not been observed before, is linked to an enstrophy-based Rossby number that grows and saturates at $Ro^{\xi_z} \simeq 0.04$, below its critical value for maximum rate of energy transfer $Ro^{\mathrm{c}} \simeq 0.2$ [29]. The non-linear regime can be described as a new steady state of the system, with saturated Rossby number, velocities, and kinetic energy, meaning that the instability and its mechanism leads the system to a bifurcated stable state with well-defined vortices. Interestingly, although an azimuthal periodicity depending on the forcing amplitude appears in the horizontal plane, there is no remarkable asymmetry between cyclonic and anticyclonic vorticities. Only a slow overall anticyclonic rotation, associated to a low frequency, is experimentally observed for the complete collection of vortices, and remains without explanation.

The findings presented in this study raise a number of interesting issues, in particular, [i] how the saturated vortex regime depends on the key parameters of the problem (Rossby and Ekman numbers, geometric aspect ratio and the particular type of forcing), [ii] whether or not the observed regime might be relevant to realistic geo- and astrophysical systems. Cyclonic clusters arranged in form of regular polygones have been reported for the polar regions of large planets, e.g. Jupiter [2], demonstrating remarkably persistent long-term behavior [1]. It has been argued that although the global pattern of the Jovian atmosphere with circumpolar cyclones and alternating flows near the equator is captured by shallow-water models (e.g.[54, 205]) the key puzzle remains [2]: "The manner in which the cyclones persist without merging and the process by which they evolve to their current configuration are unknown". The "toy system" proposed here may help to shed light on the issues related to the stability of polygonal vortex clusters and their possible existence in the interiors of natural systems admitting the existence of inertial wave attractors.

The fate of these structures, however, is still to be determined. Would they last forever? Would the number of structures always adapt to the forcing amplitude or would a triadic cascade start at very high amplitudes? What are the mechanisms behind the formation of these vortices? DNS are currently used to help answer these questions.

Part IV

Energy and Buoyancy Transport in the Arctic: A Case Study

CHAPTER 9

The Chukchi Slope Current

On était bien surpris par cette plaine grise
d'où Galilée jadis jeta ses petits pots
nous avions aussi froid que nus sur la banquise
quand les grêlons fin mars mitraillaient les bateaux
Raymond Queneau, CENT-MILLE MILLIARDS DE POÈMES.

Connecting theory and laboratory experiments to real-world is challenging but it is a prerequisite to deal with major issues in oceanography such as stratified mixing, ice melting, waves and currents, or climate changing. During my PhD, I had the oportunity to be involved in a research cruise on a small ice capable scientific boat, the R/V Sikuliaq (e.g. see [112]), shown in figure 9.1.

Figure 9.1: The R/V Sikuliaq surrounded by sea ice in the Arctic Ocean. Photography by Thomas Moore, ArcticMix research campaign, 2015.

This research campaign was part of the Stratified Ocean Dynamics of the Arctic (SODA) program [120] and consisted in a five week cruise in the Arctic Ocean in the month of September 2018. It departed from Nome, AK (USA), went North through the Bering Strait, and operated along the shelfbreak of the Chukchi Sea in the North-West edge of the Canada Basin. This cruise was the opportunity for me to have a direct contact with oceanography and in-situ measurements, participating into a collective life onboard a research vessel. I was more particularly involved in two different projects: the detection of near-inertial waves in the deep ocean [105], and the investigation of the fate of the Chukchi Slope Current [35] – a project I was in charge of – detailed in the current chapter.

Non-directly related to internal waves, this chapter presents results from a field study conducted during this campaign and is organised as follows. Section 9.1 briefly introduces the context and the goals of the ONR funded SODA program. Sections 9.2 and further are the latest version of the manuscript we submitted on our study of the Chukchi Slope Current.

Results from this chapter are published in *Journal of Physical Oceanography* [35].

9.1 Stratified Ocean Dynamics of the Arctic (SODA)

Throughout the year, seasonal sea-ice coverage of the Arctic Ocean impacts its structure and its dynamics. Current models are based on weak seasonality with long periods of ice coverage that preserves the ocean from atmospheric disturbances. As detailed in chapter 3, due to rapidly changing climate conditions, the Arctic is significantly warming up (as detailed in [120], see e.g. [165] for year 2015) with several consequences on sea-ice distribution: its summer and winter extension is shrinking, its thickness is reducing, and the ice is on average younger than before which means that old compact ice is melting while new thin ice easily subject to cracking and melting is formed. A diminished and thinner ice-coverage has consequences on the energy transfer from the atmosphere to the ocean, and is likely to have implications in mixing processes.

The Stratified Ocean Dynamics of the Arctic (SODA) program [120] is a joint effort to improve our understanding of the Arctic Ocean in the upper Beaufort Sea region, and of the complex interplay between ice coverage, currents, and stratification. According to the technical report from Lee *et al.* [120], the program focuses on the response to changes in inflow and surface forcing, addressing three key oceanographic properties: buoyancy, momentum, and heat. Several cruises are planned for deployment, recovery, and ship surveys, from 2016 through 2021, amongst which the 2018 cruise on the R/V Sikuliaq.

9.2 Whither the Chukchi Slope Current?

Pacific waters enter the western Arctic Ocean through Bering Strait, supplying nutrients, carbon, heat, and freshwater [125] to the Chukchi Sea and ultimately the interior basin. It is now well established that these waters progress through the Chukchi Sea via three main pathways: a western branch flowing into Herald Canyon, a central branch flowing between Herald and Hanna shoals, and an eastern branch situated adjacent to the Alaskan coast that feeds Barrow Canyon [243] (figure 9.2). Some portion of the western and central branches are believed to turn east before entering the Canada Basin, augmenting the flow through and out of Barrow Canyon [90, 176].

Different seasonal water masses are found in the Chukchi Sea. In winter and early spring much of the shelf contains newly ventilated winter water (WW) near the freezing point [176, 166]. This water is subsequently warmed via mixing and solar heating, becoming what is known as Remnant Winter Water (RWW) [90]. Later in the summer season two types of water enter the Chukchi Sea from the south. The warmest of these is Alaskan Coastal Water (ACW) which originates from runoff into the Gulf of Alaska and flows northward in the Alaskan Coastal Current (ACC) [168]. The second summer water mass is Bering Summer Water (BSW), which is a mixture of Anadyr water and central Bering shelf water [55]. Finally, a combination of sea ice melt water and river runoff (referred to as MWR) provides fresh water to the surface layer. How and where these water masses exit the Chukchi Sea into the Canada Basin is a subject of ongoing study.

Recent attention has been placed on Barrow Canyon and the fate of the water draining through the canyon. Originally it was thought that most of the water turned eastward, forming the Beaufort Shelfbreak Jet [175]. Mooring data from the Shelfbreak Jet, however, revealed that the volume flux of the jet is substantially less than the transport through Bering Strait [159]. This discrepancy has been reconciled with the recent discovery of the Chukchi Slope Current (CSC). Using shipboard acoustic Doppler current profiler (ADCP) data from 46 transects collected between 2002 and 2014, Corlett and Pickart [57] provided evidence of a westward-flowing current over the continental slope of the Chukchi Sea transporting 0.50 Sv of Pacific water. They demonstrated that the CSC closes the mass budget of the Chukchi shelf inflows and outflows. The hydrographic data revealed that, during the summer and early fall, the CSC advects mainly RWW. However, the relative presence of the different Pacific water masses in the current varies from month to month.

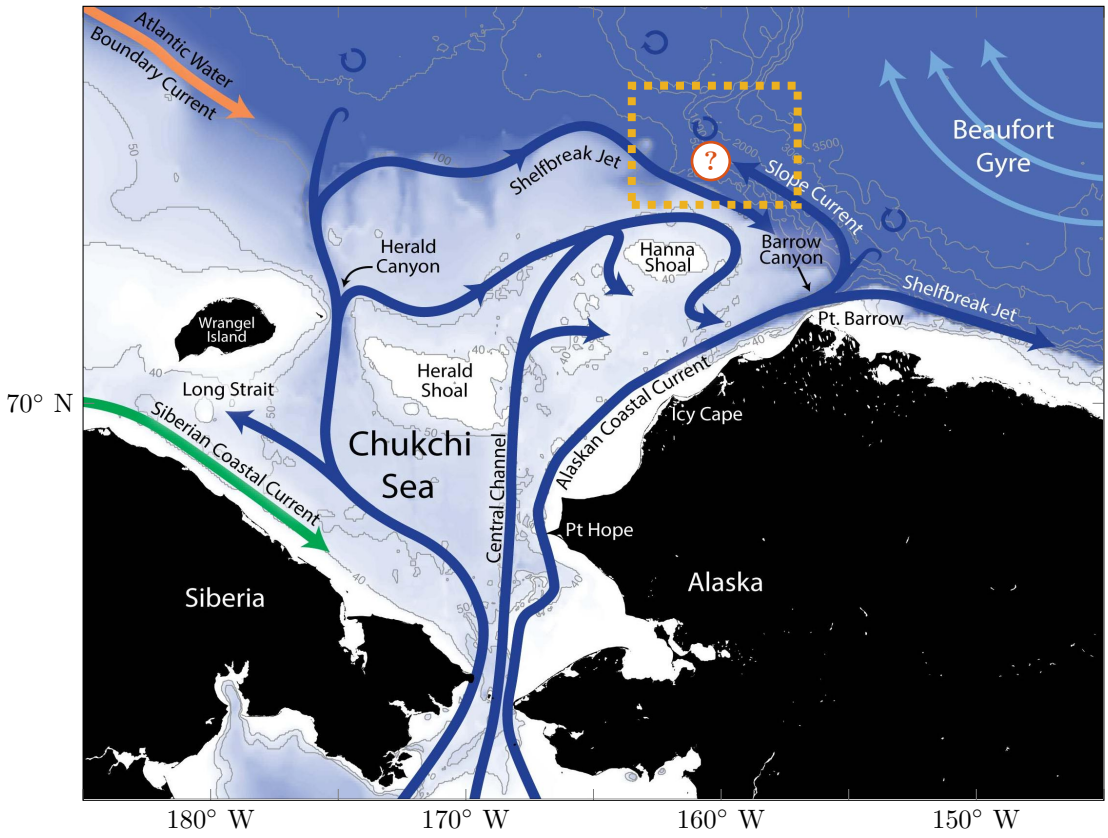

Figure 9.2: Schematic representation of the general circulation in the Chukchi Sea, adapted from [57]. The ultimate destination of the Slope Current is currently unknown, hence the reason for the question mark. The dashed yellow rectangle shows the location of the ADCP measurements shown in figure 9.3.

The year-round presence of the CSC was recently confirmed by Li *et al.* [121] using data from a mooring array deployed 100 km to the west of Barrow Canyon from 2013-2014. Li *et al.* [121] calculated a mean Pacific water transport of 0.57 Sv, in line with the shipboard estimate from Corlett and Pickart [57]. The seasonality and mesoscale spatial and temporal variability of the CSC was also investigated by Li *et al.* [121]. They determined that the current is surface intensified in summer and fall with a larger transport, and mid-depth intensified in winter and spring, as it moves shoreward, with a smaller transport. On shorter timescales the CSC was found to vary in concert with the Chukchi Shelfbreak Jet, which is located farther inshore and typically flows eastward. The dominant mode of variability was associated with two "extreme states", one in which the CSC is strong and the Shelfbreak Jet is reversed (flowing to the west), and the other in which the CSC is weak and the Shelfbreak Jet flows strongly to the east. Using reanalysis wind data and a simple model, Li *et al.* [121] demonstrated that these two states are dictated by the

wind stress curl over the Chukchi shelf. In the first state, the wind stress curl over the shelf is positive which leads to a drop in sea surface height on the shelf; this in turn drives westward flow at the edge of the shelf via geostrophic set up. In the second extreme state the curl is negative, and the associated increase in sea surface height on the shelf intensifies the Shelfbreak Jet and weakens the CSC.

While both Corlett and Pickart [57] and Li *et al.* [121] argued that the CSC emanates from Barrow Canyon, they did not have direct evidence of this. However, surface drifter data suggests that this is the case [212]. In addition, results from two recent model studies support the notion that the current forms from the outflow from the canyon. First, Spall *et al.* [210] demonstrated that the majority of the volume flux leaving the Chukchi shelf occurs in Barrow Canyon via non-linear advection. This outflow subsequently divides, with a portion forming the eastward-flowing Beaufort Shelfbreak Jet and the majority of it forming the westward-flowing CSC. The model CSC was found to transport around 0.5 Sv, consistent with in-situ measurements [57, 121]. This result is in contrast to the off-shelf subduction mechanism proposed by Timmermans *et al.* [232]. Second, the model results of Watanabe *et al.* [241] also showed evidence of the CSC, which was responsible for a plume of Pacific water extending along the slope toward the Northwind Ridge.

The observational study of Corlett and Pickart [57] revealed a second region of westward flow at the seaward edge of their mean transect across the Chukchi slope, which they interpreted to be the southern edge of the Beaufort Gyre. The model study of Spall *et al.* [210] showed a similar distinction between the CSC and the gyre. This interpretation was supported by different model runs which isolated the two circulation features. At this point, however, it is unclear what the fate of the CSC is and how the water masses within the current are modified upon leaving the shelf. Does the CSC remain a distinct feature on the continental slope? The surface drifter results of Stabeno *et al.* [212] suggests that this may be the case. Does the CSC ultimately get entrained in the Beaufort Gyre? What is the fate of the heat carried by the current? These questions motivate further investigation of the current and its downstream evolution.

In this paper we present the results of a study of the CSC using five profiling floats configured to be quasi-Lagrangian particles following the current. This is the first observational effort to address the fate of the Pacific water as it advects westward away from Barrow Canyon. Section 2 describes the data sources and methods used, namely the shipboard velocity and hydrographic data in addition to the array of profiling floats. In section 3 we first describe the basic state of the CSC as it was observed in September 2018, mapping the current and its properties along the western part of the Chukchi shelfbreak to the Northwind Ridge. This is followed by an analysis of the profiling float data showing the course of the current, including two instances in which the CSC was abruptly altered. Our conclusions are drawn in section 4.

9.3 Data Sources and Methods

The in-situ data presented in this study were collected during the Stratified Ocean Dynamics of the Arctic (SODA) cruise on the R/V Sikuliaq from 1 – 30 September 2018 (SKQ201819S). Additional data from the HLY1801 cruise on the USCGC Healy from 4 – 24 August 2018 are included.

9.3.1 Shipboard ADCP

Shipboard acoustic Doppler current profiler (ADCP) measurements of the current were obtained for nine transects across the Chukchi shelfbreak/slope during SKQ201819S. The data were acquired using the University of Hawaii Data Acquisition System (UHDAS) and processed using the Common Ocean Data Access System (CODAS). We use the data from the 300 kHz instrument, sampling at 1.1 Hz, which had reliable coverage in the upper 80 m of the water column. The accuracy is estimated to be ± 2 cm $\cdot$ s^{-1}. An additional ADCP transect across the shelfbreak/slope was obtained from HLY1801, using a 150 kHz instrument. The reader is referred to Li *et al.* [123] for information regarding the collection and processing of those data. Bathymetry along the transects was obtained by the echosounders on the two vessels.

9.3.2 SOLO Floats

Five Argo SOLO floats were deployed on 6 September while occupying a transect across the CSC. The deployment details are presented in Table 9.1. All of the floats were equipped with Sea-Bird Electronics (SBE 41) conductivity-temperature-depth (CTD) sensors, providing hydrographic profiles throughout their rise and fall. SOLO sensor accuracies are ± 0.002°C for temperature, ± 0.01 PSU for corrected salinity, and ± 2.4 dbar for pressure. Their records were transmitted with UTC time and position via Iridium satellite. The floats were configured to profile down and up to depths of $80 - 100$ m in order to stay in the core of the surface-intensified CSC. Each profile took roughly two hours to complete, of which one hour was spent at the surface for operational reasons, 25 min was spent on descent and ascent, and approximately 10 min was spent at the deepest descent depth. It took a few profiles to achieve the target depth of around 80 m, with the initial dives being as deep as 250 m, then closing in on the desired maximum depth over a few (3-5) profiles. The deployment of the floats was conducted in two steps. First, a transect across the current was carried out by the ship starting from the 100 m isobath and extending to the 2500 m isobath. This provided information on the lateral and vertical structure of the CSC. Based on this information, the floats were then deployed in the central portion of the current on a return transect a few hours later (transect 4 in figure 9.3).

Name	Float ID	Latitude (N)	Longitude (W)	Release Time (UTC)	Ocean Depth
A	11012	73°12.971′	159°44.281′	09/06 at 1 : 36 a.m.	1001 m
B	11014	73°11.710′	159°48.981′	09/06 at 1 : 55 a.m.	482 m
C	11015	73°10.365′	159°53.431′	09/06 at 2 : 14 a.m.	386 m
D	11016	73°09.091′	159°57.780′	09/06 at 2 : 32 a.m.	338 m
E	11018	73°07.808′	160°02.455′	09/06 at 2 : 41 a.m.	293 m

Table 9.1: SOLOS float deployment information.

The SOLO floats were thus used in a novel way, as quasi-Lagrangian particles in the current. The current being surface-intensified and the floats being set in a rapid shallow profiling mode, they are for most of the time in, or at least advected by the current, as long as the current exists. As a result, local temperature and salinity measurements were transmitted as a function of depth at different positions of the current, and the different profiles across the current are expected to be correlated.

9.3.3 Fast CTD

The Scripps Institution of Oceanography "Fast CTD" (FCTD) (see e.g. [182]) was deployed to collect high resolution conductivity and temperature measurements along several transects. The FCTD profiles at $5\ \mathrm{m \cdot s^{-1}}$ up and down from the end of a 32 foot long boom deployed from the starboard quarter. A Sea-Bird Electronics (SBE 39) CTD sensor on a streamlined drop body samples at 16 Hz with an accuracy of ± 0.002°C for temperature, $\pm 0.0003\ \mathrm{S \cdot m^{-1}}$ for conductivity, and ± 1 m for depth. At a typical steaming speed of 3–4 knots, profiles down to 300 m depth were spaced 400 m laterally.

9.3.4 Ancillary Data

To assess the impact of wind forcing on the CSC during our study period, we use the European Center for Medium-Range Weather Forecasts (ECMWF) ERA-Interim reanalysis 10 m wind product [22, 61]. The horizontal resolution is $0.75° \times 0.75°$, and the temporal resolution is 6 hr. These data were used to compute 6-hourly maps of the wind stress curl.

We also use the daily gridded surface geostrophic velocity data for the domain encompassing the float trajectories, provided by Copernicus Marine and Environment Monitoring Service (CMEMS, `http://marine.copernicus.eu/`). This product is gridded from multiple altimeter missions, which are all homogenized to the reference mission Jason-2. The horizontal resolution is 0.25°.

Information is used from two previous field programs that addressed aspects of the CSC. The first is the year-long mooring array mentioned in the introduction (see Li *et al.* [121]). This consisted of five moorings deployed from October 2013 to September 2014, spanning the outer shelf to upper slope near 157°W. This provided a year-long view of both the CSC and the Chukchi Shelfbreak Jet. A description of the array, including the instrumentation, data processing, and accuracy of the measurements, can be found in Li *et al.* [121]. The second field program was carried out in September 2002 aboard the Healy. It included a shipboard survey of a mid-depth anti-cyclone of Pacific WW that was embedded on the seaward side of the CSC. The eddy was first identified using expendable bathythermographs (XBTs), then it was mapped at high-resolution using expendable CTDs. The survey took roughly a day to complete and included shipboard ADCP measurements, thus providing a three-dimensional view of the eddy interacting with the CSC. The reader is referred to Scott *et al.* [204] for details.

9.4 Results

9.4.1 Vertical Transects

During the two cruises, nine transects were occupied across the continental slope of the Chukchi Sea, providing the opportunity to map the CSC (figure 9.3). Eight of the transects were done on SKQ201819S, which are numbered 1 to 8 progressing downstream, with transect $4^\star$ corresponding to a repeat of transect 4 during which the SOLO floats were deployed. Transect 0 was occupied on HLY1801 roughly two weeks before the first SKQ201819S section. Information regarding the transects is presented in table 9.2. The chronological order of the SKQ201819S sections is as follows: 6, 8, 7, 5, 4 and $4^\star$ (i.e. back and forth), 3, 2, and 1.

Figure 9.3 displays the velocity vectors averaged over the top 80 m, where the flow directed away from Barrow Canyon is coloured blue, and the flow directed towards the canyon is coloured red. The latter condition occurs on the shoreward ends of sections 1, 2, 3, 4, and 6. All of these sections extend onto the outer shelf, indicating that the eastward flow is associated with the Chukchi Shelfbreak Jet. Farther offshore the flow is consistently directed away from the canyon, associated with the CSC. The vertical sections of cross-track velocity from the shipboard ADCP confirm this interpretation. A typical example is shown in figure 9.4, showing a vertical section of cross-track velocity for transect $4^\star$. It reveals the bottom-intensified eastward flow of the Shelfbreak Jet, and, offshore of this, the surface-intensified westward flow of the CSC. This is the cannonical situation for this time of year, as demonstrated by previous shipboard measurements [57] and mooring data [121].

In order to quantify the transport of the CSC in the SKQ201819S transects, we implemented the following objective approach (the HLY1801 section was not considered since it was non-synoptic with the rest of the data set). Using the ADCP data in the top 20 m (since the CSC is surface-intensified in this season), we identified the core of the CSC and took the width of the current to be where the velocity dropped to 20% of the peak value. We have marked the lateral boundaries of the CSC based on this criterion, in figure 9.3 with green dots, and in figure 9.4 using dashed lines. The westward flow offshore of the CSC is likely the southern edge of the Beaufort Gyre (see Corlett and Pickart [57] and Spall *et al.* [210]). On two of the nine transects the 20% condition was not met on the seaward side of the CSC (i.e. the flow remained fairly strong until the edge of the section). In these two instances (sections 2 and 3) the edge of the CSC was taken to be the offshore end of the transect.

The along-slope volume flux of the CSC for the n^{th} transect is given by

$$\Phi^{(n)} = \int_{x_L}^{x_R} \int_{z=0\ \mathrm{m}}^{z=80\ \mathrm{m}} u_{c,\perp}^{(n)} \mathrm{d}x\mathrm{d}z, \tag{9.1}$$

where $u_{c,\perp}^{(n)}$ is the CSC velocity orthogonal to the considered transect, and x_L and x_R the left and right bounds of the CSC as previously defined. The integration area is therefore delimited horizontally by the bounds marked on figure 9.3 for each transect, and a vertical extension from the surface to 80 m. Each of the ADCP sections was extrapolated to the sea surface using an objective Laplacian-Spline scheme (e.g. [177]). The CSC of course extends deeper than 80 m (see

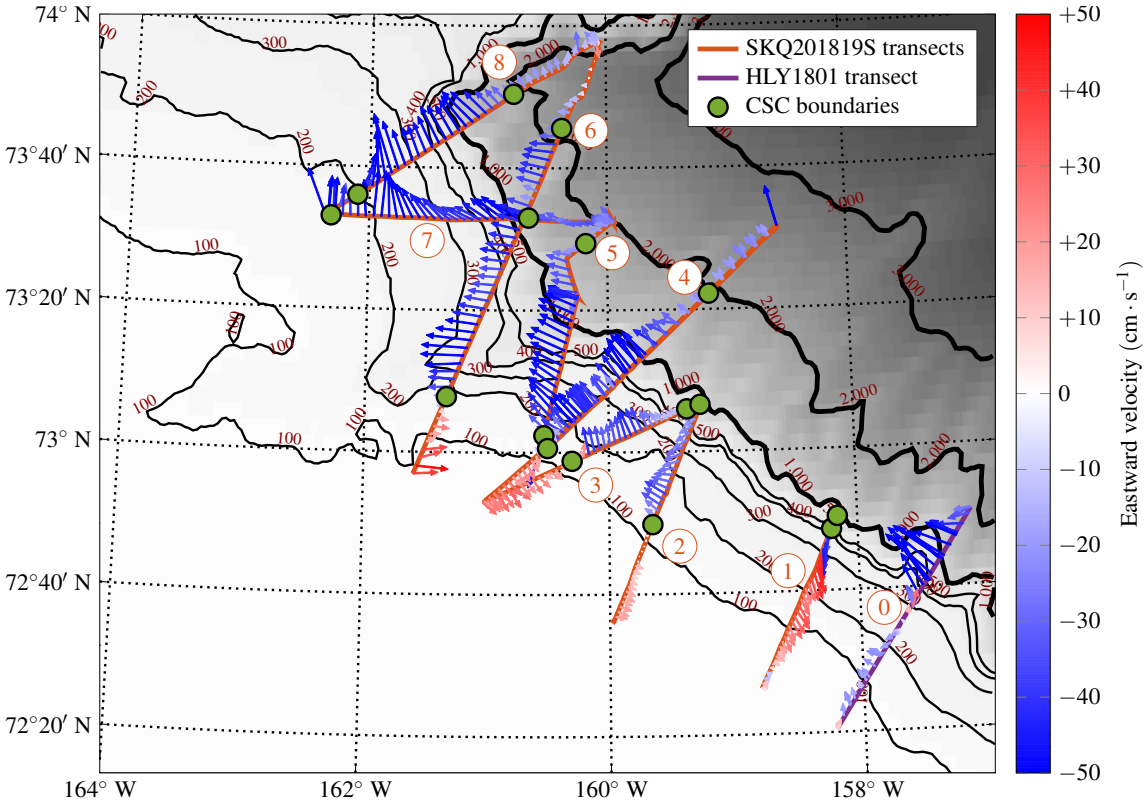

Figure 9.3: Overview of the southwest portion of the Canada Basin. The orange line segments show the ship track. The arrows represent the depth-averaged flow over the upper 80 m, coloured from blue to red depending on whether the flow is heading West (blue, associated to the CSC) or East (red, associated to the SJ). The different currents in the region are: the Shelfbreak Jet, the Chukchi Slope Current, and the southern edge of the Beaufort Gyre. Transects from upstream to downstream (in the sense of the CSC) are numbered from 0 to 8. The green dots indicate the estimated limits of the CSC on the different transects (see text).

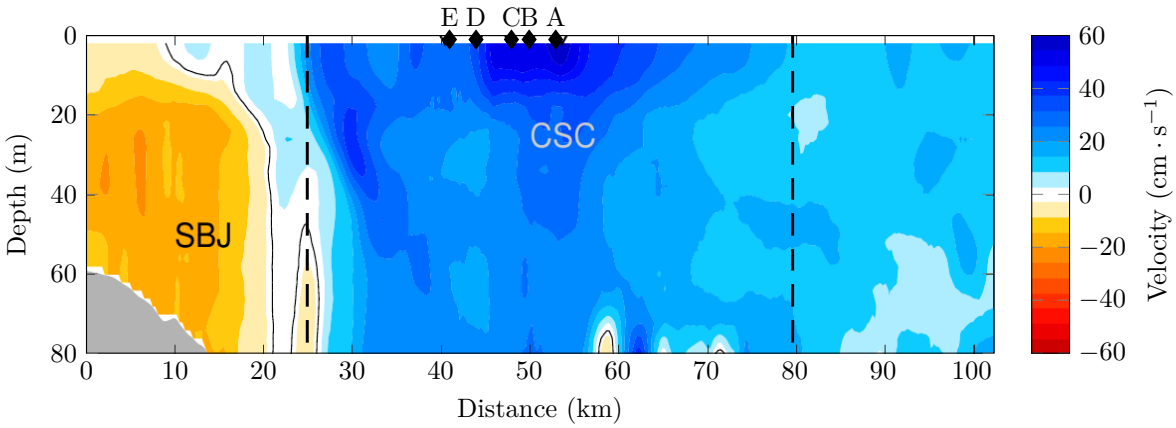

Figure 9.4: Vertical section of cross-track velocity for transect 4⋆. Positive velocity is northwestward (away from Barrow Canyon). The dashed lines indicate the lateral bounds of the Chukchi Slope Current, determined using the procedure described in the text. The labels denote the Chukchi Slope Current (CSC) and Chukchi Shelfbreak Jet (SBJ). The letters on top, from A through E, indicate the float deployment locations.

Transect	Cruise	FCTD	Time (UTC)	End points
0	HLY1801	No	08/19 – 05 : 57	(72.84° N, 157.1° W)
			to 08/19 – 14 : 12	(72.34° N, 158.2° W)
1	SKQ201819S	Yes	09/07 – 15 : 30	(72.86° N, 158.1° W)
			to 09/08 – 00 : 00	(72.46° N, 158.8° W)
2	SKQ201819S	Yes	09/06 – 22 : 50	(73.12° N, 169.2° W)
			to 09/07 – 08 : 24	(72.61° N, 159.9° W)
3	SKQ201819S	Yes	09/06 – 12 : 30	(72.89° N, 161.0° W)
			to 09/06 – 22 : 33	(73.12° N, 159.2° W)
4	SKQ201819S	No	09/05 – 17 : 16	(72.99° N, 160.6° W)
			to 09/05 – 19 : 55	(73.52° N, 158.6° W)
4⋆	SKQ201819S	No	09/05 – 22 : 19	(73.52° N, 158.6° W)
			to 09/06 – 12 : 30	(72.89° N, 161.0° W)
5	SKQ201819S	No	09/05 – 09 : 36	(73.54° N, 159.9° W)
			to 09/05 – 16 : 48	(72.99° N, 160.6° W)
6	SKQ201819S	No	09/04 – 00 : 00	(72.95° N, 161.6° W)
			to 09/04 – 13 : 12	(73.96° N, 160.1° W)
7	SKQ201819S	No	09/04 – 23 : 16	(73.55° N, 162.4° W)
			to 09/05 – 09 : 36	(73.54° N, 159.9° W)
8	SKQ201819S	No	09/04 – 19 : 12	(73.96° N, 160.1° W)
			to 09/04 – 23 : 16	(73.55° N, 162.4° W)

Table 9.2: Records of the different transects. Transect 4⋆ corresponds to the SOLO deployments.

[57, 121]), but we are limited here by the range of the 300 kHz ADCP. To account for this we used the data from a year-long array of five moorings described in section 9.3.4, which was located 25 km to the east of transect 0. These data indicate that, for the month of September, integrating to 80 m accounts for 72% of the CSC transport. As such, we scaled-up our estimates by a factor of $1/0.72 = 1.39$. The resulting CSC transports for the SKQ201819S transects are given in table 9.3 and shown in figure 9.5(a). The measured volume flux systematically decreased from 1.95 Sv (transect 6) to zero (transect 1) over the course of the experiment with an average value of 1.03 Sv for the 9 transects. The mean is substantially larger than the year-long mean value reported by Li *et al.* [121] (0.57 Sv) and the summertime mean value given by Corlett and Pickart [57] (0.50 Sv). The latter of these two values, however, represent the Pacific water component of the current, i.e. excluding the meltwater and riverine contributions that are mainly present in the upper layer. While we have no way of extracting the Pacific water contribution, we note that the full transport of the CSC for the month of September 2014 reported by Li *et al.* [121] was 0.99 Sv, which is in line with the mean value reported here for the September 2018 survey.

Why is there such a large range of transport values in the SKQ201819S data set? We argue that this is due to the variable wind forcing during the survey. As noted in the introduction, Li *et al.* [121] demonstrated that the strength of the CSC is strongly modulated by the wind stress curl on the Chukchi shelf via geostrophic set up. When the wind stress curl is positive, the corresponding drop in sea surface height (leading to a sea surface gradient across the Chukchi slope) results in a stronger CSC. When the wind stress curl is negative on the shelf the opposite happens and the CSC weakens or reverses. To assess this effect in our data set, we constructed a time series of average wind stress curl over the same region of the shelf considered by Li *et al.* [121], presented in figure 9.5(b). Our study reveals that there was a prolonged period of positive wind stress curl during the first part of the SKQ201819S survey, followed by a prolonged period of negative wind stress curl during the later part of the survey. This result is corroborated by considering the gridded absolute geostrophic velocity productThe results in figure 9.5 reveals that there is a general consistency between the wind stress curl and the CSC transport in line with the previous results of Li *et al.* [121]. That is, the current tends to be strong during periods of positive curl, and weak (or reversed) during periods of negative curl.

This result is corroborated by considering the gridded absolute geostrophic velocity product from altimetry described in section 9.3.4. Since the CSC is surface-intensified at this time of year,

the daily satellite-derived velocity data contains a signal of the current. As such, for each of the SKQ201819S transects in figure 9.3 we computed the width-integrated surface current normal to the transect between the endpoints of the CSC determined above (green curve in figure 9.5(a)). This quantity revealed the same trend as was found for the ADCP-derived transports (black curve in figure 9.5(a)), providing compelling support for the role of the wind stress curl in dictating the transport of the CSC during the shipboard survey.

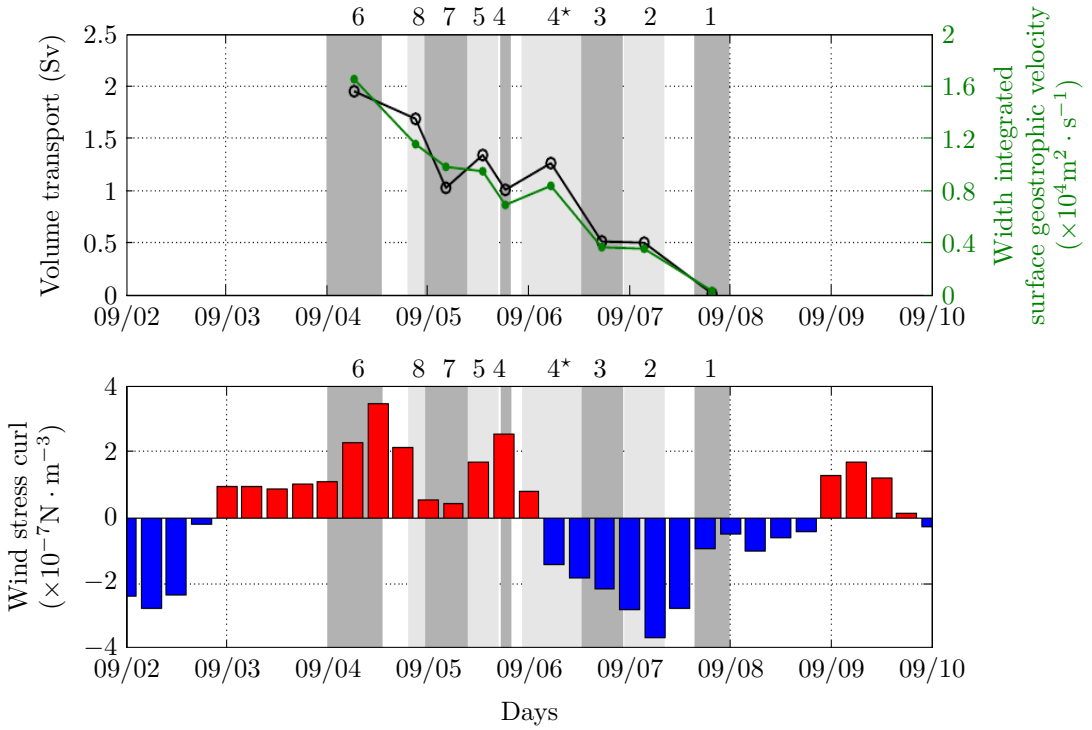

Figure 9.5: Top: (a) Volume transport of the CSC using the SKQ201819S shipboard ADCP data (black symbols) and laterally integrated cross-track surface velocity over the width of the CSC (green symbols). Bottom: (b) Wind stress curl every 6 hours averaged over the northeast Chukchi shelf (see text). The time of occupation of the SKQ201819S transects are shaded grey and numbered along the top.

Transect	Volume transport (Sv)	Laterally integrated surface geostrophic velocity ($\times 10^4 m^2 \cdot s^{-1}$)
1	1.947	1.651
2	1.683	1.152
3	1.022	0.978
4	1.336	0.945
4*	1.003	0.687
5	1.259	0.833
6	0.508	0.362
7	0.496	0.351
8	0.009	0.027

Table 9.3: Volume transport for the different transects.

9.4.2 Float Data

Figure 9.6 presents the trajectories of the SOLO floats after they were deployed on 6 September on transect 4* within the CSC (figure 9.3). The initial deployment positions of the floats favored the

inshore side of the current, due to the fact that the current had shifted a bit offshore subsequent to the occupation of transect 4 that was used to determine the launch positions. The deployment transect is indicated as line (i) in figure 9.6. The floats transmitted their first data a few hours after deployment. Their trajectory can be divided into three main phases: an initial very coherent motion, followed by a disruption, and finally a reappearence of a coherent behaviour.

Before Northwind Ridge: Initial Coherent Motion

Traveling along the continental slope the floats stayed together in a very coherent fashion. Shortly after deployment, the floats encountered Hanna Canyon near 161° W. Previous studies have shown that the behaviour of a current impinging upon a canyon depends on both the canyon topography and the stratification of the water column (e.g. [100, 111, 244]). The pertinent parameter is the ratio of the width of the canyon, W, and the internal Rossby radius of deformation, $R = NH/f$, where N is the buoyancy frequency, H is the water depth, and f is the Coriolis parameter. If this ratio is larger than two, then the canyon is considered dynamically wide and the incident current will feel the entire canyon. The width of Hanna Canyon is approximately 100 km. We used the mooring data of Li *et al.* [121], described in section 9.3.4, to estimate R, and found it to be 15-20 km. Hence, Hanna Canyon is dynamically wide. As such, a current encountering the canyon should not simply follow the isobaths around the canyon, but instead get partially diverted into the canyon and progress across isobaths to its downstream flank [102]. As discussed in [102], when the current encounters the downstream flank, the water column compresses, and, in order to conserve potential vorticity, this induces a negative relative vorticity which causes the current to divert back offshore into deeper water.

This scenario is consistent with the behaviour of the CSC in figure 9.6. When the floats first encounter Hanna Canyon they flow into deeper water; i.e. they are unable to stay on an isobath and subsequently cross to the other side of the canyon. As this happens they progress into shallower water until about 162° W (figure 9.6), at which point they turn anti-cyclonically into deeper water again. This northward excursion appears to be critical to the fate of the CSC; we return to this in the discussion section. It is worth noting as well that the wind stress curl was weak throughout this time period, implying that wind did not play a role in this change in the float trajectories.

On 10 September, roughly four days after their release, the floats passed over the Northwind Ridge. Importantly, the floats were shoreward enough that they did not feel the topography of the ridge. That is, the floats continued to flow into deeper water after exiting Hanna Canyon as they flowed past line (ii) in Figure 9.6. During these first four days, the fastest floats were A and B, originally deployed around the 1000 m and the 500 m isobaths. Floats D and E, deployed farther onshore, were the slowest. This difference between the float velocities reveals the structure of the current, stronger offshore around the 1000 m isobath. As they were advected by the CSC, the floats did not stay in the same cross-shelf configuration and their trajectories crossed each other. This means that, due to the complexities of the CSC structure interacting with the vertical profiling action of the floats, two different floats can pass through the same location at different times. Float E had the least coherent motion, crossing twice over the other trajectories while still remaining in the current. Before leaving the edge of the Canada Basin and crossing the Northwind Ridge (the location labeled as line (ii) in figure 9.6) at the end of the fourth day, the fastest floats had migrated onshore and the slowest offshore. All floats went through line (ii) within a few hours time difference, which indicates a very coherent CSC during this time window.

Figure 9.7 (left) presents the temperature profiles of all five floats during their passage along the edge of the Canada Basin. The first profile is taken at deployment location (line (i) in figure 9.6). The first 100 hours of each data set roughly correspond to the trajectory before the floats escape the Canada Basin going over the Northwind Ridge (74°06′ N, line (ii) in figure 9.6). All of the time series have a very coherent structure with cold water at the surface, above a layer of warm water up to 5.5°C between 20 and 40 m. After 50 hours the three floats at the outer edge of the current – A, C, and D – show the appearance of cold water, centered around 30 m (figure 9.7). This happened when the floats reached 162° W and started heading north into deeper water instead of going West.

Figure 9.8 shows a temperature-salinity (TS) plot from the five floats at different locations. In figure 9.8(a) float profiles are taken at the deployment location (line (i) in figure 9.6). As noted

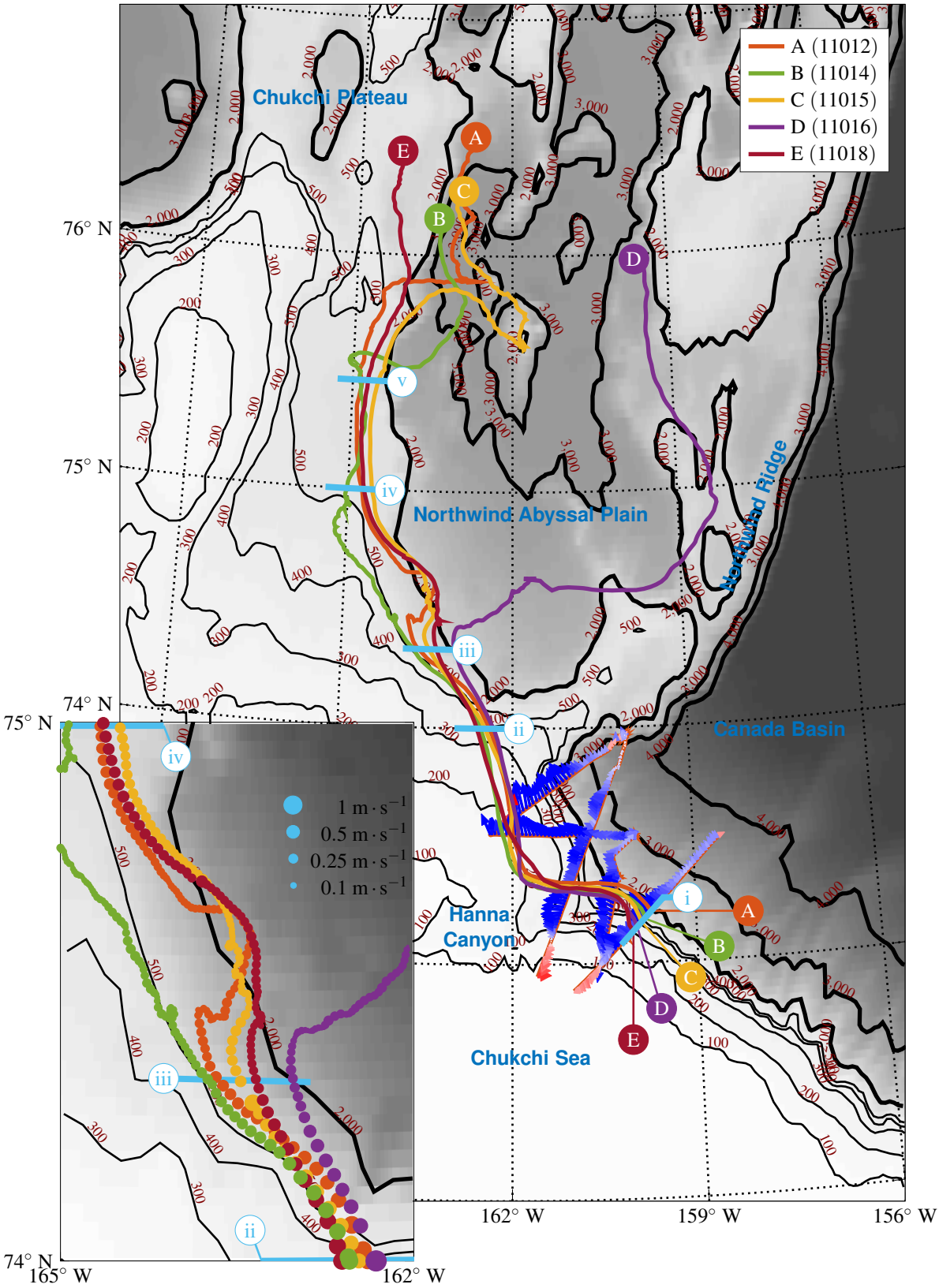

Figure 9.6: Trajectories of the five SOLO floats (A – E) superimposed onto the ADCP data and ship transects, indicating the path of the CSC, following the shelfbreak from the Canada Basin to the Northwind Basin. Sections (i) to (v) are relevant delimitations for the different parts of the float trajectories (see explanation throughout the text). Bottom-left inset: Enlarged view of the SOLO float trajectories from 74° N to 75° N. The size of the dots represents the instantaneous velocities of the floats (see the legend).

in the introduction, upon deployment the floats initially profiled as deep as 250 m, and these deeper data are included in figure 9.8(a). It reveals that the CSC was advecting MWR at the surface, ACW and BSW below this in the core of the current (20-40 m depth), and RWW deeper than 100 m. Notably, Corlett and Pickart [57] saw very little ACW in their vertical sections, whereas our results demonstrate that, at times, the CSC can advect a large amount of this warm water westward. This is contrary to the common notion that the ACC mostly feeds the Beaufort Shelfbreak Jet. It also provides further evidence that the CSC emanates from the outflow from Barrow Canyon (see also [210, 121]). Since the floats profiled to deeper depths at the start of their mission, they measured the presence of Atlantic Water (AW) in figure 9.8(a). Both Corlett and Pickart [57] and Li *et al.* [121] found that the CSC advected AW at depth, and the reason for this remains unexplored. At line (ii) the CSC was still advecting ACW (figure 9.8(a)), but one also sees the presence of MWR between 0°C and −1°C in the salinity range 28–30. This is the same cold water mentioned above measured by the offshore floats A, C, and D starting around 50 hours. The water likely originated from the interior of the Canada Basin resulting from local ice melt.

After Northwind Ridge: Possible Disruption by an Eddy

After passing the Northwind Ridge, the floats proceeded northwest following the bathymetry until around 13 September when they were nearly arrested on the edge of the Northwind Abyssal Plain, around 74°20′ N (line (iii) in figure 9.6). Starting from the East, the floats peeled off one after the other and followed more intricate trajectories; during this time only float B remained relatively close to following an isobath. This is also the time that the warm water signature disappeared rapidly in the float profiles (figure 9.7, dashed line), even showing the presence of WW below 40 m depth for floats C and E. As shown in figure 9.7, this transition to cold water occurred very abruptly, over a period of 2 to 10 hours. This state persisted for approximately four days until floats A, C, and E, veered back into shallower water and started to follow the bathymetry again. By contrast, float D permanently left the region and proceeded into the Northwind Abyssal Plain. During this period, the float velocities dropped from 1 $\mathrm{m \cdot s^{-1}}$ to 0.1–0.2 $\mathrm{m \cdot s^{-1}}$, which is nearly an order of magnitude smaller, as shown in the inset of figure 9.6. Such a large decrease in velocity, together with the wandering motion experienced by the floats, show that the current was strongly perturbed.

This region of altered behavior, between 74°20′ N and 75° N, is depicted with TS plots in figure 9.8. In 9.8(c), one sees a pronounced difference in the TS characteristics. The water composition measured by the floats is now mainly MWR with RWW and some BSW, indicative of strong mixing and influx of cold water into the CSC. A standard feature of figure 9.8(c) is the absence of the relatively warm ACW peak, these waters having undergone substantial change in properties due to mixing processes. When the floats enter the main part of the current again, this hydrographic structure is still present, although some of the cold, fresh MWR measured upstream reappears (compare 9.8(b) and 9.8(d)). Vertically averaged temperature signals in figure 9.7 (right) show a clear cold signature at the beginning of the perturbed period, with a drop of about 3°C in the core of the CSC (from 20 to 40 m depth, in red). Table 9.4 presents the densities and temperatures averaged in the vertical from 20 to 40 m depth for the 5 floats from deployment to line (iii), and from line (iii) to line (iv), and for floats A, B, and E from line (iv) to (v), as their profiles show clear signature of the CSC. These three regions – corresponding to the well-established CSC, the period of disruption, and the re-established CSC, respectively – have no significant variation in the mean density, but there is a drop in the mean temperature, from 1.25°C to 0.16°C, during the perturbed state. When the current re-establishes, the temperature slightly rises from 0.16°C to 0.35°C. This variation supports the idea that a cold water mass of about the same density influenced the CSC between locations (iii) and (iv). After this event, the average temperature of the CSC is lower than before. Furthermore, the TS plots in figures 9.8 indicate that the upper layer of the stratification remained unchanged, which is confirmed by the nearly constant heat content in the top 10 m (in blue in figure 9.7 (right)). As a result, the water column sees supply of cold water from the surroundings, pointing towards a horizontal exchange process rather than vertical mixing for which the vertically averaged heat content would have remain unchanged.

What was the reason for this sudden offshore excursion of the floats and change in hydrographic character? Examination of the wind field during this time indicates that the wind stress curl over

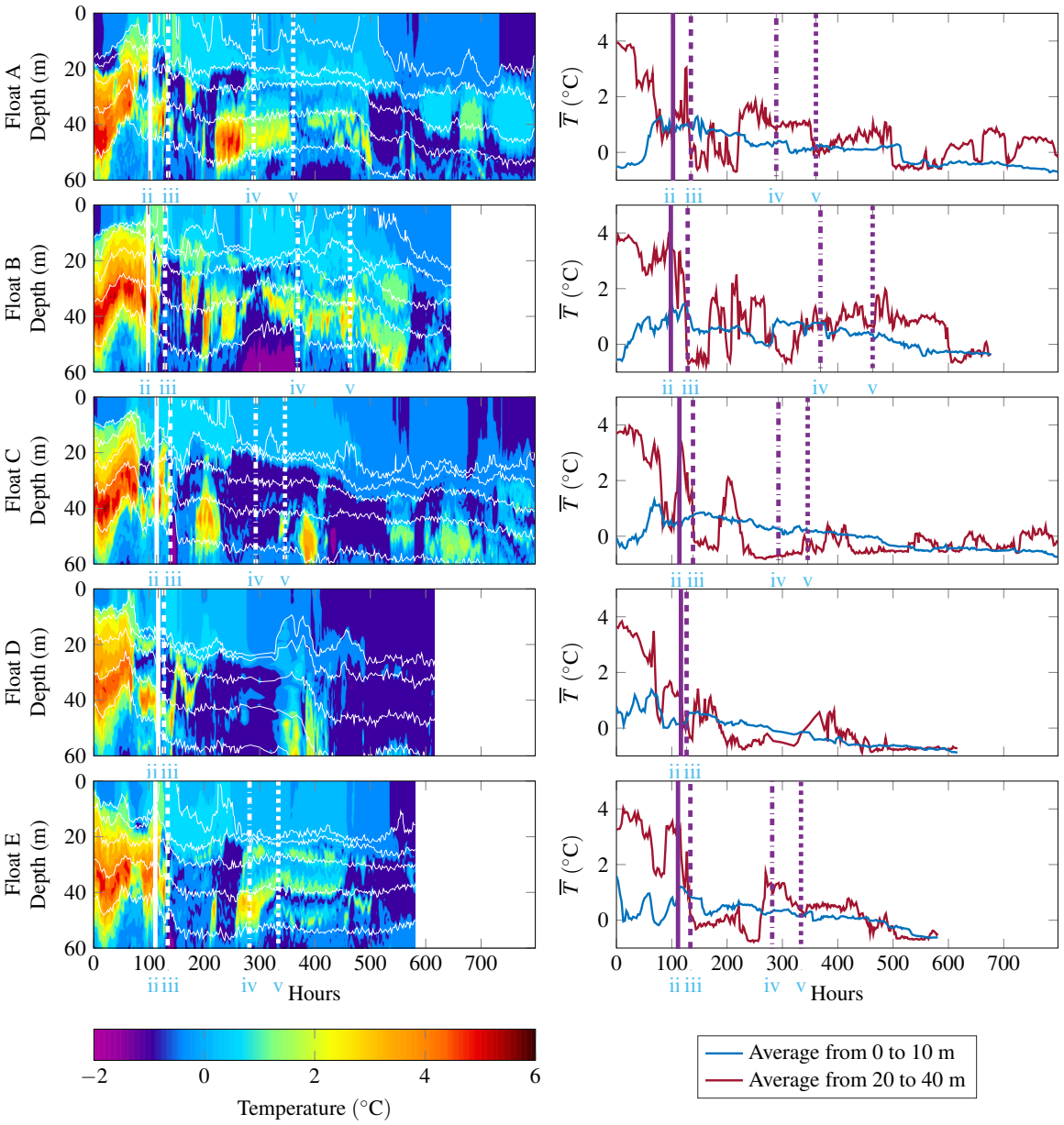

Figure 9.7: Left : Depth-time plot of temperature (color) and density (white contours, $\mathrm{kg \cdot m^{-3}}$) for each of the five SOLO floats, from top to bottom: A, B, C, D, and E. The selected isopycnals are 21, 22, 23, 24, and 25 $\mathrm{kg \cdot m^{-3}}$. Right : Averaged temperature $\overline{T}$ over the top 10 m (blue) and from $20 - 40$ m (red). The thick vertical white lines in the left-hand column and purple lines in the right-hand column indicate select locations discussed in the text: the first line (solid) shows when the floats are beyond the Northwind Ridge and corresponds to label (ii) in figure 9.6 the second line (dashed) shows when the floats were disrupted, corresponding to label (iii); the third line (dashed-dotted) shows when the floats became well-behaved again, corresponding to label (iv); and the fourth line (dotted) shows when the coherence of the current is lost, marked as line (v).

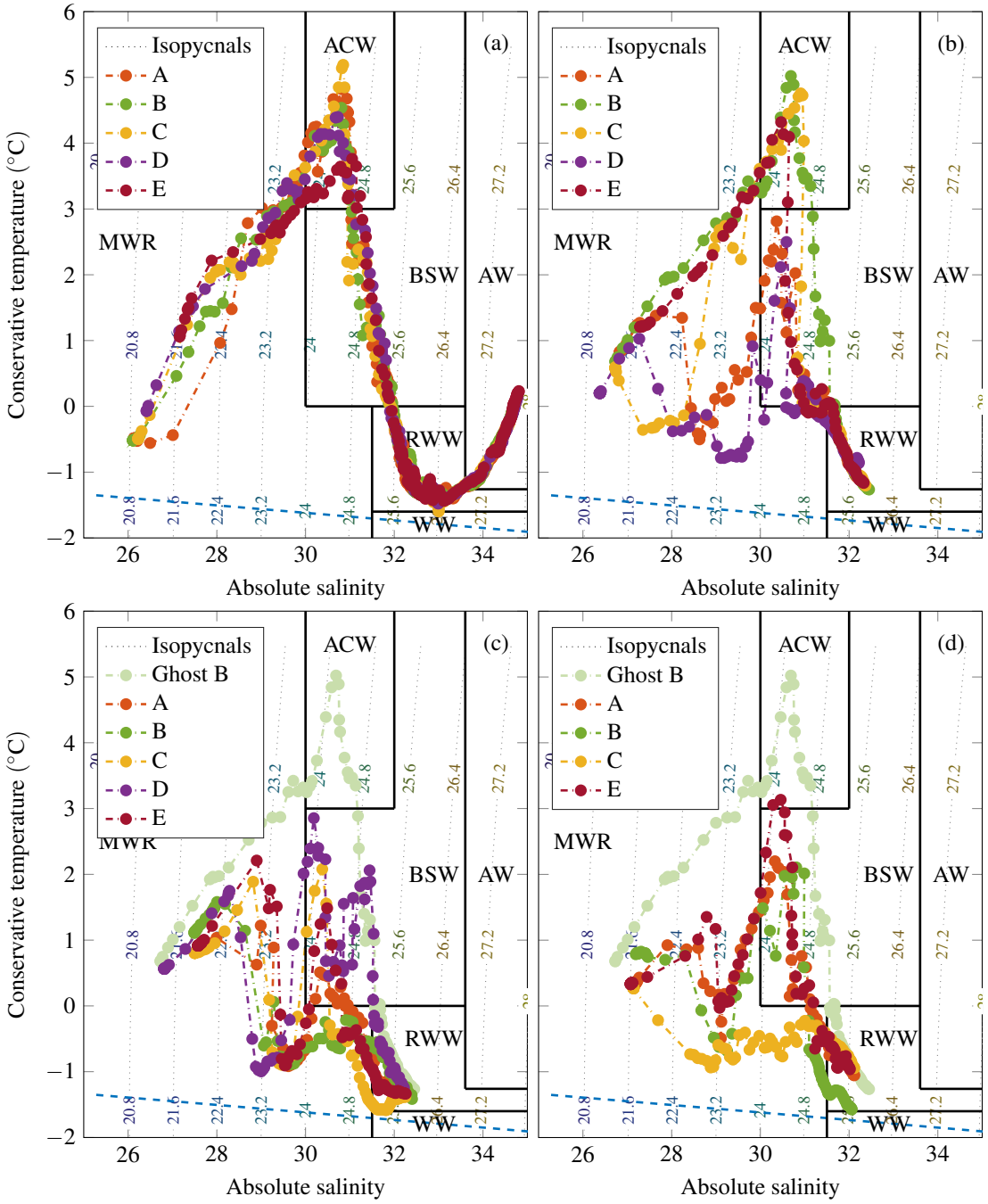

Figure 9.8: Temperature-salinity (TS) plots of the five floats (a) at deployment location on the shelfbreak of the Canada Basin, from 250 m deep profiles (location (i) in figure 9.6); (b) at 74°06′ N, just after leaving the Canada Basin and the Northwind Ridge (location (ii) in figure 9.6), from 80 m depth profiles; (c) at 72°20′ N, during the interaction with the eddy (location (iii) in figure 9.6); and (d) at 75° N, after the eddy event (location (iv) in figure 9.6). The thick lines show boundaries between water masses and are taken from [57] Fig.3. The water mass abbreviations are MWR = sea ice melt water / river runoff; ACW = Alaskan Coastal Water; BSW = Bering Summer Water; RWW = Remnant Winter Water; and AW = Atlantic Water; WW = Winter Water. A "ghost profile" (float B, before the eddy event) shows the original TS structure of the CSC.

Region (see figures 9.6 and 9.7)	Mean density ρ ($\times 10^3$ kg $\cdot$ m^{-3})	Mean temperature T (°C)
From (i) to (iii) (in the CSC)	1.0240	1.251
From (iii) to (iv) (eddy disruption)	1.0235	0.162
From (iv) to (v) (back in the CSC)	1.0236	0.346

Table 9.4: Densities and temperatures averaged in the vertical between 0 m and 80 m from the profiles in figure 9.7 in the different regions. Last line concerns only floats A, B, and E.

the Chukchi shelf was positive. Such forcing would tend to cause the CSC to proceed farther shoreward; hence this cannot explain the offshore excursion. We postulate that an anti-cyclonic eddy impinged upon the CSC from offshore, perturbing the CSC and mixing the water within the current with surrounding water masses. We note that mid-depth-intensified anti-cyclonic eddies are very common in this region [78, 136, 137, 180, 183, 256]. Two examples of interactions of these features with the offshore side of the CSC are shown in figure 9.9. Figures 9.9 (a) and (b) show along-slope velocity and temperature measurements made in August 2004 [204], in the area near transect 8 in our study (see section 2d for a description of the data). The presence of a cold core eddy, with a core temperature near -1.8°C, interacting with the CSC is clearly seen. Anomalously cold water in such a feature mixing with the CSC could help explain the sudden drop in temperature recorded by the floats near line (iii)(figure 9.7). Figures 9.9 (c) and (d) show along-slope velocity and temperature from a shipboard CTD section occupied in August 2017, roughly corresponding to transect 5 in the present survey. In this section, a warm-core anti-cyclone is centered near 80 m water depth. In both cases, the familiar widening of the isopycnals is associated with the azimuthal flow of the eddy. However, in both instances the onshore side of the eddy is essentially merged with the offshore side of the CSC. One can envision a float getting entrained and mixed into the eddy, and subsequently getting deflected offshore. Such a scenario is consistent with the fact that, after section (iii), the offshore-most SOLO float underwent the largest excursion, while the onshore-most float remained unperturbed. We note that cold core anti-cyclones are far more common than warm core anti-cyclones [255], so it is more likely for the CSC to be impacted by a cold core in the manner seen in our data.

Farther North: Resurrection of the CSC

After wandering for four days, three of the floats – A, C, and E – came back into the restored CSC, joined five days later by a fourth one – B –, while the outer-most float – D – was permanently expelled from the current. The reconnection of the four floats infers that the CSC was well re-established for several days beyond 75°N (line (iv) in figure 9.6). These four floats headed north, generally following the bathymetry, at 165° W, but slower than before the disruption of the CSC due to the presumed interaction with an eddy. Furthermore, the warm temperature signal for the returning floats was not as strong as before the interruption. As shown in figure 9.7, the warm water signature went up to 3°C instead of 5°C. In addition, occurrences of warm water were less continuous as we can identify some smoothly varying features and some strongly intermittent patches within the current (especially for float C). We note that the decrease in velocity, along with the change in temperature of the current from warm to cold, could be explainable by a temporal change in the CSC rather than a consequence of the eddy encounter. Since the floats spent roughly 4-5 days seaward of the main flow of the CSC, it could be that during this intervening period the current slowed and cooled due to other reasons. For example, the wind stress curl on the Chukchi shelf transitioned from positive to negative as the floats were re-joining the current, which would tend to weaken the CSC.

On 24 September the two leading floats C and E took different paths: C started to progress into the Northwind Abyssal Plain to the east before going back to the west; E progressed northward more in line with the bathymetry towards the Chuckhi Plateau. Later on, floats A and B did a short excursion into the Northwind Abyssal Plain as well. Overall, these float trajectories suggest that at least part of the water in the CSC is able to get entrained into the edge of the Beaufort Gyre in this general vicinity. We identified the corresponding location (line (v)) in figure 9.6 as the

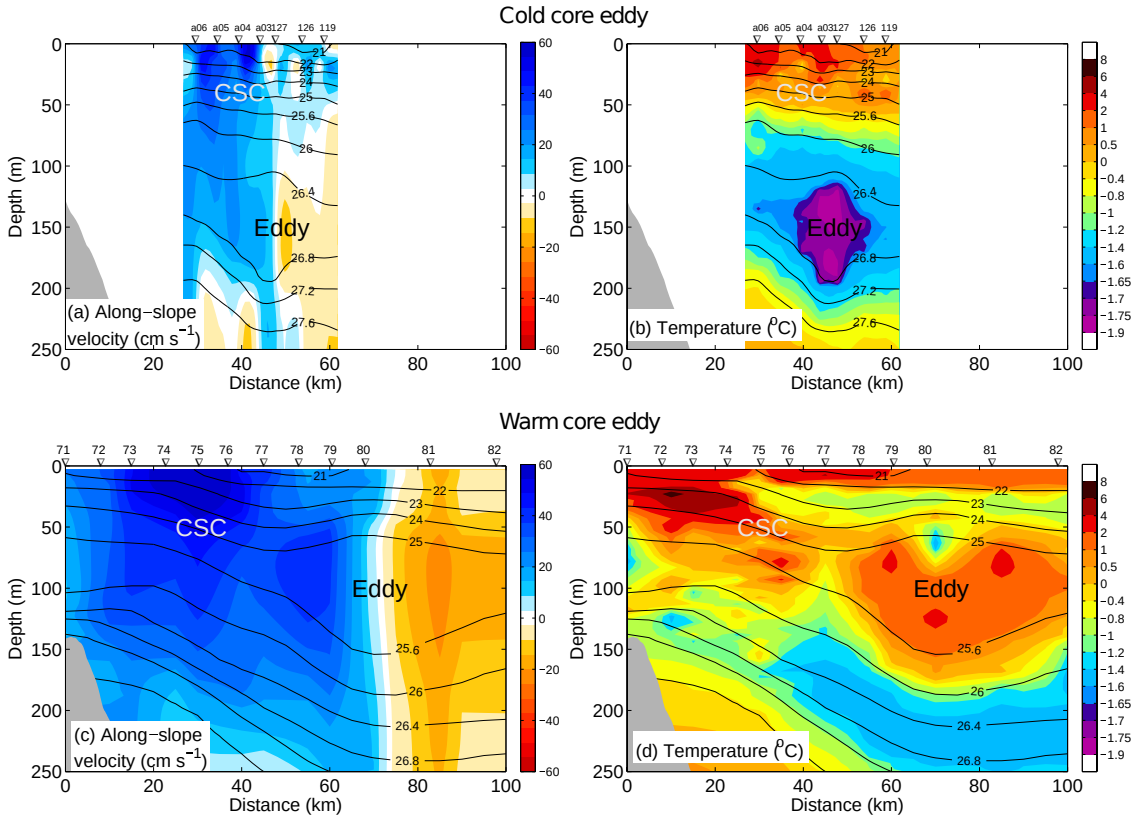

Figure 9.9: Vertical sections from an occupation near transect 8 in September 2004 showing a cold core eddy (top row, (a) and (b)) [204] and near transect 5 in August 2017 showing a warm core eddy (bottom row, (c) and (d)). (a) and (c): absolute geostrophic velocity (color) overlain by potential density (contours, $\mathrm{kg} \cdot \mathrm{m}^{-3}$). Positive velocity is northwestward (away from Barrow Canyon). The labels denote the Chukchi Slope Current (CSC) and the anti-cyclonic eddy. CTD Station locations are marked along the top. (b) and (d): potential temperature (color) overlain by potential density (contours).

end of a coherent and localized CSC current, around 75°30′ N, which can be seen as transition to a more widespread outflow towards the Northwind Abyssal Plain and the Chukchi Plateau. Around 10 October we lost track of the floats likely because of ice coverage in this region. Interestingly, warm water was still measured in the last few profiles.

9.5 Summary and Conclusions

We have presented results from a field study investigating the evolution and fate of the Chukchi Slope Current (CSC). A novel method was employed using profiling SOLO floats as quasi-Lagrangian particles deployed across the current. In addition to this, velocity data were collected along several transects using the shipboard ADCP. The transect data showed good agreement with earlier measurements of the CSC during this time of year, revealing a strong surface intensified current flowing westward along the continental slope. The corresponding volume flux estimates ranged from near zero to nearly 2 Sv. This wide range can be explained by the variation in wind forcing during the cruise: the first part of the survey was characterized by positive wind stress curl on the Chukchi shelf, which is conducive for a strong CSC, while the latter part of the survey was characterized by negative wind stress curl on the shelf, which weakens or reverses the CSC.

The float trajectories were characterized into three basic regimes. Initially the floats traveled rapidly in the CSC, turning sharply to the north as they negotiated Hanna Canyon. This path is consistent with the shipboard ADCP transect data. The next phase occurred after the floats passed the Northwind Ridge. At this point they abruptly slowed, and four of them veered offshore (only the shoreward-most float continued to follow an isobath). We argue that this interruption was likely caused by the CSC interacting with a cold-core, anti-cyclonic eddy at the offshore edge of the current. While not identified in our data set, such eddies are common in this region, and are known to come in contact with the CSC. This presumed encounter with the eddy permanently expelled the offshore-most float from the CSC, but the three other floats eventually re-joined the CSC and proceeded northward again. During the final phase, the floats started to diverge and take more chaotic trajectories, entering the western side of the Northwind Abyssal Plain. It is likely that the floats were becoming entrained into the edge of the Beaufort Gyre at this point.

The water mass structure measured by the floats also varied along their pathways. During the initial phase, the CSC was advecting a range of Pacific summer and winter waters, including the very warm and relatively fresh Alaskan Coastal Water (ACW) in the depth range $20 - 40$ m. This supports the notion that the CSC originates from the outflow from Barrow Canyon, which has been argued in previous studies. During the eddy encounter the ACW signature disappeared. This provides supporting evidence that the floats were pulled out of the core of the CSC by the anti-cyclone. After the three floats re-joined the CSC, the ACW signature did not re-appear. Instead, the water mass occupying this depth range was predominantly Bering Summer Water (BSW). It is not clear if the floats simply measured a different part of the CSC upon rejoining the current, or if lateral mixing during the eddy encounter converted the ACW to BSW. In any case, the CSC continued to advect warm water to the north until the current eventually subducted under the ice.

Our results have provided new observational insights regarding the fate of the CSC. The previous study of Corlett and Pickart [57] showed that the current typically resides on the upper continental slope (median isobath of 238 m), consistent with the surface drifter results of Stabeno *et al.* [212]. Notably, the orientation of the isobaths on the upper Chukchi slope (shallower than about 300 m) are oriented more zonally to the west of the Northwind Ridge than those of the deep slope (deeper than about 400 m). This suggests that when the CSC is located over relatively shallow depths it might continue westward toward the East Siberian Sea, while in those cases when it is situated in deeper water it will flow more northward into the Chukchi Borderland. The results of Corlett and Pickart [57] suggest that the former scenario might be more common, although the divergence of the isobaths could lead to a bifurcation of the current.

The float trajectories presented here suggest that there is another aspect of the topography that could play a critical role in the fate of the CSC: in particular, Hanna Canyon. Consistent with the numerical study of Hyun [102], as the CSC encountered the dynamically wide canyon it flowed across isobaths to the far side of the canyon, before turning anti-cyclonically to the north. This abrupt turn was likely due to the current trying to conserve its potential vorticity

when experiencing layer compression as it flowed up the far side of the canyon. A nearly identical northward excursion of the CSC on the western flank of Hanna Canyon was reported by Scott *et al.* [204]. While other factors such as wind [121] and instabilities [57] undoubtedly influence the path of the CSC, the evidence presented here in conjunction with the previous observations of Scott *et al.* [204] implicate the topography of the canyon as a major factor. This is supported by the fact that when the SOLO floats turned offshore, the wind stress curl on the Chukchi shelf was in fact conducive to drive an onshore excursion of the CSC.

It is intriguing to think that a local bathymetric feature such as Hanna Canyon could help dictate the downstream path of the CSC, and in turn influence the fate of most of the Pacific-origin water entering the Arctic Ocean. If the CSC were to remain on the upper Chukchi slope it would flow towards the Eurasian Arctic. By contrast, if it gets diverted to the north – the fate suggested by the float data presented here – it would be more apt to get entrained in the Beaufort Gyre, trapping the water in the Amerasian Arctic. Further work will be necessary to better determine the likelihood of these different scenarios, as well as the role of CSC-eddy interaction in altering the current and the water masses it advects.

Acknowledgments: This work was principally supported by the Stratified Ocean Dynamics of the Arctic (SODA) program under ONR grant N000141612450. S.B. wants to thank Labex iMust for supporting his research. R.S.P. thanks National Science Foundation for fundings through grants OPP-1702371, OPP-1733564, and PLR-1303617. P.L. thanks National Oceanic and Atmospheric Administration grant NA14-OAR4320158. M.L. thanks National Natural Science Foundation of China grants 41706025 and 41506018. T.P. thanks ENS de Lyon for travel support funding. The Authors gratefully acknowledge the support of Steve Jayne, Pelle Robins, and Alex Ekholm at WHOI for preparation, deployment, and data provision for the SOLO floats; and also Chanhyung Jeon for his assistance in preparing and deploying the floats. The invaluable support of the crew of the R/V Sikuliaq is also gratefully acknowledged.

Part V

Conclusion

CHAPTER 10

Conclusion

La mer est ton miroir ; tu contemples ton âme
Dans le déroulement infini de sa lame
Charles Baudelaire, Les Fleurs du Mal.

The main objective of this thesis was to investigate energy and buoyancy transfer by axisymmetric inertia-gravity waves in regards to oceanic applications. Such waves can be created by atmospheric storms at the surface of the ocean or by tides over topography in the abyss, and are likely to be involved in mixing of highly stratified regions such as the Arctic Ocean. To improve our understanding of these waves, we first derived the theoretical framework in part I, then we explored the linear and non-linear regimes in parts II and III. An in-situ oceanographic study on energy transport in the Arctic is presented in part IV.

First, we chose to focus on the linear regime of axisymmetric internal waves by assuming that all non-linear terms involved in the equations are negligible. Willing to understand wave propagation through non-uniform stratifications, we identified the different scenarios that could be found in real-world density profiles: there can be domains of constant buoyancy frequency, transitions between such regions, and inclusions of weakly – or even un- – stratified layers. Hence, we studied wave fields in three different idealised configurations: a linear stratification (chapter 4), a bi-linear stratification (chapter 5), and a gapped stratification (chapter 6).

Previous experiments [141, 140] have studied fields generated by an axisymmetric wave generator and shown that they can be decomposed over the basis of Bessel functions thanks to a Hankel transform. Since the behaviour of any wave field is given by the sum of all its modal contributions, we studied wave fields shaped as a single Bessel function in order to provide a more accurate description of axisymmetric wave dynamics. This was made possible by confining the wave field radially with a cylinder of the same diameter as the generator. We characterised radial modes (standing waves) propagating downwards in this geometry, and we developped a method for amplitude measurements based on Root Mean Square values. Additional reflections at the top and at the bottom of the confined domain led to the observation of cavity resonant effects as in electromagnetism and optics, with beating behaviour (chapter 7) or constructive and destructive interference (chapters 4 and 5) that produces high amplitude wave fields.

After studying linear stratifications, we naturally focused on the dynamics of internal waves in bi-linear stratifications, i.e. in stratifications with a layer on top of another layer at two different buoyancy frequencies. A downward propagating mode has been studied, to delve into transmission and reflection properties across such a buoyant interface in two different cases: a free incoming wave arriving from a semi-infinite layer, and a confined wave field reflected in the top layer while being continuously forced. We derived the theory to predict transmission coefficients in velocity

and energy and checked the validity of the theoretical and numerical model thanks to experimental measurements before applying it to a real oceanic stratification approximated by two layers. These results help understand the propagation of waves from the surface of the ocean through the pycnocline, and can predict the amount of energy transferred to the deep ocean. Thanks to in-situ measurements of Arctic near-inertial waves [105], we extended this work to study transmission in complex non-linear stratifications using numerical methods to explain the impact of the stratification on the presence or absence of wave signals.

Motivated by the presence of gaps in real-world stratifications, i.e. layers of weak or even zero buoyancy frequency, we studied their impact on wave propagation. As observed in Cartesian geometry [45, 224], waves can go through a constant density layer by a phenomenon called internal wave tunneling. We numerically checked the existence of the phenomenon and we ran experiments in such stratifications to find evidence of axisymmetric internal wave tunneling. A simple model of amplitudes transmitted through the finite layer has been developed and verified experimentally. Complementary to the two previous works on linear and bi-linear stratifications, this study can find application in most layered and staircase stratifications. Combined with the previous findings on wave dynamics in linear and bi-linear stratifications, this work provides a better description of propagation of axisymmetric internal waves in geophysical fluids.

Having explored the linear regime on internal waves, the next step was to look at the non-linear effects. Two different configurations were used to challenge non-linearities in axisymmetric geometry: the confined and unconfined domain with a Bessel forcing at the top of the tank (chapter 7), and a doubly confined domain made of two cylinders to create and study inertial wave attractors from a cubic forcing at the top (chapter 8).

Non-linear effects have been studied in a linear stratification and a surprising discovery was the generation of super-harmonics by self-interaction of the wave field. Contrary to Cartesian geometry, in which super-harmonics can only be created in non-linear stratifications because all the self-interacting Jacobians of the wave equation are zero otherwise, we showed theoretically and experimentally that the cylindrical geometry made this self-interaction possible. The wave field of the super-harmonics generated through this process remained axisymmetric and can be described by cavity modes, which are radially and vertically standing wave fields of wave lengths and frequency set by the cavity boundaries. We adapted a projection method to study the energetic distribution of the modes created and showed that the governing feature is the double frequency set by non-linear wave-wave interaction.

Inspired by Cartesian plane wave studies on Triadic Resonant Instability, we also looked for sub-harmonics generation with wave triads in linearly stratified fluids. They were observed in the confined setup and we showed that, although the frequencies satisfy the resonant condition $\omega_0 = \omega_1 + \omega_2$, this is not the case for wave numbers because of the confinement. With experiments in stratified rotating fluids, however, we showed that the resonant conditions are satisfied in 3D axisymmetric unconfined geometries. Some theoretical developments were proposed to study the non-trivial radial condition.

The non-linear beating behaviour, evidenced in the experiments of modes in a cavity, were also discussed. Such a phenomenon can be observed when the wave frequency does not match with a cavity frequency. We briefly described this observation and the modulation of the wave field created by this kind of interaction between two modes.

To delve into non-linear in even more complex cylindrical configurations, we performed experiments of inertial wave attractors in a novel axisymmetric trapezoidal geometry. The attractor is first axisymmetric in the linear regime, then undergoes a non-linear destabilisation in which vortices are created. These structures evolving at very low frequency gradually appear close to the former most energetic branch, and seem to re-stabilise the system in a different state with energy exchanges between a forcing at non-zero frequency and these columnar slowly rotating vortices. Our experimental study is supported by Direct Numerical Simulations run by that show the same behaviour as observed in our setup.

As regards the connection to ocean, in September 2018, I took part in a five week research cruise of the Stratified Ocean Dynamics of the Arctic (SODA) program on the R/V Sikuliaq. The newly discovered Chukchi Slope Current [57] in the shelfbreak of the Chukchi Sea has been investigated thanks to a novel method of five quasi-Lagrangian floats deployed in the core of the current. GPS trajectories of the floats, combined with the temperature and salinity profiles they recorded along

their travel were used to provide information on the complex dynamics of the Arctic region and on the fate of heat content carried by Pacific waters in the Arctic Ocean. We discovered that the Chukchi Slope Current goes far North and can be strongly impacted by oceanic events, such as eddy disruption.

Perspectives

Upon the findings of this thesis, made possible by the capabilities of the axisymmetric wave generator, several phenomena have been observed but are not completely understood or are rising new questions. Hence, this work opens to various interesting problems and here are a few of them.

Non-Uniform Stratifications

We explored layered stratifications, with continuous buoyancy interfaces. Thanks to the computer controlled double-bucket filling process, more complex profiles could be studied such as the exponential buoyancy frequency used in focusing experiments [140]. This can be done in Cartesian geometry as well as in axisymmetric geometry, and could help understand propagation of internal waves through more complex stratifications.

Super-Harmonics in Unconfined Geometry

Non-linear self-interaction of the wave is possible in linearly stratified fluids for axisymmetric geometry. In our study, we discussed Super-Harmonic Generation in cavity, meaning a fully confined geometry, and we have shown that cavity modes are created at integer multiples of the forcing frequency. This result is to be put in parallel with the case of Triadic Resonant Instability: for confined TRI, we observed the excitation of cavity modes that do not satisfy the resonance condition on wave numbers but only on frequencies, whereas for unconfined TRI the resonance condition is satisfied both for the wave numbers and the frequencies. A similar discussion arises for SHG, for which we could have a resonance condition on wave numbers satisfied in unconfined geometry with. This would give, for example, the creation of vertical wave numbers of $2m_0$ starting from a wave field at m_0, and imply a relation on the radial wave numbers as well that could be tested experimentally.

Exact Derivation of Triadic Resonant Interaction

Our understanding of the Triadic Resonant Interaction in axisymmetric geometry has improved, but we still lack an exact analytical derivation of the resonance condition for the radial wave number. In unconfined cases, we have verified experimentally our assumptions that the relationship between l_0, l_1, and l_2 is the same as in Cartesian, and a more established theoretical study would be useful to confirm this conjecture.

Moreover, the solution of internal waves equations in cylindrical geometry, i.e. without prescribing the independence in the azimuthal coordinate, shows that non-axisymmetric wave fields can exist. They have been observed experimentally, but are still non entirely described theoretically. When involved in TRI, the azimuthal wave numbers appearing with non axisymmetric wave fields also satisfy a resonance condition, but this will likely impact the condition on the radial wave numbers. A more detailed theoretical study could be undertaken to target this problem.

Towards Other Geometries

The goal of this thesis was to investigate the impact of a change of geometry on internal wave dynamics. To this extent, we studied an axisymmetric domain, but other geometries might display interesting features. We can think, for example, of conical, spherical, or ellipsoidal geometries, that could be studied numerically and theoretically on the basis of the present work.

Notably, we have made a very interesting theoretical and experimental discovery that Bessel function internal waves can self-interact to excite superharmonics, even in linearly stratified fluids. This is an important difference with Cartesian plane waves, for they can only self-interact in non-uniform stratifications to generate super-harmonics. In other geometries, this question has not

been explored: does this happen in spheres? Could this be a new mechanism for the breakdown of spherical modes in spherical and elliptical systems such as stars and planetary cores?

Stability of Inertial Wave Attractors

We have run a set of experiments showing the existence of axisymmetric inertial wave attractors in a linear regime, but also their possible destabilisation through non-linear processes and their re-stabilisation with the creation of vortices rotating at very low frequency. The origin and the exact mechanisms involved in such a dynamic are still unknown, and could be the subject of further studies. A change in the forcing could also be investigated, as already mentioned for positive and negative nutation [209], and this is likely to excite rim currents in enclosed basins. These works would have direct oceanographic applications.

Fate of Energy in the Arctic

Near-inertial waves in the Arctic are now detected thanks to a novel cost-effective facility of PDS-CPIES. The project is still on-going and has various objectives on understanding the transmission of near-inertial waves and the impact of sea-ice coverage. Additional studies with these sensors could be conducted in other regions of the world to monitor wave and current activity in remote regions.

Lastly, the quasi-Lagangian floats deployed in the core of the Chukchi Slope Current revealed its trajectory North of the Northwind Ridge and possible interactions with eddies. The fate of the current, however, is not entirely understood. As we lost track of the floats, we could not state whether the current is going further North or is going back into the Canada Basin at some latitude. Furthermore, the data were acquired at a given time and under specific oceanic conditions, so we could not discuss the repeatability. The Chukchi Slope Current is already known to have a seasonal behaviour along the shelfbreak of the Canada Basin, and there is a chance that its fate North of the Ridge would have significant variability and seasonality, for example switching from going North to going West. These open questions could lead to new field studies using floats and moorings deployments.

Appendix

APPENDIX A

Vectorial Calculus in Cylindrical Coordinates

Y nos vamos corriendo
a la oficina,
al taller,
a la fábrica,
a comenzar de nuevo el infinito
número 1 de cada día.
Pablo Neruda, ODAS ELEMENTALES.

In this appendix, for the sake of clarity, we briefly remind the reader how vectorial operators are written in cylindrical coordinates.

A.1 Cylindrical Basis

Figure A.1 shows in the left-hand side the basis $(\mathbf{e_x}, \mathbf{e_y}, \mathbf{e_z})$ of Cartesian coordinates (x, y, z), and in the right-hand side the basis $(\mathbf{e_r}, \mathbf{e}_\theta, \mathbf{e_z})$ of cylindrical (or polar) coordinates (r, θ, z). We recall that, in all this manuscript, we denote the particular case of θ-invariant geometry using the adjective axisymmetric.

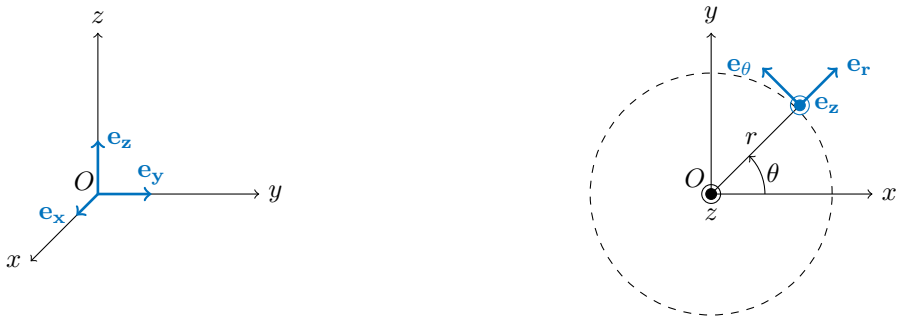

Figure A.1: Left: Cartesian coordinates (x, y, z). Right: Cylindrical (polar) coordinates (r, θ, z).

The z coordinate remains unchanged. In the horizontal plane, the transformation of coordinates from Cartesian to cylindrical can be done by the rotation matrix $\mathcal{R}(\theta)$ defined as

$$\mathcal{R}(\theta) = \begin{bmatrix} \cos\theta & -\sin\theta \\ \sin\theta & \cos\theta \end{bmatrix}, \tag{A.1}$$

which satisifies $\mathcal{R}(-\theta) = \mathcal{R}^T(\theta) = \mathcal{R}^{-1}(\theta)$ (see chapter 1). Hence, the coordinates x, y, r, and θ, are linked through the relation $x = r\cos\theta$ and $y = r\sin\theta$.

A.2 Differential Operators

We consider V a scalar function, and $\mathbf{A}$ a vector, both depending on (r, θ, z). The formulaes for differential (and vectorial) operators are recalled below

$$\nabla V = \frac{\partial V}{\partial r}\mathbf{e_r} + \frac{1}{r}\frac{\partial V}{\partial \theta}\mathbf{e}_\theta + \frac{\partial V}{\partial z}\mathbf{e_z}, \tag{A.2}$$

$$\nabla \cdot \mathbf{A} = \frac{1}{r}\frac{\partial r A_r}{\partial r} + \frac{1}{r}\frac{\partial A_\theta}{\partial \theta} + \frac{\partial A_z}{\partial z}, \tag{A.3}$$

$$\nabla \times \mathbf{A} = \left(\frac{1}{r}\frac{\partial A_z}{\partial \theta} - \frac{\partial A_\theta}{\partial z}\right)\mathbf{e_r} + \left(\frac{\partial A_r}{\partial z} - \frac{\partial A_z}{\partial r}\right)\mathbf{e}_\theta + \frac{1}{r}\left(\frac{\partial r A_\theta}{\partial r} - \frac{\partial A_r}{\partial \theta}\right)\mathbf{e_z}, \tag{A.4}$$

$$\Delta V = \frac{1}{r}\frac{\partial}{\partial r}\left(r\frac{\partial V}{\partial r}\right) + \frac{1}{r^2}\frac{\partial^2 V}{\partial \theta^2} + \frac{\partial^2 V}{\partial z^2}, \tag{A.5}$$

$$\Delta \mathbf{A} = \Delta^{\odot}\mathbf{A} = \left[\Delta v_r - \frac{1}{r^2}\left(v_r + 2\partial_\theta v_\theta\right)\right]\mathbf{e_r} + \left[\Delta v_\theta - \frac{1}{r^2}\left(v_\theta - 2\partial_\theta v_r\right)\right]\mathbf{e}_\theta + \Delta v_z \mathbf{e_z}. \tag{A.6}$$

The common operations involving gradient and curls still hold, which means that for V and W two scalar fields and $\mathbf{A}$ and $\mathbf{B}$ two vectorial fields, the first derivatives of their products can be expressed as

$$\nabla(VW) = V\nabla W + W\nabla V, \tag{A.7}$$

$$\nabla(\mathbf{A}\cdot\mathbf{B}) = \mathbf{A}\cdot(\nabla\times\mathbf{B}) + \mathbf{B}\cdot(\nabla\times\mathbf{A}) + (\mathbf{A}\cdot\nabla)\mathbf{B} + (\mathbf{B}\cdot\nabla)\mathbf{A}, \tag{A.8}$$

$$\nabla\cdot(V\mathbf{A}) = V\nabla\cdot\mathbf{A} + \mathbf{A}\cdot(\nabla V), \tag{A.9}$$

$$\nabla\times(V\mathbf{A}) = (\nabla V)\times\mathbf{A} + V(\nabla\times\mathbf{A}), \tag{A.10}$$

$$\nabla\cdot(\mathbf{A}\times\mathbf{B}) = \mathbf{B}\cdot(\nabla\times\mathbf{A}) - \mathbf{A}\cdot(\nabla\times\mathbf{B}), \tag{A.11}$$

$$\nabla\times(\mathbf{A}\times\mathbf{B}) = \mathbf{A}(\nabla\cdot\mathbf{B}) - \mathbf{B}(\nabla\cdot\mathbf{A}) + (\mathbf{B}\cdot\nabla)\mathbf{A} - (\mathbf{A}\cdot\nabla)\mathbf{B}, \tag{A.12}$$

and, the second derivatives of the fields are

$$\nabla\cdot(\nabla V) = \nabla^2 V = \Delta V, \tag{A.13}$$

$$\nabla\times(\nabla V) = 0, \tag{A.14}$$

$$\nabla\cdot(\nabla\times\mathbf{A}) = 0, \tag{A.15}$$

$$\nabla\times(\nabla\times\mathbf{A}) = \nabla(\nabla\cdot\mathbf{A}) - \nabla^2\mathbf{A}. \tag{A.16}$$

The material derivative can also be derived from the previous relations and

$$(\mathbf{A}\cdot\nabla)\mathbf{B} = \left(A_r\frac{\partial B_r}{\partial r} + \frac{A_\theta}{r}\frac{\partial B_r}{\partial \theta} + A_z\frac{\partial B_r}{\partial z} - \frac{A_\theta B_\theta}{r}\right)\mathbf{e_r} \tag{A.17}$$

$$+\left(A_r\frac{\partial B_\theta}{\partial r} + \frac{A_\theta}{r}\frac{\partial B_\theta}{\partial \theta} + A_z\frac{\partial B_\theta}{\partial z} + \frac{A_\theta B_r}{r}\right)\mathbf{e}_\theta \tag{A.18}$$

$$+\left(A_r\frac{\partial B_z}{\partial r} + \frac{A_\theta}{r}\frac{\partial B_z}{\partial \theta} + A_z\frac{\partial B_z}{\partial z}\right)\mathbf{e_z}. \tag{A.19}$$

APPENDIX B

Basics of Trigonometry

It is the uncertainty that charms one.
A mist makes things wonderful.
Oscar Wilde, The picture of Dorian Gray.

Circular functions, i.e. sine, cosine, tangent, and cotangent, are used in this thesis to describe the oscillatory behaviour of wave fields. In chapter 7, especially, these functions are involved in non-linear calculus and are either linearised or factorised thanks to well-known properties and relations. For convenience, some of them are recalled in this appendix.

B.1 Trigonometric Circle

Figure B.1 illustrates the definition of the 2π-periodic circular functions sine, cosine, tangent, and cotangent. Tangent and cotangent are related to sine and cosine functions through the relations $\tan\theta = \sin\theta/\cos\theta$ for $\theta \in [0;\ 2\pi] \setminus \{\pi/2;\ 3\pi/2\}$ and $\operatorname{cotan}\theta = \cos\theta/\sin\theta$ for $\theta \in]0;\ 2\pi[\setminus\{\pi\}$.

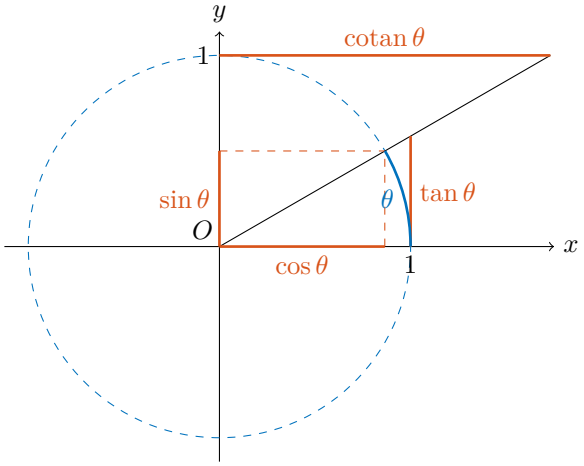

Figure B.1: Unit circle defining the sine, cosine, tangent, and cotangent, of an angle θ.

θ (rad)	0	$\frac{\pi}{6}$	$\frac{\pi}{4}$	$\frac{\pi}{3}$	$\frac{\pi}{2}$
θ (°)	0	30°	45°	60°	90°
$\sin\theta$	0	$\frac{1}{2}$	$\frac{\sqrt{2}}{2}$	$\frac{\sqrt{3}}{2}$	1
$\cos\theta$	1	$\frac{\sqrt{3}}{2}$	$\frac{\sqrt{2}}{2}$	$\frac{1}{2}$	0
$\tan\theta$	0	$\frac{1}{\sqrt{3}}$	1	$\sqrt{3}$	∞
$\operatorname{cotan}\theta$	∞	$\sqrt{3}$	1	$\frac{1}{\sqrt{3}}$	0

Table B.1: Most common trigonometric values of the first quadrant $\theta \in [0;\ \pi/2]$.

B.2 Common Circular Relations

B.2.1 Sums and Products

In this section, we assume that the arguments of the different functions are taken in the appropriate domain of definition, avoiding singularities. Squared circular functions satisfy the following relations

$$\cos^2\theta + \sin^2\theta = 1, \qquad 1 + \tan^2\theta = \frac{1}{\cos^2\theta}, \qquad \text{and} \qquad 1 + \operatorname{cotan}^2\theta = \frac{1}{\sin^2\theta}. \tag{B.1}$$

The sums of arguments lead to

$$\cos(a+b) = \cos a \cos b - \sin a \sin b, \tag{B.2}$$

$$\sin(a+b) = \cos a \sin b + \cos b \sin a. \tag{B.3}$$

Sine-cosine products can be linearised thanks to

$$2\cos a \cos b = \cos(a-b) + \cos(a+b), \tag{B.4}$$

$$2\sin a \sin b = \cos(a-b) - \cos(a+b), \tag{B.5}$$

$$2\sin a \cos b = \sin(a-b) + \sin(a+b), \tag{B.6}$$

and sums can be factorised using

$$\cos p + \cos q = 2\cos\left(\frac{p+q}{2}\right)\cos\left(\frac{p-q}{2}\right), \tag{B.7}$$

$$\cos p - \cos q = -2\sin\left(\frac{p+q}{2}\right)\sin\left(\frac{p-q}{2}\right), \tag{B.8}$$

$$\sin p + \sin q = 2\sin\left(\frac{p+q}{2}\right)\cos\left(\frac{p-q}{2}\right). \tag{B.9}$$

B.2.2 Complex Exponential

The complex exponential, used throughout the manuscript in the complex formalism for writing wave fields (e.g. plane waves) is defined by

$$e^{i\theta} = \cos\theta + i\sin\theta, \tag{B.10}$$

from which can be deduced the two Euler's formulae

$$\cos\theta = \frac{e^{i\theta} + e^{-i\theta}}{2} \qquad \text{and} \qquad \sin\theta = \frac{e^{i\theta} - e^{-i\theta}}{2i}. \tag{B.11}$$

APPENDIX C

Bessel and Hankel Functions

Une mer qu'aucun bord n'arrête
S'étendait bleue à l'horizon
Alphonse de Lamartine, MÉDITATIONS POÉTIQUES.

The variable separation method used to solve the tri-dimensional differential equation for inertia-gravity waves in a rotating and stratified fluid leads to a second order differential equation in the radial coordinate. This equation does not have trivial solutions unlike the vertical or temporal equations do. Nonetheless, its complete solutions have already been studied and are known as *Bessel functions*. This appendix summarises their main properties, which are useful in this thesis. A more complete description can be found in the NIST Handbook [163].

C.1 Bessel Differential Equation

C.1.1 A Second Order Differential Equation

For a given parameter $n \in \mathbb{N}$, the Bessel differential equation of rank n is

$$r^2 \frac{\mathrm{d}^2 f}{\mathrm{d}r^2} + r \frac{\mathrm{d}f}{\mathrm{d}r} + (r^2 - n^2) f = 0. \tag{C.1}$$

The case $n = 1$ is naturally obtained from the wave equation as it appears in writing down the Laplacian operator in axisymmetric coordinates. Note that this equation can be extended to non-integer parameters n.

C.1.2 A Mode Basis: Bessel Functions

As the equation (C.1) is of order two, the associated vectorial space of solutions is described by two orthonormal vectors. Any linear combination of these two functions satisfies the Bessel equation.

A first couple of orthonormal solutions is known as the Bessel functions of first and second kind, J_n and Y_n, also called Bessel and Neumann functions. They are real solutions, and they represent a modal evolution of a wave field with fixed nodes and anti-nodes. While the J_n functions are bounded in magnitude for every order n, the Y_n functions diverge at $r = 0$.

These functions are originally defined over $\mathbb{R}^+$ as the radial coordinate is, but can be analytically extended to $\mathbb{R}$ by symmetry

$$\forall r \in \mathbb{R},\ J_n(-r) = J_n(r) \qquad \text{and} \qquad \forall r \in \mathbb{R},\ Y_n(-r) = Y_n(r). \tag{C.2}$$

Symmetry also applies to define these functions for $n < 0$, as

$$J_{-n} = (-1)^n J_n \qquad \text{and} \qquad Y_{-n} = (-1)^n Y_n. \tag{C.3}$$

Plots of the solutions J_n and Y_n for $n \in \{0, 1, 2, 3\}$ for $r \in [0;\ 25]$, are presented in figures C.1(a) and C.1(b), respectively.

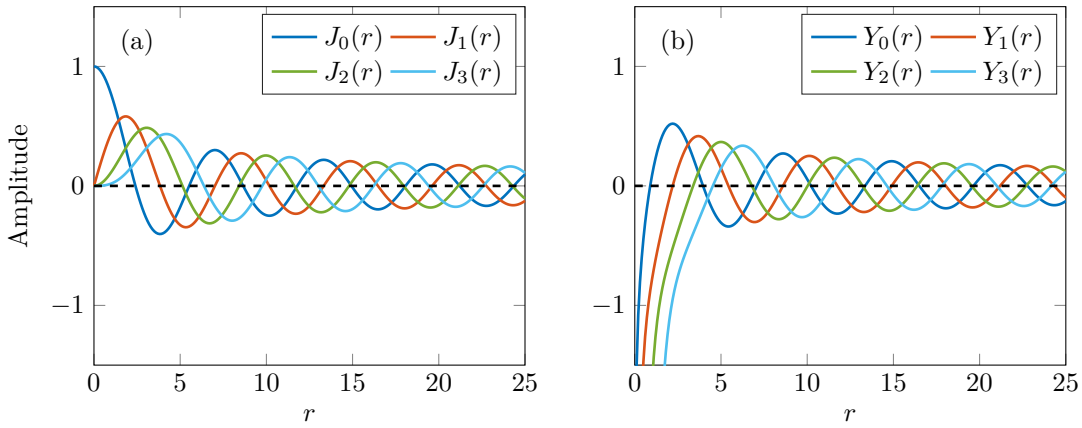

Figure C.1: Natural solutions of the Bessel differential equation of orders 0, 1, 3, and 3, for (a) J_n functions and (b) Y_n functions.

In the manuscript, we refer to the J_n and Y_n functions as *Bessel functions*.

C.1.3 A Propagative Basis: Hankel Functions

Another orthonormal basis can be set up with the complex functions known as Bessel functions of the third and fourth kind, or Hankel functions of the first and second kind, $H_n^{(1)}$ and $H_n^{(2)}$. Both of them diverge at $r = 0$, similarly to the Y_n function. They satisfy the same symmetry properties as mentioned above for the Bessel functions.

We refer to the $H_n^{(1)}$ and $H_n^{(2)}$ functions as *Hankel functions*.

C.1.4 Connection Formulae

As the vectorial space of solutions is of dimension 2, the Hankel and Bessel functions can be expressed in terms of each other allowing to go from one basis to the other. They are connected by the following relations

$$H_n^{(1)} = J_n + iY_n, \tag{C.4}$$
$$H_n^{(2)} = J_n - iY_n, \tag{C.5}$$

and

$$J_n = \frac{1}{2}(H_n^{(1)} + H_n^{(2)}), \tag{C.6}$$
$$Y_n = \frac{1}{2i}(H_n^{(1)} - H_n^{(2)}). \tag{C.7}$$

These relations are analoguous to the connection between the cosine-sine basis and the exponentials in cartesian coordinates. As the solution for the wave field is given by the real part of the whole field, a description in terms of cosine and sine gives a mode (the spatial propagation is not coupled with the temporal evolution) whereas the exponentials give a propagative field coupling time and space variations. The distinction is identical here with the real Bessel functions and the complex Hankel ones, as detailed in table C.1.

	Cartesian		Axisymmetric	
	ψ	$\Re(\psi)$	ψ	$\Re(\psi)$
Modes	$\propto \cos(lr)e^{-i\omega t}$	$\propto \cos(lr)\cos(\omega t)$	$\propto J_n(lr)e^{-i\omega t}$	$\propto J_n(lr)\cos(\omega t)$
	$\propto \sin(lr)e^{-i\omega t}$	$\propto \sin(lr)\cos(\omega t)$	$\propto Y_n(lr)e^{-i\omega t}$	$\propto Y_n(lr)\cos(\omega t)$
Propagating	$\propto e^{i(lr-\omega t)}$	$\propto \cos(lr-\omega t)$	$\propto H_n^{(1)}(lr)e^{-i\omega t}$	$\propto \Re(H_n^{(1)}(lr)e^{-i\omega t})$
	$\propto e^{-i(lr+\omega t)}$	$\propto \cos(lr+\omega t)$	$\propto H_n^{(2)}(lr)e^{-i\omega t}$	$\propto \Re(H_n^{(2)}(lr)e^{-i\omega t})$

Table C.1: Cartesian vs. axisymmetric functions, describing modes and propagating waves.

C.2 Series Expansion

Solutions of the Bessel differential equation can be found using a series expansion. This method holds for bounded series and we have

$$\forall n \in \mathbb{N},\ \forall r \in \mathbb{R},\ J_n(r) = \sum_{p=1}^{\infty} \frac{(-1)^p}{p!(n+p)!}\left(\frac{r}{2}\right)^{2p+n}. \tag{C.8}$$

C.3 Asymptotics

For large values or r, the functions J_n can be approximated by the functions $\tilde{J}_n$ defined as follows

$$\forall n \in \mathbb{N},\ \forall r \in \mathbb{R}^*,\ \tilde{J}_n(r) = \sqrt{\frac{2}{\pi r}}\cos\left(r - \frac{\pi}{2}\left(n+\frac{1}{2}\right)\right). \tag{C.9}$$

These approximations are presented in figure C.2 for (a) $n = 0$ and (b) $n = 1$.

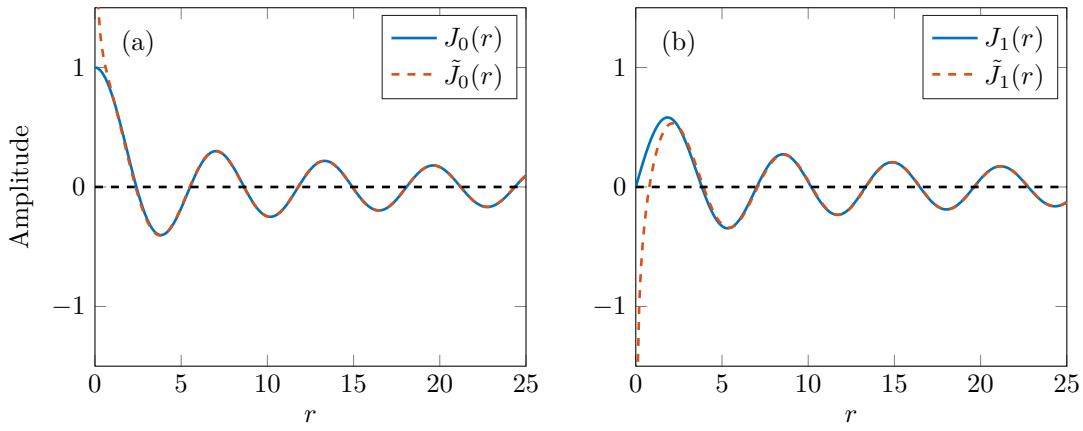

Figure C.2: Plots of the functions (a) J_0 and (b) J_1 (solid line) with the asymptotics approximation $\tilde{J}_0$ and $\tilde{J}_1$ (dashed lines).

C.4 Orthogonality

C.4.1 Norms

For a given $n \in \mathbb{N}$, we have

$$\int_0^{+\infty} J_n(r)\mathrm{d}r = 1. \tag{C.10}$$

This holds for Bessel functions of the first kind but, because of the divergence at $r = 0$ of the Y_n functions, the integrals of Y_n, $H_n^{(1)}$, and $H_n^{(2)}$ do not have a finite value.

C.4.2 Orthogonalities

Integral relations on the Bessel functions help define different kinds of orthogonalities.

Local orthogonality

Let λ and μ two zeros, eventually identical, of J_n. Then

$$\int_0^1 r J_n(\lambda r) J_n(\mu r) \mathrm{d}r = \frac{\delta(\lambda-\mu)}{2} \left(J_n'(\lambda)\right)^2. \tag{C.11}$$

Index orthogonality

If n, m, and l are integers such as $n+m+l > -1$, then

$$\int_0^{+\infty} \frac{1}{r} J_{n+2l+1}(r) J_{n+2m+1}(r) \mathrm{d}r = \frac{\delta_{l,m}}{2(n+m+l+1)}. \tag{C.12}$$

C.5 Integral and Derivative Relations

Let $\mathcal{F}$ be a Bessel or a Hankel function. Starting from the differential equation (C.1), the following recurrence relation can be derived

$$\mathcal{F}_{n+1}(r) = \frac{n\mathcal{F}_n(r)}{r} - \frac{\mathrm{d}\mathcal{F}_n(r)}{\mathrm{d}r}. \tag{C.13}$$

This recurrence relation is the key point to link the different orders of the basis functions. Their sum and differences satisfy

$$\mathcal{F}_{n-1}(r) + \mathcal{F}_{n+1}(r) = \frac{2n}{r}\mathcal{F}_n(r), \tag{C.14}$$

$$\mathcal{F}_{n-1}(r) - \mathcal{F}_{n+1}(r) = 2\frac{\mathrm{d}\mathcal{F}_n(r)}{\mathrm{d}r}, \tag{C.15}$$

and the first derivative gives

$$\frac{\mathrm{d}\mathcal{F}_n(r)}{\mathrm{d}r} = \mathcal{F}_{n-1}(r) - \frac{n}{r}\mathcal{F}_n(r), \tag{C.16}$$

$$\frac{\mathrm{d}\mathcal{F}_n(r)}{\mathrm{d}r} = -\mathcal{F}_{n+1}(r) + \frac{n}{r}\mathcal{F}_n(r). \tag{C.17}$$

Higher derivation orders can also be expressed and, for $k \in \mathbb{N}$

$$\left(\frac{1}{r}\frac{\mathrm{d}}{\mathrm{d}r}\right)^k \left(r^n \mathcal{F}_n(r)\right) = r^{n-k}\mathcal{F}_{n-k}(r), \tag{C.18}$$

$$\left(\frac{1}{r}\frac{\mathrm{d}}{\mathrm{d}r}\right)^k \left(r^{-n} \mathcal{F}_n(r)\right) = (-1)^k r^{-(n+k)}\mathcal{F}_{n+k}(r). \tag{C.19}$$

Hence, zeroth and first order functions can be linked thanks to the very useful relations

$$\mathcal{F}_1(r) = -\frac{\mathrm{d}\mathcal{F}_0(r)}{\mathrm{d}r} \qquad \text{and} \qquad \frac{1}{r}\frac{\mathrm{d}(r\mathcal{F}_1(r))}{\mathrm{d}r} = \mathcal{F}_0(r). \tag{C.20}$$

C.6 Radial-Like Fourier Transform: the Hankel Transform

For a given integer n, the family of Bessel functions $\mathcal{B} = \{r \mapsto J_n(lr), l \text{ is a zero of } J_n\}$ is a basis of the vectorial space of continuous and derivative functions, as described previously. Therefore, a

function from this particuliar vectorial space can be decomposed over the family $\mathcal{B}$. This decomposition is called the *Hankel transform* and is very similar to the Cartesian Fourier transform. The direct transform is

$$g(y) = \mathcal{H}[f](y) = \int_0^{+\infty} f(x) J_n(xy) \sqrt{xy}\, \mathrm{d}x, \tag{C.21}$$

and the inverse transform is

$$f(x) = \mathcal{H}^{-1}[g](x) = \int_0^{+\infty} g(y) J_n(xy) \sqrt{xy}\, \mathrm{d}y. \tag{C.22}$$

As a trivial property, the combination of the direct and inverse transform returns the initial function

$$\mathcal{H}^{-1}[\mathcal{H}[f]](x) = f(x). \tag{C.23}$$

APPENDIX D

Fresnel Integrals

On ne découvre pas de terre nouvelle sans consentir
à perdre de vue, d'abord et longtemps, tout rivage.
André Gide, Les Faux-Monnayeurs.

Integrating the asymptotic Bessel approximations $\tilde{J}_n$ defined in appendix C leads to particular functions called *Fresnel integrals*. They have been first introduced by Augustin Fresnel to describe the interference pattern at the edge of a shadow [82]. The present appendix, based on the NIST Handbook [163], goes through some of their properties that are used in the discussion of non-linear sub-harmonic generations in chapter 7. Additional properties and relations on these functions can be found in [163].

D.1 Fresnel Integrals

D.1.1 Definition and Properties

The Fresnel integral F, and the cosine and sine Fresnel integrals C and S, respectively, are defined for $x \in \mathbb{R}$ as follows[1]

$$\mathsf{F}(x) = \int_x^\infty e^{\frac{1}{2}i\pi t^2}\mathrm{d}t, \tag{D.1}$$

$$\mathsf{C}(x) = \int_0^x \cos\left(\frac{1}{2}\pi t^2\right)\mathrm{d}t, \tag{D.2}$$

$$\mathsf{S}(x) = \int_0^x \sin\left(\frac{1}{2}\pi t^2\right)\mathrm{d}t. \tag{D.3}$$

These three functions are linked by

$$\mathsf{C}(x) + i\mathsf{S}(x) = \frac{1}{2}(1+i) - \mathsf{F}(x), \tag{D.4}$$

meaning, in particular, that

$$|\mathsf{F}(x)|^2 = \left(\mathsf{C}(x) - \frac{1}{2}\right)^2 + \left(\mathsf{S}(x) - \frac{1}{2}\right)^2. \tag{D.5}$$

[1] These integrals are actually defined for variables $z \in \mathbb{C}$, but this is beyond our interests.

A graphical representation of these functions is shown in figure D.1 with (a) the plot of $|\mathsf{F}|^2$ for $x \in [-10;\ 10]$, and (b) the plots of C and S for $x \in [0;\ 5]$. The plot of the squared magnitude of F shows a clear limit towards 2 for x goes to $-\infty$, whereas is quickly goes to zero for positive values of x. As specified in the introduction of this appendix, the shape of this function is reminiscent of the interference pattern at the edge of a shadow in optics [82]. The cosine and sine Fresnel integrals, on the contrary, are oscillating around $1/2$ for positive values of x.

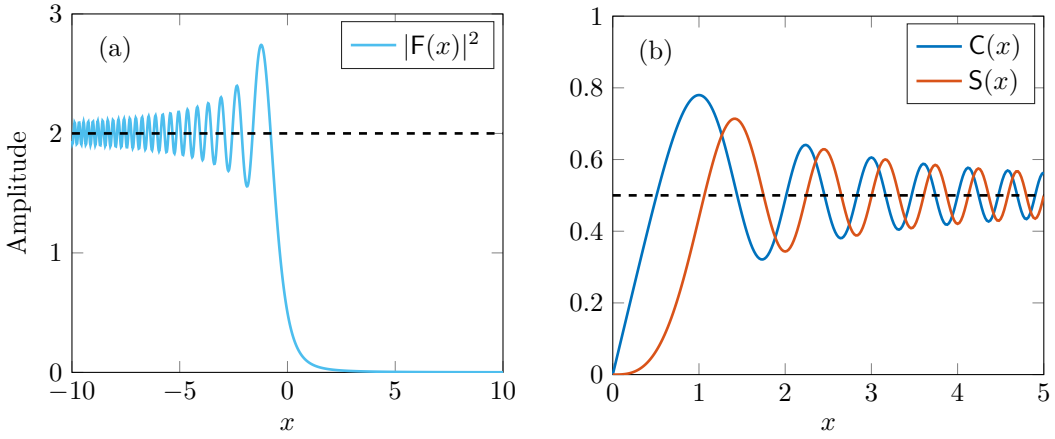

Figure D.1: Plots of the Fresnel integrals, with (a) the squared magnitude of the Fresnel integral, $|\mathsf{F}|^2$, and (b) the cosine and sine Fresnel integrals C and S. The dashed lines indicate the limits of the functions.

Amongst other properties, note that C and S satisfy symmetry relations

$$\mathsf{C}(-x) = -\mathsf{C}(x), \tag{D.6}$$
$$\mathsf{S}(-x) = -\mathsf{S}(x), \tag{D.7}$$

and that they have the following limits

$$\lim_{x\to\infty} \mathsf{C}(x) = \frac{1}{2}, \tag{D.8}$$
$$\lim_{x\to\infty} \mathsf{S}(x) = \frac{1}{2}. \tag{D.9}$$

D.1.2 Relation to Asymptotics Bessel Functions

Using trigonometric relations, we derive that for all $x \in \mathbb{R}$ and all $n \in \mathbb{N}$

$$\int_0^x \tilde{J}_n(r)\mathrm{d}r = \int_0^x \sqrt{\frac{2}{\pi r}} \cos\left(r - \frac{\pi}{2}\left(n+\frac{1}{2}\right)\right) \mathrm{d}r, \tag{D.10}$$
$$= 2\mathsf{C}\left(\frac{2x^2}{\pi}\right) \cos\left(\frac{\pi}{2}\left(n+\frac{1}{2}\right)\right) - 2\mathsf{S}\left(\frac{2x^2}{\pi}\right) \sin\left(\frac{\pi}{2}\left(n+\frac{1}{2}\right)\right). \tag{D.11}$$

D.2 Series Expansions

The cosine and sine Fresnel integrals have the following series expansions

$$\forall x \in \mathbb{R},\ \mathsf{C}(x) = \sum_{p=0}^{\infty} \frac{(-1)^p \left(\frac{1}{2}\pi\right)^{2p}}{(2p)!(4p+1)} x^{4p+1}, \tag{D.12}$$
$$\forall x \in \mathbb{R},\ \mathsf{S}(x) = \sum_{p=0}^{\infty} \frac{(-1)^p \left(\frac{1}{2}\pi\right)^{2p+1}}{(2p+1)!(4p+3)} x^{4p+3}. \tag{D.13}$$

D.3 Modified Fresnel Integrals

We define the modified cosine and sine Fresnel integrals as $x \mapsto \mathsf{C}(x)/x$ and $x \mapsto \mathsf{S}(x)/x$ for $x \in \mathbb{R}$. Given the series expansions of the Fresnel integrals, these two functions are well-defined and, in particular, have no singularity at $x = 0$. Figure D.2 presents plots of the modified Fresnel integrals for (a) $x \in [0;\ 30]$, and (b) $x \in [0;\ 5]$ (zoomed-in version). The limit at $x \to 0$ can be clearly observed, as well as the rapid decay of the modified cosine Fresnel integral when increasing x.

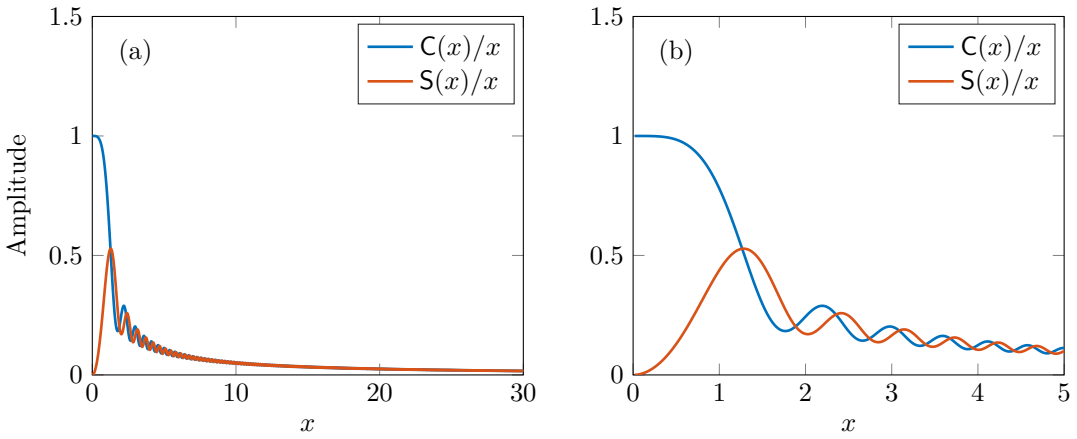

Figure D.2: Plots of the modified cosine and sine Fresnel integrals, for (a) $x \in [0;\ 30]$, and (b) $x \in [0;\ 5]$. The limits can be clearly identified.

These two functions have the following limits

$$\lim_{x \to 0} \frac{\mathsf{C}(x)}{x} = 1, \tag{D.14}$$

$$\lim_{x \to \infty} \frac{\mathsf{C}(x)}{x} = 0, \tag{D.15}$$

and

$$\lim_{x \to 0} \frac{\mathsf{S}(x)}{x} = 0, \tag{D.16}$$

$$\lim_{x \to \infty} \frac{\mathsf{S}(x)}{x} = 0. \tag{D.17}$$

APPENDIX E

Kelvin Modes

Cuando llegó a la mancha verde entró en un mundo donde el olor del tomillo y de la salvia era una misma materia con el fuego del sol y la brisa del mar.
Julio Cortázar, TODOS LOS FUEGOS EL FUEGO.

In this appendix, we present the calculus leading to the radial, azimuthal, and vertical velocities (v_r, v_θ, v_z) presented at the end of chapter 1 and known as *Kelvin modes*. These modes are cylindrical, with an azimuthal periodic dependence through a wave number p. In the case $p = 0$, these modes are purely aisymmetric and correspond to the modes discussed throughout the manuscript. The resolution of the wave equations presented here are based on a separation variable method and on properties of Bessel functions (see appendix C and [163] for more details).

E.1 Differential Equations

As detailed in chapter 1, three velocity equations can be derived using the vorticity equation. Two of them couple the radial and orthoradial velocities v_r and v_θ, with v_z acting as a forcing term that can be determined independently thanks to a third equation. They are recalled as follows

$$\partial_t^2 \Delta v_r - \frac{1}{r^2}\partial_t^2 \left(v_r + 2\partial_\theta v_\theta\right) + f\partial_t\partial_z \left(\frac{1}{r}\partial_\theta v_z - \partial_z v_\theta\right) - N^2 \partial_r\partial_z v_z = 0, \tag{E.1}$$

$$\partial_t^2 \Delta v_\theta - \frac{1}{r^2}\partial_t^2 \left(v_\theta - 2\partial_\theta v_r\right) + f\partial_t\partial_z \left(\partial_z v_r - \partial_r v_z\right) - N^2 \frac{1}{r}\partial_\theta\partial_z v_z = 0, \tag{E.2}$$

$$\partial_t^2 \Delta v_z + f^2\partial_z^2 v_z + N^2 \left(\frac{1}{r}\partial_r(r\partial_r v_z) + \frac{1}{r^2}\partial_\theta^2 v_z\right) = 0. \tag{E.3}$$

E.2 Vertical Velocity Field

We first focus on equation (E.3) satisfied by the vertical velocity v_z. As mentioned in chapters 1 and 4, it can be solved by using a variable separation method if the boundary conditions are differentiable. In this section, we conduct the whole calculus and show that it naturally leads to the internal wave dispersion relation.

Let's assume that v_z writes

$$v_z(r, \theta, z, t) = R(r)\Theta(\theta)Z(z)T(t), \tag{E.4}$$

where R, Θ, and Z are spatial functions for the radial, azimuthal, and vertical directions, respectively, and T is a temporal function. Equation (E.3) can then be rewritten

$$(N^2T + T'')\left(r^2R''\Theta Z + rR'\Theta Z + R\Theta''Z\right) + (f^2T + T'')r^2R\Theta Z'' = 0, \tag{E.5}$$

where the primed quantities stand for derivatives. Hence, for t such that $T(t) \neq 0$, we can write

$$\frac{T''}{T} = -\frac{N^2\left(r^2R''\Theta Z + rR'\Theta Z + R\Theta''Z\right) + f^2r^2R\Theta Z''}{r^2R''\Theta Z + rR'\Theta Z + R\Theta''Z + r^2R\Theta Z''}. \tag{E.6}$$

The left-hand side of this equation is a temporal function, whereas the right-hand side only depends on spatial variables. These two quantities are therefore constant, and if we note Λ_t this constant we will write the time-evolution equation

$$T'' - \Lambda_t T = 0, \tag{E.7}$$

and the DEcoupled spatial equation

$$\left(N^2 + \Lambda_t\right)\left(r^2R''\Theta Z + rR'\Theta Z + R\Theta''Z\right) + \left(f^2 + \Lambda_t\right)r^2R\Theta Z'' = 0. \tag{E.8}$$

Similarly, for z such that $Z(z) \neq 0$ we can write that

$$\frac{Z''}{Z} = -\frac{\left(N^2 + \Lambda_t\right)\left(r^2R''\Theta + rR'\Theta + R\Theta''\right)}{\left(f^2 + \Lambda_t\right)r^2R\Theta}, \tag{E.9}$$

where the left-hand side is a function of the vertical coordinate z and the right-hand side is a function of the horizontal coordinates r and θ. Again, these two quantities are equal to a constant Λ_z and we have the vertical equation

$$Z'' - \Lambda_z Z = 0, \tag{E.10}$$

and the horizontal equation

$$\left(N^2 + \Lambda_t\right)\left(r^2R''\Theta + rR'\Theta + R\Theta''\right) - \Lambda_z\left(f^2 + \Lambda_t\right)r^2R\Theta = 0. \tag{E.11}$$

For θ such that $\Theta(\theta) \neq 0$ we can rewrite this equation as

$$\frac{\Theta''}{\Theta} = \frac{\Lambda_z\left(f^2 + \Lambda_t\right)r^2R - \left(N^2 + \Lambda_t\right)\left(r^2R'' + rR'\right)}{\left(N^2 + \Lambda_t\right)R}, \tag{E.12}$$

with the left-hand side being a function of θ while the right-hand side is a function of r. They are both equal to a constant Λ_θ, which leads to two decoupled equation, one azimuthal

$$\Theta'' - \Lambda_\theta\Theta = 0, \tag{E.13}$$

and another one radial

$$r^2R'' + r'R' + \left(\Lambda_z\frac{f^2 + \Lambda_t}{N^2 + \Lambda_t}r^2 + \Lambda_\theta\right)R = 0. \tag{E.14}$$

This decomposition gives us three constant Λ_t, Λ_z, and Λ_θ, that set the shape of the wave field. In particular, we should pay attention to their real and imaginary parts, as this will change the solution of the equations from damped or growing exponentials to periodic oscillations. We first note that Θ is a 2π-periodic function by definition, hence from equation (E.13) we have Λ_θ negative and more exactly, we can write $\Lambda_\theta = -p^2$ with $p \in \mathbb{Z}$, leading to

$$\Theta'' + p^2\Theta = 0, \tag{E.15}$$

that can be solved into

$$\Theta(\theta) = \Theta_0 e^{-ip\theta} + \text{ c.c.}, \tag{E.16}$$

with Θ_0 a constant.

From equation (E.7) follows the temporal evolution of the system, which is periodic by definition as we are looking for a wave phenomena. Thus, the constant Λ_t is also negative and can be written $\Lambda_t = -\omega^2$ with $\omega \in \mathbb{R}$ a frequency, so that

$$T'' + \omega^2 T = 0, \tag{E.17}$$

and

$$T(t) = T_0 e^{i\omega t} + \text{c.c.}, \tag{E.18}$$

with T_0 a constant.

We now write the radial equation as

$$r^2 R'' + r' R' + \left(\Lambda_r r^2 + \Lambda_\theta\right) R = 0, \tag{E.19}$$

were the constant Λ_r is defined by

$$\Lambda_r = \Lambda_z \frac{f^2 + \Lambda_t}{N^2 + \Lambda_t} = \Lambda_z \frac{f^2 - \omega^2}{N^2 - \omega^2}. \tag{E.20}$$

Two cases can be studied, as follows:

1. If $\Lambda_r > 0$, we can write $\Lambda_r = l^2$ and equation (E.19) becomes

   $$r^2 R'' + r' R' + \left(l^2 r^2 - p^2\right) R = 0, \tag{E.21}$$

   known as the *Bessel equation* (see appendix C and the NIST Handbook [163]). Only one of its solutions is not diverging, hence we have

   $$R(r) = R_0 J_p(lr), \tag{E.22}$$

   with R_0 a constant.

2. On the contrary, if $\Lambda_r < 0$, then we write $\Lambda_r = -l^2$ and equation (E.19) becomes

   $$r^2 R'' + r' R' - \left(l^2 r^2 + p^2\right) R = 0, \tag{E.23}$$

   which is a *modified Bessel equation* [163]. Its solutions are noted I_p and K_p. The K_p solution diverges as $r \to 0$, and the I_p solution diverges as $r \to +\infty$, and they will therefore not be considered.

The vertical function Z can now be studied in more detail. Equation (E.10) leads, again, to two different cases which are both physical solutions:

1. If $\Lambda_z < 0$, then we write $\Lambda_z = -m^2$ and equation (E.10) becomes

   $$Z'' + m^2 Z = 0, \tag{E.24}$$

   that has oscillatory solutions, and

   $$Z(z) = Z_0 e^{-imz} + \text{ c.c.}, \tag{E.25}$$

   with Z_0 a constant.

2. If $\Lambda_z > 0$, then we write $\Lambda_z = m^2$ and equation (E.10) leads to

   $$Z'' - m^2 Z = 0, \tag{E.26}$$

   that has exponential solutions as

   $$Z(z) = Z_0^+ z^{mz} + Z_0^- z^{-mz}, \tag{E.27}$$

   with Z_0^+ and Z_0^- two constants.

In both cases, the dispersion relation given by equation (E.20) and that can be re-written

$$\Lambda_z = l^2 \frac{N^2 - \omega^2}{f^2 - \omega^2}, \tag{E.28}$$

is satisfied, meaning that $\Lambda_z < 0$ imposes either $f < \omega < N$ or $N < \omega < f$ (propagating waves), whereas $\Lambda_z > 0$ requires either $\omega < \min(f, N)$ or $\omega > \max(f, N)$ (evanescent waves). This is further discussed in chapter 1. As a result, for propagating waves, the vertical velocity field writes

$$v_z(r, \theta, z, t) = v_z^0 J_p(lr) e^{i(\omega t - mz - p\theta)}, \tag{E.29}$$

with v_z^0 a constant, ω the wave frequency, and l, m, and p the radial, vertical, and azimuthal wave numbers, respectively.

E.3 Radial and Azimuthal Velocity Fields

Equation (E.3) on the vertical velocity being solved, we can now focus on the equations coupling the horizontal velocities v_r and v_θ, given by (E.1) and (E.2). To proceed, we will assume that these two velocities can be written under the following form

$$v_r(r, \theta, z, t) = \left[B \frac{\mathrm{d}J_p(lr)}{\mathrm{d}r} + C \frac{J_p(lr)}{r} \right] e^{i(\omega t - mz - p\theta)}, \tag{E.30}$$

$$v_\theta(r, \theta, z, t) = \left[D \frac{\mathrm{d}J_p(lr)}{\mathrm{d}r} + E \frac{J_p(lr)}{r} \right] e^{i(\omega t - mz - p\theta)}, \tag{E.31}$$

where $(B, C, D, E) \in \mathbb{C}^4$ are constants. The reason for such a decomposition, not discussed further here, comes from Fourier transforms (for the temporal, vertical, and azimuthal dependence), and from a Hankel transform (for the radial dependence). In what follows, for consistency, we will note $A = v_z^0$ the real amplitude of the vertical velocity field. Indices $_r$ and $_i$ will be used for real and imaginary parts of the different coefficients B, C, D, and E.

E.3.1 Radial Equation

Replacing v_r and v_θ in equation (E.1) by their form (E.30) and (E.31), with v_z known thanks to equation (E.29), leads to an equation that only depends on r. Using the differential equation of which Bessel functions are solutions, as well as the recurrence relation between Bessel functions of different orders, this equation can be written as a sum of terms proportional to $J_p(lr)$ and of terms proportional to $J_{p+1}(lr)$ (calculus not shown here). To satisfy the equation, the prefactors of these two functions have to be zero at all radial position, hence this "projection" over J_{p+1} and J_p gives the following system

$$0 = -2C_r - 2pD_i, \tag{E.32}$$

$$0 = -\omega k^2 B_r + f m^2 D_i, \tag{E.33}$$

$$0 = -2C_i + 2pD_r, \tag{E.34}$$

$$0 = -\omega^2 k^2 B_i - \omega f m^2 D_r + N^2 m A, \tag{E.35}$$

$$0 = -2pC_r - 2p^2 D_i - 2p^2 B_r - 2pE_i, \tag{E.36}$$

$$0 = -\omega k^2 p B_r + f m^p D_i - \omega k^2 C_r + f m^2 E_i, \tag{E.37}$$

$$0 = -2pC_i + 2p^2 D_r - 2p^2 B_i + 2pE_r, \tag{E.38}$$

$$0 = -\omega^2 k^2 p B_i - \omega f m^2 p D_r + pm(f\omega + N^2) A - \omega^2 k^2 C_i - \omega f m^2 E_r. \tag{E.39}$$

E.3.2 Azimuthal Equation

We apply the same method to the azimuthal equation (E.2), from which we can derive the following system of equations

$$\begin{aligned}
0 &= -2E_r + 2pB_i, && \text{(E.40)}\\
0 &= -\omega k^2 D_r - f m^2 B_i + f m A, && \text{(E.41)}\\
0 &= -2E_i - 2pB_r, && \text{(E.42)}\\
0 &= -\omega k^2 D_i + f m^2 B_r, && \text{(E.43)}\\
0 &= -2E_r + 2p^2 B_i - 2p^2 D_r + 2pC_i, && \text{(E.44)}\\
0 &= -\omega^2 k^2 p D_r - \omega f m^p B_i + pm(f\omega + N^2)A - \omega^2 k^2 E_r - \omega f m^2 C_i, && \text{(E.45)}\\
0 &= -2pE_i - 2p^2 B_r - 2p^2 D_i - 2pC_r, && \text{(E.46)}\\
0 &= -\omega k^2 p D_i - f m^2 p B_r - \omega k^2 E_i + f m^2 C_r. && \text{(E.47)}
\end{aligned}$$

E.3.3 Horizontal Velocities

The two previous systems of 8 equations (E.32)–(E.39) and (E.40)–(E.47) are equivalent, and lead to the same solutions. We first obtain that

$$B_r = C_r = D_i = E_r = 0, \tag{E.48}$$

and the complete resolution of the system yields

$$\begin{aligned}
B &= iB_i = -i\frac{m}{l^2}v_z^0, && \text{(E.49)}\\
C &= iC_i = ip\frac{fm}{\omega l^2}v_z^0, && \text{(E.50)}\\
D &= D_r = \frac{fm}{\omega l^2}v_z^0, && \text{(E.51)}\\
E &= E_r = -\frac{pm}{l^2}v_z^0. && \text{(E.52)}
\end{aligned}$$

The two horizontal velocities can therefore be written

$$\begin{aligned}
v_r(r,\theta,z,t) &= -i\frac{m}{l^2}v_z^0\left[\frac{\mathrm{d}J_p(lr)}{\mathrm{d}r} - \frac{pf}{\omega}\frac{J_p(lr)}{r}\right]e^{i(\omega t - mz - p\theta)}, && \text{(E.53)}\\
v_\theta(r,\theta,z,t) &= \frac{m}{l^2}v_z^0\left[\frac{f}{\omega}\frac{\mathrm{d}J_p(lr)}{\mathrm{d}r} - p\frac{J_p(lr)}{r}\right]e^{i(\omega t - mz - p\theta)}. && \text{(E.54)}
\end{aligned}$$

E.4 Complete Solution and Representations

Expressions (E.53) and (E.54) can be further simplified by using recurrence relations on Bessel functions (see appendix C), namely

$$\begin{aligned}
\frac{\mathrm{d}J_p(lr)}{\mathrm{d}r} &= l\left[J_{p-1}(lr) - J_{p+1}(lr)\right], && \text{(E.55)}\\
\frac{1}{r}J_p(lr) &= \frac{l}{2p}\left[J_{p-1}(lr) + J_{p+1}(lr)\right]. && \text{(E.56)}
\end{aligned}$$

As a result, we can finally write the radial, azimuthal, and vertical velocities in their complete form

$$\begin{aligned}
v_r(r,\theta,z,t) &= i\frac{mv_z^0}{4l\omega}\left[(f-2\omega)J_{p-1}(lr) + (f+2\omega)J_{p+1}(lr)\right]e^{i(\omega t - mz - p\theta)} + \text{c.c.}, && \text{(E.57)}\\
v_\theta(r,\theta,z,t) &= \frac{mv_z^0}{4l\omega}\left[(2f-\omega)J_{p-1}(lr) - (2f+\omega)J_{p+1}(lr)\right]e^{i(\omega t - mz - p\theta)} + \text{c.c.}, && \text{(E.58)}\\
v_z(r,\theta,z,t) &= v_z^0 J_p(lr)e^{i(\omega t - mz - p\theta)} + \text{c.c.}. && \text{(E.59)}
\end{aligned}$$

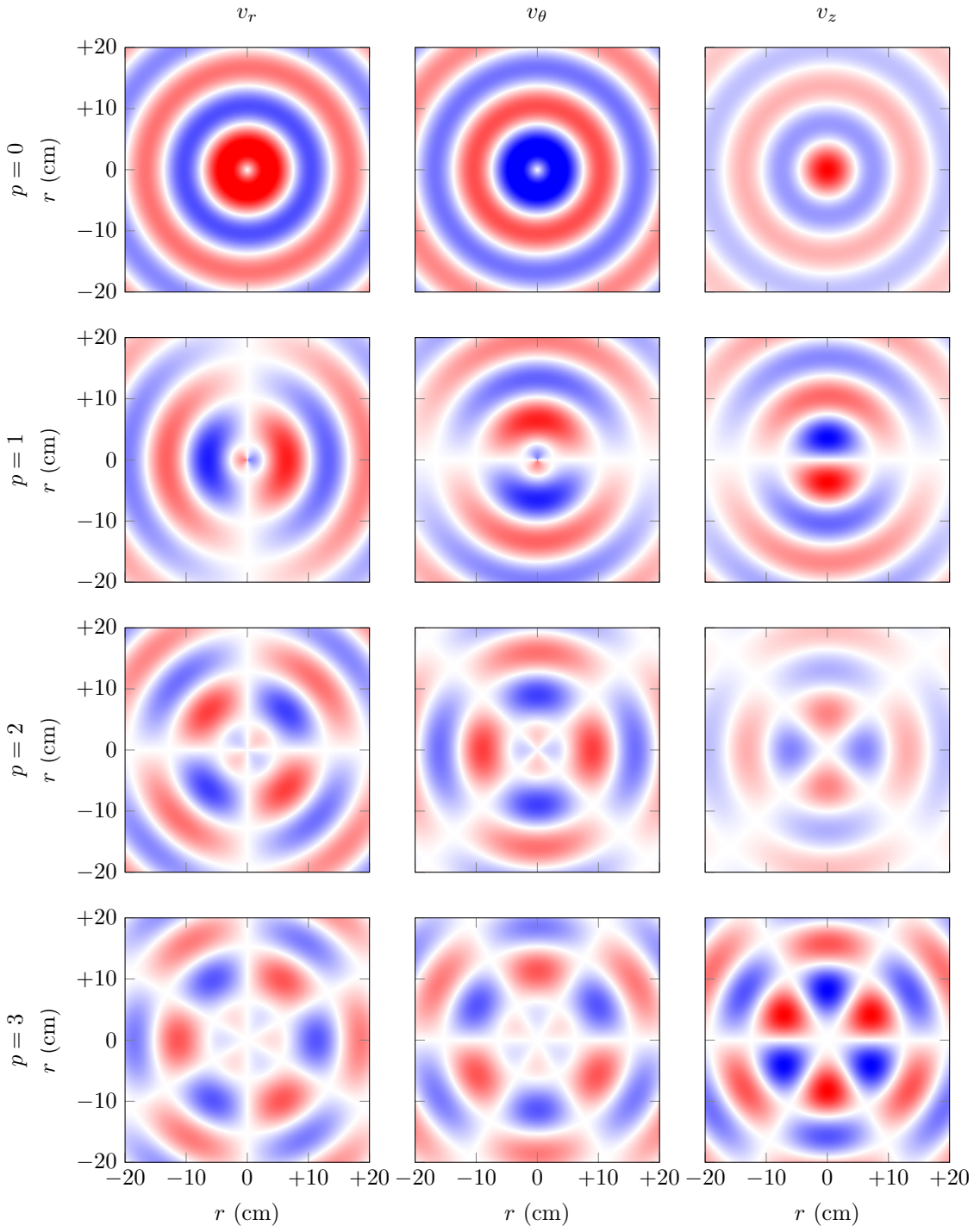

Figure E.1: Velocities of various Kelvin modes shown in the horizontal plane. From left to right: radial velocity v_r, azimuthal velocity v_θ, and vertical velociry v_z. From top to bottom: $p = 1$ through 4. All velocity fields are plotted for $\omega/f = 1$, and the magnitude is indicative.

The corresponding wave field is helical and known as a *Kelvin mode* that has a given periodicity in the azimuthal coordinate θ. Note that the previous resolution of the system of equation does not take into account the physical boundaries imposed to the fluid and may therefore have to be adapted. Figure E.1 presents the horizontal structure of the velocity field for $p = 1$ through 4 at $\omega/f = 1$. As previously discussed, the case $p = 0$ is axisymmetric. The radial and the azimuthal velocities are in phase opposition regarding their variations with the angle θ, and so are the radial and the vertical velocities.

Bibliography

Bibliography

[1] A. Adriani, A. Bracco, D. Grassi, M. L. Moriconi, A. Mura, G. Orton, F. Altieri, A. Ingersoll, J. Lunine, A. Migliorini, R. Noschese, A. Cicchetti, F. Tosi, C. Plainaki, B.M. Dinelli, D. Turrini, G. Filacchione, G. Piccioni, and S.J. Bolton. Two-year observations of the jupiter polar regions by jiram on board juno. *Journal of Geophysical Research: Planets*, page (in press), 2020.

[2] A. Adriani, A. Mura, G. Orton, C. Hansen, F. Altieri, M.L. Moriconi, J. Rogers, G. Eichstädt, T. Momary, A.P. Ingersoll, G. Filacchione, G. Sindoni, F. Tabataba-Vakili, B.M. Dinelli, F. Fabiano, S.J. Bolton, J.E.P. Connerney, S.K. Atreya, J.I. Lunine, F. Tosi, A. Migliorini, D. Grassi, G. Piccioni, R. Noschese, C. Plainaki, A. Olivieri, M.E. O'Neill, D. Turrini, S. S. Stefani, R. Sordini, and M. Amoroso. Clusters of cyclones encircling Jupiter's poles. *Nature*, 555:216–219, 2018.

[3] D.A. Aguilar and B.R. Sutherland. Internal wave generation from rough topography. *Physics of Fluids*, 18:1 – 9, 2006.

[4] A. Alastuey, M. Magro, and P. Pujol. *Physique et outils mathématiques, Méthodes et exemples*. EDP Sciences, 2008.

[5] T. Albrecht, H.M. Blackburn, J.M. Lopez, R. Manasseh, and P. Meunier. Triadic resonances in precessing rapidly rotating cylinder flows. *Journal of Fluid Mechanics*, 778:R1, 2015.

[6] T. Albrecht, H.M. Blackburn, J.M. Lopez, R. Manasseh, and P. Meunier. On triadic resonance as an instability mechanism in precessing cylinder flow. *Journal of Fluid Mechanics*, 841:R3, 2018.

[7] K.D. Aldridge and A. Toomre. Axisymmetric inertial oscillations of a fluid in a rotating spherical container. *Journal of Fluid Mechanics*, 27:307 – 323, 1969.

[8] M. Alexander, J. Holton, and D. Durran. The gravity-wave response above deep convection in a squall line simulation. *Journal of Atmospheric Science*, 52:2212 – 2226, 1995.

[9] M.H. Alford. Internal swell generation: The spatial distribution of energy flux from the wind to mixed layer near-inertial motions. *Journal of Physical Oceanography*, 31:2359 – 2368, 2001.

[10] M.H. Alford. Redistribution of energy available for ocean mixing by long-range propagation of internal waves. *Nature*, 423:159 – 162, 2003.

[11] M.H. Alford, J.M. Klymak, and G.S. Carter. Breaking internal lee waves at kaena ridge, hawaii. *Geophysical Research Letters*, 41:906 – 912, 2014.

[12] M.H. Alford, J.A. MacKinnon, Z. Zhao, R. Pinkel, J. Klymak, and T. Peacock. Internal waves across the pacific. *Geophysical Research Letters*, 34:L24601, 2007.

[13] J.K. Ansong and B.R. Sutherland. Internal gravity waves generated by convective plumes. *Journal of Fluid Mechanics*, 648:405 – 434, 2010.

[14] J.C. Appleby and D.G. Crighton. Internal gravity waves generated by oscillations of a sphere. *Journal of Fluid Mechanics*, 183:439 – 450, 1987.

[15] G.B. Arfken and H.J. Weber. *Mathematical methods for physicists*. Elsevier, 2005.

[16] L.E. Baker and B.R. Sutherland. The evolution of superharmonics excited by internal tides in non-uniform stratification. *Journal of Fluid Mechanics*, 2020.

[17] C.L. Beattie. Table of first 700 zeros of bessel functions – $J_l(x)$ and $J_l'(x)$. *The Bell system technical journal*, pages 689 – 697, 1958.

[18] F. Beckebanze. *Boundary layer dynamics of internal gravity waves*. PhD thesis, Utrecht University, 2019.

[19] F. Beckebanze, C. Brouzet, I.N. Sibgatullin, and L.R.M. Maas. Damping of quasi-two-dimensional internal wave attractors by rigid-wall friction. *Journal of Fluid Mechanics*, 841:614 – 635, 2018.

[20] T.H. Bell. Radiation damping of inertial oscillations in the upper ocean. *Journal of Fluid Mechanics*, 88:289 – 308, 1978.

[21] D. Benielli and J. Sommeria. Excitation and breaking of internal gravity waves by parametric instability. *Journal of Fluid Mechanics*, 374:117 – 144, 1998.

[22] P. Berrisford, D. Dee, K. Fielding, M. Fuentes, P. Kallberg, S. Kobayashi, and S. Uppala. The ERA-interim archive. *ERA report series*, 1:1 – 16, 2009.

[23] G.P. Bewley, DD.P. Lathrop, L.R.M. Maas, and K.R. Sreenivasan. Inertial waves in rotating grid turbulence. *Physics of Fluids*, 19(7):071701, 2007.

[24] J. Boisson, C. Lamriben, L.R.M. Maas, P.-P. Cortet, and F. Moisy. Inertial waves and modes excited by the libration of a rotating cube. *Physics of Fluids*, 24(7):076602, 2012.

[25] G. Bordes. *Interactions non-linéaires d'ondes et tourbillons en milieu stratifié ou tournant*. PhD thesis, Université de Lyon, 2012.

[26] G. Bordes, A. Venaille, S. Joubaud, P. Odier, and T. Dauxois. Experimental observation of a strong mean flow induced by internal gravity waves. *Physics of Fluids*, 24, 2012.

[27] B. Bourget. *Ondes internes, de l'instabilité au mélange. Approche expérimentale*. PhD thesis, Université de Lyon, 2014.

[28] B. Bourget, T. Dauxois, S. Joubaud, and P. Odier. Experimental study of parametric sub-harmonic instability for internal plane waves. *Journal of Fluid Mechanics*, 723:1 – 20, 2013.

[29] L. Bourouba and P. Bartello. The intermediate rossby number range and two-dimensional–three-dimensional transfers in rotating decaying homogeneous turbulence. *Journal of Fluid Mechanics*, 587:139 – 161, 2007.

[30] S. Boury, S. Joubaud, and M. Le Bars. Pourquoi les meddies existent-ils ? *Bulletin de l'Union des Physiciens*, 2020.

[31] S. Boury, P. Maurer, S. Joubaud, T. Peacock, and P. Odier. Triadic resonant instability in confined and unconfined axisymmetric geometries. *Journal of Fluid Mechanics*, in preparation.

[32] S. Boury, P. Odier, and T. Peacock. Axisymmetric internal wave transmission and resonance in non-linear stratifications. *Journal of Fluid Mechanics*, 886:A8, 2020.

[33] S. Boury, T. Peacock, and P. Odier. Excitation and resonant enhancement of axisymmetric internal wave modes. *Physical Review Fluids*, 4:034802, 2019.

[34] S. Boury, T. Peacock, and P. Odier. Experimental self-generation of axisymmetric internal wave super-harmonics. *Physical Review Fluids*, in preparation.

[35] S. Boury, R.S. Pickart, P. Odier, P. Lin, M. Li, E.C. Fine, H.L. Simmons, J.A. MacKinnon, and T. Peacock. Whither the chukchi slope current? *in preparation for Journal of Physical Oceanography*, 50:1717 – 1732, 2020.

[36] S. Boury, I. Sibgatullin, E. Ermanyuk, N. Shmakova, P. Odier, S. Joubaud, and T. Dauxois. Vortex cluster arising from an axisymmetric wave attractor. *Journal of Fluid Mechanics*, in preparation.

[37] S. Boury, B.R. Sutherland, P. Odier, and T. Peacock. Axisymmetric internal wave tunelling. *Physical Review Fluids*, in preparation.

[38] P. Bradshaw. The analogy between streamline curvature and buoyancy in turbulent shear flow. *Journal of Fluid Mechanics*, 36:177 – 191, 1969.

[39] A. Brandt and K.R. Shipley. Internal gravity waves generated by an impulsive plume. *Physical Review Fluids*, 4:014803, 2019.

[40] F.P. Bretherton. Low frequency oscillations trapped near the equator. *Tellus*, 16:181–185, 1964.

[41] W.S. Broecker. The great ocean conveyor. *Oceanography*, 4:79 – 89, 1991.

[42] C. Brouzet. *Internal wave attractors: from geometrical focusing to non-linear energy cascade and mixing.* PhD thesis, Université de Lyon, 2016.

[43] C. Brouzet, E.V. Ermanyuk, S. Joubaud, I.N. Sibgatullin, and T. Dauxois. Energy cascade in internal wave attractors. *Europhysics Letters*, 113:44001, 2016.

[44] C. Brouzet, I.N. Sibgatullin, H. Scolan, E.V. Ermanyuk, and T. Dauxois. Internal wave attractors examined using laboratory experiments and 3d numerical simulations. *Journal of Fluid Mechanics*, 793:109 – 131, 2016.

[45] G.L. Brown and B.R. Sutherland. Internal wave tunnelling through non-uniformly stratified shear flow. *Atmosphere-Oceans*, 45:47 – 56, 2007.

[46] E. T. Brugler, R. S. Pickart, G. W. K. Moore, S. Roberts, T. J. Weingartner, and H. Statscewich. Seasonal to interannual variability of the Pacific water boundary current in the Beaufort Sea. *Progress in Oceanography*, 127:1 – 20, 2014.

[47] M. Brunet, T. Dauxois, and P.-P. Cortet. Linear and nonlinear regimes of an inertial wave attractor. *Physical Review Fluids*, 4:034801, 2019.

[48] O. Bühler. *Waves and Mean Flows.* Cambridge University Press, 2014.

[49] O. Bühler and C.J. Muller. Instability and focusing of internal tides in the deep ocean. *Journal of Fluid Mechanics*, 588:1 – 28, 2007.

[50] K.J. Burns, G.M. Vasil, J.S. Oishi, D. Lecoanet, and B.P. Brown. Dedalus: A flexible framework for numerical simulations with spectral methods. *arXiv (draft)*, 2019.

[51] D. Cacchione and C. Wunsch. Experimental study of internal waves over a slope. *Journal of Fluid Mechanics*, 66:223 – 239, 1974.

[52] M.I. Castillo, O. Pizarro, N. Ramírez, and M. Cáceres. Seiche excitation in a highly stratified fjord of southern chile: the reloncaví fjord. *Ocean Science*, 13:145 – 160, 2017.

[53] G.P. Chini and S. Leibovich. Resonant langmuir-circulation–internal-wave interaction. part 2. langmuir circulation instability. *Journal of Fluid Mechanics*, 524:519 – 120, 2005.

[54] J.Y.-K. Cho and L.M. Polvani. The emergence of jets and vortices in freely evolving, shallow-water turbulence on a sphere. *Physics of Fluids*, 8(6):1531–1552, 1996.

[55] L. K. Coachman, K. Aagaard, and R. B. Tripp. *Bering Strait, The Regional Physical Oceanography.* University of Washington Press, Seattle and London, 1975.

[56] S.T. Cole, M.-L. Timmermans, J.M. Toole, R.A. Krishfield, and F.T. Thwaites. Ekman veering, internal waves, and turbulence observed under arctic sea ice. *Journal of Physical Oceanography*, 44:1306 – 1328, 2013.

[57] B. W. Corlett and R. S. Pickart. The Chukchi slope current. *Progress in Oceanography*, 153:50 – 65, 2017.

[58] E.A. D'Asaro. The energy flux from the wind to near-inertial motions in the surface mixed layer. *Journal of Physical Oceanography*, 15:1043 – 1059, 1985.

[59] T. Dauxois and W.R. Young. Near-critical reflection of internal waves. *Journal of Fluid Mechanics*, 390:271 – 295, 1999.

[60] A.M.J. Davis and S.G.L. Smith. Tangential oscillations of a circular disk in a viscous stratified fluid. *Journal of Fluid Mechanics*, 656:342 – 359, 2010.

[61] D. P. Dee, S. M. Uppala, A. J. Simmons, P. Berrisford, P. Poli, S. Kobayashi, U. Andrae, M. A. Balmaseda, G. Balsamo, P. Bauer, P. Bechtold, A. C. M. Beljaars, L. van de Berg, J. Bidlot, N. Bormann, C. Delsol, R. Dragani, M. Fuentes, A. J. Geer, L. Haimberger, S. B. Healy, H. Hersbach, E. V. Hólm, L. Isaksen, P. Kallberg, M. Köhler, M. Matricardi, A. P. McNally, B. M. Monge-Sanz, J.-J. Morcrette, B.-K. Park, C. Peubey, P. de Rosnay, C. Tavolato, J.-N. Thépaut, and F. Vitart. The ERA-interim reanalysis: configuration and performance of the data assimilation system. *Q.J.R. Meteorological Society*, 137:553 – 597, 2011.

[62] P.J. Diamessis, S. Wunsch, I. Delwiche, and M.P. Richter. Nonlinear generation of harmonics through theinteraction of an internal wave beam with amodel oceanic pycnocline. *Dynamics of Atmospheres and Oceans*, 66:110 – 137, 2014.

[63] B. Dintrans, M. Rieutord, and L. Valdettaro. Gravito-inertial waves in a rotating stratified sphere or spherical shell. *Journal of Fluid Mechanics*, 398:271–297, 1999.

[64] Y. Dossmann, F. Pollet, P. Odier, and T. Dauxois. Mixing and formation of layers by internal wave forcing. *Journal of Geophysical Research: Oceans*, 122:1 – 12, 2017.

[65] P.G. Drazin and W.H. Reid. *Hydrodynamic Stability.* Cambridge University Press, 1981.

[66] M. Duran-Matute, J.-B. Flór, F.S. Godeberd, and C. Jause-Labert. Turbulence and columnar vortex formation through inertial-wave focusing. *Physical Review E*, 87, 2013.

[67] T. Eaves and N.J. Balmforth. Instability of sheared density interfaces. *Journal of Fluid Mechanics*, 860:145 – 171, 2019.

[68] P. Echeverri, M.R. Flynn, K.B. Winters, and T. Peacock. Low-mode internal tide generation by topography: an experimental and numerical investigation. *Journal of Fluid Mechanics*, 636:91 – 108, 2009.

[69] P. Echeverri, T. Yokossi, N.J. Balmforth, and T. Peacock. Tidally generated internal-wave attractors between double ridges. *Journal of Fluid Mechanics*, 669:354 – 374, 2011.

[70] G.D. Egbert. Semi-diurnal and diurnal tidal dissipation from TOPEX/Poseidon altimetry. *Geophysical Research Letters*, 30:1907, 2003.

[71] G.D. Egbert and R.D. Ray. Estimates of m2 tidal energy dissipation from topex/poseidon altimeter data. *Journal of Geophysical Research*, 106:22475, 2001.

[72] C. Eloy, P. Le Gal, and S. Le Dizés. Elliptic and triangular instabilities in rotating cylinders. *Journal of Fluid Mechanics*, 476:357 – 388, 2003.

[73] C.C. Eriksen. Observations of internal wave re1ection on sloping bottoms. *Journal of Geophysical Research*, 87:525 – 538, 1982.

[74] E.V. Ermanyuk, J.-B. Flór, and B. Voisin. Spatial structure of first and higher harmonic internal waves from a horizontally oscillating sphere. *Journal of Fluid Mechanics*, 671:364 – 383, 2011.

[75] E.V. Ermanyuk and N. Gavrilov. On internal waves generated by large-amplitude circular and rectilinear oscillations of a circular cylinder in a uniformly stratified fluid. *Journal of Fluid Mechanics*, 613:329 – 356, 2008.

[76] E.V. Ermanyuk, N.D. Shmakova, and J.-B. Flór. Internal wave focusing by a horizontally oscillating torus. *Journal of Fluid Mechanics*, 813:695 – 715, 2017.

[77] A. Fincham and G. Delerce. Advanced optimization of correlation imaging velocimetry algorithms. *Experiments in Fluids*, 29:13 – 22, 2000.

[78] E.C. Fine, J.A. MacKinnon, M.H. Alford, and J.B. Mickett. Microstructure observations of turbulent heat fluxes in a warm-core canada basin eddy. *Journal of Physical Oceanography*, 48:2397 – 2418, 2018.

[79] P. Flandrin. *Time-frequency/time-scale analysis*, volume 10. Academic Press, 1999.

[80] M.R. Flynn, K. Onu, and B.R. Sutherland. Internal wave excitation by a vertically oscillating sphere. *Journal of Fluid Mechanics*, 494:65 – 93, 2003.

[81] J.M.H. Fortuin. Theory and application of two supplementary methods of constructing density gradient columns. *Journal of Polymer Science*, 44:505 – 515, 1960.

[82] A. Fresnel. *Mémoire sur la diffraction de la lumière*. Mémoires de l'Académie des Sciences, 1818.

[83] S. Friedlander and W.L. Siegmann. Internal waves in a contained rotating stratified fluid. *Journal of Fluid Mechanics*, 114:123 – 156, 1982.

[84] C. Garrett. Internal tides and ocean mixing. *Science*, 301:1858 – 1859, 2003.

[85] T. Gerkema, J.T.F. Zimmerman, L.R.M. Maas, and H. van Haren. Geophysical and astrophysical fluid dynamics beyond the traditional approximation. *Reviews od Geophysics*, 46:1 – 33, 2008.

[86] S.J. Ghaemsaidi, H.V. Dosser, L. Rainville, and T. Peacock. The impact of multiple layering on internal wave transmission. *Journal of Fluid Mechanics*, 789:617 – 629, 2016.

[87] S.J. Ghaemsaidi and T. Peacock. 3d stereoscopic piv visualization of the axisymmetric conical internal wave field generated by an oscillating sphere. *Experiments in Fluids*, 54:1454, 2013.

[88] A. Giesecke, T. Albrecht, T. Gundrum, J. Herault, and F. Stefani. Triadic resonances in nonlinear simulations of a fluid flow in a precessing cylinder. *New Journal of Physics*, 17:113044, 2015.

[89] F.S. Godeferd and L. Lollini. Direct numerical simulations of turbulence with confinement and rotation. *Journal of Fluid Mechanics*, 393:257 – 308, 1999.

[90] D. Gong and R.S. Pickart. Summertime circulation in the eastern chukchi sea. *Deep Sea Research II*, 118:18 – 31, 2015.

[91] H. Görtler. Uber eine schwingungserscheinung in flussigkeiten mit stabiler dichteschichtung. *ZAMM Journal of Applied Mathematics and Mechanics / Zeitschrift fur Angewandte Mathematik und Mechanik*, 23:65 – 71, 1943.

[92] L. Gostiaux, H. Didelle, S. Mercier, and T. Dauxois. A novel internal waves generator. *Experiments in Fluids*, 42:123 – 130, 2006.

[93] N. Grisouard, C. Staquet, and I. Pairaud. Numerical simulation of a two-dimensional internal wave attractor. *Journal of Fluid Mechanics*, 614:1 – 14, 2008.

[94] S. Groeskamp, J.J Nauw, and L.R.M. Maas. Observations of estuarine circulation and solitary internal waves in a highly energetic tidal channel. *Ocean Dynamics*, 61:1767 – 1782, 2011.

[95] D. Guimbard. *L'instabilité elliptique en milieu stratifié tournant.* PhD thesis, Université du Sud Toulon Var, 2008.

[96] D. Guimbard, S. Le Dizès, M. Le Bars, P. Le Gal, and S. Leblanc. Elliptic instability of a stratified fluid in a rotating cylinder. *Journal of Fluid Mechanics*, 660:240 – 257, 2010.

[97] J. Hazewinkel, L.R.M. Maas, and S. Dalziel. Tomographic reconstruction of internal wave patterns in a paraboloid. *Experiments in Fluids*, 50:247 – 258, 2018.

[98] J. Hazewinkel, P. van Breevoort, S. Dalziel, and L.R.M. Maas. Observations on the wavenumber spectrum and evolution of an internal wave attractor. *Journal of Fluid Mechanics*, 598:373 – 382, 2008.

[99] M.C. Hendershott. Impulsively started oscillations in a rotating stratified fluid. *Journal of Fluid Mechanics*, 36:513 – 527, 1968.

[100] B.M. Hickey. The response of a steep-sided, narrow canyon to time-variable wind forcing. *Journal of Physical Oceanography*, 27:697 – 726, 1997.

[101] P. Husseini, D. Varma, T. Dauxois, S. Joubaud, P. Odier, and Manikandan Mathur. Experimental study on superharmonic wave generation by resonant interaction between internal wave modes. *Physical Review Fluids (submission)*, 2019.

[102] K.-H. Hyun. *The effect of submarine canyon width and stratification on coastal circulation and across shelf exchange.* PhD thesis, 2004.

[103] J.D. Jackson. *Classical Electrodynamics, third edition.* John Wiley & Sons, 1999.

[104] T. Jamin. *Interactions entre ondes de surface et écoulements hydrodynamiques.* PhD thesis, Université Paris Diderot, 2016.

[105] C. Jeon, S. Boury, T. Peacock, J.-H. Park, and Kyoung-Ho Cho. Observation of spatial and temporal variability of deep near-inertial waves in the western arctic ocean. *Geophysical Research Letters*, in preparation.

[106] O.M. Johannessen and O.S. Lee. Thermohaline staircase structure in the Tyrrhenian sea. *Deep-Sea Research*, 21:629, 1974.

[107] S. Joubaud, J. Munroe, P. Odier, and T. Dauxois. Experimental parametric subharmonic instability in stratified fluids. *Physics of Fluids*, 24, 2012.

[108] L. Jouve and G.I. Ogilvie. Direct numerical simulations of an inertial wave attractor in linear and nonlinear regime. *Journal of Fluid Mechanics*, 745:223 – 250, 2014.

[109] B. King, M. Stone, H.P. Zhang, T. Gerkema, M. Marder, R.B. Scott, and H.L. Swinney. Buoyancy frequency profiles and internal semidiurnal tide turning depths in the oceans. *Journal of Geophysical Research*, 117:C04008, 2012.

[110] Y.V. Kistovich and Y.D. Chashechkin. Linear theory of the propagation of internal wave beams in an arbitrarily stratified liquid. *Journal of Applied Mechanics and Technical Physics*, 39:729 – 737, 1998.

[111] J.M. Klinck. Circulation near submarine canyons: A modeling study. *Journal of Geophysical Research*, 101:1211 – 1223, 1996.

[112] B. Konar, L. Frisch, and S.B. Moran. Development of best practices for scientific research vessel operations in a changing Arctic: A case study for R/V Sikuliaq. *Marine Policy*, 86:182 – 189, 2017.

[113] K.N. Kumar, T.K. Ramkumar, and M. Krishnaiah. Mst radar observation of inertia-gravity waves generated from tropical cyclones. *Journal of Atmospheric and Solar-Terrestrial Physics*, 73:1890 – 1906, 2011.

[114] E. Kunze. Internal-wave-driven mixing: Geography and budgets. *Journal of Physical Oceanography*, 47:1325 – 1345, 2017.

[115] R. Lagrange, P. Meunier, and C. Eloy. Triadic instability of a non-resonant precessing fluid cylinder. *Comptes Rendus Mécanique*, 344:418 – 433, 2016.

[116] R. Lagrange, P. Meunier, F. Nadal, and C. Eloy. Precessional instability of a fluid cylinder. *Journal of Fluid Mechanics*, 666:104 – 145, 2011.

[117] R.B. Lambert and W. Sturges. A thermohaline staircase and vertical mixing in the thermocline. *Deep-Sea Research*, 24:211, 1977.

[118] C. Lamriben, P.-P. Cortet, F. Moisy, and L.R.M. Maas. Excitation of inertial modes in a closed grid turbulence experiment under rotation. *Physics of fluids*, 23(1):015102, 2011.

[119] S. Le Dizès. Wave field and zonal flow of a librating disk. *Journal of Fluid Mechanics*, 782:178 – 208, 2015.

[120] C.M. Lee, S. Cole, M. Doble, J.D. Guthrie, S. Harper, J.A. MacKinnon, J. Morison, R. Musgrave, T. Peacock, L. Rainville, T. Stanton, J. Toole, J. Thomson, J. Wilkinson, M. Alford, D. Chayes, L. Freitag, S. Jayne, J.-H. Park, H.L. Simmons, O. Sun, D. Torres, and L. Valcic. Stratified Ocean Dynamics of the Arctic: Science and experiment plan. *Technical Report*, APL-UW 1601, 2016.

[121] M. Li, R.S. Pickart, M.A. Spall, T.J. Weingatner, P. Lin, G.W.K. Moore, and Y. Qi. Circulation of the Chukchi Sea shelfbreak and slope from moored timeseries. *Progress in Oceanography*, 2019.

[122] M.J. Lighthill. On waves generated in dispersive systems by travelling forcing effects, with applications to the dynamics of rotating fluids. *Journal of Fluid Mechanics*, 27:725 – 752, 1967.

[123] P. Lin, R.S. Pickart, L.T. McRaven, K.R. Arrigo, F. Bahr, K.E. Lowry, D.A. Stockwell, and C.W. Mordy. Water mass evolution and circulation of the northeastern chukchi sea in summer: Implications for nutrient distributions. *Journal of Geophysical Research*, page (in press), 2019.

[124] K.N. Liou. *An introduction to Atmospheric Radiation*. Academic Press San Diego, 2002.

[125] K.E. Lowry, R.S. Pickart, M.M. Mills, Z.W. Brown, G.L. van Dijken, N.R. Bates, and K.R. Arrigo. The influence of winter water on phytoplankton blooms in the Chukchi Sea. *Deep Sea Research II*, 118:53 – 72, 2015.

[126] L.R.M. Maas. Wave focusing and ensuing mean flow due to symmetry breaking in rotating fluids. *Journal of Fluid Mechanics*, 437:13, 2001.

[127] L.R.M. Maas. On the amphidromic structure of inertial waves in a rectangular parallelepiped. *Fluid Dynamics Research*, 33(4):373, 2003.

[128] L.R.M. Maas. Wave attractors: linear yet non linear. *International Journal of Bifurcation and Chaos*, 15:2757 – 2782, 2005.

[129] L.R.M. Maas, D. Benielli, J. Sommeria, and F. P. A. Lam. Observation of an internal wave attractor in a confined stably stratified fluid. *Nature*, 388:557 – 561, 1997.

[130] L.R.M. Maas and U. Harlander. Equatorial wave attractors and inertial oscillations. *Journal of Fluid Mechanics*, 570:47 – 67, 2007.

[131] L.R.M. Maas and F.P.A. Lam. Geometric focusing of internal waves. *Journal of Fluid Mechanics*, 300:1 – 41, 1995.

[132] J.A. MacKinnon and K.B. Winters. Subtropical catastrophe: Significant loss of low-mode tidal energy at 28.9°. *Geophysical Research Letters*, 32, 2005.

[133] J.A. MacKinnon, Z. Zhao, C.B. Whalen, A.F. Waterhouse, O.M. Trossman, D.S. ans Sun, L.C. St.Laurent, H.L. Sommons, K. Polzin, R. Pinkel, A. Pickering, N.J. Norton, J.D. Nash, R. Musgrave, L.M. Merchant, A.V. Melet, B. Mater, S. Legg, W.G. Large, Z. Kunze, J.M. Klymak, M. Jochum, S.R. Jayne, R.W. Hallberg, S.M. Griffies, S. Diggs, G. Danabasoglu, E.P. Chassignet, M.C. Buijsman, F.O. Bryan, B.P. Briegleb, A. Barna, B.K. Arbic, J.K. Ansong, and M.H. Alford. Climate process team on internal wave-driven ocean mixing. *Bulletin of the American Meteorological Society*, 98:2429 – 2454, 2017.

[134] A.M.M. Manders and L.R.M. Maas. Observations of inertial waves in a rectangular basin with one sloping boundary. *Journal of Fluid Mechanics*, 493:59 – 88, 2003.

[135] A.M.M. Manders and L.R.M. Maas. On the three-dimensional structure of the inertial wave field in a rectangular basin with one sloping boundary. *Fluid Dynamics Research*, 35:1 – 21, 2004.

[136] T.O. Manley and K. Hunkins. Mesoscale eddies of the Arctic Ocean. *Journal of Geophysical Research*, 90:4911 – 4930, 1985.

[137] J.T. Mathis, R.S. Pickart, D.A. Hansell, D. Kadko, and N.R. Bates. Eddy transport of organic carbon and nutrients from the Chukchi shelf into the deep Arctic basin. *Journal of Geophysical Research*, 112:c05011, 2007.

[138] M. Mathur and T. Peacock. Internal wave beam propagation in non-uniform stratifications. *Journal of Fluid Mechanics*, 639:133 – 152, 2009.

[139] M. Mathur and T. Peacock. Internal wave interferometry. *Physical Review Letters*, 104:118501, 2010.

[140] P. Maurer. *Approche expérimentale de la dynamique non-linéaire d'ondes internes en rotation.* PhD thesis, Université de Lyon, 2017.

[141] P. Maurer, S.J. Ghaemsaidi, S. Joubaud, T. Peacock, and P. Odier. An axisymmetric inertia-gravity wave generator. *Experiments in Fluids*, 58:143, 2017.

[142] P. Maurer, S. Joubaud, and P. Odier. Generation and stability of inertia-gravity waves. *Journal of Fluid Mechanics*, 808:539 – 561, 2016.

[143] P.A. Mazeika. Subsurface mixed layers in the northwest tropical Atlantic. *Journal of Physical Oceanography*, 4:446, 1974.

[144] A.D. McEwan. Inertial oscillations in a rotating fluid cylinder. *Journal of Fluid Mechanics*, 30:603–640, 1970.

[145] A.D. McEwan. Degeneration of resonantly excited standing internal gravity waves. *Journal of Fluid Mechanics*, 50:431–448, 1971.

[146] A.D. McEwan, D.W. Mander, and R.K. Smith. Forced resonant second-order interaction between damped internal waves. *Journal of Fluid Mechanics*, 55:589, 1972.

[147] F. Melde. Ueber die erregung stehender wellen eines fadenförmigen körpers. *Annalen Der Physik Und Chemie*, 185:193 – 215, 1860.

[148] J.M. Mercier, D. Martinand, M. Mathur, L. Gostiaux, T. Peacock, and T. Dauxois. New wave generation. *Journal of Fluid Mechanics*, 2017.

[149] M.J. Mercier, N.B. Garnier, and T. Dauxois. Reflection and diffraction of internal waves analyzed with the hilbert transform. *Physics of Fluids*, 20:086601, 2008.

[150] P. Meunier, C. Eloy, R. Lagrange, and F. Nadal. A rotating fluid cylinder subject to weak precession. *Journal of Fluid Mechanics*, 599:405 – 440, 2008.

[151] Y.Z. Miropol'sky and O.D. Shishkina. *Dynamics of Internal Gravity Waves in the Ocean*. Springer, 2001.

[152] R. Molcard and A.J. Williams. Deep-stepped structure in the Tyrrhenian sea. *Mémoires de la Société Royale des Sciences de Liège*, 8:191, 1975.

[153] P.M. Morse. *Vibration and Sound*. MGH, 1948.

[154] D.E. Mowbray and B.S.H. Rarity. The internal wave pattern produced by a sphere moving vertically in a density stratified liquid. *Journal of Fluid Mechanics*, 30:489 – 495, 1967.

[155] D.E. Mowbray and B.S.H. Rarity. A theoretical and experimental investigation of the phase configuration of internal waves of small amplitude in a density stratified liquid. *Journal of Fluid Mechanics*, 28:1 – 16, 1967.

[156] W.H. Munk. Abyssal recipes. *Deep-Sea Research*, 13:707 – 730, 1966.

[157] W.H. Munk and C. Wunsch. Abyssal recipes ii: Energetics of tidal and wind mixing. *Deep-Sea Research I*, 45:1977 – 2010, 1998.

[158] J.T. Nault and B.R. Sutherland. Internal wave transmission in non-uniform flows. *Physics of Fluids*, 19, 2007.

[159] A. Nikolopoulos, R. S. Pickart, P. S. Fratantoni, K. Shimada, D. J. Torres, and E. P. Jones. The western Arctic boundary current at 152°W: Structure, variability, and transport. *Deep Sea Research II*, 56:1164 – 1181, 2009.

[160] M. Nikurashin and R. Ferrari. Overturning circulation driven by breaking internal waves in the deep ocean. *Geophysical Research Letters*, 40:3133 – 3137, 2013.

[161] A. Nummelin, C. Li, and L.H. Smedsrud. Response of arctic ocean stratification to changing river runoff in a column model. *Journal of Geophysical Research: Oceans*, 120:2655 – 2675, 2015.

[162] J. Nycander. Generation of internal waves in the deep ocean by tides. *Journal of Geophysical Research: Oceans*, 110:C10028, 2005.

[163] F.W.J. Olver, D.W. Lozier, R.F. Boisvert, and C.W. Clark. *NIST Handbook of Mathematical Functions*. Cambridge University Press, 2010.

[164] G. Oster and M. Yamamoto. Density gradient techniques. *Chemical Review*, 63:257 – 268, 1963.

[165] J. Overland, E. Hanna, I. Hanssen-Bauer, S.-J. Kim, J.E. Walsh, U.S. Wang, M. ans Bhatt, and R.L. Thoman. 2015: Surface air temperature. *NOAA Arctic Report Card*, 2016.

[166] A. Pacini, G.W.K. Moore, R.S. Pickart, C. Nobre, F. Bahr, K. Vage, and K.R. Arrigo. Characteristics and transformation of the pacific winter water on the chukchi sea shelf in late-spring. *Journal of Geophysical Research: Oceans*, page accepted, 2019.

[167] M.S. Paoletti and H.L. Swinney. Propagating and evanescent internal waves in a deep ocean model. *Journal of Fluid Mechanics*, 706:571 – 583, 2012.

[168] R.G. Paquette and R.H. Bourke. Observations on the coastal current of Arctic Alaska. *Journal of Marine Research*, 32:195 – 207, 1974.

[169] T. Peacock and P. Weidman. The effect of rotation on conical wave beams in a stratified fluid. *Experiments in Fluids*, 39:32 – 37, 2005.

[170] T. Pedley. On the stability of viscous flow in a rapidly rotating pipe. *Journal of Fluid Mechanics*, 36:177 – 191, 1969.

[171] J. Pedlosky. *Waves in the Ocean and Atmosphere: Introduction to Wave Dynamics*. Springer, 2003.

[172] A. Perot. On the application of interference phenomena to the solution of various problems of spectroscopy and metrology. *Astrophysical Journal*, 9:87, 1899.

[173] O.M. Phillips. Energy transfer in rotating fluids by reflection of inertial waves. *Physics of Fluids*, 6:513 – 520, 1963.

[174] O.M. Phillips. *The dynamics of the Upper Ocean*. Cambridge University Press, 1966.

[175] R.S. Pickart. Shelfbreak circulation in the Alaskan Beaufort Sea: Mean structure and variability. *Journal of Geophysical Research*, 109:c04024, 2004.

[176] R.S. Pickart, G.W.K. Moore, C. Mao, F. Bahr, C. Nobre, and T.J. Weingartner. Circulation of winter water on the Chukchi shelf in early summer. *Deep-Sea Research II*, 130:56 – 75, 2016.

[177] R.S. Pickart and W.M.Jr. Smethie. Temporal evolution of the deep western boundary current where it enters the subtropical domain. *Deep-Sea Research I*, 45:1053 – 1083, 1998.

[178] R.S. Pickart, M.A. Spall, and J.T. Mathis. Dynamics of upwelling in the Alaskan Beaufort Sea and associated shelfbasin fluxes. *Deep-Sea Research I*, 76:35 – 51, 2013.

[179] R.S. Pickart and G. Stossmeister. Outflow of Pacific water from the Chukchi Sea to the Arctic Ocean. *Chinese Journal of Polar Science*, 19:135 – 148, 2008.

[180] R.S. Pickart, T.J. Weingartner, S. Zimmermann, D.J. Torres, and L.J. Pratt. Flow of winter-transformed Pacific water into the western Arctic. *Deep-Sea Research II*, 52:3175 – 3198, 2005.

[181] G. Pillet, E.V. Ermanyuk, L.R.M. Maas, I.N. Sibgatullin, and Dauxois T. Internal wave attractors in three-dimensional geometries: trapping by oblique reflection. *Journal of Fluid Mechanics*, 845:203 – 225, 2018.

[182] R. Pinkel, M.C. Buijsman, and J.M. Klymak. Breaking topographic lee waves in a tidal channel in luzon strait. *Oceanography*, 25:160 – 165, 2012.

[183] A.J. Plueddemann, R. Krishfield, T. Takizawa, K. Hatakeyama, and S. Honjo. Upper ocean velocities in the Beaufort Gyre. *Geophysical Research Letters*, 25:183 – 186, 1998.

[184] J.A. Polton, J.A. Smith, J.A. MacKinnon, and A.E. Tejada-Martínez. Rapid generation of high-frequency internal waves beneath a wind and wave forced oceanic surface mixed layer. *Geophysical Research Letters*, 35:L13602, 2008.

[185] I.V. Polyakov, A.V. Pnyushkov, and L.A. Timokhov. Warming of the intermediate atlantic water of the arctic ocean in the 2000s. *Journal of Climate*, 25:8362 – 8370, 2012.

[186] K.L. Polzin, J.M. Toole, J.R. Ledwell, and R.W. Schmitt. Spatial variability of turbulent mixing in the abyssal ocean. *Science*, 276:93 – 96, 1997.

[187] J. Pryce. Internal wave wake of a moving storm. part i. scales, energy budget and oservations. *Journal of Physical Oceanography*, 13:949 – 965, 1983.

[188] A. Rabiti and L.R.M. Maas. Equatorial wave attractors and inertial oscillations. *Journal of Fluid Mechanics*, 729:445 – 470, 2013.

[189] L. Rainville, C.M. Lee, and R.A. Woodgate. Impact of wind-driven mixing in the Arctic Ocean. *Oceanography*, 24:136, 2011.

[190] L. Rainville and R. Pinkel. Propagation of low-mode internal waves through the ocean. *Journal of Physical Oceanography*, 36:1220, 2006.

[191] L. Rainville and P. Winsor. Mixing across the Arctic Ocean: Microstructure observations during the Beringia 2005 expedition. *Geophysical Research Letters*, 35:L08606, 2008.

[192] L. Rainville and R.A. Woodgate. Observations of internal wave generation in the seasonally ice-free Arctic. *Geophysical Research Letters*, 36:L23604, 2009.

[193] J.W.S Rayleigh. *Theory of Sound (1896) 2nd ed.* Dover, 1945.

[194] M. Rieutord, B. Georgeot, and L. Valdettaro. Inertial waves in a rotating spherical shell: attractors and asymptotic spectrum. *Journal of Fluid Mechanics*, 85:4277 – 4280, 2000.

[195] M. Rieutord, B. Georgeot, and L. Valdettaro. Wave attractors in rotating fluids: a paradigm for ill-posed cauchy problems. *Physical Review Letters*, 435:103 – 144, 2001.

[196] M. Rieutord and L. Valdettaro. Inertial waves in a rotating spherical shell. *Journal of Fluid Mechanics*, 341:77 – 99, 1997.

[197] M. Rieutord and L. Valdettaro. Viscous dissipation by tidally forced inertial modes in a rotating spherical shell. *Journal of Fluid Mechanics*, 643:363 – 394, 2010.

[198] M. Rieutord, L. Valdettaro, and B. Georgeot. Analysis of singular inertial modes in a spherical shell: the slender toroidal shell model. *Journal of Fluid Mechanics*, 463:345 – 360, 2002.

[199] B. Rodenborn, D. Kiefer, H.P. Zhang, and H.L. Swinney. Harmonic generation by reflecting internal waves. *Physics of Fluids*, 23:026601, 2011.

[200] R.W. Schmitt. Double diffusion in oceanography. *Annual Review of Fluid Mechanics*, 26:255, 1994.

[201] R.W. Schmitt, H. Perkins, J.D. Boyd, and M.C. Stalcup. C-SALT: An investigation of the thermohaline staircase in the western tropical North Atlantic. *Deep-Sea Research*, 34:1655, 1987.

[202] W.H. Schubert, J.J. Hack, P.L. Silva Dias, and S.R. Fulton. Geostrophic adjustment in an axisymmetric vortex. *Journal of Atmospheric and Solar-Terrestrial Physics*, 37:1464 – 1484, 1980.

[203] H. Scolan, E. Ermanyuk, and T. Dauxois. Nonlinear fate of internal waves attractors. *Physical Review Letters*, 110:234501, 2013.

[204] R. Scott, R.S. Pickart, P. Lin, A. Munchow, M. Li, D.A. Stockwell, and G.W.K. Moore. Three dimensional structure of a cold-core arctic eddy interacting with the chukchi slope current. *Journal of Geophysical Research: Oceans*, pages 8375 – 8391, 2019.

[205] R.K. Scott and L.M. Polvani. Forced-dissipative shallow-water turbulence on the sphere and the atmospheric circulation of the giant planets. *Journal of Atmospheric Sciences*, 64:3158–3176, 2007.

[206] D.D Sentman, E.M Wescott, R.H. Picard, J.R. Winick, H.C. Stenbaeck-Nielsen, E.M. Dewan, D.R. Moudry, F.T. São Sabbas, M.J. Heavner, and J. Morrill. Simultaneous observations of mesospheric gravity waves and sprites generated by a midwestern thunderstorm. *Journal of Atmospheric and Solar-Terrestrial Physics*, 65:537 – 550, 2003.

[207] W.J. Shaw and T.P. Stanton. Vertical diffusivity of the Western Arctic Ocean halocline. *Journal of Geophysical Research: Oceans*, 119:5017 – 5038, 2014.

[208] N.D. Shmakova and J.-B. Flór. Nonlinear aspects of focusing internal waves. *Journal of Fluid Mechanics*, 862:R4, 2019.

[209] I. Sibgatullin, E.V. Ermanyuk, X. Xiulin, L.R.M. Maas, and T. Dauxois. Direct numerical simulation of three–dimensional inertial wave attractors. *Ivannikov ISPRAS Open Conference*, 2017.

[210] M.A. Spall, R.S. Pickart, M. Li, M. Itoh, P. Lin, T. Kikuchi, and Y. Qi. Transport of Pacific water into the Canada Basin and the formation of the Chukchi Slope Current. *Journal of Geophysical Research: Oceans*, 2018.

[211] E.A. Spiegel and G. Veronis. On the boussinesq approximation for a compressible fluid. *Astrophysical Journal*, 131:442 – 447, 1960.

[212] P. Stabeno, N. Kachel, C. Ladd, and R. Woodgate. Flow patterns in the eastern Chukchi Sea: 2010–2015. *Journal of Geophysical Research*, 123:1177 – 1195, 2018.

[213] C. Staquet and J. Sommeria. Internal gravity waves: From instabilities to turbulence. *Annual Review of Fluid Mechanics*, 34:559, 2002.

[214] M.E. Stern. Trapping of low frequency oscillations in an equatorial boundary layer. *Tellus*, 15:246 – 250, 1963.

[215] T.N. Stevenson. Axisymmetric internal waves generated by a travelling oscillating body. *Journal of Fluid Mechanics*, 35:219 – 224, 1969.

[216] K. Stewartson. On trapped oscillations of a rotating fluid in a thin spherical shell. *Tellus*, 23:506 – 510, 1971.

[217] K. Stewartson. On trapped oscillations of a rotating fluid in a thin spherical shell ii. *Tellus*, 24:283 – 287, 1972.

[218] I Stirling and A.E. Derocher. Effects of climate warming on polar bears: a review of the evidence. *Global Change Biology*, 18:2694 – 2706, 2012.

[219] R. Supekar and T. Peacock. Interference and transmission of spatiotemporally locally forced internal waves in non-uniform stratifications. *Journal of Fluid Mechanics*, 2019.

[220] B.R Sutherland. *Internal Gravity Waves*. Cambridge University Press, 2010.

[221] B.R. Sutherland. Excitation of superharmonics by internal modes in non-uniformly stratified fluid. *Journal of Fluid Mechanics*, 793:335 – 352, 2016.

[222] B.R. Sutherland. Inernal wave transmission through a thermohaline staircase. *Physical Review Fluids*, 1:013701, 2016.

[223] B.R. Sutherland, S.B. Dalziel, G.O. Hughes, and P.F. Linden. Visualization and measurement of internal waves by 'synthetic schlieren'. part 1. vertically oscillating cylinder. *Journal of Fluid Mechanics*, 390:93 – 126, 1999.

[224] B.R. Sutherland and K. Yewchuck. Internal wave tunnelling. *Journal of Fluid Mechanics*, 2004.

[225] N.H. Thomas and T.N. Stevenson. A similarity solution for viscous internal waves. *Journal of Fluid Mechanics*, 54:495 – 506, 1972.

[226] W. Thomson. Vibrations of a columnar vortex. *Philosophy Magasine*, 10:152 – 165, 1880.

[227] S.A. Thorpe. On wave interactions in a stratified fluid. *Journal of Fluid Mechanics*, 24:737 – 751, 1966.

[228] S.A. Thorpe. On standing internal gravity waves of finite amplitude. *Journal of Fluid Mechanics*, 32:489 – 528, 1968.

[229] S.A. Thorpe. On the shape of progressive internal waves. *Philosophical Transactions of the Royan Society London: Series A*, 263:563 – 614, 1968.

[230] S.A. Thorpe. *The Turbulent Ocean*. Cambridge University Press, 2005.

[231] M.-L. Timmermans, S. Cole, and J. Toole. Horizontal density structure and restratification of the Arctic Ocean surface layer. *Journal of Physical Oceanography*, 42:659, 2012.

[232] M.-L. Timmermans, J. Marchall, A. Proshutinsky, and J. Scott. Seasonally derived components of the Canada Basin halocline. *Geophysical Research Letters*, 44:5008 – 5015, 2017.

[233] M.-L. Timmermans, J. Toole, R. Krishfield, and P. Winsor. Ice-tethered profiler observations of the double-diffusive staircase in the Canada Basin thermocline. *Journal of Geophysical Research*, 113:C00A02, 2008.

[234] U. Tricoli. *Electromagnetic scattering with the GDT-matrix method: an application to irregular ice particles in cirrus*. PhD thesis, Ruperto-Carola-University of Heidelberg, 2014.

[235] D. Varma and M. Mathur. Internal wave resonant triads in finite-depth non-uniform stratifications. *Journal of Fluid Mechanics*, 824:286 – 311, 2017.

[236] S.K. Venayagamoorthy and O.B. Fringer. On the formation and propagation of nonlinear internal boluses across a shelf break. *Journal of Fluid Mechanics*, 577:137 – 159, 2007.

[237] B. Voisin. Limit states of internal waves beams. *Journal of Fluid Mechanics*, 496:243 – 293, 2003.

[238] B. Voisin, E.V. Ermanyuk, and J.-B. Flór. Internal wave generation by oscillation of a sphere, with application to internal tides. *Journal of Fluid Mechanics*, 666:308 – 357, 2011.

[239] G.L. Wagner and W.R. Young. A three-component model for the coupled evolution of near-inertial waves, quasi-geostrophic flow and the near-inertial second harmonic. *Journal of Fluid Mechanics*, 802:806 – 837, 2016.

[240] F.W.G. Warren. Wave resistance to vertical motion in a stratified fluid. *Fluid Mechanics*, 7:209 – 229, 1960.

[241] E. Watanabe, J. Onodera, M. Itoh, S. Nishino, and T. Kikuchi. Winter transport of subsurface warm water toward the Arctic Chukchi borderland. *Deep-Sea Research I*, 128:115 – 130, 2017.

[242] A.F. Waterhouse, J.A. MacKinnon, J.D. Nash, M.H. Alford, E. Kunze, H.L. Simmons, K.L. Polzin, L.C. St Laurent, O.M. Sun, R. Pinkel, L.D. Talley, C.B. Whalen, T.N. Huussen, G.S. Carter, I. Fer, S. Waterman, A.C. Naveira Garabato, T.B. Sanford, and C.M. Lee. Global patterns of diapycnal mixing from measurements of the turbulent dissipation rate. *Journal of Physical Oceanography*, 44:1854 – 1872, 2014.

[243] T. Weingartner, K. Aagaard, R. Woodgate, S. Danielson, Y. Sasaki, and D. Cavalieri. Circulation on the north central Chukchi Sea shelf. *Deep-Sea Research II*, 52:3150 – 3174, 2005.

[244] W.J. Williams, E.C. Carmack, K. Shimada, H. Melling, K. Aagaard, R.W. Macdonald, and R. Grant Ingram. Joint effects of wind and ice motion in forcing upwelling in Mackenzie Trough, Beaufort Sea. *Continental Shelf Research*, 26:2352 – 2366, 2006.

[245] K.B. Winters, P.N. Lombard, J.J. Rilez, and E.A. D'Asaro. Available potential energy and mixing in density-stratified fluids. *Journal of Fluid Mechanics*, 289:115 – 128, 1995.

[246] R.A. Woodgate. Increases in the Pacific inflow to the Arctic from 1990 to 2015, and insights into seasonal trends and driving mechanisms drom year-round Bering Strait mooring data. *Progress in Oceanography*, 160:124 – 164, 2018.

[247] R.A. Woodgate, K. Aagaard, J.H. Swift, W.M. Jr. Smethie, and K.K. Falkner. Atlantic water circulation over the Mendeleev Ridge and Chukchi Borderland from thermohaline intrusions and water mass properties. *Journal of Geophysical Research*, 112:C02005, 2007.

[248] K. Wu, B.D. Welfert, and J.M. Lopez. Reflections and focusing of inertial waves in a librating cube with the rotation axis oblique to its faces. *Journal of Fluid Mechanics*, 896, 2020.

[249] C. Wunsch and R. Ferrari. Vertical mixing energy, and the general circulation of the oceans. *Annual Review of Fluid Mechanics*, 36:281 – 314, 2004.

[250] S. Wunsch. Nonlinear harmonic generation by internal waves in a density staircase. *Physical Review Fluids*, 3:114803, 2018.

[251] S. Wunsch, I. Delwiche, G. Frederick, and A. Brandt. Experimental study of nonlinear harmonic generation by internal waves incident on a pycnocline. *Experiments in Fluids*, 56:87, 2015.

[252] S. Wunsch, H. Ku, I. Delwiche, and R. Awadallah. Simulations of nonlinear harmonic generation by an internal wave beam incident on a pycnocline. *Nonlinear Processes in Geophysics*, 21:855 – 868, 2014.

[253] W.R. Young, Y.-K. Tsang, and N.J. Balmforth. Near-inertial parametric subharmonic instability. *Journal of Fluid Mechanics*, 607:25 – 49, 2008.

[254] R.K. Zeytounian. Joseph boussinesq and his approximation: a contemporary view. *C.R. Mecanique*, 331:575 – 586, 2003.

[255] M. Zhao, M. L. Timmermans, S. Cole, R. Krishfield, A. Proshutinsky, and J. Toole. Characterizing the eddy field in the arctic ocean halocline. *Journal of Geophysical Research: Oceans*, 119:8800–8817, 2014.

[256] M. Zhao, M.-L. Timmermans, S. Cole, R. Krishfield, and J. Toole. Evolution of the eddy field in the Arctic Ocean's Canada Basin, 2005–2015. *Journal of Geophysiscal Research*, 43:8106 – 8114, 2016.

[257] Z. Zhao, M.H. Alford, J.A. MacKinnon, and R. Pinkel. Long-range propagation of the semidiurnal internal tide from the hawaiian ridge. *Journal of Physical Oceanography*, 40:713 – 736, 2010.